

A Cryogenic Mass Spectrometer for Action Spectroscopy of Single Nanoparticles

Von der Fakultät für Chemie und Mineralogie

der Universität Leipzig

genehmigte

D I S S E R T A T I O N

zur Erlangung des akademischen Grades

DOCTOR RERUM NATURALIUM

(Dr. rer. nat.)

vorgelegt

von

M.Sc. Tim Esser

geboren am 16.06.1989 in Duisburg

Angenommen aufgrund der Gutachten von:

Prof. Dr. Knut R. Asmis

Prof. Dr. Stephan Schlemmer

Tag der Verleihung: 25.03.2019

Die vorliegende Dissertation wurde im Zeitraum vom November 2013 bis Januar 2019 unter Betreuung von Prof. Dr. Knut R. Asmis am Wilhelm-Ostwald-Institut mit Genehmigung der Fakultät für Chemie und Mineralogie der Universität Leipzig angefertigt. Die ersten sechs Monate wurden in der Abteilung Molekülphysik des Fritz-Haber-Instituts der Max-Planck-Gesellschaft durchgeführt.

Bibliographische Daten

A Cryogenic Mass Spectrometer for Action Spectroscopy of Single Nanoparticles
Tim Esser, Universität Leipzig, Dissertation, 21.01.2019
182 Seiten, 61 Abbildungen, 15 Tabellen, 209 Referenzen

Selbständigkeitserklärung gemäß § 9 (2) der Promotionsordnung

Ich versichere, dass die vorliegende Arbeit ohne unzulässige Hilfe und ohne Benutzung anderer als der angegebenen Hilfsmittel angefertigt wurde und dass die aus fremden Quellen direkt oder indirekt übernommenen Gedanken in der Arbeit als solche kenntlich gemacht worden sind.

Alle Personen, von denen ich bei der Erstellung, Auswahl und Auswertung des Materials sowie bei der Erstellung des Manuskripts Unterstützungsleistungen erhalten habe, sind in der Dissertationsschrift angegeben.

Ich versichere, dass außer den genannten keine weiteren Personen bei der geistigen Herstellung der vorliegenden Arbeit beteiligt waren, insbesondere auch nicht die Hilfe eines Promotionsberaters in Anspruch genommen wurde, und dass Dritte von mir weder unmittelbar noch mittelbar geldwerte Leistungen für Arbeiten erhalten haben, die im Zusammenhang mit dem Inhalt der vorgelegten Dissertation stehen.

Außerdem versichere ich, dass die vorgelegte Arbeit weder im Inland noch im Ausland in gleicher oder in ähnlicher Form einer anderen Prüfungsbehörde zum Zwecke einer Promotion oder eines anderen Prüfungsverfahrens vorgelegt wurde.

Es haben keine früheren erfolglosen Promotionsversuche stattgefunden.

Ort, Datum

Tim Esser

Zusammenfassung

Die physikalischen, chemischen und biologischen Eigenschaften von Nanopartikeln weichen aufgrund von Form, Oberflächen-zu-Volumen-Verhältnis und Quanten-Effekten deutlich von denen größerer Partikel und von Festkörpern ab. Sie werden für Solarzellen, Lichtquellen, Katalysatoren, Solarbrennstoffe, Nanokomposite wie Beton, Krebstherapie und medizinische Bildgebung eingesetzt. Aufgrund ihres umfangreichen Potenzials für technologische Anwendungen sind sie Gegenstand aktiver Forschung. Parallel zur rasanten Entwicklung der Nanotechnologie werden vermehrt die Auswirkungen von natürlichen und künstlichen Nanopartikeln auf Gesundheit und Klima untersucht.

Herkömmliche experimentelle Techniken sind oft auf Untersuchungen von Nanopartikeln in Lösungen oder auf Oberflächen beschränkt und sind auf eine große Anzahl von Partikeln angewiesen. Dadurch können die grundlegenden, größenabhängigen Eigenschaften von Nanopartikeln verschleiert werden. Neue Techniken sind erforderlich, um ein tieferes Verständnis dieser Größenabhängigkeit zu ermöglichen, z.B. durch Analyse einzelner Nanopartikel mit klar definierter Masse und Ladung und ohne störende Wechselwirkungen.

Diese Dissertation legt den Grundstein für eine neue experimentelle Technik zur Untersuchung einzelner Nanopartikel in der Gasphase, durch Kombination von Nanopartikel-Massenspektrometrie (NPMS) mit Photodissoziations-Wirkungsspektroskopie. Zu diesem Zweck wurde ein neues NPMS Experiment entworfen, konstruiert und charakterisiert. NPMS, derzeit nur in wenigen Labors weltweit eingesetzt, ist eine Technik bei der die absolute Masse eines einzelnen Nanopartikels in einer Paul-Falle optisch und daher zerstörungsfrei bestimmt wird. Die wesentliche Neuerung des aktuellen Aufbaus, und Kernelement dieser Arbeit, ist eine neue Tieftemperatur-Ionenfalle, mit verbessertem optischen Zugang, Temperaturkontrolle (8 to 350 K) und elektrischem Potential im Vergleich zu bisher verwendeten Modellen.

Der Fangmechanismus im neuen Aufbau wird durch Experimente und Simulationen analysiert und praktische Betriebsparameter werden diskutiert. Bei Raumtemperatur werden Coulomb-Kristalle aus Nanopartikeln gebildet, um die Vorbereitung von Experimenten mit einzelnen Partikeln zu erleichtern. Temperaturabhängige Verdampfung von einzelnen Eispartikeln wurde beobachtet, was eine mögliche Anwendung der Technik in der Astrophysik und atmosphärischen Chemie aufzeigt. Die Massenbestimmung von einzelnen Polymethylmethacrylat (PMMA) und SiO_2 Nanopartikeln über Fourier-Transformation und resonante Anregung wird demonstriert. Im Experiment kann die Massenänderung eines einzelnen Nanopartikels in Abhängigkeit von der Falltemperatur, Zusammensetzung und Druck des Hintergrundgases sowie Laserstrahlung über mehrere Tage verfolgt werden. Erstmals konnte Adsorption von Argon auf einem einzelnen SiO_2 -Nanopartikel in einer Tieftemperatur-Ionenfalle beobachtet werden. Zusammen mit laserinduzierten Veränderungen der Desorptionsraten, stellt dies einen wesentlichen Schritt in Richtung Wirkungsspektroskopie einzelner Nanopartikel dar.

Abschließend werden die noch fehlenden Schritte zur Erfassung von Wirkungsspektren und mögliche erste Modellsysteme diskutiert. Experimentelle und theoretische

Anforderungen zur Bestimmung von Partikeltemperaturen und Adsorbatbindungsenergien aus Desorptionsraten werden zusammengefasst. Der neue NPMS Aufbau wird die Messung der ersten UV-VIS und Infrarot Spektren einzelner Nanopartikel in naher Zukunft ermöglichen.

Summary

Nanoparticles have physical, chemical and biological properties that are distinct from bulk matter, due to their shape, surface-to-volume ratio and quantum effects. They are used for solar cells, light sources, catalysts, solar fuels, nanocomposite materials like concrete, cancer therapy and medical imaging. Because of their extensive potential for technological applications, they are subject to active research. Parallel to the rapid expansion of nanotechnology, substantial efforts have been made to assess the effects of natural and man-made nanoparticles on health and climate.

Conventional experimental techniques are often limited to studies of nanoparticles in solutions or on surfaces and rely on a large number of particles. Thus, the fundamental, size-dependent properties of nanoparticles can be obscured. Novel techniques are required, to provide a deeper understanding of this size-dependence, *e.g.* by analysis of single nanoparticles with well-defined mass and charge and in the absence of perturbing interactions with an environment.

This doctoral thesis lays the foundations for a novel experimental technique, combining nanoparticle mass spectrometry (NPMS) with photodissociation action spectroscopy, to investigate single nanoparticles in the gas phase. To this end, a new NPMS setup was designed, constructed and characterized. NPMS, currently used in only a few laboratories worldwide, is a technique where the absolute mass of a single nanoparticle, trapped in a quadrupole ion trap (QIT), is determined non-destructive by optical means. The essential novelty of the current setup, and core element of this thesis, is a new cryogenic split-ring electrode trap (SRET) design, with improved optical access, temperature control (8 to 350 K) and trapping potential compared to previously used versions.

The trapping mechanism in the novel setup is analyzed by experiments and simulations and practical operating parameters are discussed. Room-temperature Coulomb crystals of nanoparticles are formed to facilitate the preparation of single particle experiments. Temperature-dependent evaporation of single trapped water-ice particles was observed, revealing a potential application of the technique in astrophysics and atmospheric chemistry. Mass determination of single poly(methyl methacrylate) (PMMA) and SiO₂ nanoparticles using the Fourier transformation (FT) and resonant excitation methods is demonstrated. The setup can monitor the mass variation of a single nanoparticle, as a function of ion-trap temperature, composition and pressure of background gas, and laser irradiation, over multiple days. Argon messenger-tagging of a single SiO₂ nanoparticle in a cryogenic ion trap was performed for the first time. Together with laser induced changes in argon desorption rates, this represents a fundamental step towards action spectroscopy of single nanoparticles.

Finally, the missing steps towards acquisition of action spectra and possible initial model systems are discussed. Experimental and theoretical requirements to infer particle temperatures and adsorbate binding energies from desorption rates are given. The novel NPMS setup will enable the acquisition of the first UV-VIS and infrared (IR) spectra of single nanoparticles, in the near future.

Contents

Abbreviations	xiii
1 Introduction	1
1.1 Nanoparticles: Properties, Impact and Applications	1
1.2 Experimental Techniques for Nanoparticle Analysis	2
1.3 Infrared Photodissociation Spectroscopy of the Microhydrated Proton and Cs ⁺	3
1.4 Goal and Outline of This Thesis	4
2 Nanoparticle Mass Spectrometry (NPMS)	7
2.1 Mass-Spectrometric Techniques for Nanoparticle Analysis	7
2.2 Theory of the 3D Quadrupole Ion Trap (QIT)	11
2.2.1 Perturbations in a Real QIT	16
2.2.2 RF Supplies for Quadrupole Ion Trap Operation	17
2.3 History of NPMS and Measurement Modes	18
2.3.1 Star Pattern Imaging	19
2.3.2 Fourier Transformation	19
2.3.3 Resonant Excitation	20
2.3.4 Absolute Mass Measurement	22
2.4 Precision and Accuracy of NPMS Measurements	23
2.4.1 NPMS for Particle Sizes Below 50 nm	25
3 The Nanoparticle Mass Spectrometry Setup	27
3.1 Overview of the Experimental Setup	27
3.2 Vacuum System	29
3.3 Nanoparticle Source	34
3.4 Ion Optics	39
3.4.1 Gate Valve	39
3.4.2 Electrostatic Quadrupole Deflector	40
3.5 Linear RF Multipoles	41
3.6 Split-Ring Electrode Trap (SRET)	46
3.6.1 Genetic Algorithm	47
3.6.2 Optimization of the SRET Geometry	48
3.6.3 Implementation of the SRET Design	52
3.7 Light Sources and Optical Detection	57
3.8 Ion Detection	60

3.9	Cryogenic Cooling	61
3.10	Electronics, Measurement Control and Data Acquisition	62
3.11	Simulation of Guiding and Trapping	63
3.12	The Linear Setup	66
4	Characterization and Initial Observations	69
4.1	Trapping a Single Particle	69
4.2	Room-Temperature Coulomb Crystals	73
4.3	Water-Ice Particles	74
4.4	Peak Shapes and Shifts in FT Spectra	74
4.5	Peak Shapes in Resonant Excitation Spectra	78
5	Single Nanoparticle Messenger-Tagging	83
5.1	Argon Adsorption on Single SiO ₂ Particles	83
5.2	Argon Ad- and Desorption Experiments on a Single SiO ₂ Particle	86
5.3	Ad- and Desorption Kinetics of Single Nanoparticles	93
6	Outlook	95
6.1	Towards Action Spectroscopy of Single Nanoparticles	95
6.1.1	Future Research and Applications	97
6.2	Suggested Instrumental Upgrades	98
6.3	Other Directions for NPMS Experiments	99
Appendix A Deconstructing Prominent Bands in the Terahertz Spectra of H₇O₃⁺ and H₉O₄⁺		101
A.1	Experimental Details	107
A.2	Computational Details	108
A.3	References	109
Appendix B Influence of Argon and D₂ Tagging on the Hydrogen Bond Network in Cs⁺(H₂O)₃		117
B.1	Introduction	117
B.2	Experimental Details	119
B.3	Computational details	121
B.4	Results	123
B.5	References	133
Appendix C LabVIEW Measurement Software		141
C.1	Implementation and Device Communication	143
C.2	Recording and Saving of Data	143
C.3	Devices and Corresponding VIs	148
C.4	Anticipated Upgrades	149

Appendix D Virtual Setup and Trap Geometry Optimization	151
D.1 SIMION User Programs	151
D.2 Concept and Implementation of the Genetic Algorithm	152
Bibliography	157
List of Publications	175
Talks and Poster Contributions	177
Curriculum Vitae	179
Danksagung / Acknowledgments	181

Abbreviations

AC	alternating current
AFM	atomic force microscopy
APD	avalanche photodiode
AWG	American wire gauge
BEM	boundary element method
BOMD	Born-Oppenheimer Molecular Dynamics
CAD	computer aided design
CCD	charge coupled device
CDMS	charge detection mass spectrometry
CFD	computational fluid dynamics
CID	collision induced dissociation
CNC	condensation nuclei counter
CRM	charge residue model
CVD	chemical vapor deposition
CW	continuous wave
DC	direct current
DHO	double harmonic oscillator
DIT	digital ion trap
DLS	dynamic light scattering
DMA	differential mobility analyzer
DMD	driven molecular dynamics
DPSS	diode pumped solid state
EDB	electrodynamic balance
EDX	energy-dispersive X-ray spectroscopy
EELS	electron energy loss spectroscopy
EMCCD	electron-multiplying charge coupled device

EM	electron multiplier
ESI	electrospray ionization
FDM	finite differences method
FEM	finite element method
FTICR	Fourier transform ion cyclotron resonance
FTIR	Fourier transform infrared spectroscopy
FT	Fourier transformation
FWHM	full width half maximum
GA	genetic algorithm
HV	high vacuum
IBD	ion beam deposition
ICCD	intensified charge coupled device
IEM	ion evaporation model
IRPD	infrared photodissociation
IR	infrared
LIF	laser induced fluorescence
LIT	linear ion trap
LiTD	laser induced thermal desorption
<i>M/Q</i>	mass-to-charge ratio
MCP	micro-channel plate
MFP	mean free path
MIA	macromolecular ion accelerator
ML	monolayer
NBR	nitrile rubber
NEMS	nanoelectromechanical system
NPMS	nanoparticle mass spectrometry
PEEK	polyether ether ketone
PID	partial integral differential
PL	photoluminescence
PMMA	poly(methyl methacrylate)
PMT	photomultiplier tube

PTFE	polytetrafluoroethylene
QCMD	quasiclassical molecular dynamics
QITMS	quadrupole ion trap mass spectrometry
QIT	quadrupole ion trap
QMS	quadrupole mass spectrometer
QSM	queued state machine
RET	ring electrode trap
RF	radio frequency
SEM	scanning electron microscopy
SMMS	single molecule mass spectrometry
SPMS	single particle mass spectrometry
SPM	scanning probe microscopy
SRET	split-ring electrode trap
STJ	superconducting tunnel junction
STM	scanning tunneling microscopy
TEM	transmission electron microscopy
TOFMS	time-of-flight mass spectrometer
TOF	time-of-flight
TPD	temperature programmed desorption
TTL	transistor transistor logic
UHV	ultra-high vacuum
UV-VIS	ultraviolet-visible spectroscopy
VI	virtual instrument
VSCF/VCI	vibrational self-consistent field/virtual state configuration interaction
VUV	vacuum ultraviolet
XAS	X-ray absorption spectroscopy
XPS	X-ray photoelectron spectroscopy
XRD	X-ray diffraction
ZPE	zero-point energy

1 Introduction

The development of modern nanotechnology and nanoscience dates back to Richard Feynman's famous lecture "There's Plenty of Room at the Bottom", in 1959 in which he envisioned the manipulation of matter at the atomic scale and discussed implications for data storage, biology, computer technology and other fields.[1] With the development of scanning tunneling microscopy (STM) and atomic force microscopy (AFM) in the 1980s, the field started a rapid expansion which is continuing to the present day. A multitude of new functions and applications result from the enhancement of physical, chemical and biological properties of nanoparticles compared to bulk matter, due to shape, surface-to-volume ratio and quantum effects.[2–8] Many applications of nanotechnology, such as sunscreen, paints, hydrophobic surfaces, and antibacterial clothing, are already part of our everyday life. The structures of computer chips recently reached dimensions as small as 10 nm, allowing to further increase processing speed and capacity.[9]

Nanomaterials are defined as matter with structures in the size range of 1 to 100 nm in at least one spatial dimension and are categorized according to their origin, composition, size and shape.[5, 10] While nanoscience aims to improve our knowledge of the fundamental principles behind their unique properties, nanotechnology encompasses the fabrication and manipulation of nanomaterials using this scientific knowledge.[5]

Man-made nanomaterials are either specifically engineered, like quantum dots and carbon nanotubes, or formed as byproducts in industrial processes and combustion engines, like dust and soot particles. Natural nanomaterials include animal skin and hair, plant tissue, minerals and aerosols particles formed during fires, dust storms, volcanic eruptions and from sea spray. Organic nanomachines like viruses and proteins are formed from single atoms in a bottom-up approach, while man-made structures, like computer chips, are often made from bigger precursors using a less accurate top-down approach. Based on their shape, nanomaterials are divided into nanoobjects, like nanofibers, nanowires, nanoplates or nanoparticles, and nanostructured materials, like agglomerates, aggregates of nanoobjects and nanocomposite materials.

Nanoparticles are of particular interest due to their potential for technological advancements, but also due to their effects on human health and climate, which is still not well understood and subject to active research.[5, 11, 12]

1.1 Nanoparticles: Properties, Impact and Applications

Nanoobjects with all three dimensions between 1 and 100 nm are called nanoparticles.[5] They were used by men as early as 5000, 4000 and 1400 BC as bleach and as hair

and glass dyes, respectively. The first scientific description of nanoparticle synthesis was made in 1857 by Michael Faraday, who investigated the optical characteristics of gold colloids.[13] Nanoparticles are synthesized either bottom-up, *e.g.* by condensation, chemical vapor deposition (CVD) and molecular self-assembly, or top-down, *e.g.* by ball milling, etching and sputtering.[14] Optical, electrical, thermodynamical, mechanical and catalytical characteristics can often be controlled by changing the particle size, shape and composition. Natural sources include the above-mentioned aerosol formation mechanisms and organic nanoparticles like viruses and proteins.

For diameters above 100 nm, the particle properties are comparable to bulk matter.[15] Between 10 nm and 100 nm properties change continuously with size and below 10 nm quantum effects become increasingly relevant.[4, 16, 17] For even smaller particles, like molecules and molecular clusters, properties can significantly change upon addition of single atoms.[7, 18, 19]

Examples for nanoparticle applications include solar cells[20, 21] other optoelectronic devices,[22] catalysts,[23, 24] solar fuels,[25] nanocomposite materials like concrete,[26] cancer therapy,[27, 28] medical imaging[29] and drug delivery.[30, 31] Parallel to the rapid expansion of nanotechnology, substantial efforts have also been made to assess the effects of natural and man-made nanoparticles on health and climate.[5, 11, 32, 33] Medical applications also require detailed analysis of organic nanoparticles like proteins.[34–36]

Nanoparticles in the gas phase occur primarily in the earth's atmosphere, around planets and moons and in interstellar space.[5, 10, 33, 37, 38] Investigation of corresponding particles under pristine conditions (defined by temperature, pressure and background gas composition) is an increasingly active research field.[11, 39]

Primary nanoparticle aerosols in the atmosphere originate from the above-mentioned emission sources. Secondary nanoparticle aerosols are formed by nucleation, coagulation and aggregation of primary aerosols and gases within the atmosphere.[5, 33, 37, 40] They have a significant effect on climate, directly by light scattering and absorption[37] and indirectly as cloud condensation and ice nuclei.[41, 42] Breathing in dust nano- and microparticles can cause lung cancer, cardiovascular and respiratory diseases.[32, 43]

Nanoparticles based on carbon and silicates form the majority of interstellar dust and originate *e.g.* from supernovae events.[5, 38, 44] They catalyze the formation of H₂, methanol, HO₂, H₂O₂ and other compounds,[45, 46] affect the gas-phase chemistry by ad- and desorption[38, 47] and play an important role in the initial steps of planet formation.[39]

1.2 Experimental Techniques for Nanoparticle Analysis

The broad range of nanoparticle types and properties is reflected by the large amount of methods used for their characterization.[10, 14, 37, 48] Electronic and optical properties are probed by ultraviolet-visible spectroscopy (UV-VIS) and photoluminescence (PL).

The size and shape of particles deposited on surfaces can be analyzed using scanning probe microscopy (SPM) and scanning electron microscopy (SEM). In addition, X-ray diffraction (XRD), X-ray photoelectron spectroscopy (XPS), transmission electron microscopy (TEM), energy-dispersive X-ray spectroscopy (EDX), electron energy loss spectroscopy (EELS), Fourier transform infrared spectroscopy (FTIR) and Raman spectroscopy provide information on physical and chemical properties. The size distribution of aerosols is characterized by a combination of a differential mobility analyzer (DMA) and a condensation nuclei counter (CNC).[37] Surface charge and zeta potential of nanoparticles dispersed in a liquid can be analyzed by dynamic light scattering (DLS).

Gas-phase studies of size-selected nanoparticles are particularly useful for aerosol characterization and allow to eliminate perturbing interactions with a substrate or solution.[49] This can be achieved by suspending particles in electrodynamic, optical or acoustic traps or by mass spectrometry.[50–52] Mass-spectrometric techniques provide access to charge, mass and composition, and allow to select particles for further analysis.[11, 53] They often rely on averaging over an ensemble of particles and the size-dependence of nanoparticle properties can be obscured by the intrinsic size distribution, incomplete desolvation and different charge states. Single particle techniques are generally experimentally more demanding and slower compared to conventional mass spectrometry (see Sec. 2.1), but provide mass and size specific information that cannot be obtained in any other way.[11, 40, 54]

This thesis lays the foundations for a novel experimental technique, combining nanoparticle mass spectrometry (NPMS) with cryogenic ion-trap spectroscopy, to analyze single nanoparticles in the gas phase. It aims to provide a deeper understanding of the above-mentioned size-dependence by spectroscopic analysis of single nanoparticles with well-defined mass and charge. In NPMS, the absolute mass and charge of a single nanoparticle are determined non-destructively as described in Chapter 2. The technique can be used to investigate model systems related to most of the fields mentioned in Sec. 1.1.

1.3 Infrared Photodissociation Spectroscopy of the Microhydrated Proton and Cs⁺

Parallel to the work presented in the main body of this thesis, infrared photodissociation (IRPD) action spectroscopy was conducted on a 6 K ion-trap triple mass spectrometer, which is described in detail elsewhere.[55] This work focused on analysis of hydrogen bond networks in microhydrated ions and molecules as a benchmark for electronic structure calculations and to improve the fundamental understanding of water, the most ubiquitous solvent. IRPD allows the use of infrared (IR) spectroscopy as a sensitive probe for molecular structures for low-density gas-phase samples, where the absorption of IR radiation cannot be detected directly, but the action of IR radiation on matter,

e.g. dissociation, is experimentally accessible using mass spectrometry. The laser induced dissociation yields are monitored as the laser frequency is scanned to record IR spectra.[56] Molecular structures are typically assigned on the basis of comparison with electronic structure calculations. The multitude of successful applications of this technique, over the last three decades,[56–63] motivated the extension of the mass range to enable action spectroscopy of nanoparticles. The IRPD experiments, conducted as part of this thesis over a total of about 18 months, contributed to six publications. Two first author publications, prepared in collaboration with the groups of Joel M. Bowman, Marie-Pierre Gageot, James M. Lisy and Martina Kaledin, are reproduced in Appendix A and Appendix B.

1.4 Goal and Outline of This Thesis

The goal of this doctoral thesis was the design, construction and characterization of a mass spectrometer for action spectroscopy of single nanoparticles, in order to provide new insights into the size-dependence of physical and chemical properties of nanoparticles. Though the Asmis group already had many years of experience in instrument design and action spectroscopy on molecules, this thesis marks the first step towards investigation of real nanoparticles within the group.

The long-term goal is to study the size-dependent evolution of spectral features and structural motives over many orders of magnitude by comparison of action spectra of molecular clusters, nanoparticles and macroscopic surfaces. Action spectroscopy of surfaces is currently under active development[64, 65] and IRPD is routinely used for action spectroscopy of molecular ions and clusters,[56] where relative mass changes due to dissociation are large. Detecting mass changes due to loss or gain of a few molecules on a nanoparticle however, requires much higher precision than is typically achieved with conventional mass spectrometers (see Sec. 2.1). The instrument described in this thesis, is able to resolve such mass changes using NPMS and will bridge the gap between the other two techniques by enabling action spectroscopy in the intermediate size range. Though the underlying principles have been known for decades, NPMS experiments are currently conducted only in a few laboratories worldwide.[66–68] The current NPMS setup, including a novel design of a cryogenic split-ring electrode trap (SRET), is described in detail in Chapter 3. The ability to control the ion-trap temperature from 8 and 350 K and the optimized electric trap-potential are currently unique among all NPMS instruments.

The experimental design phase was supported by many discussions with Dieter Gerlich and Scott Anderson, who stimulated many developments in the field of NPMS within the past two decades. A three week visit in the laboratory of Scott Anderson provided invaluable practical experience and influenced many design decisions.

First results and the characterization of the current setup are presented in Chapter 4. Mass changes induced by ad- and desorption of molecules, depending on buffer gas composition and pressure, particle temperature and exposure to external light sources,

can be recorded over extended periods of time. Messenger tagging of a single SiO₂ particle with argon in a cryogenic ion trap was demonstrated for the first time and is presented in Chapter 5. Laser induced changes in ad- and desorption rates represent the first step towards action spectroscopy of single nanoparticles. The final steps towards acquisition of spectra, additional instrumental upgrades and possible initial model systems are discussed in the outlook (Chapter 6). In the near future, the novel instrument will enable acquisition of the first UV-VIS and infrared spectra of single nanoparticles.

2 Nanoparticle Mass Spectrometry

The ultimate goal of this thesis is to enable action spectroscopy of single nanoparticles, by way of photodesorption. This requires the detection of small mass changes by means of mass spectrometry. Various mass-spectrometric techniques are briefly reviewed in Sec. 2.1 and compared to NPMS. After a general introduction to the theory of the ideal quadrupole ion trap (QIT) in Sec. 2.2, determination of the mass-to-charge ratio (M/Q) via imaging of star-like standing wave patterns, Fourier transformation (FT) and resonant excitation will be presented in Sec. 2.3, followed by the determination of the absolute nanoparticle mass using charge steps. Finally, aspects relevant for high precision and high accuracy measurements as well as the applicability of NPMS for the investigation of nanoparticles in the range below 50 nm will be discussed in Sec. 2.4.

2.1 Mass-Spectrometric Techniques for Nanoparticle Analysis: State-Of-The-Art and Limitations

Wilhelm Wien identified the mass of a proton in 1898, by deflecting a beam of ionized gas in a magnetic field.[69] In 1909 Robert Millikan determined the charge of the electron using optically detected droplets, suspended in an electrostatic balance.[70] His experiment enabled the determination of the droplet mass with a precision of 10 pg and represents the beginning of mass spectrometry. Today, various powerful mass-spectrometric techniques are routinely used to obtain information on atomic and molecular sample composition, molecular structure, reaction rates and mechanisms, sample homogeneity and isotope abundance. The developments and multitude of applications of mass-spectrometric techniques are subject of many contributions in the literature.[54, 71–80] The full potential of mass spectrometry is only reached when it is combined with other techniques, like spectroscopy, ion mobility, gas chromatography, collision induced dissociation (CID), or ion beam deposition (IBD), in more advanced experiments. While the development of mass spectrometry was initially focused on atoms and small molecules, the applicable mass range and precision continuously increased over time. The following discussion will focus on state-of-the-art implementations of the currently most widely used mass-spectrometry techniques and their mass detection and precision limits. Selected experimental results are summarized in Tab. 2.1. A rough overview of the relevant mass ranges is shown in Fig. 2.1.

For both, quadrupole mass spectrometers (QMSs) and time-of-flight mass spectrometers (TOFMSs), the ions are detected destructively by charge amplification detectors, *e.g.* micro-channel plates (MCPs) and channeltrons, with velocity depended detection

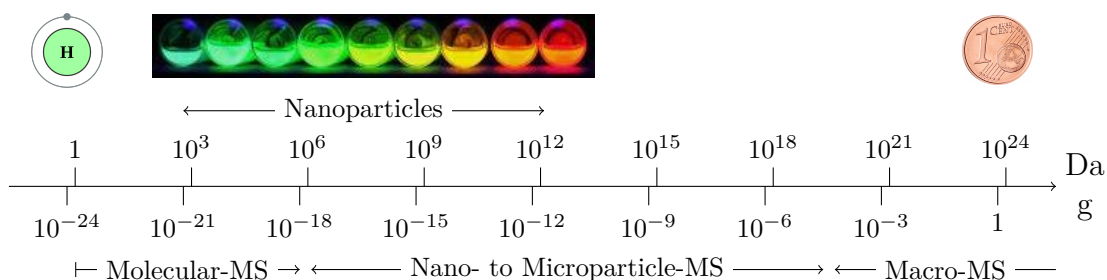


Fig. 2.1: Overview of mass ranges in mass spectrometry. Atomic and molecular ions up to 1 MDa can be investigated using a variety of established techniques. Particles with a mass above 0.1 mg are weighed with standard analytical scales. Mass spectrometry in the intermediate mass range is much more challenging, due to sample heterogeneity, limited precision and detection efficiency.

efficiency. While for ion energies of 10 keV the detection efficiency of MCPs is around 80 % for 2 kDa particles it drops to 5 % for 10 kDa and will thus be unreasonably low for detection of much larger single nanoparticles.[81] The upper M/Q limit is below $6 \text{ kDa} e^{-1}$ and $50 \text{ kDa} e^{-1}$ for most commercial QMSs and TOFMSs.[72, 82] The mass range can be extended up to $30 \text{ MDa} e^{-1}$ by accelerating ions using a macromolecular ion accelerator (MIA).[72] Detection of 1 MDa particles was demonstrated using field emission from a nanomembrane.[82] The sensitivity for heavy ions is also increased by detection using a scintillator and photomultiplier tube (PMT).[83] Alternatively, different types of cryogenic detectors are used, where detection efficiency depends only on ion energy and not on velocity.[84–86] For low charge states and sufficient energy resolution, which is not generally given, these detectors also allow for determination of the absolute mass. However, they have to be operated at cryogenic temperatures, have long response times and a small detection area.[87] Even the most sensitive TOFMSs are restricted to particles with masses less than a few MDa, corresponding to a diameter of approx. 10 nm, and the precision is typically limited by the detection response time and intrinsic mass distribution of the sample.[54, 75, 88]

Orbitrap and Fourier transform ion cyclotron resonance (FTICR) mass spectrometry are non-destructive techniques that rely on image charge detection and have the potential for very high precision.[89] The lower detection limit is given by the charge state and number of particles. The finite charge capacity can become a problem for analysis of broad M/Q distributions.[54] Single particle experiments and absolute mass determination by changing charge states is possible with both techniques. Particles with masses as high as 1 MDa and 110 MDa were analyzed by Orbitrap and FTICR, respectively, but with much lower precision than in the kDa range.[90, 91]

Charge detection mass spectrometry (CDMS) is a single particle technique where charge is measured, either non-destructively by image charge detection or destructively using a Faraday plate.[72, 92] The absolute mass is found from the charge and M/Q , which is determined either simultaneously, from the flight time through the charge

Table 2.1: Comparison of mass-spectrometric techniques for nano- and microparticles. The values given here represent results from state-of-the-art experiments and no theoretical limits. For large particles, the precision is often limited by the intrinsic mass distribution of the sample instead of the spectrometer, unless single particle detection is possible. Note that the term non-destructive indicates that the ion is not lost by the detection, though its lifetime may still be restricted by other mechanisms.

Technique	Mass Range	Charge Range	Precision	N. D. ^a	A. M. ^b	S. P. ^c	Reference
TOFMS							
-MCP	<18 MDa	n/a	200 ppm	x	x	x	Snijder <i>et al.</i> [88]
-STJ	<18 MDa	/	n/a	x	✓	✓	Plath <i>et al.</i> [99]
Orbitrap							
	<66 kDa	>4 e	10 ppm	✓	✓	✓	Makarov and Denisov [89]
	<1.3 MDa	n/a	300 ppm	✓	✓	✓	Dyachenko <i>et al.</i> [90]
FTICR							
	<115 kDa	>30 e	5 ppm	✓	✓	✓	Ge <i>et al.</i> [100]
	<110 MDa	>3 · 10 ⁴ e	10 %	✓	✓	✓	Chen <i>et al.</i> [91]
CDMS							
-QIT + Faraday Disc	6 · 10 ¹⁵ Da	>1 · 10 ³ e	2 %	x	✓	✓	Lin, Lin and Chen [72]
-Detector Array	150 kDa-10 GDa	>100 e	n/a	✓	✓	✓	Smith <i>et al.</i> [101]
-Cone Trap	240 kDa-2 MDa	>6 e	2 %	✓	✓	✓	Keifer, Shinholt and Jarrold [92]
NEMS							
- Si oscillator	900 MDa	/	70 ppm	x	✓	x	Ilic, Yang and Craighead [94]
- SiC oscillator	1 MDa	/	5 %	x	✓	✓	Hanay <i>et al.</i> [102]
NPMS							
	7 · 10 ¹⁵ Da	/	n/a	✓	✓	✓	Wuerker, Shelton and Langmuir [103]
	1 · 10 ¹¹ Da	/	10 ppm	✓	✓	✓	Schlemmer <i>et al.</i> [104]

^a non-destructive technique, ^b absolute mass determination, ^c single particle detection, n/a: not available

detector, or by a previous measurement using a different technique. For particles with masses below 1 MDa, the absolute charge was determined accurately by trapping ions for up to 3 seconds in an electrostatic cone trap.[92] In this example, the precision was only limited by an independent M/Q measurement. Other variants of CDMS provide much higher sample rates, but at the cost of reduced precision.[72]

Nanoelectromechanical system (NEMS) oscillators are a different approach to mass spectrometry, where the mass is deduced from a change in the resonance frequency upon particle adsorption on the oscillator.[54] Different oscillators give access to different mass ranges, and detection of atoms as well as viruses has been shown.[93, 94] Mass spectra obtained in this way are generally easier to interpret as there is no convolution due to different charge states.[95] The technique also works for neutral particles, removing the need for ionization. If further investigations of the adsorbed particles, *e.g.* by spectroscopy, are planned, the change of particle properties due to interaction with the oscillator needs to be considered. The technique is still under active development and many aspects remain to be characterized.[54]

Finally, the mass of particles with almost arbitrary mass and charge can be determined in various ways by quadrupole ion trap mass spectrometry (QITMS).[74] A QIT is referred to as an electrodynamic balance (EDB), in experiments where M/Q is determined from the direct current (DC) potential between the end caps, required to balance out the gravitational pull on a trapped particle. This method is only applicable for sufficiently heavy ions and provides a precision in the percent range.[96, 97] More commonly, QITMS makes use of the M/Q specific stability diagram in mass-selective detection, mass-selective storage and mass-selective ejection, which is discussed in more detail in Sec. 2.2. QITs have also been used in combination with CDMS or measurements at different charge states to determine the absolute mass.[72, 96] Fluorescence detection in a second QIT has been used to detect particles with a mass of hundreds of MDa and low charge states.[98]

In conclusion, mass spectrometry is a powerful tool for analysis of particles in the mass range above 1 MDa, but high-resolution single-particle experiments remain challenging. To achieve the goals stated in Sec. 1.4 a suitable technique had to be selected and implemented. It should allow to work with single nanoparticles in the kDa to GDa mass range and to confine them spatially, such that they can be brought to overlap with laser beams. A non-destructive ultra-high vacuum (UHV) application is desired to monitor changes in the particle properties due to precisely controlled interactions with the local environment. The mass-spectrometric techniques discussed above are disqualified for one or more of these reasons as apparent from Tab. 2.1.

Another, less established technique, which meets all the requirements mentioned above, is the determination of the mass of a single nanoparticle trapped in a QIT by optical means. It is commonly referred to as NPMS in the literature,[67, 68, 105] and this nomenclature is adopted in this thesis. Other authors refer to this technique more generally as QITMS[106, 107], single particle mass spectrometry (SPMS)[108, 109] or single molecule mass spectrometry (SMMS)[54] of nano- and microparticles. In NPMS, typically a single nanoparticle is trapped inside a QIT and its M/Q is

determined by optically detecting its axial secular frequency ω_z . Since the detection is non-destructive, nanoparticles can be analyzed over extended time periods, during which trap temperature, background gas composition and pressure as well as laser irradiation can be altered to deduce chemical and physical properties from changes in particle mass. Confinement of the particle in the trap center facilitates overlap with lasers for optical detection and spectroscopy. In contrast to most conventional mass-spectrometric techniques, where the intensity, proportional to the number of ions, is plotted against the mass M or M/Q , in NPMS the mass of a single particle is repeatedly determined and plotted against time. The unique combination of experimental control and accessible mass range provided by NPMS cannot be obtained with any alternative technique.

2.2 Theory of the 3D Quadrupole Ion Trap

The ideal QIT is also known as the Paul trap, after its inventor Wolfgang Paul, who was awarded the Noble prize in physics in 1989, together with Hans Dehmelt, "for the development of the ion-trap technique".[110] The three-dimensional form was published only three years after the two-dimensional linear ion trap (LIT).[111, 112] It has been used for a variety of applications including non-destructive mass-selective detection of trapped ions via their effects on an electric circuit or optical detection[103, 113, 114], mass-selective storage for spectroscopy[115] and mass spectrometry[116] as well as mass spectrometry by mass-selective ejection.[117] While in the mass-selective storage mode, a mass spectrum is obtained by storing ions of a single M/Q before sending them onto an electron multiplier (EM) using an ejecting potential, in the mass-selective ejection mode, ions of different M/Q are trapped simultaneously and are ejected consecutively by destabilization of their M/Q -dependent trajectories. Mass spectrometry based on mass-selective ejection is the most commonly used technique today, though multiple implementations, and their combinations in tandem mass spectrometers, were developed.[74] Depending on the amplitude and frequency of the used oscillating voltage, electrons, molecular ions, nano- or microparticles can be trapped and analyzed.[76] Further applications of QITs are summarized in the literature.[74, 118]

In this thesis a modified QIT (see Sec. 3.6) was designed, implemented and used for non-destructive mass determination of single nanoparticles. The theory of the ideal QIT is discussed in the following, based on March and Todd,[74, p. 52ff.] followed by a summary of perturbations that are present in a real QIT in Sec. 2.2.1.

Particles can be confined inside a certain volume by an attractive force \vec{F} , which increases linearly with distance r

$$\vec{F} = -k\vec{r} = -\nabla\Phi(x, y, z), \quad (2.1)$$

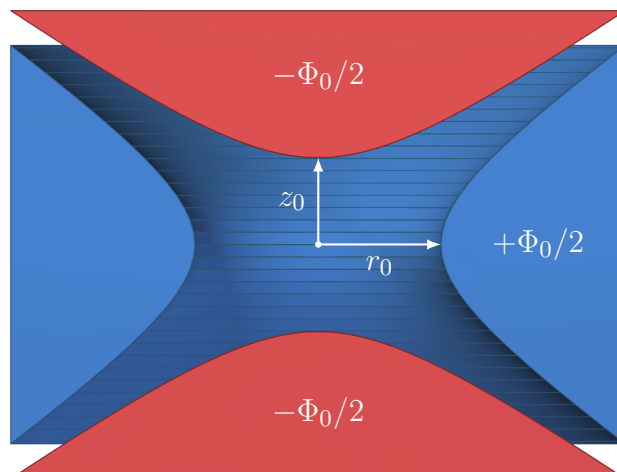


Fig. 2.2: Schematic cross section of an ideal QIT consisting of a hyperbolic ring electrode (blue) and two hyperbolic end cap electrodes (red).

where k is a constant. This corresponds to a harmonic potential of the form

$$\Phi(x, y, z) \propto (\alpha x^2 + \beta y^2 + \gamma z^2) \quad (2.2)$$

with the constant coefficients α , β and γ , which have to sum up to zero to fulfill the Laplace condition $\nabla^2 \Phi \propto \alpha + \beta + \gamma = 0$. From the infinite number of possible combinations of coefficients, the two simplest lead to the two dimensional potential of a linear ion trap (LIT) ($\alpha = 1 = -\beta$, $\gamma = 0$; compare Sec. 3.5) and, with $\alpha = \beta = 1$, $\gamma = -2$, to the potential of an ideal three-dimensional QIT,

$$\Phi(r, z) = \Phi_0 \frac{r^2 - 2z^2}{r_0^2 + 2z_0^2} + C \frac{r_0^2 = 2z_0^2}{2} \frac{\Phi_0}{2} \left(\frac{r^2}{r_0^2} - \frac{z^2}{z_0^2} \right) + C, \quad (2.3)$$

with $r^2 = x^2 + y^2$. This implies that the potential is $+\Phi_0/2$ on a hyperbolic surface given by $\frac{r^2}{r_0^2} - \frac{z^2}{z_0^2} = 1$ (ring electrode) and $-\Phi_0/2$ on a hyperbolic surface given by $\frac{r^2}{r_0^2} - \frac{z^2}{z_0^2} = -1$ (end caps), which are the boundary conditions leading to the electrode geometries shown in Fig. 2.2. Φ_0 is the potential difference between the ring and end cap electrodes. The characteristic parameters r_0 and z_0 represent the closest distance from the trap center to the ring and end cap electrodes, respectively.

The relation $r_0^2 = 2z_0^2$ was historically used for the ideal QIT and has later been shown to minimize the contribution of higher-order terms (compare Sec. 2.2.1) for real traps with truncated electrodes.[103, 112, 119] Instead, a stretched geometry with increased z_0 is used in most commercial QITs to compensate for field imperfections, due to entrance and exit holes in the end cap electrodes.[120] The trap geometry developed in the present thesis is far from the ideal one, but it was possible to tune it such that the condition $r_0^2 = 2z_0^2$ is fulfilled close to the trap center, as will be shown in Sec. 3.6.2,

and the following discussion will assume this equality.

The constant C is determined by the boundary conditions and is zero if the potentials are applied to the electrodes symmetrically as described above. If the end caps would be held at ground and the potential is applied to the ring electrode only, the potential at the ion-trap center would be non-zero:[74, p. 56]

$$\Phi_{\text{grounded end caps}}(r, z) = \Phi_0 \left(\frac{1}{2} + \frac{r^2 - 2z^2}{r_0^2 + 2z_0^2} \right). \quad (2.4)$$

For this mode of operation, the type of motion of the ions inside the trap is still the same, but the potential difference Φ_0 between ring and end cap electrodes and thus the maximum M/Q of particles that can be stored is only half compared to the symmetric configuration, when using the same power supply. Here, the symmetric case will be discussed, since it avoids the constant offset that would create a field gradient towards the grounded elements around the trap and pull the particle away from the trap center. Also, the constant C might represent a constant potential offset on all electrodes, which can be useful to slow down particles entering the trap.

Since the Laplace condition imposes that not all coefficients α , β and γ have the same sign, the force cannot be attractive in all three dimensions for a static potential. Instead a time-dependent potential of the form

$$\Phi_0 = 2U_0 + 2V_0 \cos(\Omega t) \quad (2.5)$$

is used, with the DC component U_0 , the radio frequency (RF) amplitude V_0 and the trap frequency $F = 2\pi\Omega$, so that the particles are alternately focused and defocused in all three dimensions. Due to the inhomogeneity of the time-dependent field, particles experience a changing field strength during their motion, causing a net attractive force towards the trap center.[121, p. 11] This leads to the following decoupled equations of motion for a particle of mass M and charge Q :

$$M \frac{d^2 r}{dt^2} = -Q \frac{d\Phi}{dr} = -Q (U_0 + V_0 \cos \Omega t) \frac{r}{z_0^2}, \quad (2.6)$$

$$M \frac{d^2 z}{dt^2} = -Q \frac{d\Phi}{dz} = -Q (U_0 + V_0 \cos \Omega t) \frac{-2z}{z_0^2}, \quad (2.7)$$

which can be written in the general form of the Mathieu differential equation,[122]

$$\frac{d^2 u}{d\tau^2} + (a_u - 2q_u \cos 2\tau) u = 0 \quad \text{with} \quad u = r, z \quad (2.8)$$

where $a_z = -2a_r = \frac{-8QU_0}{Mz_0^2\Omega^2}$, $q_z = -2q_r = \frac{4QV_0}{Mz_0^2\Omega^2}$ are dimensionless stability parameters and $\tau = \Omega t/2$ is the dimensionless time.

The complete solutions to the Mathieu equation represent an infinite sum of stable

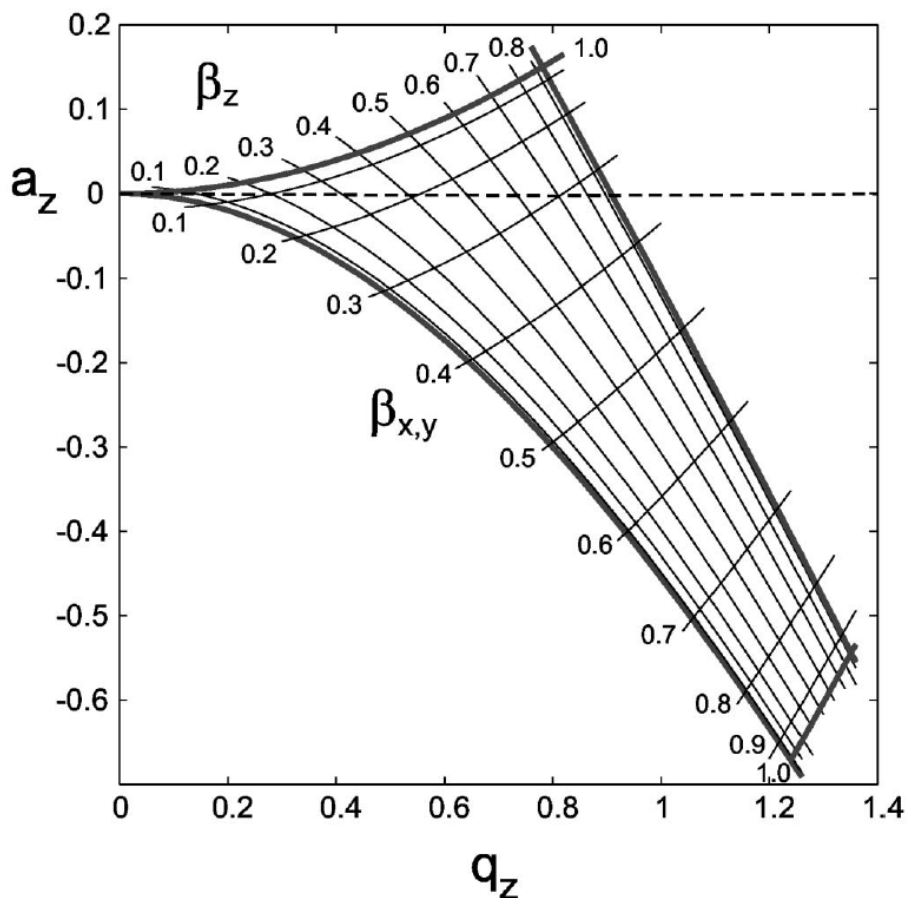


Fig. 2.3: Stability diagram of an ideal QIT expressed in terms of the trapping parameters a_z , q_z , β_z and $\beta_r = \beta_{x,y}$. The boundaries are given by integer multiples of β_z and β_r . Reproduced from Leibfried *et al.*[123]

and unstable periodic trajectories, depending on the values of a_u and q_u , and can be found in the literature.[74, p. 65] Stable and instable regions are separated by integer multiples of the stability parameter $\beta_u(a_u, q_u)$, which is obtained from a continued fraction expression.[74, p. 67] The main stability region is defined by $0 < \beta_u < 1$ and is shown for $u = z$ in Fig. 2.3.

The ion motion in radial and axial direction consists of a smooth secular motion $u(t)$ and a fast oscillation $\delta(t)$ at the trap frequency Ω . The frequencies of the secular ion motion are defined as

$$\omega_{u,n} = \left(n + \frac{1}{2}\beta_u\right)\Omega \quad \text{with } 0 \leq n < \infty, \quad (2.9)$$

$$\omega_{u,n} = -\left(n + \frac{1}{2}\beta_u\right)\Omega \quad \text{with } -\infty < n \leq 0, \quad (2.10)$$

of which only $\omega_{z,0} = 2\omega_{r,0} = \frac{1}{2}\beta_z\Omega$ are relevant, since the magnitudes of higher-order

solutions fall off rapidly. Interpretation of the ion motion can be simplified by separating the two components in the superposition ansatz $U(t) = u(t) + \delta(t)$. [74, p. 75ff.] Assuming that the amplitude of $u(t)$ is much bigger but its frequency is much lower compared to $\delta(t)$, generally valid for $q_z < 0.4$, and by taking the time average over a period of the RF trap frequency, the equation of motion can be transformed into

$$M \frac{d^2 u}{dt^2} = -Q \frac{d}{du} \Phi_{\text{eff},u} = -\frac{d}{du} V_{\text{eff},u}, \quad (2.11)$$

with the time independent effective potential or pseudopotential

$$V_{\text{eff},u} = \frac{Q^2 V_0^2}{M \Omega^2 u_0^2} \left(\frac{u}{u_0} \right)^2. \quad (2.12)$$

This is known as the Dehmelt approximation and was first used by Wuerker, Shelton and Langmuir [103] and later extended by Dehmelt [124]. The same technique can also be applied to interpret the motion of ions in time-dependent inhomogeneous electric fields of higher-order multipole devices (compare Sec. 3.5), where it is generally called the adiabatic approximation and its validity is characterized by the dimensionless adiabaticity parameter η . For quadrupolar fields, η is equal to the stability parameter q . Based on numeric calculations, the condition $\eta < 0.3$ is recommended for safe operation instead of $\eta < 0.4$. [121, p. 20]

A simplified expression for the stability parameter β_u is found in the Dehmelt approximation: [74, p. 60f.]

$$\beta_u \approx \sqrt{a_u + \frac{1}{2} q_u^2}. \quad (2.13)$$

If the trap is operated in RF only mode, such that $a_u = 0$, it follows that $\beta_u = \frac{q_u}{\sqrt{2}}$. The fundamental secular frequency in axial direction is then given by $\omega_{z,0} \equiv \omega_z = (\sqrt{2} Q V_0) / (M z_0^2 \Omega)$. This equation can be rearranged to obtain M/Q from a measurement of the secular frequency:

$$\frac{M}{Q} = \frac{\sqrt{2} V_0}{\omega_z \Omega z_0^2}. \quad (2.14)$$

The amplitudes of thermal motion can be derived by equating the effective potential at the turning points with the thermal energy: [104]

$$u_m^2 = k_B T \frac{M u_0^4 \Omega^2}{2 Q^2 V_0^2} \quad \text{with} \quad u = r, z \quad (2.15)$$

where r_m and z_m are the maximum amplitudes in radial and axial direction, respectively. For the particles and trapping conditions used in the experiments presented in this

thesis, z_m is typically below 200 μm . When cooling the SRET from room temperature to 10 K and neglecting heating mechanisms, the amplitudes decrease by a factor of ~ 6 .

2.2.1 Perturbations in a Real QIT

The previous discussion was limited to an ideal QIT, neglecting effects of buffer gas, gravity, mechanical imperfections, non-ideal RF supplies and truncated electrodes. The potential does not need to be harmonic, as in Eq. 2.2, to fulfill the Laplace equation. The general solution is a linear combination of spherical harmonics:[74, p. 93f.]

$$\Phi(\rho, \theta, \varphi) = \Phi_0 \sum_{k=0}^{\infty} c_k \left(\frac{\rho}{r_0}\right)^k P_k(\cos(\theta)), \quad (2.16)$$

with the Legendre polynomials $P_k(\cos(\theta))$ and multipole coefficients c_0 (monopole), c_1 (dipole), c_2 (quadrupole), c_3 (hexapole), c_4 (octopole), etc. In cylindrical coordinates the potential takes the form

$$\begin{aligned} \Phi(r, z) = \Phi_0 \left(c_0 + c_2 \frac{r^2 - 2z^2}{2r_0^2} + c_4 \frac{3r^4 - 24r^2z^2 + 8z^4}{8r_0^4} \right. \\ \left. + c_6 \frac{5r^6 - 90r^4z^2 + 120r^2z^4 - 16z^6}{16r_0^6} + \dots \right) \end{aligned} \quad (2.17)$$

Note that for a rotationally symmetric trap the φ dependence can be neglected and the coefficients for odd powers of r and z are zero if the trap electrodes have reflection symmetry.[125] For the ideal QIT, c_2 is equal to one and all other coefficients are zero. The effect of a non-zero c_0 is equivalent to the offset described for the trap with grounded electrodes in Eq. 2.4. While for a trap in free space there is no effect on the ion motion, in reality, the c_0 term decays towards the grounded radiation shield and vacuum chamber. This leads to an effective field gradient pulling the particle out of the center.[126] The higher-order components become relevant only with increasing amplitudes of particle motion and have multiple effects.[127] They lead to an amplitude dependence of the stability parameters and the secular frequency, which are thus no longer independent on the initial conditions of the ion motion. When the motion of the ion is resonantly excited, this effect can shift the secular frequency out of resonance and limit further excitation. In addition, they induce a coupling between the radial and axial motion that leads to energy exchange and the occurrence of non-linear resonances where energy is taken up from the RF field under the condition that $k_r\omega_r + k_z\omega_z = k\Omega$, with integer values k_r , k_z and k .[74, p. 98] The corresponding unstable lines in the stability diagram have been mapped experimentally by Bandelow, Marx and Schweikhard,[128] who measured the storage efficiency of Ar^+ ions at $1 \cdot 10^{-6}$ mbar for multiple combinations of a_z and q_z .[128]

As part of this thesis work, a split-ring electrode trap (SRET) was designed, described in Sec. 3.6, to allow for optical access to the trap center. This design was optimized to

minimize the deviations from the potential of an ideal QIT close to the trap center (see Sec. 3.6.2).

In real traps, ω_r can split into ω_x and ω_y components due to geometry imperfections, gravity, light pressure and asymmetrical charge distribution.[104] This can be partially compensated by introducing a DC compensation field and changing the trap orientation if needed. Further influences on the ion motion, like the inhomogeneity of the gravity compensation field, thermal and electronic noise, higher harmonics in the RF trap voltage, damping due to buffer gas, dielectrophoretic force, accumulated photon impulse, photophoretic force (net impulse due to emission of gas particles from unequally heated particles) and magnetic fields have been discussed in detail by Illemaann.[129, p. 18ff.] The influence of the individual effects varies with the deviation from an ideal QIT and RF supply, the particle properties and other experimental conditions. For most practical applications they can be neglected, though they become more relevant with increasing measurement precision.

2.2.2 RF Supplies for Quadrupole Ion Trap Operation

Multipole ion guides and traps are used for a variety of applications including ion guiding, mass selection, trapping, storage, reaction studies and spectroscopy. To that end, an RF voltage is typically supplied by either an RF generator, RF amplifier or digital voltage switch. The type of RF voltage supply has to be chosen for each application, depending on the requirements with regard to shape of the waveform and the range and stability of the frequency and amplitude.

RF Generator. For RF generators the capacitive load itself is part of a resonant circuit, decreasing power dissipation. During operation, the frequency is only variable in a limited window of approx. 10%. This type of generator has the clearest frequency spectrum and the frequency can be stabilized to a few ppm using a quartz crystal. Though free running versions are available, a matching network is typically used for frequencies above 200 kHz to improve efficiency. The amplitude can be regulated with a precise rectifier. Ideally, two phase-coupled generators are used to get perfectly symmetrical phases, but this approach is complicated and expensive. RF generators are typically not used in the frequency range below 200 kHz, since the reduction in power dissipation in the resonant circuit only becomes relevant for higher frequencies. Below 200 kHz less power is needed to reload the capacitor, making an RF amplifier the preferred solution.

RF Amplifier. RF amplifiers are limited to low frequencies since the power consumption increases with frequency. The maximum achievable frequency is limited by the peak current of the operational amplifier $I_{\max} = 2\pi V_0 C F$. For an amplitude of $V_0 = 200\text{ V}$, the upper limit is currently around 200 kHz. A precision of 10 ppm at 10 kHz can be achieved with high-end devices.

Voltages up to 1.5 kV, can be achieved using step-up transformers at the cost of frequency range. In practice, frequency control is often more important than high amplitudes, when working with nanoparticles smaller than 50 nm.[68, 130, 131]

Digital Voltage Switch. Instead of a sine waveform, a rectangular waveform can be used for trapping, which is easier to implement, using a pulse generator, power switches and precision power supplies, and thus cheaper. This approach, often referred to as the digital ion trap (DIT) method, also allows to span a bigger amplitude and frequency range with a single RF supply. Due to temperature fluctuations, the period can only be stabilized down to 1 ns, which corresponds to 10 ppm at 10 kHz. The rectangular waveform is equivalent to a superposition of sine waves, which will affect the secular frequency spectrum. However, it has been shown experimentally that only the zeroth and first order component are needed to describe the particle motion and the relations derived in Sec. 2.2 are still valid using scaled versions of a_u and q_u . [128] This approach allows for more complicated waveforms including field free periods, which might be beneficial for trapping and exposure to ion and electron beams.[132] Fast high-voltage switches can induce noise, which may affect other sensitive electronic devices. The problem can be reduced by making the edges of the waveform less steep.

2.3 History of NPMS and Measurement Modes

Building on the initial developments of mass spectrometry, summarized in Sec. 2.1, in 1959 Wuerker, Shelton and Langmuir [103] presented the first study of microparticles using QITMS. In their seminal work they visually observed the Lissajous trajectories of single trapped aluminum microparticles inside a QIT. A photomicrograph of a 2:1 Lissajous curve is shown on the left side in Fig. 2.4. Other Lissajous curves were produced by fine tuning the DC component of the trap potential. The secular frequency, and thus M/Q , was determined by applying a weak excitation potential and visually observing the transition of the ion trajectory from a beating motion close to resonance to a stable elongated motion on resonance. Further experiments in this direction were not conducted until Hars and Tass [133] analyzed masses of single nano- and microparticles by imaging star-like trajectories in 1995.

In the following sections, the three most commonly used methods for determination of the mass-to-charge ratio (M/Q), star pattern imaging, Fourier transformation (FT) and resonant excitation, as well as determination of the absolute mass M for a single nanoparticle is discussed based on results from the literature and from the present NPMS setup. They all rely on experimental determination of the secular frequency ω_z by detection of scattered light or laser induced fluorescence (LIF) from a single trapped nanoparticle. The implementation of light collection and detection for the experiments presented in this thesis is discussed in Sec. 3.7. Note that in the experiment $f = \omega/2\pi$ is determined and thus secular frequencies are typically given in Hz instead of rads^{-1} .

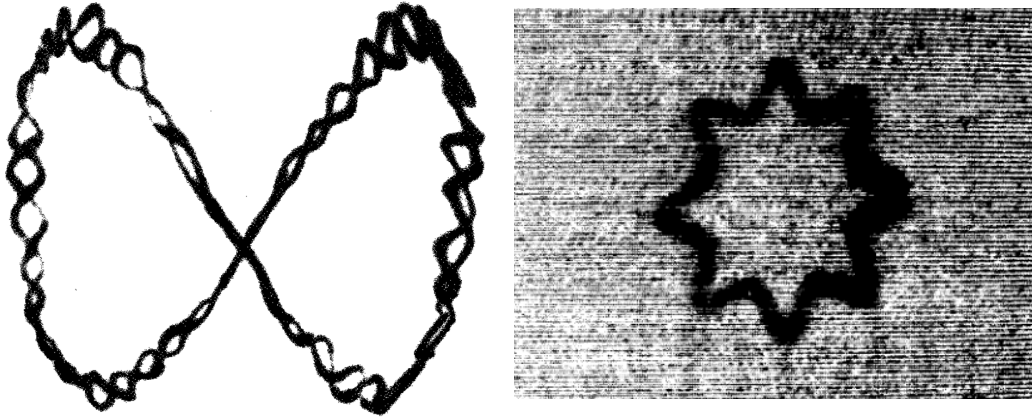


Fig. 2.4: Left: 2:1 Lissajous curve of a 20 μm aluminum dust particle at a pressure of $2.5 \cdot 10^{-2}$ mbar. The driving frequency $F = 200$ Hz is superimposed on the secular motion with $f_z = 16.3$ Hz. Image taken along the radial trap axis. Adapted from Wuerker, Shelton and Langmuir.[103] Right: Eight branch trajectory ($8\omega_r = \Omega$) of an 4 μm agglomerate of bacillus spores. Image taken along the cylindrical trap axis. From the frequency ratio M/Q was determined as $673 \text{ MDa} e^{-1}$. Reproduced from Hars and Tass.[133]

2.3.1 Star Pattern Imaging

If the trap frequency Ω is tuned such that $n \cdot \omega_r = \Omega$, with $n = 1, 2, 3, \dots$, star-like standing wave patterns can be observed (see Fig. 2.4 right). The factor n and thus the secular frequency can be obtained from the number of branches with a precision of 1000 ppm, as first demonstrated by Hars and Tass [133] with polystyrene and bacillus spore agglomerates and later by Peng *et al.* [107] for viruses, bacteria and human red blood cells. For small values of n , the adiabatic approximation is not valid and the use of Eq. 2.14 is not justified. Further, the star patterns tend to have high amplitudes, which increases the influence of higher multipole components on the secular frequency. The fact that star patterns start to rotate after a small frequency change, due to a charge step, was used to obtain quick feedback between longer measurements using the FT method described below.[106]

2.3.2 Fourier Transformation

The intensity of detected light from a single trapped particle is modulated by its motion relative to the laser beam and detection volume. Thus, the secular frequency can directly be obtained by Fourier transformation (FT) of a time record of detected light intensity. A precision of better than 1 % has been reported for a simple cylindrical ion trap with transparent end cap electrodes.[134] Up to 10 ppm precision was reached when using a modified QIT and averaging over 1 h.[104] An example of an FT spectrum obtained for a single NaCl particle is shown in Fig. 2.5. Side bands and overtones are visible, which are caused by some of the perturbations mentioned in Sec. 2.2.1 and will

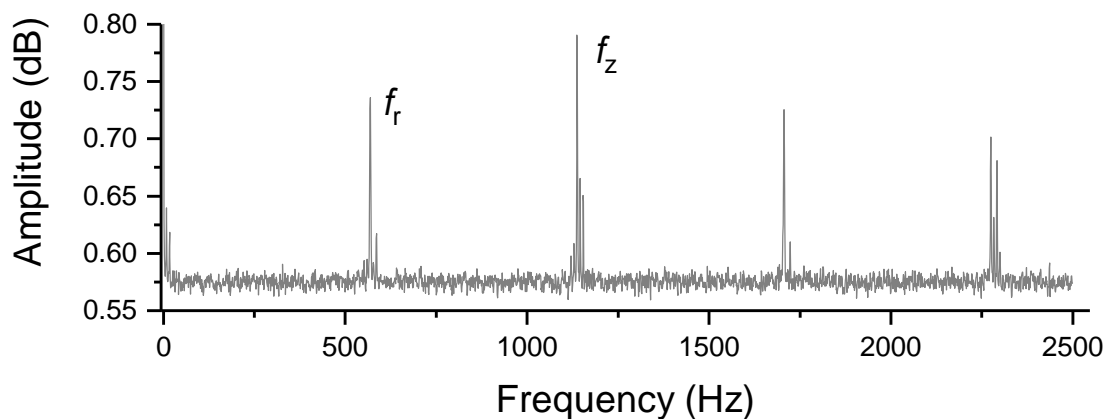


Fig. 2.5: Example of a Fourier transform measurement of a single NaCl particle (see Tab. 4.1 b). The spectrum was recorded at a trap pressure of $1.6 \cdot 10^{-6}$ mbar (Ar) with a bin size of $100 \mu\text{s}$ and 1 s acquisition time. The axial secular frequency, f_z , was determined as (1137.5 ± 2.4) Hz.

be addressed in Sec. 4.4.

With decreasing M/Q , higher frequencies are needed for stable trapping leading in turn to higher secular frequencies. To detect these higher frequencies using the FT approach, the light intensity has to be collected in smaller time bins, which leads to an increase of acquisition time or decrease in signal to noise ratio. This can be resolved by applying a weak alternating current (AC) drive potential or a mechanical vibration, close to the secular frequency and recording the resulting much lower beat frequency $f_{\text{beat}} = f_{\text{drive}} - f_u$. [135] For large particles on the other hand, where the frequencies are lower and detected light is more intense (more than 100000 photons per second) the FT method can be used with low pressures to obtain fast acquisition times or high precision. [136, p. 33] Larger particle amplitudes will increase the intensity modulation, but can lead to frequency shifts due to higher multipole components. When possible, the amplitude should be reduced by increasing the effective potential and lowering the nanoparticle temperature.

2.3.3 Resonant Excitation

Another approach for determination of the secular frequency is realized by sweeping the frequency of a weak excitation potential, applied to the end cap or excitation electrodes for axial excitation, through resonance with the particle motion. In conventional quadrupole ion trap mass spectrometry (QITMS), this is typically used for resonant ejection followed by external detection of the particle. The detectable light intensity decreases as the particle amplitude of motion increases and the particle spends less time in the area defined by the overlap of laser beam and detection volume. When choosing an appropriate amplitude $V_{0,\text{ex}}$ and sweep speed \dot{F}_{ex} of the excitation potential and sufficient pressure, the particle motion is damped to its original state after excitation,

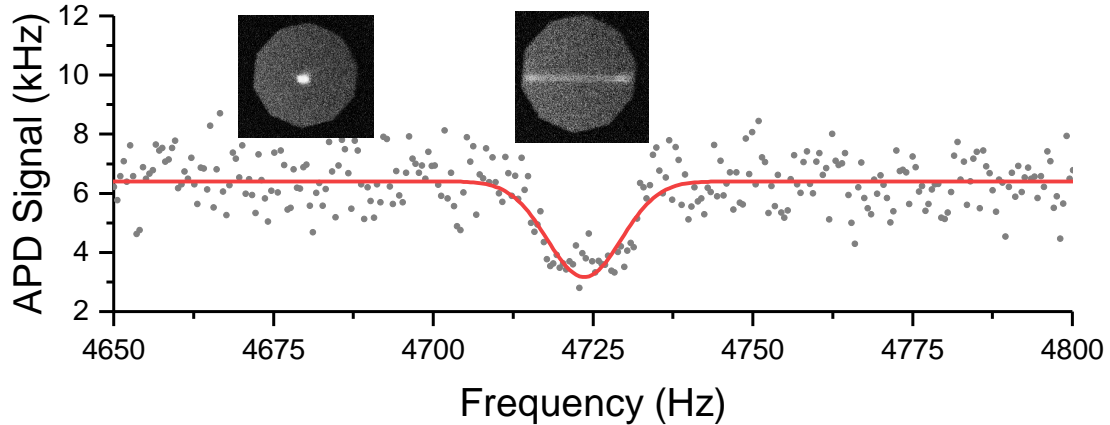


Fig. 2.6: Example of a resonant excitation measurement of a 54 nm SiO₂ particle (see Tab. 4.1 j). The spectrum was recorded at a pressure of $6.7 \cdot 10^{-4}$ mbar (Ar) with an excitation amplitude of 1.2 V and a relatively high sweep rate of 5 Hz s^{-1} to keep track of mass changes. The axial secular frequency was determined as $(4723.6 \pm 5.8) \text{ Hz}$. The pictures show the particle amplitude in equilibrium and on resonance. Adapted from the master thesis of Benjamin Hoffmann.[138]

as shown in Fig. 2.6, making the technique non-destructive. A precision of M/Q approaching 1 ppm has been reported for a single 90 s measurement.[137]

A variation of this technique was already used by Wuerker, Shelton and Langmuir,[103] as mentioned above. Other variations use modulation of the laser intensity, instead of the weak AC potential, to reduce the excitation strength and thus the maximal amplitude of motion.[68, 137] Resonant excitation is typically as fast as the star pattern method and often reaches a precision even higher than for the FT approach. Especially for smaller particles it is more suitable, since the modulation of the light with the secular frequency f_z does not have to be resolved and the signal can be averaged over longer time periods compared to the short time bins used for FT analysis. This makes the technique much more sensitive and typically only a few tens of photons per second are required as opposed to 100 000 photons per second for FT.[136, p. 29] Another argument is that particles with lower M/Q and lower mass will have smaller equilibrium amplitudes according to Eq. 2.15. When the amplitude is smaller than the laser focus and the detection volume, no intensity modulation can be observed, and no frequencies can be determined via the FT method, but resonant excitation is still applicable. When taking FT spectra, side bands can appear, caused by low frequency vibrations of the trap relative to the detector, *e.g.* from mechanical pumps. Typically, these vibrations do not affect the much faster motion of the ions relative to the trap, so that side bands do not appear in resonant excitation spectra.

Higher buffer gas pressures will broaden the resonance and thus limit precision, but buffer gas damping induced frequency shifts can typically be ignored.[74, 129, 133] At low pressure, the resonance is narrow and high precision can be reached, but the motion may take minutes to return to its equilibrium due to the weak damping. Thus, when

working at low pressures, a long idle time or a temporary pressure increase are needed between two subsequent measurements. If the rough value of the secular frequency is not known from previous experiments, the FT approach or resonant excitation overview scans with higher sweep rate, excitation amplitude and pressure are done preceding higher precision measurements.

The peak width and shape is further affected by the amplitude dependence of the secular frequencies caused by higher multipole components (see Sec. 4.5). The excitation of particle motion leads to an increase in collision energies for collisions with the buffer gas particles, which may ultimately lead to CID.[74, p. 120ff.] It also affects the particle temperature, which has to be considered in investigation of ad- and desorption kinetics as discussed in Chapter 5. Finally, resonant excitation can be used to selectively eject particles from an ion cloud in preparation for a single particle experiment.

2.3.4 Absolute Mass Measurement

Measuring the secular frequency allows to determine M/Q , but not the absolute mass of the particle. The latter can be determined from multiple measurements at different charge states, which was first done by Arnold in an electrostatic balance and Philip, Gelbard and Arnold in an EDB.[96, 139] Rewriting Eq. 2.14 leads to a relation for the absolute charge:

$$Q = \frac{\Delta Q}{\Delta \omega_z} \omega_z. \quad (2.18)$$

Thus, the absolute charge and mass can be determined from a charge-frequency diagram such as the example shown in Fig. 2.7.

To achieve high precision, it is important to assure mass stability during the measurements. Absolute mass determination via charge stepping is not recommended in periods of particle growth and shrinking. However, once the absolute charge and mass are established, they can be tracked during those periods. While particles with lower charge states are favorable, since a single charge step would result in a larger relative change in ω_z , absolute charges have been determined accurately for particles with up to a few hundred charges.[68, 135, 140]

Here, changes in charge are triggered using electrons or ions generated by a cold cathode pressure gauge in the SRET chamber, which is turned on for a few seconds to induce single or multiple steps. This leads either to an increase or decrease of charge due to collisions with Ar^+ , metastable Ar^* or e^- , when using argon buffer gas. To regulate the direction and number of charge steps, a lens or grid at variable potential can be installed between pressure sensor and trap. Other pressure sensors at positions further away from the trap can also induce charge steps, but with a much lower probability. Typically, no charge steps are seen over several hours when the sensor in the SRET chamber is off. Other methods used in the past include a vacuum

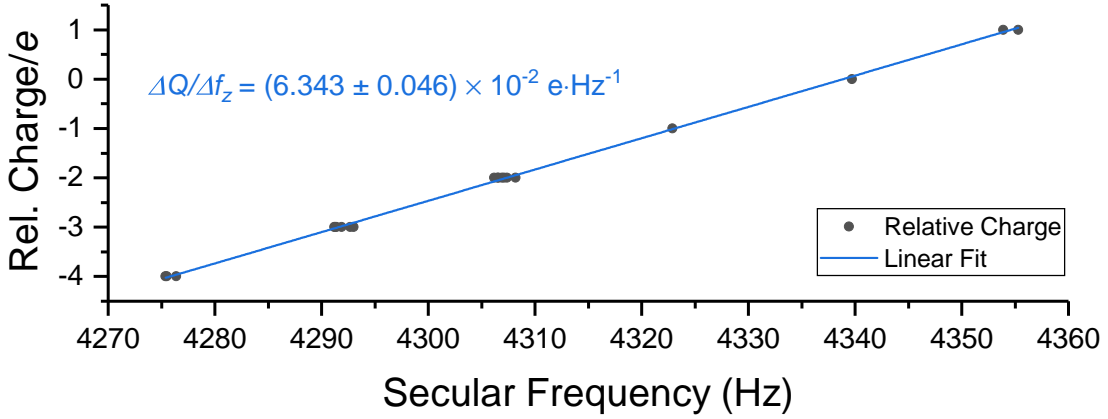


Fig. 2.7: Charge-frequency diagram for absolute mass determination of a 54 nm SiO₂ particle (see Tab. 4.1 j). The slope corresponds to a frequency change of (15.77 ± 0.12) Hz for a single charge step and the absolute charge was determined as (277 ± 2) *e*. Higher precision can be achieved with better statistics. Reproduced from Hoffmann.[138]

ultraviolet (VUV) lamp,[131] which was tuned to selectively remove electrons from the particle or from the trap electrodes, and an electron gun[129, p. 52] for change of the charge state by emission of secondary electrons.

Most experiments reported in the literature have been conducted on cations. The technique is equally suitable for anions, however, they tend to lose their charge faster, due to electron emission, which has to be compensated by the methods described above. Charge steps due to thermal electron emission can be observed when heating with a laser power of $\simeq 50$ mJ. For the experiments presented in this thesis, the laser intensity was typically low enough that thermal electron emission can be neglected.

2.4 Precision and Accuracy of NPMS Measurements

In theory, the amplitude V_0 and frequency $F = \Omega/2\pi$ of the trapping potential, the secular frequency ω_z and the characteristic parameter z_0 have to be measured with ppm accuracy to achieve a corresponding accuracy for M/Q . Measuring the frequency is relatively easy, but it cannot always be stabilized on the ppm level. Measuring the amplitude is more demanding, especially for higher frequencies. The secular frequency ω_z can be determined in various ways, as discussed in Sec. 2.3. Even for the optimized SRET geometry, higher multipole moments can introduce frequency shifts, which will become relevant for precision measurements. This effect will become larger with increasing amplitude of motion. The characteristic parameter z_0 is constant, as long as the trap temperature does not change.

For accurate measurements, the accuracy of RF amplitude, frequency and phase on all amplitudes is relevant, as well as higher multipole components of the trap. Similarly to the charge stepping method described above, mass stepping has been suggested for

accurate mass determination.[137] By changing the mass in well-defined steps, *e.g.* due to adsorption of single C_{60} molecules or other mass selected clusters, the ratio z_0^2/V_0 can be calibrated, allowing for accurate mass determination. Alternatively, well-defined M/Q standards, *e.g.* Ca_2^+ or C_{60}^+ , can be trapped for calibration of z_0 . On the other hand, for precise, reproducible, measurements it is sufficient to monitor the stability of those parameters without the need to know their accurate values. With a precision of 1 ppm, a mass change corresponding to a single water molecule on a 18 MDa particle can be resolved. This requires a particle growth rate well below one molecule per second to avoid multiple steps between measurements.

Single measurement precision approaching 10 ppm for full width half maximum (FWHM) and 1 ppm for the peak center frequency have been reported for a ~ 600 kDa e^{-1} polystyrene particle using the resonant excitation method (see. Sec. 2.3.3) at low pressures ($1 \cdot 10^{-8}$ mbar), low excitation amplitude (125 mV) and low sweep speed (5.5 MHzs $^{-1}$).[137, p. 28-31] Two successive measurements of the same particle with different sweep directions showed an agreement of the center frequency within 1 ppm. At this low pressure, relaxation of the ion motion after excitation can take hundreds of seconds, which is inconvenient for tracking of M/Q and for absolute mass and charge determination (see. Sec. 2.3.4).

Currently, precision of absolute charge and mass measurements via NPMS are on the order of 0.5 %, limited by the long-term stability of the RF amplitude. This makes exact charge determination only possible for particles with less than a few hundred charges.[136, p. 37]

For the experiments planned on the new NPMS setup, the focus lies on particles with a diameter below 50 nm, which are typically in the M/Q range below 500 kDa e^{-1} . Especially for lighter particles a precision of 10 to 100 ppm, and even 1000 ppm, is sufficient for a variety of experiments since relative mass changes become larger with decreasing absolute mass. For larger particles, in the MDa to GDa range, the RF and secular frequencies become smaller, allowing higher precision to be reached, though relative mass changes are decreasing as well. Since the change in M/Q needs to be monitored, the trapping frequency might need to be adjusted during the experiment to maintain stable trapping conditions, making RF amplifiers the RF device of choice.

The signal bandwidth of an RF amplifier is defined as the frequency above which drifts in internal parameters cannot be compensated. For the HV-AMP400FN from CGC Instruments, which will ultimately replace the currently used, home build RF amplifier, the signal bandwidth is 10 to 20 MHz. For frequencies 1000 times smaller, the drifts will be suppressed by a factor of 1000. Thus, for drifts on the order of 1 % giving 10 ppm at 10 kHz. The amplitude can only be measured with ppm precision for frequencies much smaller than 100 kHz. The effect of thermal drifts can be reduced by complex circuits, but it is also important to minimize those drifts in the first place by using proper cooling and allowing for thermal equilibration.[141]

In summary, ppm accuracy is currently impossible to reach for RF devices in the 100 to 200 kHz range. Theoretical predictions regarding precision should be viewed with caution, but allow to understand stability trends. Precision can approach the

ppm range and is best determined by measuring the secular frequency of a particle of constant mass over an extended period of time.

2.4.1 NPMS for Particle Sizes Below 50 nm

Particles with diameters below 50 nm are particularly interesting as quantum effects start to become more relevant with decreasing particle size. Light scattering of spherical particles depends on the particle radius r , the wavelength λ and the complex index of refraction $m = n + ik$, where n is the index of refraction and k is the extinction coefficient. For particles much smaller than the wavelength, the scattered light irradiance $I_s(\theta)$ can be approximated as Rayleigh scattering,[142, p. 132]

$$I_s(\theta) = \frac{8\pi r^6}{\lambda^4 R^2} \left| \frac{m^2 - 1}{m^2 + 2} \right|^2 (1 + \cos^2 \theta) I_i, \quad (2.19)$$

with the irradiance of unpolarized incoming light I_i , the scattering angle θ and the distance to the particle R . Note that the isotropic and angle-dependent terms are due to incoming light polarized perpendicular and parallel to the scattering plane, respectively. The intensity decreases rapidly with particle size and for particles below 50 nm light scattering is typically not sufficient for optical detection of single nanoparticles.[137] One solution to this problem is to use intrinsically fluorescing or fluorescence labeled particles.[98, 143] Another approach is to co-trap a fluorescent particle together with a "dark" one. For lower charge states the coupling between the two particles, and thus the mutual perturbation of their motion, will be reduced. On resonant excitation of the dark particle the fluorescent particle will be indirectly driven as well, revealing both frequencies in the spectrum.[143] If the M/Q of the co-trapped particles differ significantly from each other, trapping both simultaneously may not work. This problem can be overcome by using a "two-frequency" QIT.[144]

Of the two methods, fluorescence is preferred, as it works for any mass range. Particle interactions are avoided and high sensitivity can be obtained by blocking the wavelength of the probe laser using optical filters. Further improvements in light collection and detection increase the sensitivity of NPMS, making it more widely applicable for measurements in the size range below 50 nm.

3 The Nanoparticle Mass Spectrometry Setup

This chapter gives a detailed description of the nanoparticle mass spectrometry (NPMS) setup, shown in Fig. 3.1, that was designed, built and characterized as part of this doctoral thesis. A brief overview of the setup is given in Sec. 3.1. Non-destructive mass and charge determination is achieved by optical detection of the secular frequency ω_z of single nanoparticles in a QIT followed by charge stepping (Sec. 2.3). To this end, electrospray ionization (ESI) (Sec. 3.3), RF guiding and trapping (Sec. 3.5), cryogenic cooling (Sec. 3.9) and various optical detection schemes (Sec. 3.7) are combined. A LabVIEW based software controls the measurement and data acquisition (Sec. 3.10, Appendix C).

While most technologies applied here are long-established, many components were customized to meet the specific requirements regarding size, mobility, cost, ease of assembly and maintenance. In the following sections, fundamental operation principles of all relevant components are discussed along with their specific implementations. Simulations of nanoparticle guiding through the complete setup and trapping are discussed in Sec. 3.11.

The essential novelty of this setup, and core element of this thesis, is a new SRET design, described in Sec. 3.6, with improved optical access, temperature control (8 to 350 K) and shape of the electric potential compared to previous versions from Gerlich and Decker [67] and Howder, Bell and Anderson [68]. Characterization and first experimental results on particle growth by argon attachment are discussed in Chapter 4 and Chapter 5.

3.1 Overview of the Experimental Setup

The key components of the experimental setup are shown in Fig. 3.1. Nanoparticles contained in a solution are brought into the gas phase by a nano ESI ion source. They are transferred via a heatable capillary ($\leq 100^\circ\text{C}$) and two skimmers, separating differentially pumped vacuum chambers, to create an ion beam. The beam of nanoparticles is then collimated by an octopole ion-guide, passes through a custom-built gate valve and is deflected 90° by an electrostatic quadrupole deflector into a quadrupole ion-guide where molecular ions are filtered out. The nanoparticles are trapped in an SRET (8 to 350 K) and thermalized through collisions with buffer gas particles. The gate valve can be closed after a single nanoparticle is trapped, to block the ion beam, reach

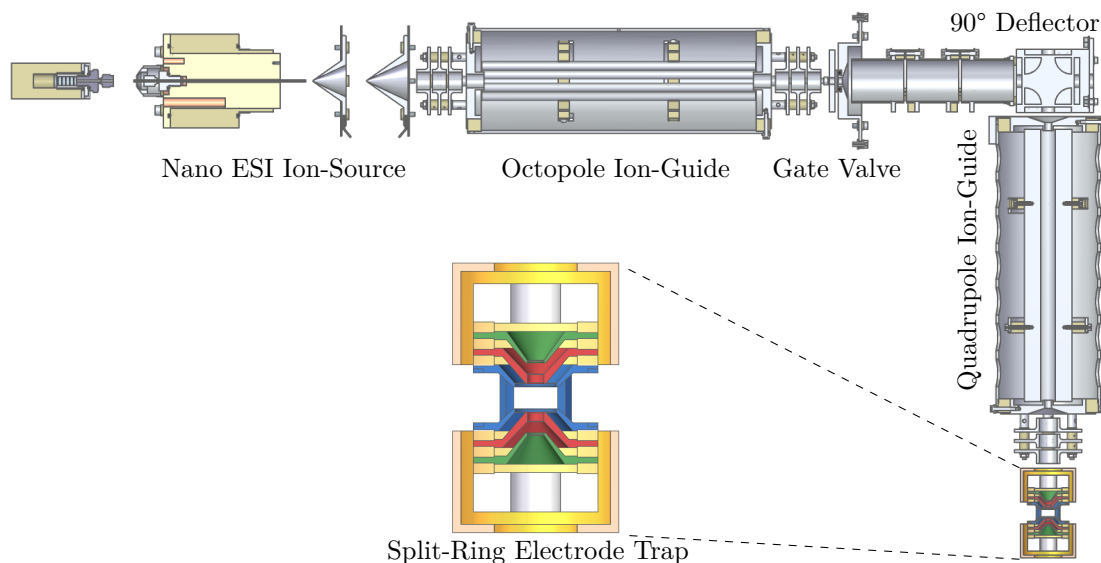


Fig. 3.1: Schematic cross section of the nanoparticle mass spectrometry (NPMS) setup. The beam of nanoparticles from the nano ESI ion source is skimmed and collimated in an octopole ion-guide. After deflection by 90° ions with low M/Q are filtered out by a quadrupole ion-guide and the beam is confined close to its central axis. The nanoparticles are then trapped in a buffer gas filled split-ring electrode trap (SRET) (8 to 350 K). The gate valve can be closed after a single nanoparticle is trapped to block the ion beam and gas flow from the source. After thermalization through collisions with the buffer gas particles, ad- and desorption kinetics and spectroscopic experiments can be performed using lasers on up to three optical axes. Optics and detectors are not shown. See Fig. C.2 for a larger overview with labeled ion optics.

lower pressures or to reduce the partial pressure of atmospheric molecules. The single nanoparticle is then exposed to up to three laser beams for heating, detection and spectroscopy. Scattering or fluorescence light is detected either by a charge coupled device (CCD) or an avalanche photodiode (APD) photodetector and analyzed to obtain the mass and charge non-destructively as discussed in Sec. 2.3. The mass can then be monitored over several hours or days as the background gas pressure, composition and temperature as well as wavelength and intensity of the incident light are varied.

The instrument is mounted on top of an actively pneumatically damped laser table (M-VIS3648-PG4-325A - Newport). Custom holes in the table allow to separate the pumping system from the rest of the experiment and keep the center of mass low over the table. A frame (item Industrietechnik GmbH) was built around the whole apparatus to provide more space for electronics and to mount a vibration isolated closed-cycle helium cryostat (see Sec. 3.9). It was sealed with dark room blinds (The Imaging Warehouse) in order to shield the experiment from light and sound waves. Using the casters of the optical table the experiment can be moved easily. Only the frame has to be reassembled when moving to another lab. Variable height adjusters (NAEK 20-6.6 - WASI GmbH & Co. KG) were used to align the vacuum chambers to

each other and redistribute the weight evenly on the table.

3D and technical drawings of all components of the experimental setup were prepared using the computer aided design (CAD) software Solid Edge. Fig. 3.1 and most other schematics presented in this chapter are based on those drawings.

3.2 Vacuum System

A schematic of the vacuum chambers is shown in Fig. 3.2. Neutral molecules and ions enter the instrument from atmospheric pressure through a stainless-steel capillary. The first two chambers of the nano ESI ion-source (1,2) are used for differential pumping. They accommodate two skimmers, that separate the ion beam from the majority of the neutral gas flow, which is pumped away by scroll pumps. Next, an adapter (3a) is used for mounting the octopole ion-guide. A first turbo molecular pump is mounted below the octopole chamber (3). The gate valve, mounted in an additional adapter (3b), allows to block the ion beam and reach lower pressures in the following chambers. It also provides a second mounting point for the octopole ion-guide. The quadrupole chamber (4) is pumped from below by a second turbo molecular pump and allows to mount flanges with the quadrupole ion-guide and electrostatic quadrupole deflector. The adapter (4b) acts as a spacer to define the distance between quadrupole ion-guide and ion trap and is also used to mount four parabolic mirrors. Finally the ion-trap chamber (5) is only indirectly pumped via a large conductance towards the quadrupole chamber. The SRET is mounted on a cryogenic sample mount, not shown in Fig. 3.2. Electrical and gas feedthroughs for the trap are provided by an adapter (5a) and a port aligner (5b) allows to align it relative to the other ion optics. When cooling the ion trap down to 8 K, it acts as a cryogenic pump. Vacuum chambers, flanges and feedthroughs were obtained from VACOM Vakuum Komponenten & Messtechnik GmbH. Tubing and flanges were made from austenitic stainless steel 316 and 304, respectively. Most chambers were designed with ISO-K 100 flanges before and CF 100 flanges after the gate valve. This size was chosen to keep the instrument small enough to fit on a mobile 900×1200 mm optical table.

Fully magnetically levitated water cooled turbo pumps (STPL301 - Edwards) were used for the UHV chambers. Those pumps are maintenance free and eliminate the need for vibration isolators, typically used with hybrid pumps, while providing similar low vibration characteristics. Thus, less space is used and the reduction of pumping speed by a vibration isolator is avoided. In order to reduce vibrations, acoustic noise and contamination of the ion optics, oil free scroll pumps (nXDS20i and nXDS15i - Edwards) are used for the source region and for backing the turbo pumps. The scroll pumps were connected via flexible metal hoses, which were wrapped in thin rubber sheets and sandwiched between two 20 kg concrete blocks to further reduce vibrations. Pressures in the source chambers and backing lines are measured with active pirani gauges (APG100-XLC - Edwards), which operate in the $1 \cdot 10^{-4}$ to 1000 mbar pressure range. For the high vacuum chambers combined cold cathode and pirani

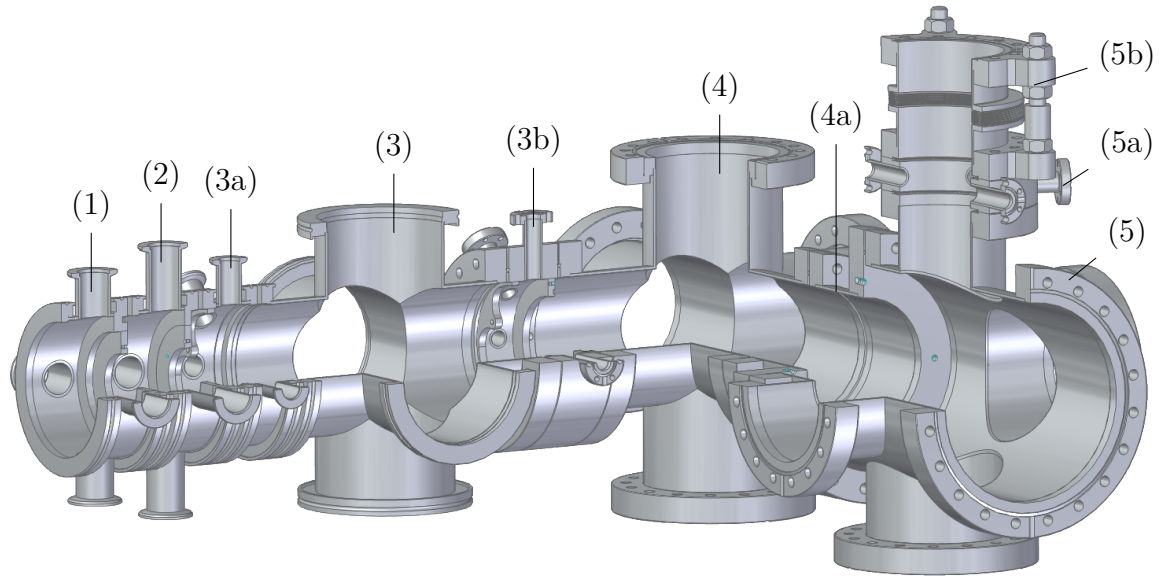


Fig. 3.2: Schematic of the vacuum chambers. Five main chambers (1-5) are connected with adapters, which provide mounting points and additional feedthroughs. (1) first source chamber, (2) second source chamber, (3) octopole chamber, (3a) octopole mounting adapter, (3b) gate valve adapter, (4) electrostatic quadrupole deflector and quadrupole guide chamber, (4a) quadrupole adapter, (5) ion-trap chamber, (5a) ion-trap adapter, (5b) port aligner.

gauges (WRGSDN40CF - Edwards) operating in the $1 \cdot 10^{-9}$ to 1000 mbar range are used. All pressure sensors are operated and read out by a dedicated controller (TIC instrument controller - Edwards), which is connected to the measurement computer via an RS232 interface. The pressures are continuously monitored by the measurement software and written to a log file.

All ion optics were mounted on flanges. These provide the corresponding feedthroughs, allowing to complete the mechanical and electric assembly outside of the chamber. This concept was particularly important since the small vacuum chambers made access to the ion optics inside the chamber difficult. Most feedthroughs were mounted on individual flanges, typically CF 16 or KF 25, instead of welding multiple feedthroughs to a single flange. Thus, they can easily be exchanged for different applications and replaced individually in case of damage. Oil free vacuum is important to keep the surface of the ion optics clean. Contaminated ion optics can charge up and perturb the ion beam. The front part of the instrument, up to the gate valve, is sealed with O-rings and cannot be baked out. In the remaining part, seals are typically made with copper gaskets. The cryostat can be removed from the sample mount, allowing for heating up to 200°C . The turbo pumps, as well as special isolators (Krüpax[®] - Krüger und Sohn GmbH) used in the ion trap, should not be exposed to temperatures above 120°C . Baking out is currently not necessary as $1 \cdot 10^{-8}$ mbar are sufficient for all experiments.

Theory and Dimensioning. Based on previous experiments[68] the desired pressure limits were defined as $1 \cdot 10^{-5}$ mbar in the octopole guide, $1 \cdot 10^{-6}$ mbar in the quadrupole ion-guide and $1 \cdot 10^{-8}$ mbar in the SRET region with closed gate valve. The fundamentals of vacuum design, needed to quantify vacuum conditions and estimating the pump requirements, will be discussed in the following, based on Moore, Davis and Coplan.[145] Specific parameters for the NPMS setup are given in Tab. 3.1.

The volume rate of flow S is defined as the pumping speed

$$S = \frac{dV}{dt} \quad (3.1)$$

and the speed S_p at the pump inlet is the pumps capacity. The volumetric throughput, proportional to the mass rate of flow, is given by

$$Q = pS \quad (3.2)$$

where pressure p and pumping speed should be measured at the same place since they vary throughout the system. The conductance C of a tube or aperture, *i.e.* its ability to transmit gas, is defined by the volumetric throughput for a given pressure gradient.

$$Q = C\Delta p \quad (3.3)$$

The mean velocity of a gas molecule of mass m at temperature T is given by

$$\bar{v} = \sqrt{\frac{8kT}{\pi m}}, \quad (3.4)$$

with the Boltzmann constant $k = 1.381 \cdot 10^{-23}$ JK⁻¹. The distance a particle can travel before colliding with another is called the mean free path (MFP) λ . For a neutral molecule in air at 20 °C it can be estimated by $\lambda = 7 \cdot 10^{-3}/p$ cm with the pressure p in mbar. At a pressure of $1 \cdot 10^{-3}$ mbar the MFP is ~ 10 cm and thus close to the dimensions of the vacuum chamber. At higher pressures, λ is smaller and the gas flow is described as a viscous flow where gas molecules frequently interact with each other. Below $1 \cdot 10^{-4}$ mbar, λ is much larger than the vacuum chamber dimensions and collision between gas molecules become rare. Instead, collisions between molecules and the vacuum chamber dominate and the flow is characterized as molecular. This regime is called high vacuum (HV) and below $1 \cdot 10^{-6}$ mbar ultra-high vacuum (UHV).

Conductance is described differently in the viscous and molecular flow regimes. The conductance of a tube for viscous flow is given by

$$C = 24450 \frac{d^4}{\eta l} \bar{p} \xrightarrow{\eta_{\text{air}, 20^\circ\text{C}} \approx 180 \text{ g cm}^{-1} \text{ s}^{-1}} 135 \frac{d^4}{l} \bar{p} \quad (3.5)$$

where d and l are the diameter and the length in cm, respectively, η the viscosity in g cm⁻¹ s⁻¹ and \bar{p} the average pressure in mbar.

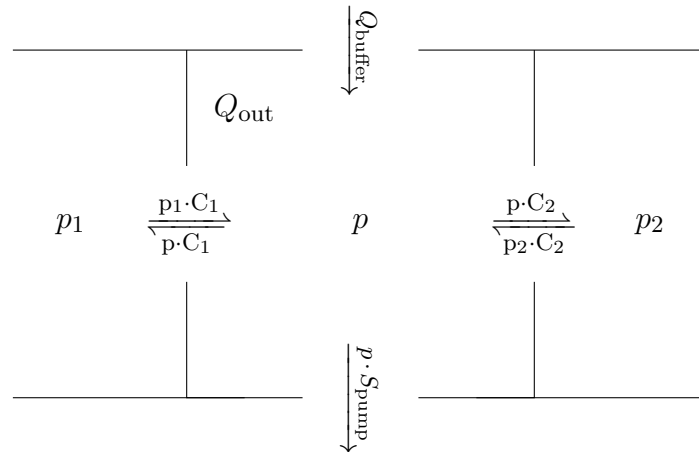


Fig. 3.3: General scheme of a vacuum chamber with pressure p , two apertures with conductance C_1 and C_2 , a pump with pumping speed S_{pump} , outgassing rate of Q_{out} and buffer gas throughput of Q_{buffer} .

For an aperture ($d > l$) the conductance for viscous flow at 20 °C is given, independent of the pressure, by

$$C \approx 20A \text{ Ls}^{-1}, \quad (3.6)$$

where A is the area in cm^2 .

For molecular flow on the other hand the conductance of an aperture is given by

$$C = 3.7A \sqrt{\frac{T}{M}} \text{ Ls}^{-1}, \quad (3.7)$$

where M is the molecular weight and A is the area in cm^2 .

In addition to gas flow into a vacuum chamber, outgassing of the chamber walls and other components within the chamber has to be considered. In the UHV regime the ultimate pressure is limited by the rate of outgassing rather than the pump speed. For stainless steel, it is specified as $1.3 \cdot 10^{-9} \text{ mbar Ls}^{-1} \text{ cm}^{-2}$ after one day of pumping, but depends on surface texture and adsorbates like H_2O or CO_2 . The latter can be significantly reduced by baking the chamber to 150 to 200 °C, leaving H_2 as the predominant residual gas in the chamber.[145]

In conclusion, the pressure p inside a vacuum chamber can be obtained by comparing the in and outgoing volumetric throughputs. For the exemplary vacuum chamber shown in Fig. 3.3 the pressure is given by

$$p = \frac{p_1 C_1 + p_2 C_2 + Q_{\text{outgassing}} + Q_{\text{buffer}}}{S_{\text{pump}} + C_1 + C_2} \quad (3.8)$$

Table 3.1: Calculated vacuum parameters of the NPMS setup with no buffer gas, closed gate valve and SRET at room temperature: λ is the mean free path (MFP), \bar{v} is the mean velocity, d is the diameter of orifices between adjacent vacuum chambers, p denotes the pressure and S is the flow rate of the used pumps. Nano 1 and Nano 2 label the first two differential pumping stages of the nano ESI ion source.

Chamber	λ (cm)	\bar{v} (ms ⁻¹)	d (mm)	C (Ls ⁻¹)	p (mbar)	S_{calc} (Ls ⁻¹)
Atm	$7 \cdot 10^{-6}$	476 (N ₂)	/	/	$1 \cdot 10^3$	/
Nano 1	$2 \cdot 10^{-3}$	476 (N ₂)	0.75	0.01	4	2.7
Nano 2	$5 \cdot 10^{-2}$	476 (N ₂)	0.75	0.09	$2 \cdot 10^{-1}$	2.1
Guide	$2 \cdot 10^2$	405 (Ar)	0.75	0.05	$4 \cdot 10^{-5}$	190
Quad	$8 \cdot 10^3$	405 (Ar)	4	4.03	$9 \cdot 10^{-7}$	190
SRET	$8 \cdot 10^3$	405 (Ar)	60	906	$9 \cdot 10^{-7}$	/

In calculations for a differential pumping system with small apertures and $p_1 \gg p \gg p_2$ the gas flow from the chambers downstream can typically be neglected.

Estimated and Measured Pressures. Based on the equations given above the pressures achievable with different sets of pumps were initially estimated. The relevant parameters for the final configuration are summarized in Tab. 3.1 for operation with no buffer gas, closed gate valve and with the SRET at room temperature. The estimation includes the effects of reduced pump speeds, due to the finite conductance of vacuum tubing and protective meshes, as well as outgassing from the vacuum chamber. Note that the conductance of the stainless-steel capillary, representing the interface between atmospheric pressure and the first source chamber, was determined empirically, since the simple analytic model given in Eq. 3.5 does not account for effects present in long thin tubes such as turbulence and viscous drag. More advanced models can describe those effects, but extensive optimization of the atmospheric interface was not a part of this thesis since low intensity nanoparticle beams are sufficient for NPMS.[146, 147] The actual pressures found in the experiment are shown in Fig. 3.4. They are generally close to the estimated values. Deviations in the trap chamber, where the ultimate pressure is dominated by the rate of outgassing rather than the pump speed, are likely due to the various materials used for mounting the ion optics. During operation, the pressures in the ion guides and trap can be increased up to $5 \cdot 10^{-2}$ mbar using needle valves to control Ar or He buffer gas flow. Higher pressures can also be achieved by reducing the pumping speeds of the turbo molecular pumps, which not only decreases the consumption of buffer gas but also prevents overheating of the pumps. The pressures in the source are adjusted using membrane valves that gradually reduce the effective pumping speed of the scroll pumps.

The pressures given in Tab. 3.1 and Fig. 3.4 correspond the original, non-linear, version of the setup. After installation of the parabolic mirrors, see Sec. 3.7, the

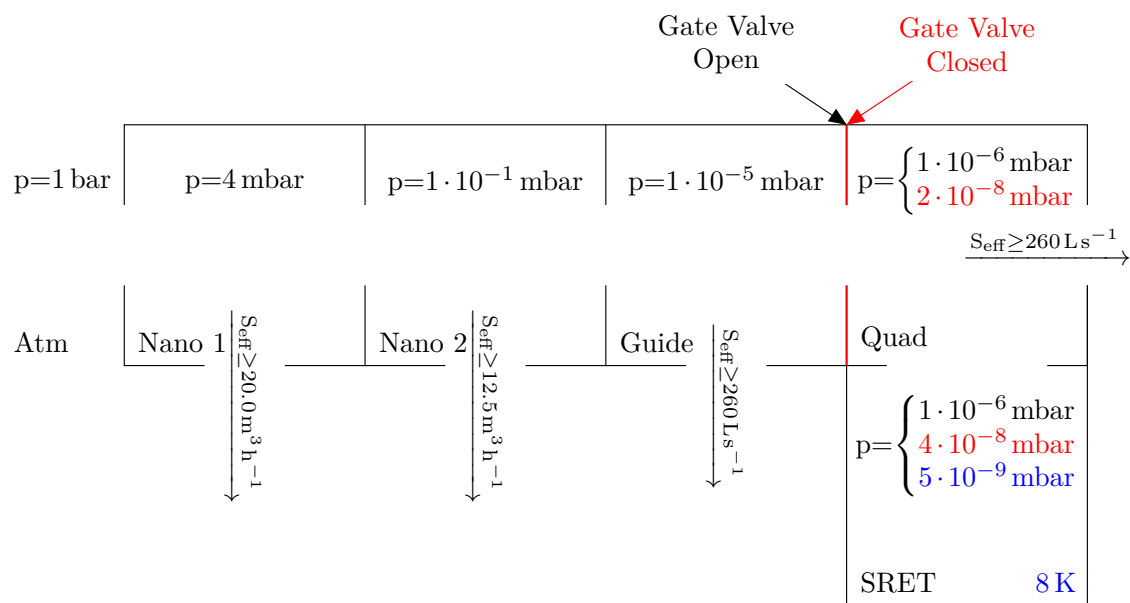


Fig. 3.4: Schematic of the vacuum system of the NPMS setup with measured pressures, with opened atmospheric pressure interface and in the absence of buffer gas, and nominal pump speeds. Nano 1 and Nano 2 label the first two differential pumping stages of the nano ESI ion source. The pressures measured for closed gate valve and cold SRET are given in red and blue, respectively.

ultimate pressure in the trap chamber increased to $1 \cdot 10^{-6}$ mbar. Since thorough testing using a He leak tester has shown no indications for external leaks the pressure increase is attributed to outgassing or a trapped volume inside the instrument. Since operation was generally possible at those pressures and mounting of the mirrors is time demanding further tests were postponed.

3.3 Nanoparticle Source

Electrospray ionization (ESI) was used to produce a beam of charged nanoparticles from nanoparticle solutions. Though the fundamentals of the technique had been known for a long time[148] widespread use of ESI ion sources started only after pioneering work by Fenn *et al.*,[149] who transferred large biomolecules solvent and fragmentation-free into the gas phase. This was awarded with the Nobel Prize in Chemistry in 2002.[150]

Today, ESI is widely used to transfer biomolecules, molecular ions and weakly bound clusters into the gas phase, and provides precise control on solvation and charge states.[36, 151–154] However, only a few non-biologic applications of ESI as a source of gas-phase nanoparticles have been reported.[68, 155] Though an ESI ion source was used successfully for the initial experiments, other sources based on laser ablation, sputtering, discharges and condensation, can be advantageous, *e.g.* for the production of metal particles over a wide size range. Those can be used for mass stepping to

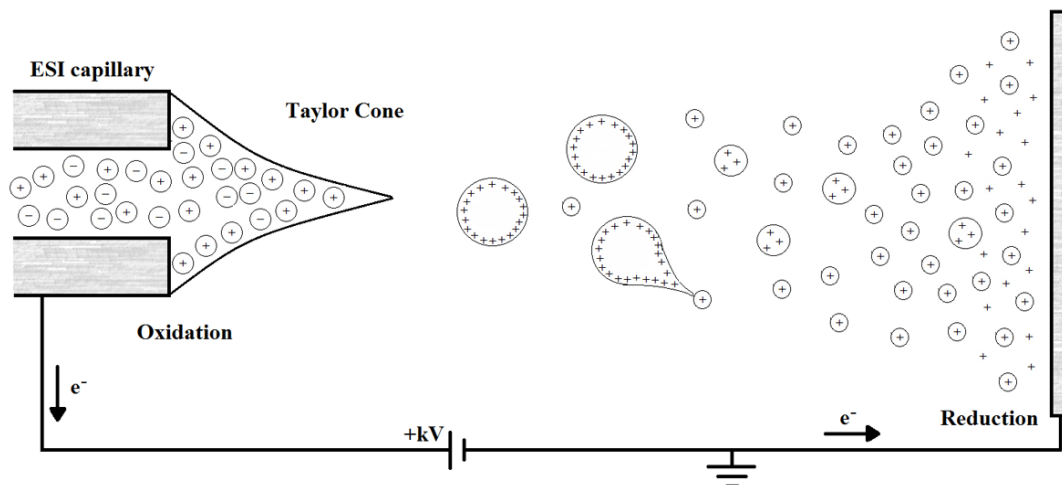


Fig. 3.5: Schematic of the ESI process in the positive ion mode. When a potential $\geq V_{\text{on}}$ is applied between a solution and a target electrode, a Taylor cone forms and charged droplets are emitted. The evaporating droplets undergo Coulomb explosions resulting in (molecular) ions and charged clusters. Reproduced from Fagiani.[156]

obtain accurate mass values or to modify the surface of a trapped nanoparticle.

ESI Technique. The ESI process is shown schematically in Fig. 3.5. A solution containing the analyte of interest passes through an emitter, either due to constant solvent supply by a syringe pump (online) or capillary forces (offline), with a tip held at high-voltage relative to a counter electrode at distance d_c . The solution is polarized at the liquid gas interface and deformed due to the electric potential. A Taylor cone (see Fig. 3.5 and also Fig. 3.7) is formed when the onset potential V_{on} is exceeded. The latter can be estimated by[157]

$$V_{\text{on}} = \sqrt{\frac{r_e \gamma \cos \theta}{2\epsilon_0}} \ln \left(\frac{4d_c}{r_e} \right), \quad (3.9)$$

with the emitter radius r_e , surface tension of the solvent γ , the half angle of the Taylor cone $\theta = 49.3^\circ$ [158] and the vacuum permittivity ϵ_0 . The corresponding electric field at the tip of a thin emitter in front of a large counter electrode is given by

$$E_{\text{on}} = \frac{2V_{\text{on}}}{r_e \ln(4d_c/r_e)} = \sqrt{\frac{2\gamma \cos \theta}{\epsilon_0 r_e}}. \quad (3.10)$$

A thin liquid jet is emitted from the Taylor cone, destabilized by the repulsion of charges and forms charged droplets. Due to evaporation of the solvent the charge density increases. With decreasing droplet radius R the Rayleigh limit ($q = 8\pi\sqrt{\epsilon_0\gamma R^3}$ [154])

is reached and they explode into smaller droplets in a process called Coulomb fission. While molecular ions, that are already present in the solution, are ejected due to the electric field of the charged droplet, described by the ion evaporation model (IEM), larger, possibly neutral, particles stay solvated and get charged as the surrounding droplet evaporates as described by the charge residue model (CRM).[154] Ultimately, stable analyte particles, analyte-ion adducts or analyte-solvent clusters remain.

The degree of solvation can be controlled by application of (heated) nebulizer gas or by CID in the subsequent elements of the ion source. While in conventional ESI ion sources a solution is fed to a steel capillary at flow rates of several $\mu\text{L min}^{-1}$ nano ESI ion sources typically use thinner glass emitters and are able to work with less concentrated solutions and flow rates below 1000 nL min^{-1} , which is useful when working with rare or expensive samples. The potential is applied either by a conductive coating, a wire placed inside the capillary or directly through the solution from an electrode upstream the emitter (liquid junction).[159]

Nano ESI Ion Source. A linear nano ESI ion source, shown schematically in Fig. 3.6, was adapted from a previous design.[55] Solvent ions and nanoparticles are sprayed by two different kinds of emitters, which are described further below. They pass through a counter propagating N_2 nebulizer gas, which accelerates desolvation. Then, they are transmitted via a 12.5 cm long, 0.75 mm inner diameter stainless-steel capillary (CS-Chromatographie Service GmbH) into the first vacuum chamber. The capillary is mounted inside of a copper block and can be heated via a heating cartridge, typically up to 100°C . The temperature can be monitored using a platinum resistance thermometer. Heating reduces the abundance of weakly bound systems such as clusters of molecular components of the solution including protonated water and methanol clusters. Next, ions and nanoparticles pass through two skimmers, each with a 0.75 mm aperture and with a distance of 4 cm between the apertures. The skimmers are mounted using six M3 screws on a 56 mm circle, compatible with the previous design. They are isolated electrically from the chamber using a 1 mm thick polytetrafluoroethylene (PTFE) ring, which also creates the vacuum seal between the differential pumping stages.

The original version was designed to be compatible with a large source chamber, which was used for a variety of different ion sources. As a consequence, the differential pumping stages had to be custom made. The new version is more compact, made from commercially available standard components and is easier to disassemble and reassemble for cleaning. It allows to monitor the distance between the capillary and the first skimmer as well as possible contaminations in this area via viewports. The pumps are connected using flexible metal hoses, which run through the optical table, leaving more access to the spraying region.

Initial experiments were conducted using an offline front end. Borosilicate emitters were pulled from thin wall capillaries (Harvard Apparatus), coated with a platinum/-palladium layer, opened with tweezers and filled with $10 \mu\text{l}$ of solution. The inner diameter at the emitter tip is typically in the 10 to $100 \mu\text{m}$ range. These type of

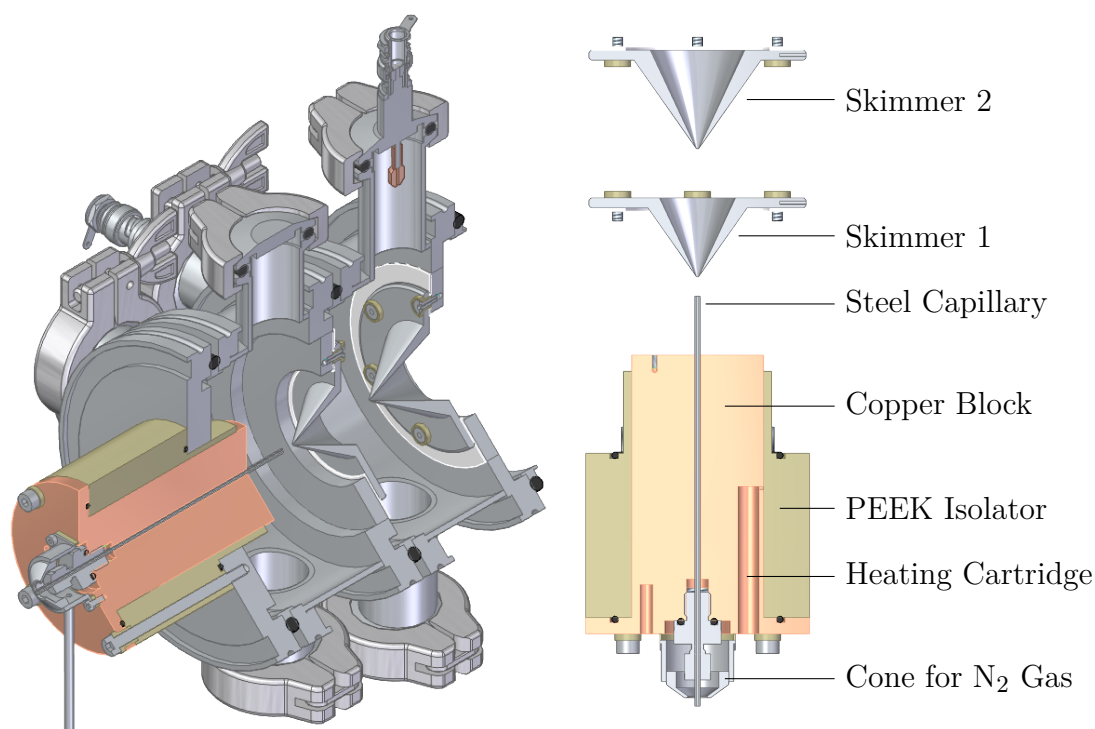


Fig. 3.6: Schematic of the linear nano ESI ion source. Ions are produced at atmospheric pressure by an ESI emitter (not shown) and are transmitted through a stainless-steel capillary into the first differential pumping chamber. They are then separated from the majority of the neutral gas flow by two skimmers. N_2 gas and heating accelerate the evaporation of droplets produced by the emitter. Direct current (DC) potentials on the capillary and the two skimmers as well as the pressure in the first two differential pumping stages can be used to control collision energies and thus the distribution of ions in the resulting ion beam.

emitters are especially suited for weakly bound systems.

As with many ion beam experiments, the ion source is the main cause for instabilities and requires a lot of attention. For highly concentrated solutions of nanoparticles the long-term stability of this emitter was not practical, since the emitters had to be modified or replaced multiple times per day. Though for the setup described here an unstable and weak ion beam would be sufficient to trap a single nanoparticle, this holds true only if all parameters are already set up for trapping. Especially during the characterization phase and first experiments a stable, intense ion beam was needed.

Thus, an online method was implemented, where the solution is pushed through an untreated $20\ \mu\text{m}$ fused silica emitter (FS-120 - Postnova Analytics GmbH) by a syringe pump (11 Plus Elite - Harvard Apparatus), at flow rates in the 100 to $1000\ \text{nL}\ \text{min}^{-1}$ range. The emitter was connected to a polyether ether ketone (PEEK) capillary via a stainless-steel adapter, shown in Fig. 3.7, where an electric potential of typically $2\ \text{kV}$ was applied. Tab. 3.2 gives estimated onset voltages for conditions used in experiments with poly(methyl methacrylate) (PMMA) nanoparticles, where water and

Table 3.2: Surface tension and estimated onset voltages for different solvents for an ESI emitter with radius $r_e = 10\mu\text{m}$ and distance $d_c = 2\text{mm}$ to the counter electrode. Calculated using Eq. 3.9.

	CH ₃ OH	H ₂ O	CH ₃ OH:H ₂ O 1:1
γ (mN m ⁻¹) at 20 °C[160]	22.95	72.75	~ 40
V_{on} (V)	780	1391	1030

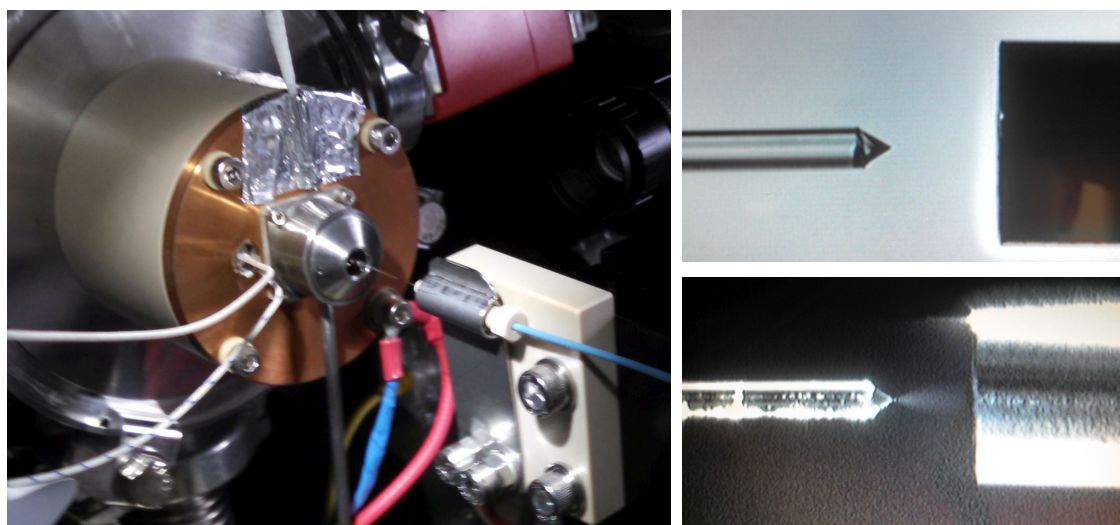


Fig. 3.7: Photographs of the online emitter interface (left) and Taylor cone during emission of fluorescing PMMA nanoparticles (right). The jet of liquid drops is visible in the bottom right photograph.

methanol, mixed 1:1 by volume, was used as a solvent. The values are smaller than the experimentally determined 2kV, however, it is reasonable to expect a reduced voltage at the tip itself due to the equilibrium between charge transport through the low conductive solution channel and charge emission. For pure water, much higher potentials are required due to its large surface tension, increasing the risk of discharges.

Once emission is stabilized by choosing the right voltage, flow rate and emitter position, the source typically runs stable until the solution in the syringe is used up, which may take up to a few days. When using PMMA solutions, it was found that the tip will get clogged after some hours, which can easily be resolved by heating the emitter with a lighter. A CCD camera was used to monitor the stability of the Taylor cone. Discharges can occur when the electric field between emitter and stainless-steel capillary is too large. They become visible on the camera if all lights are turned off and can then be avoided by reducing the emitter potential or by increasing the distance between emitter and capillary.

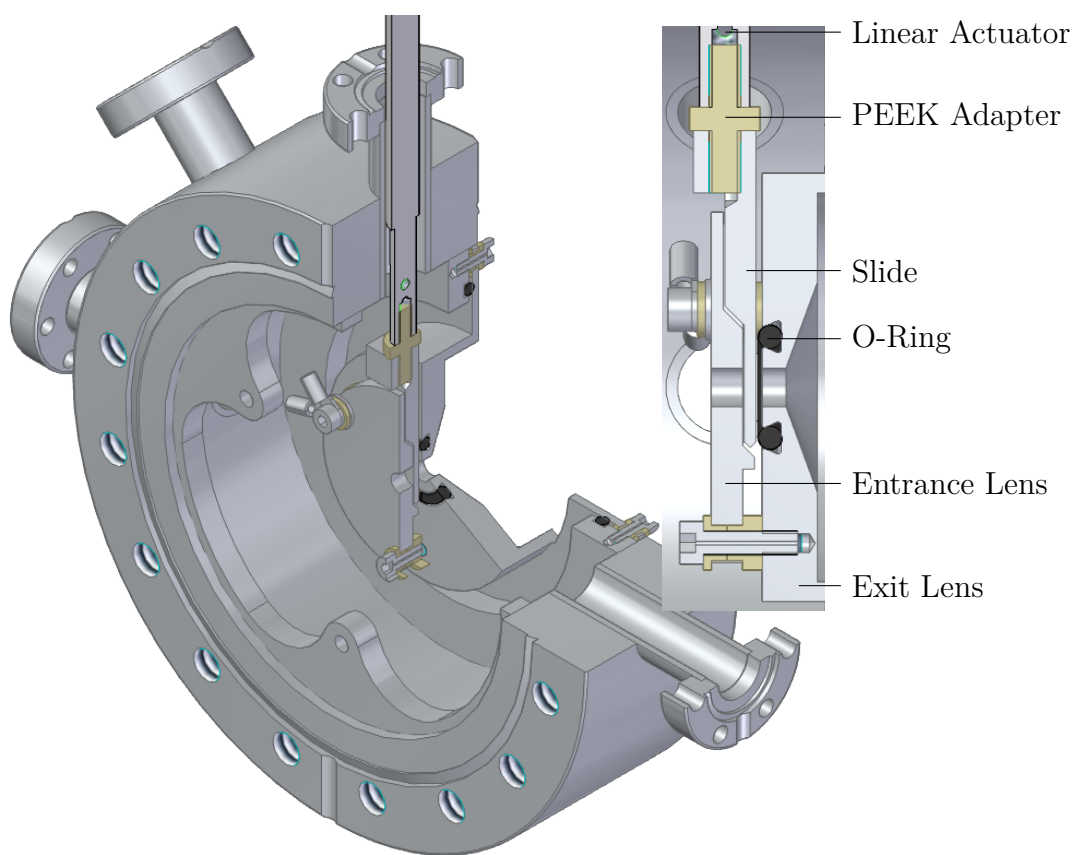


Fig. 3.8: Schematic of the custom gate valve, used to block the ion beam and gas flow from the nano ESI ion source. A linear actuator, isolated by a PEEK adapter, pushes (pulls) a stainless-steel slide against (away from) an O-ring. A DC potential on the entrance and exit lenses can be used to optimize transmission while the valve is open.

3.4 Ion Optics

All ion optics, apart of the SRET, were manufactured at the mechanical workshop of the Physics Department at the Universität Leipzig. Most ion optics were made from stainless steel 304 and most electrical connections within the vacuum chambers were made using Kapton isolated American wire gauge (AWG) 28 copper wires. Einzel lenses are used between elements to focus the beam into the next element without changing the beam energy.

3.4.1 Gate Valve

A custom gate valve design was adapted[161] to separate the source and trapping regions and allows to vent them independently. The design is shown schematically in Fig. 3.8 A pneumatic linear actuator (LBD16-25-PR - UHV Design), which is controlled

via an 5/2 solenoid spool valve (6519 - Bürkert), moves a stainless-steel slide against an edge that directs the force towards an O-ring (inner diameter 10 mm; thickness 3 mm; nitrile rubber (NBR) - Apeltrath & Rundt GmbH). The O-ring was covered with a thin layer of high vacuum grease to make a better seal. A PEEK adapter is used to connect the linear actuator to the slide while keeping them electrically isolated. The entrance and exit lens of the valve, labeled in Fig. 3.8, are electrically isolated when the valve is open. DC potentials on those lenses can be used to optimize transmission through the 4 mm apertures. However, typically they remain grounded as a reference point and the potential of the surrounding ion optics are adjusted instead.

By blocking the gas flow from the source region, lower pressure can be reached in the ion trap. In case of vacuum problems in one part of the instrument, the gate valve will be closed by the interlock to prevent an effect on the other part. The custom design is more compact compared to commercial gate valves and avoids the typical unguided region. The small slide will also cause less vibrations when moving. During initial testing, a pressure of $2 \cdot 10^{-7}$ mbar was maintained in a test chamber, while the other side was at atmospheric pressure. This allows to reach lower pressures for mass determination in the trapping chamber. Also, the abundance of molecules from the atmosphere, which might interfere with reaction experiments, can be reduced. It also provides a quick way for stopping the nanoparticle beam after single particles have been trapped.

3.4.2 Electrostatic Quadrupole Deflector

A 90° electrostatic quadrupole deflector, schematically shown in Fig. 3.9, was used to bend the beam towards the ion trap. The design utilizes 40 ruby balls of diameter $d_b = 2$ mm, which simultaneously act as spacers and fix the relative positions of the lenses. In order to compromise between force on the hole edge, centering precision and spacing, the holes have a diameter of $d = d_b \sin(45)$. [145] Four stainless-steel bending electrodes are used to deflect the ion beam. Lenses on all sides are used to fine tune the transfer into and out of the deflector.

The main purpose of the deflector is to create an optical axis on the cylindrical ion-trap axis. In a linear arrangement, a laser beam aligned on this axis would hit the gate valve or source region and cause a background signal on the photo detectors due to scattered light. A single turbo pump mounted below the deflector is used to indirectly pump the trap chamber. Thus, no dedicated turbo pump has to be mounted to the trap chamber and the cryostat can be mounted instead. Another advantage of this configuration is that the turbo pump vibrations are reduced before reaching the ion trap, due to the 90° angle between pump and trap chamber. The deflector can be used as a filter, since the ion trajectories depend on charge and kinetic energy. It also provides the option to characterize the ion beam half way through the instrument, *e.g.* by adding an ion detector or TOFMS behind one of the two free outputs. This would also be helpful to optimize the transmission of nanoparticles towards the SRET.

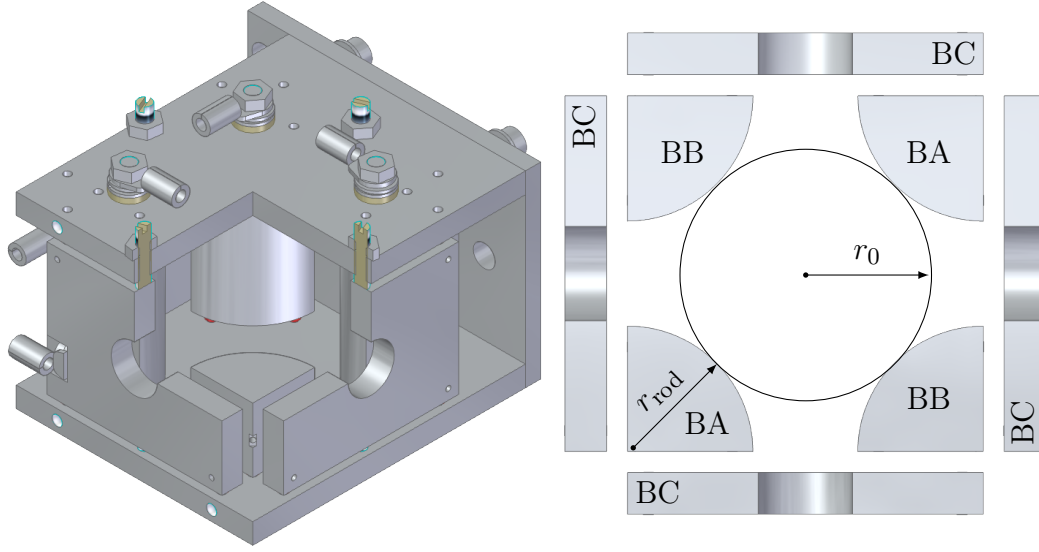


Fig. 3.9: Schematic of the 90° electrostatic quadrupole deflector. The bending electrodes BA and BB with a radius of $r_{\text{rod}} = 12\text{mm}$ and a height of 25.7 mm are arranged on a circle with radius $r_0 = 12\text{mm}$. They are charged oppositely for bending and equally for straight transmission of the ion beam. The BC lenses on all sides are connected to the same DC potential and are used to control transmission into and out of the bending region.

3.5 Linear RF Multipoles

Linear RF multipoles consist of $2n$ parallel rod-shaped electrodes arranged on a radius r_0 . They are frequently used for collimation, guiding, mass selection (only $n = 2$) and trapping. In the NPMS setup presented in this thesis a quadrupole ($n = 2$) and octopole ($n = 4$) ion guide are used.

Here only the fundamental aspects relevant for guiding of nanoparticles will be covered, while more detailed discussion of the theory of multipole RF devices can be found in the literature.[121]

The theory of the linear quadrupole ion-guide is very similar to the three-dimensional QIT described in more detail in Sec. 2.2 . In general, to confine particles with charge Q and mass M in two space dimensions an alternating potential

$$\Phi_0(t) = V \cos(\Omega t) \quad (3.11)$$

is applied, with amplitude V , frequency $F = \Omega/2\pi$ and adjacent rods having opposite polarity. The potential inside a linear $2n$ -multipole device is described in polar coordinates by

$$\Phi(r, \phi, t) = \Phi_0(t) \left(\frac{r}{r_0}\right)^n \cos(n\phi), \quad (3.12)$$

where ϕ is the azimuth angle and the z dependence can be neglected in the limit of infinitely long electrodes. This arrangement creates a time-dependent inhomogeneous electric field, which causes a net attractive force (field gradient force) towards regions of weaker electric fields and thus forces the particles towards the central axis of the multipole. While the stability parameters a and q can be used to predict stable conditions for quadrupolar fields, general a_n and q_n parameters for higher multipoles are not particularly useful, as stable transmission depends on the initial particle conditions for $n > 2$. [121, p. 41] The motion of the particle in a general multipole field is composed of a rapid oscillatory and a slower secular drift component, caused by the direct and time-averaged effect of the inhomogeneous electric field, respectively. Under the adiabatic approximation the secular component can be described as the motion of the particle in an effective (time-averaged) potential $V^*(r)$ given by [121, p. 33f.]

$$V^*(r) = \frac{n^2 Q^2 V^2}{4M\Omega^2 r_0^2} \left(\frac{r}{r_0}\right)^{2n-2}. \quad (3.13)$$

The validity of the adiabatic approximation is characterized by the adiabaticity parameter

$$\eta = 2n(n-1) \frac{QV}{M\Omega^2 r_0^2} \left(\frac{r}{r_0}\right)^{n-2}. \quad (3.14)$$

Note that for $n = 2$ the adiabaticity parameter does not depend on the coordinate r and thus the stability does not depend on the initial conditions of the ion. This leads to the unique mass selection ability of quadrupolar devices. Since particles can be lost due to collisions with the electrodes, for safe operation the turning point of the particles should be below $0.8r_0$. This is equivalent to demanding $V^*(0.8r_0) \geq E_t$ with the initial transverse kinetic energy E_t . At the maximum turning point, the adiabaticity parameter should be $\eta(0.8r_0) \leq 0.3$ to ensure the validity of the adiabatic approximation. [121, p. 38] While stable transmission can be achieved outside these limits, there are generally no practical reasons to use linear multipole ion guides in this way.

Fig. 3.10 compares the effective potentials of several linear multipoles. The effective field free region in the multipole center increases with n , which is beneficial for applications where efficient collisional cooling is needed. In addition, a larger number of rods leads to an increase in acceptance angle and transmission range. On the other hand, if confinement close to the central axis is required, a smaller n should be chosen. When buffer gas is added to multipoles, collisions will typically reduce the transverse kinetic energy E_t of incoming particles. They are then confined closer to the center, where η approaches zero, leading to increased transmission. When using a linear quadrupole in mass-selective mode, however, collisions should be avoided.

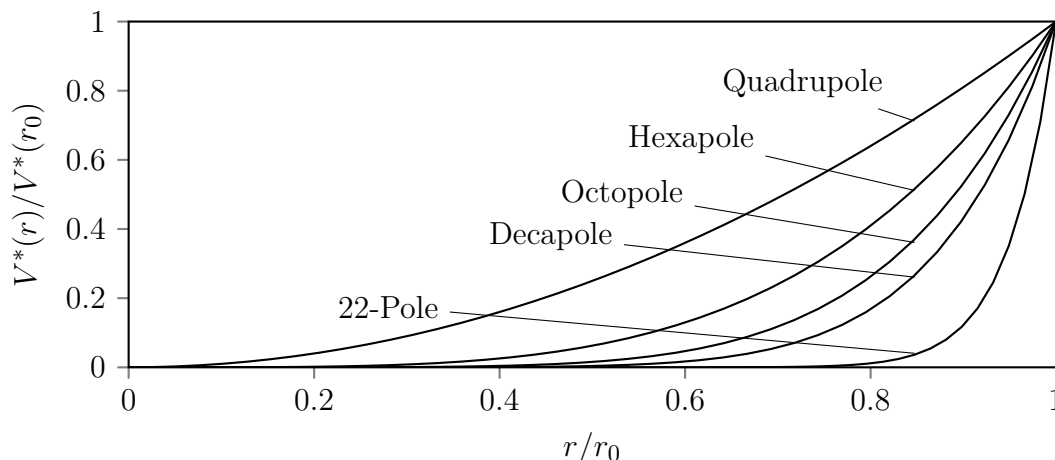


Fig. 3.10: Comparison of the radial components of the relative effective potentials of RF devices. Higher multipoles produce a larger field free region, which is advantageous to avoid RF heating, while lower multipoles confine the ion beam closer to the axis. Adapted from Esser.[162]

Ion Beam Collimation and Thermalization. Solvent ions and nanoparticles leave the ion source typically with wide distribution in phase space. The ion beam can be collimated and thermalized in an ion guide in order to increase transmission efficiency in subsequent parts of the instrument.[163–165] For stable transmission conditions, as discussed above, ions are confined in the radial direction, but are free to move along the ion guide axis and their kinetic energy is separable in an axial ($E_{\text{kin}}^{\parallel}$) and a thermal component ($k_B T$) in radial direction[166]

$$E_{\text{kin}} = \frac{1}{2m} (p_{\parallel}^2 + \Delta p^2) = E_{\text{kin}}^{\parallel} + k_B T. \quad (3.15)$$

The spread in kinetic energy relates to the ion beam temperature T , which can be cooled by collisions with buffer gas particles. For sufficient amount of collisions the ion beam temperature equilibrates with the buffer gas temperature and the beam is thermalized. Collimation here corresponds to a reduction of thermal motion in radial direction, making the ions in the beam move more parallel. The average kinetic energy is reduced inside the guide and approaches zero for sufficient amount of collisions. The DC potentials of entrance and exit lenses penetrate only a finite distance into the guide, *e.g.* a few centimeter, while in its center the axial field is essentially zero.[167] Eventually, the ions will come close to the exit lens and are accelerated out of the guide. This process is even more efficient when the DC offset of the ion guide rods is close to the average incident ion energy, reducing the initial $E_{\text{kin}}^{\parallel}$. For ion guides, thermalization depends on the number of collisions and thus on initial particle conditions, pressure and the length of the guide. For ion traps, however, storage times can be chosen

large enough to assure thermalization. For other applications, like trapping of single nanoparticles, it might even be advantageous to work with a broader energy distribution such that some particles will have the right energy to be trapped (compare Sec. 3.11).

The octopole and quadrupole ion-guides, described in the following, were driven by the same RF generator (RFG50-0.1MHz - CGC Instruments) at a fixed frequency close to 100 kHz with amplitudes V_0 adjustable up to 800 V. For each guide, an individual DC offset of ≤ 100 V is added to all rods.

Octopole Ion-Guide. An octopole ion-guide ($n = 4$) was used for guiding and for collimation to increase transmission through the following parts of the instrument. A schematic of the octopole ion-guide with dimensions is shown in Fig. 3.11. The ion guide, based on a previous design,[55] is mounted inside a stainless-steel tube, which is filled with buffer gas via a PTFE tube. By partially separating the ion guide from the vacuum chamber the steel tube allows to reach higher pressures inside the guide. PEEK holders are used to position and isolate the rods inside the tube and stainless-steel contact rings are used for their electric connection. A capacity of (33.6 ± 0.1) pF was measured at the vacuum feedthroughs. Additional PEEK holders on the tube ends are used to mount entrance and exit lenses. A DC potential on these lenses is used to optimize guiding and for particle trapping. Compact Einzel lenses are used to focus the particle beam into and out of the octopole guide.

Quadrupole Ion-Guide. Though a linear quadrupole can be used in a mass-selective mode, the resolving power for nanoparticles is not sufficient (see Sec. 2.1). Thus, here it is only used for ion guiding, confinement of the ion beam to the axis for efficient coupling to the ion trap and as a very rough M/Q filter. A schematic of the quadrupole ion-guide along with dimensions is shown in Fig. 3.12. The design is conceptually identical to that of the octopole ion-guide. Holes are added to the steel tube to increase the gas flow from the ion-trap chamber to the turbo molecular pump in the quadrupole chamber. They also help to reach pressures $\leq 1 \cdot 10^{-5}$ mbar in the quadrupole ion-guide region as needed for potential operation in mass-selective mode. The capacity at the vacuum feedthroughs was measured to be (19.2 ± 0.1) pF.

As all ion optics in the present setup, the linear quadrupole ion-guide is mounted on a flange with feedthroughs, allowing to assemble all connections outside of the vacuum chamber. Due to its relatively high mass and distance from the flange it is prone to tilting. A pin was designed to support the quadrupole ion-guide on the exit side, however, using this pin might introduce stress once the vacuum flange is mounted. Since it was found that the tilting can be compensated using the mounting rods and careful positioning of the vacuum flange while tightening, use of the pin was omitted.

Trapping In RF Multipoles. Both multipole guides can also be used as ion traps by choosing appropriate pressure and potentials. Ions coming from the source with sufficient kinetic energy overcome the potential barrier of the entrance lens. Due to loss

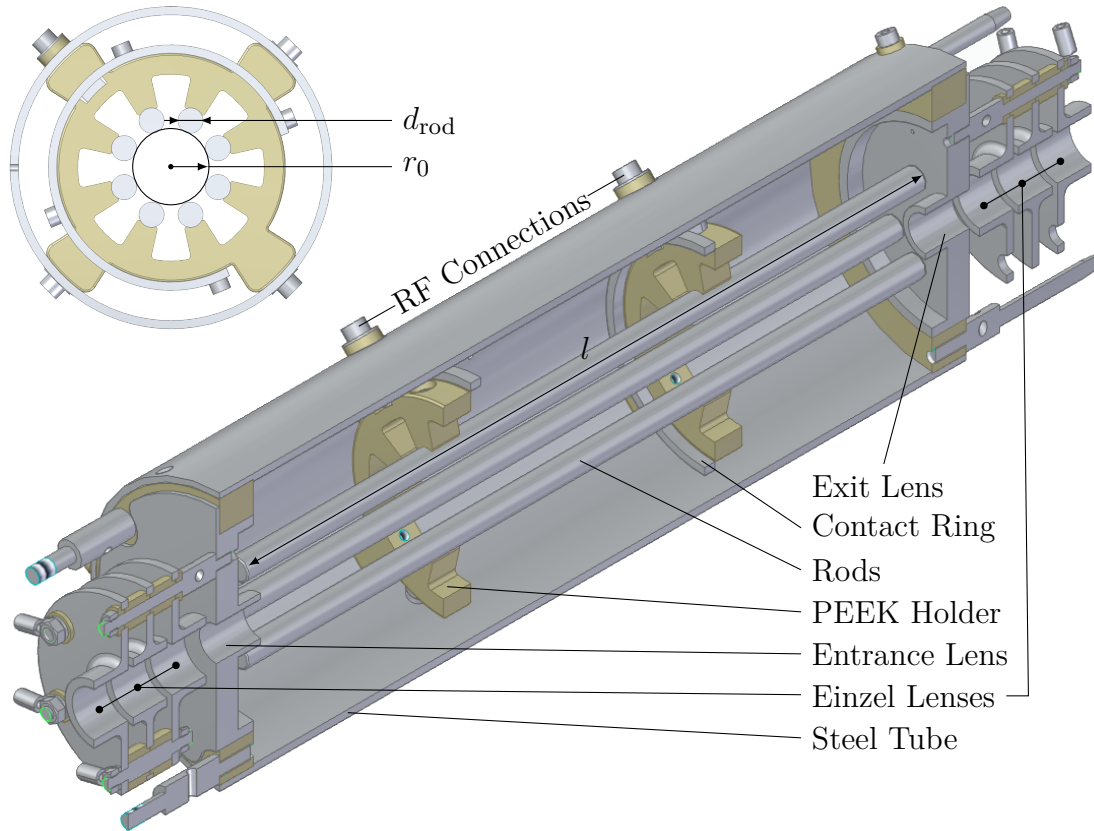


Fig. 3.11: Schematic of the octopole ion-guide. The rods have a diameter of $d = 6$ mm, a length of $l = 200$ mm and are placed on a circle with radius $r_0 = 9$ mm. Dimensions were chosen according to $r_0 = (n - 1)d/2$. [121, p. 45]

of kinetic energy by collisions with buffer gas atoms or molecules, they are reflected by the potential barrier of the exit lens. When they reach the entrance lens for the second time they will have lost sufficient energy to be reflected again and remain trapped inside the multipole. After a defined time of ion loading the potential of the entrance and exit lens can be increased and decreased respectively, to extract an ion package. Note that this mode of trapping is qualitatively different from trapping in the SRET, described in Sec. 3.11. By trapping nanoparticles in the guides and extracting them towards the ion trap, it should be possible to obtain well-defined initial conditions, which can then be used to optimize transmission in simulations (compare Sec. 3.11). This has been tried in the early stages of the characterization, before the first nanoparticle was detected, and further experiments are needed to evaluate this approach.

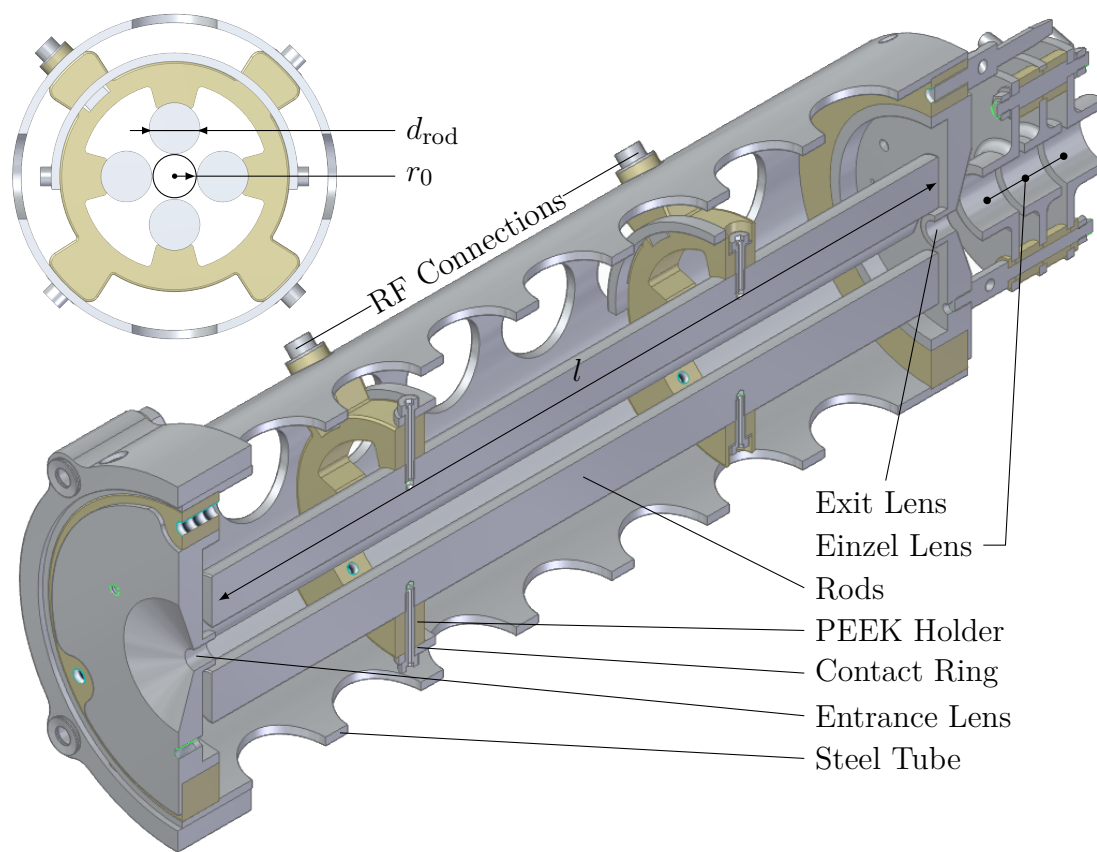


Fig. 3.12: Schematic of the quadrupole ion-guide. The rods have a diameter of $d = 12\text{mm}$, a length of $l = 198\text{mm}$ and are placed on a circle with radius $r_0 = 5.3\text{mm}$. Ideal hyperbolic electrodes were approximated by circular rods considering $d/2 = 1.148 * r_0$. [168]

3.6 Split-Ring Electrode Trap

The QIT has been used for a variety of applications as described in Sec. 2.2. Often the ideal geometry needs to be modified *e.g.* to allow for ion loading and extraction. Such modifications will inevitably effect the potential shape and thus the mass-selecting capabilities of the trap. During commercialization of QIT mass spectrometers, stretching of the distance between end cap electrodes was found to compensate for observed mass shifts. This modification became public years later and the effect was eventually attributed to field imperfections close to the holes in the end cap electrodes. [74, p. 105]

In order to provide access for laser beams, optical detection and ions a modified trap was designed by Schlemmer *et al.*, [104] where the ring electrode was replaced by eight rods. Due to the lack of rotational symmetry, which affected the periodic ion trajectories, split-ring electrode traps (SRETs) were designed in subsequent work. Fig. 3.13 shows a schematic of the ideal QIT compared to the SRET design used for the current NPMS setup. The present SRET is based on a design by Gerlich and Decker, [67] which is also used in a scaled version by Howder, Bell and Anderson. [68]

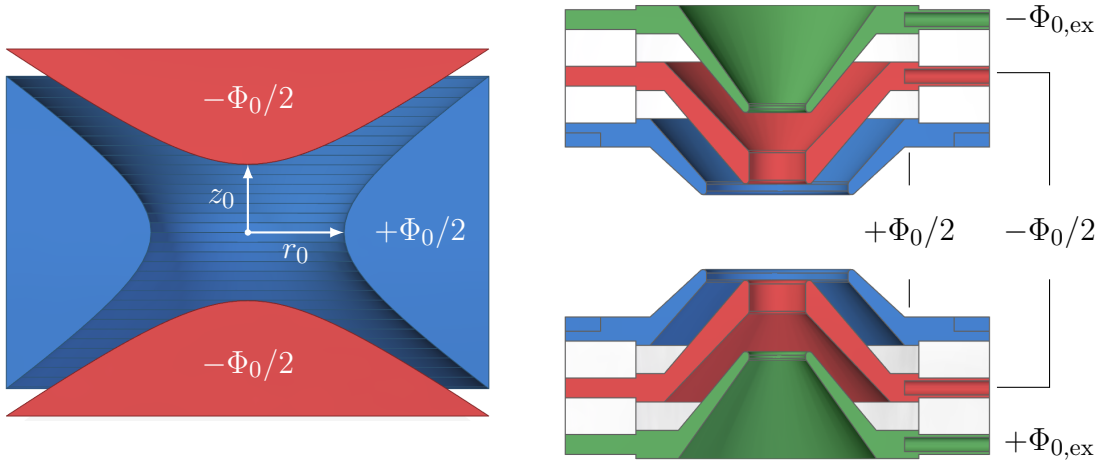


Fig. 3.13: Schematic of an ideal QIT (left) and a split-ring electrode trap (SRET) (right). End cap electrodes are color coded in red, (split) ring electrodes in blue and excitation electrodes in green. The SRET design allows for insertion of ions, irradiation by lasers and collection of light emitted by trapped particles, while maintaining an ideal quadrupolar potential close to the trap center.

The ideal QIT and the SRET produce different potential shapes and there is no reason to assume validity of Eq. 2.14 for determination of the mass-to-charge ratio (M/Q) from the secular frequency for the modified design. However, by carefully tuning the geometry of the individual lenses, the deviation of both designs close to the trap center was minimized. Systematic optimization of trap parameters to produce an ideal potential had been applied for QITs in the past, but never for an SRET.[125]

3.6.1 Genetic Algorithm

The geometry of the split-ring electrode trap (SRET) was optimized using a genetic algorithm (GA).[162] To this end, a parameterized model of the SRET was implemented and evaluated using the field and particle trajectory simulator SIMION.[169] In SIMION, arbitrary electrode geometries can be defined by the user in the form of discrete potential arrays. The electrode geometry can be defined via the basic CAD functionality of the user interface, or via geometry files (GEM files) based on a script language. The finite differences method (FDM) is used to iteratively calculate the potential on all non-electrode points of the array, such that the Laplace condition is fulfilled. Particle trajectories can then be simulated and user programs, written in the programming language Lua, can be included to enable flexible control over every individual step of the simulation.[170] The original version of the GA, made for potential optimization, was extended to allow for optimization of the geometry by automating the generation of GEM files and potential arrays, refinement and execution of Lua user programs for analysis. Further details on the general concept and implementation can be found in Appendix D.

3.6.2 Optimization of the SRET Geometry

An SRET design, used to study the thermal emission and fragmentation of hot C_{60}^+ ions, was taken as a starting point for the optimization.[67] Note that two scaled versions were mentioned in the original work, with an effective r_0 of 4.3 mm and 5.4 mm, respectively, and the parameters of the larger one were used here. Another scaled version of the same design was later used for investigations on photoluminescence of charged CdSe/ZnS quantum dots and black body radiation of hot carbon nanoparticles.[68, 130, 131, 143] Though the design has proved to be useful for many applications, the electric potential was never extensively optimized. The use of Eq. 2.14 to determine M/Q from the secular frequency is only justified if the potential in the range of particle motion is sufficiently close to that of an ideal QIT. If the potential is not harmonic, *i.e.* higher multipole terms cannot be neglected, the secular frequency will depend on the particle amplitude, and the radial and axial motions are no longer decoupled (see Sec. 2.2.1). In addition, a change in resonance frequency during excitation can affect the shape of the intensity dips in resonant excitation spectra and thus reduce precision as discussed in Sec. 4.5. Though the precision is currently limited mainly by the amplitude stability of the RF supply used for trapping, especially for higher frequencies needed for smaller particles (see Sec. 2.2.2), care must be taken to work in a regime of small amplitude motion, where the effects of geometry modification are sufficiently small. The amplitude of motion can be reduced by choosing a steeper effective potential, limited by the RF supply, or by reducing the thermal energy of the particle by cooling, increasing the complexity of the experiment.

The main goal of the optimization described in the following is to extend the quasi harmonic region to reduce the effects of higher multipole components. This will prove to be essential for accurate mass determination and detection of single molecule adsorption events in the future.

The objective can be broken down into three main requirements for the optimization. First, the potential shape should be harmonic, second, the trap design should minimize $r_0^2 - 2z_0^2$ and, third, the potential in the trap center should be zero. In addition, the optical access on the radial axis should be as unrestricted as possible. This condition can be achieved by increasing r_0 and z_0 , however, at the cost of shielding from external fields and the need for higher RF potentials to generate the same effective potential. Thus, the radial opening angle of the split ring electrode (θ in Fig. 3.14) was held fixed and an objective to minimize r_0 and z_0 was added. Since the trap is not closed, the effect of external fields, such as from the radiation shield and the excitation lenses, must be considered. Further objectives follow from practical considerations; The electrode distance should remain large enough to prevent discharges and electrode shapes should be smooth to facilitate fabrication.

The results of the optimization using SIMION will be presented here, followed by a complementary analysis using the boundary element method (BEM). A simple approach to analyze the potential along a certain axis of the SRET in SIMION is to define a neutral particle with appropriate starting position and momentum. The

position, potential and electric field along the particle trajectory can then be obtained through the user program. The effective characteristic trap parameters r_0 and z_0 were calculated from the derivative of the simulated potential using the ideal QIT potential given in Eq. 2.3.

$$\left| \partial_z^2 \Phi_z \right| = \Phi_0 / z_0^2 \quad \rightarrow \quad z_0 = \sqrt{\Phi_0 / |\partial_z^2 \Phi_z|} \quad (3.16)$$

$$\left| \partial_r^2 \Phi_r \right| = \Phi_0 / r_0^2 \quad \rightarrow \quad r_0 = \sqrt{\Phi_0 / |\partial_r^2 \Phi_r|} \quad (3.17)$$

While analysis of the potentials takes only fractions of a second, the refinement of new potential arrays is the time limiting step. In version 8.1 of SIMION refinement is parallelized, allowing to create and analyze new geometries within a few seconds and reach convergence of the GA after a few hours.

The derivatives $\partial_z^2 \Phi_z$ and $\partial_r^2 \Phi_r$ are constant for an ideal QIT, but only approximately constant for the SRET. The deviation from a constant value as a function of the distance from the trap center was used to evaluate the deviation from a harmonic potential. The fitness function Eq. 3.18 was used for the optimization and was designed to converge towards 100 as the differently weighted terms are minimized.

$$\begin{aligned} \text{fitness} = & 100 - (\sigma_z + \sigma_r) \cdot 1000 - |V_{\text{center}}| \cdot 100 \\ & - \left| r_0^2 - 2 \cdot z_0^2 \right| \cdot 100 - \max(z_0 - 3.7, 0) \cdot 10 \end{aligned} \quad (3.18)$$

The parameters σ_z , σ_r are the standard deviations of $r_0(r, z = 0)$ and $z_0(z, r = 0)$ in the range below 500 μm from the trap center. V_{center} , r_0 and z_0 are the potential and characteristic parameters at the trap center. The last term prevents the electrodes from moving away from the trap center, which improves the potential shape at the trap center, but reduces the effective potential. Limiting conditions also assure a minimum distance between all electrodes, reducing the risk of discharge. In addition to the grounded end cap electrode, also the grounded radiation shield was included, to account for perturbations of the potential from the local environment. Indeed, it was found that, especially for a large radial opening angle, the effect of these grounded lenses cannot be neglected.

Fig. 3.14 shows cross sections and characteristic trap parameters for the initial and optimized SRET designs. The relevant parameters of the fitness function are given as insets in the figure and can be used to compare the original and optimized design against each other and against the ideal quadrupolar potential. The deviation of r_0 and z_0 from a constant value was reduced to less than 10 μm for a distance below 500 μm from the center, making manufacturing precision the limiting factor. Note, in the original version the potential at the center was not zero, but 21.5% of V_0 , consistent with Decker,[171, Fig. 2.14] while it is reduced to 0.001 V_0 in the present version. The optical access to the trap center was doubled by limiting the search space to solutions with a radial opening angle θ of more than 20°. This should significantly increase the sensitivity for smaller particles given a fixed lens position.

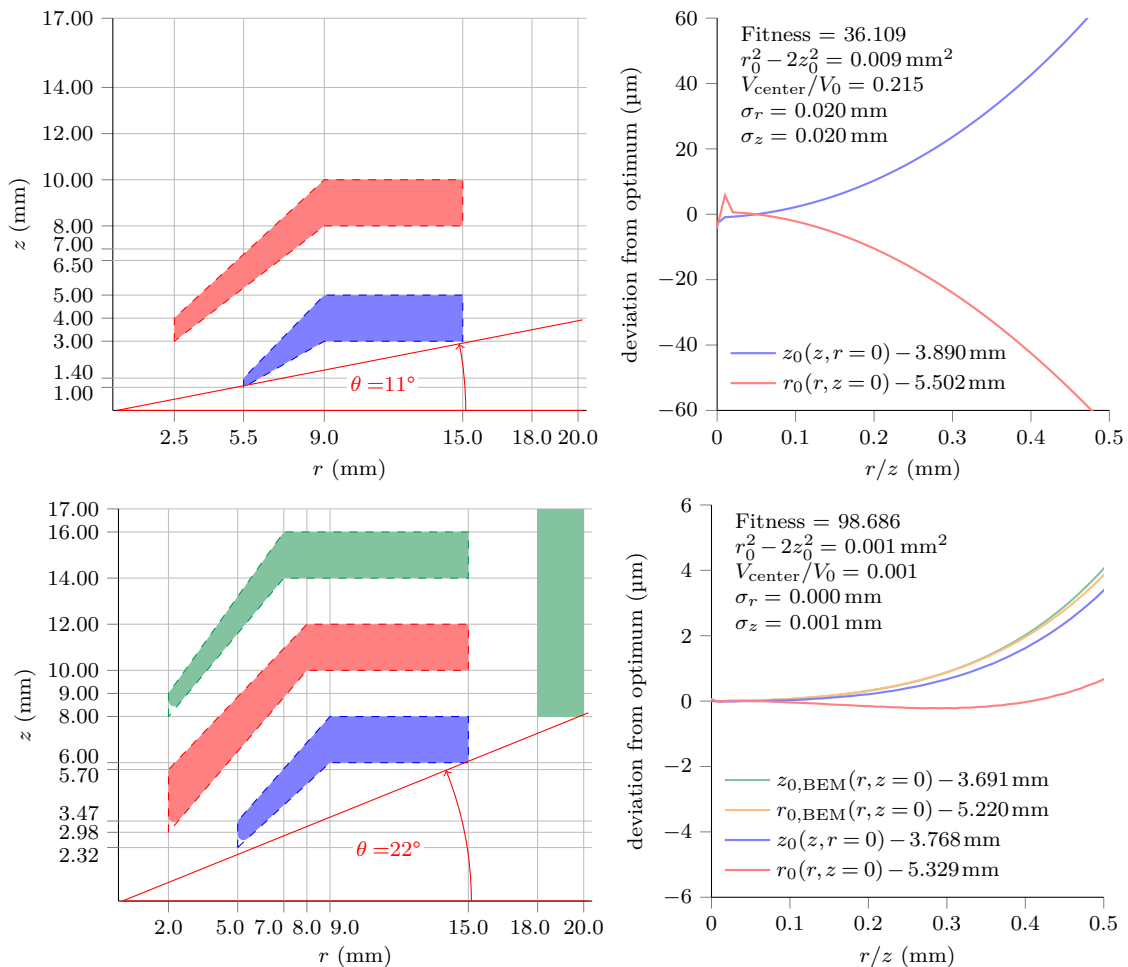


Fig. 3.14: Cross sections of the initial (top) and optimized (bottom) SRET geometries. Split ring electrodes are color coded in blue, end cap electrodes in red and excitation electrodes and radiation shield in green. All dimensions are labeled on the axes. Inner electrode edges are rounded with a radius of curvature of 0.25 mm. On the right the deviation of $r_0(r, z=0)$ and $z_0(z, r=0)$ from an ideal QIT is shown together with the fitness as defined in Eq. 3.18. Note that the y scale in the lower right panel has been magnified by a factor of 10 for clarity. For a distance $\leq 500\mu\text{m}$ from the trap center, the resemblance of an ideal quadrupolar potential is only limited by manufacturing precision of the workshop, typically within 10 to 100 μm when using a lathe. For the optimized potential the deviations are also given based on independent BEM calculations.

Other methods to describe the potential of the SRET include superposition of line charges, the finite element method (FEM) and the boundary element method (BEM). With BEM, the potential only needs to be discretized on a boundary (electrode surface) and an approximate solution can be given at any point in space. For this approach the potential is expressed as a multipole expansion as shown in Sec. 2.2.1. The optimized geometry shown in Fig. 3.14 has been analyzed by Fanghanel, Asvany and Schlemmer

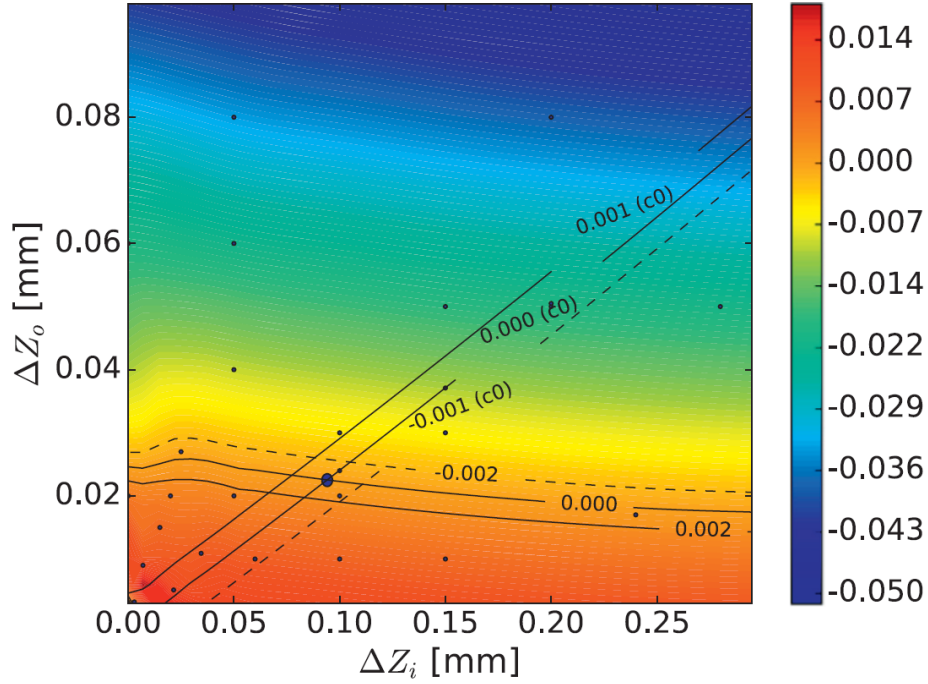


Fig. 3.15: Multipole coefficient c_4 as a function of the axial displacement of one split ring (Z_i) and one end cap (Z_o) electrode calculated using BEM. The desired conditions $c_4 = 0$ and $c_0 = 0$ are found for a displacement of less than $100\ \mu\text{m}$. Reproduced from Fanghanel, Asvany and Schlemmer [172] with permission from Elsevier.

[172] using BEM. In their work, the effect of a displacement of one split ring (Z_i) and one end cap (Z_o) electrode were changed and the geometry was found to be close to optimal regarding those two parameters as shown in Fig. 3.15. However, the influence of the radiation shield was neglected in their study. In this context, the coefficients for expansion of the potential according to Eq. 2.17 have been determined for the optimized SRET and are given in Tab. 3.3. The value found for $r_0 = \sqrt{2}z_0$ is $5.220\ \text{mm}$, deviating by $100\ \mu\text{m}$ from the value obtained in SIMION. The offset in the potential center corresponds to c_0 , which is only half compared to the SIMION calculation. Based on the coefficients, up to c_6 , the potential was calculated and analyzed in the same way as described above. The resulting deviations of r_0 and z_0 are shown in Fig. 3.14 and are in good agreement with the results obtained with SIMION. The deviation of the SRET and ideal potential is $0.001\ \%$ for $r < 100\ \mu\text{m}$ and $z < 90\ \mu\text{m}$. Determination of the coefficients takes about one hour for a 3D model, where the effect of electrode misalignments can be investigated. For a 2D calculation, exploiting cylindrical symmetry, the analysis tool about $45\ \text{s}$ compared to $10\ \text{s}$ for the generation and analysis of the potential in SIMION. These numbers will vary with resolution and computing power, but it is generally possible to couple BEM calculations to the GA in future applications. In a more detailed discussion by Fanghanel [173] it has been found that, at least in the simulation, the effects of higher multipole components are

Table 3.3: Expansion coefficients of the optimized SRET, normalized to the quadrupole coefficient c_2 by choosing $r_0=5.220$ mm.[126]

$c_0 = 0.000437$	$c_2 = 1$	$c_4 = -0.015314$
$c_6 = -1.070393$	$c_8 = -0.536459$	$c_{10} = 0.991127$
$c_{12} = 1.865672$	$c_{14} = 0.369619$	$c_{16} = -3.377410$

negligibly small for particle amplitudes of less than $100\ \mu\text{m}$. For the real trap this remains to be shown. Despite the limited manufacturing precision the results are expected to be significantly closer to the desired conditions compared to the original SRET design.

Electrode Misalignment. The design was tested against possible misalignment during the manufacturing process and the results are summarized in Fig. 3.16. The unperturbed potential shapes are given as dashed lines for reference. While 2D potential arrays have been used for the optimization, exploiting cylindrical and mirror symmetry, 3D potentials arrays were created to investigate the effect of electrode misalignments. For small tilts ($<1^\circ$) and deviations of the electrode spacing ($\sim 100\ \mu\text{m}$) the effect on the potential shapes is well below the mechanical precision of 10 to $100\ \mu\text{m}$. Tilting of the end caps is most sensitive, but should be easily avoided when using a lathe for manufacturing of the electrodes. Generally, small deviations between the physical implementation and the theoretical electrode shapes are tolerable as long as symmetry is preserved.

While rotational symmetry is important to avoid perturbation of the periodic motion, the molybdenum spacer and stainless-steel rods (see Fig. 3.17) break rotational symmetry. Their effect was simulated by four rods, of appropriate dimensions and position, either grounded or on the same potential as the split ring electrode. A hexagonal shape of the outer electrode edges, possibly useful for 3D printing, was investigated as well. Both modifications have negligible influence on the potential shape.

3.6.3 Implementation of the SRET Design

The optimized lens geometry (see Sec. 3.6.2) leaves some freedom with regard to mechanical realization. As for the other ion optics, materials were chosen to be UHV-compatible. Since the trap was designed for cryogenic operation, the thermal conductivity and expansion was considered as well. Room-temperature designs often use a stack of stainless-steel electrodes separated by ceramic spacers.[68, 171] They are not suitable for cooling, as the stainless steel contracts by a factor of $16 \cdot 10^{-6}\ \text{K}^{-1}$ and would break the brittle ceramic spacers. For the IRPD experiments, described in Appendix A and Appendix B, a cryogenic ring electrode trap (RET) was used based on a stack of molybdenum electrodes and sapphire spacers.[55, 174] In the new design,

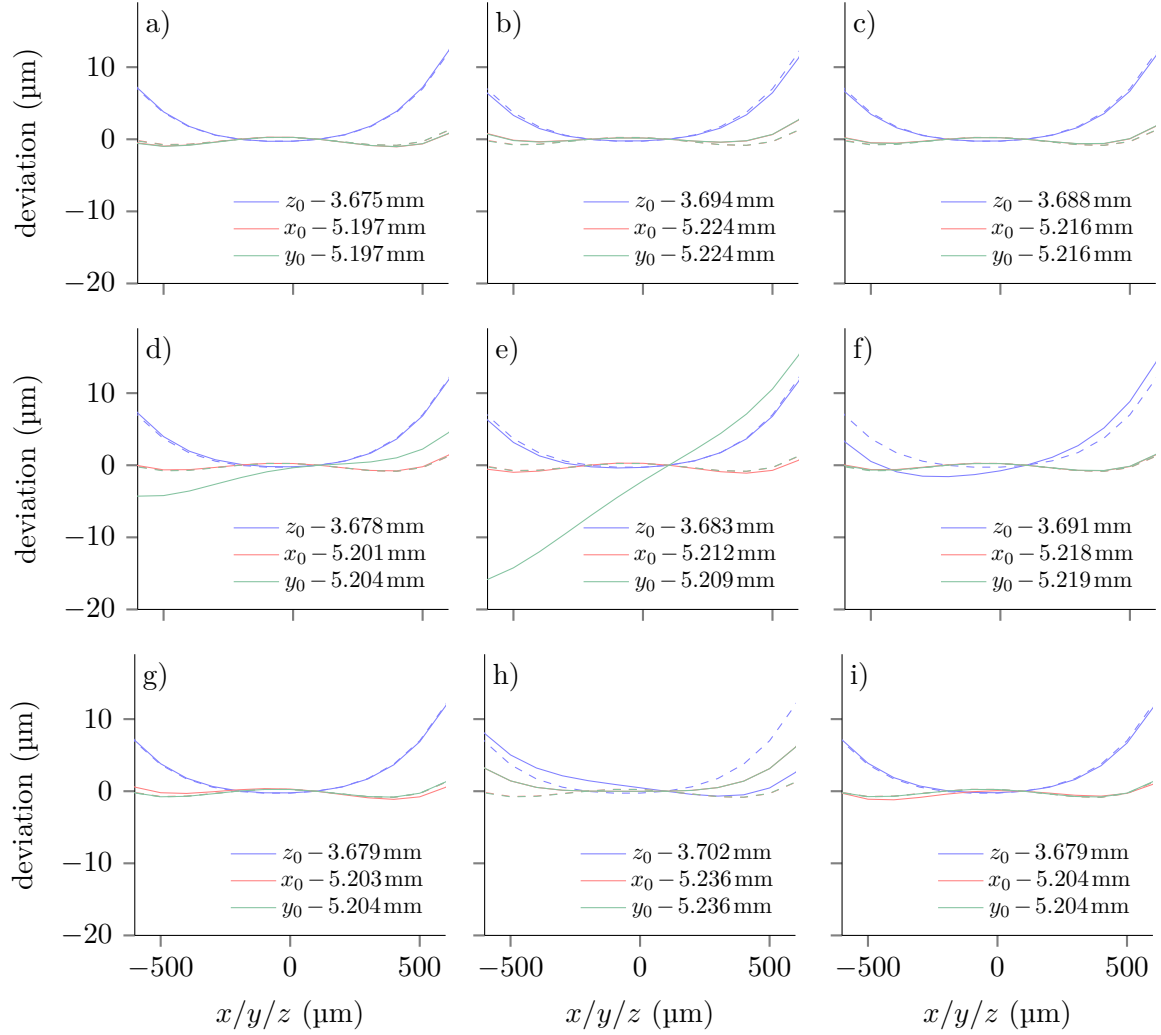


Fig. 3.16: The panels show the effect of various types of electrode misalignment and perturbation by external electrodes. Each panel shows the deviation from a harmonic potential with constant x_0 , y_0 and z_0 along the axial (z) and two radial (x and y) SRET axes as well as the effect on the characteristic trap parameters. The unperturbed potentials are shown as dashed lines for reference. a) added four rods on split ring potential (see Fig. 3.17) b) added four grounded rods, c) using hexagonal instead of circular edges (for 3D printing), d) single split ring tilted by 1° , e) single end cap tilted by 1° , f) single split ring shifted by $100\ \mu\text{m}$ in z direction, g) single split ring shifted by $100\ \mu\text{m}$ in r direction, h) single end cap shifted by $100\ \mu\text{m}$ in z direction, i) single end cap shifted by $100\ \mu\text{m}$ in r direction.

shown schematically in Fig. 3.17 and in photographs in Fig. 3.18, the experience from cryogenic RETs and room-temperature SRETs were combined in order to obtain a cryogenic SRET.

In order to allow for fabrication on a lathe, the split ring (blue) had to be made from three parts. Four thin bridges were introduced in the central part, in order to

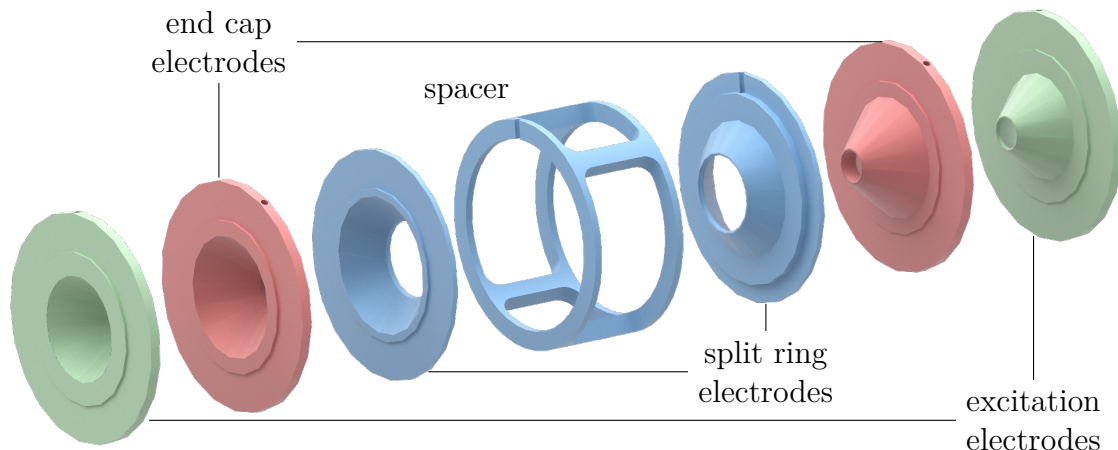


Fig. 3.17: Explosion drawing of SRET electrodes. Split ring electrode (blue), end cap electrodes (red) and excitation electrodes (green). The distance between the split ring electrodes is fixed by a molybdenum spacer, which also creates an electrical contact between them. The spacer leaves sufficient optical access while perturbing the potential in the trap center only minimally, as shown in Fig. 3.16.

Table 3.4: Room-temperature thermal conductivity λ and thermal expansion α of selected materials. Note that the thermal conductivity of sapphire significantly increases at lower temperatures and reaches a maximum of $200 \text{ W m}^{-1} \text{ K}^{-1}$ at 25 K.[176, 177]

	$\lambda \text{ (W m}^{-1} \text{ K}^{-1}\text{)}$	$\alpha \text{ (} 1 \cdot 10^{-6} \text{ K}^{-1}\text{)}$
molybdenum	138	5.4
sapphire	25	3-6
copper	400	16
copper/tungsten	150-240	6-8
manganin	22	14-19

fix the distance between the split ring electrodes. Their effect on the potential was shown to be negligible (compare Fig. 3.16). The central electrode could have been manufactured as a single part, using 3D printing, to reduce complexity. Metal 3D printing, also known as micro laser sintering, can achieve a precision of $5 \mu\text{m}$, but is currently not suitable for this application, since the resulting parts are porous and cause significant outgassing when used in a vacuum chamber. Plastic 3D printing combined with electroplating can be applied to obtain complex shapes with a precision of $<25 \mu\text{m}$, as recently shown for a hexapole guide, which smoothly transforms into two quadrupole guides, reducing production time and costs.[175] For cryogenic applications, however, the thermal conductivity and expansion of the plastic substrate and metal coating need to be considered and seem unfavorable for the present application.

Inspired by the existing SRET designs, the trap itself is a stack of molybdenum

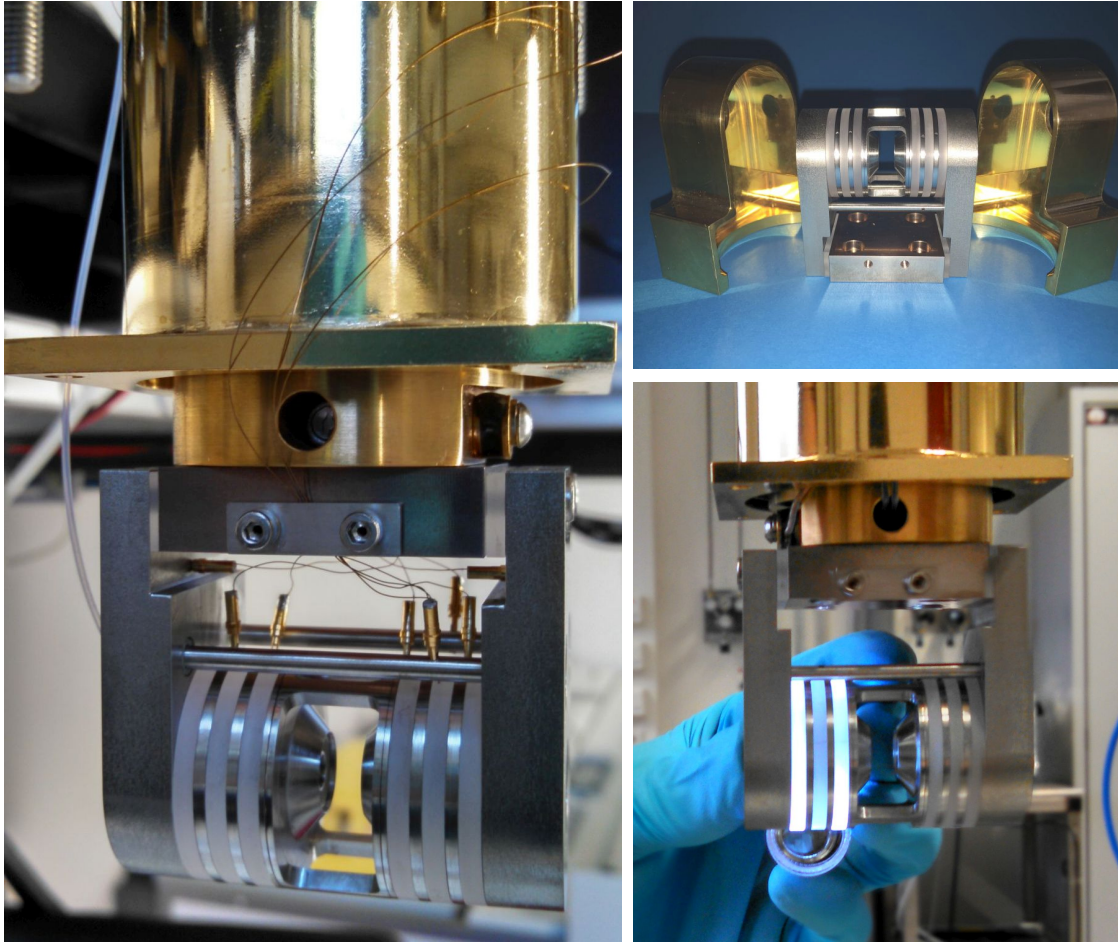


Fig. 3.18: Photographs of the split-ring electrode trap (SRET). On the left, the assembled trap is shown with electric connections and without radiation shield. Two isolated stainless-steel rods hold the stack of molybdenum electrodes and sapphire spacers together. The photograph on the top right shows the radiation shield and the adapter plate.

ring electrodes. Sapphire discs define the spacing and axial electrode alignment. Both materials exhibit low thermal expansion and high thermal conductivity at cryogenic temperatures (see Tab. 3.4). In the present design, the effect of thermal expansion changes the characteristic trap parameters, z_0 and r_0 , only by fractions of a μm . The harmonic shape of the potentials is retained even for larger displacements, as discussed in Sec. 3.6.2. The adapter plate for mounting to the cold head was made from a copper tungsten alloy (CuW), which combines high thermal conductivity with thermal expansion close to that of sapphire and molybdenum. Two rectangular sapphire spacers are used to isolate the adapter plate from the entrance and exit lenses of the trap. The complete trap is surrounded by a gold-coated copper shield that protects the trap from room-temperature black-body radiation. The shield is split along the radial axis and has apertures on the cylindrical axis for particle loading and optical access. The stack

is held together by two stainless-steel rods, to keep it under tension when cooling down. To avoid the reduction in radial optical access they were positioned at the same angle as the bridges in the central molybdenum spacer. Using two central rods, in contrast to three external rods used for most RET designs, allows to move the radiation shield as close as 3 mm to the lenses reducing the optical access only by $\approx 10\%$, as the distance of the collimating lens from the trap center is limited by the shield. The rods are electrically isolated from the entrance and exit electrodes using Krüpax, a composite of paper and resin, which is less brittle than ceramics. The potential on both rods can be controlled individually allowing to move trapped particles within the radial trap plane. The DC component of the potential on the excitation electrodes is used to move the particle along the cylindrical trap axis. Moving the trapped particles helps with detector alignment or, especially for larger agglomerates, helps to compensate for gravity.

Kapton-coated manganin (CuNiMn) wires with a diameter of 0.14 mm (312-KAP-MAN-014 - Alletra GmbH) were used for electrical connection of the trap electrodes to the feedthroughs in the vacuum chamber. They combine high and thermally stable conductivity of $4.8 \cdot 10^{-7} \Omega\text{m}$ with a low thermal conductivity. On the ring electrode side they were soldered using UHV compatible solder (Sn95Ag4Cu1 - STANNOL) into gold coated copper beryllium pins (212-PINM - Alletra GmbH), which in turn are plugged into 1 mm holes in the electrodes.

The trap is driven by a home-built RF amplifier, which is based on a design from the Anderson group.[178] It amplifies a sine wave, generated by a function generator (33510B - Keysight), and can be run at 25 to 200 kHz with amplitudes V_0 up to 200 V. The amplifier has an integrated circuit that allows for superposition of a DC offset to the RF outputs. Analysis of the frequency spectrum by FT revealed that the amplitude of the second harmonic component is about 2% of the main component. The contribution to the effective potential decreases quadratic with frequency and amplitude and is thus in the order of $1 \cdot 10^{-4}$

Gas is introduced to the trap chamber using a 1 mm outer and 0.5 mm inner diameter PTFE tube. Initially it was mounted inside a diagonal hole in the entrance lens (see Fig. 3.17) to create a locally high pressure region for particle deceleration. The tube was later realigned such that the gas diffuses into the ion-trap chamber, to eliminate turbulences and avoid complications while trapping. It was found that trapping at high pressures is fast in this configuration. Further tests need to be done to evaluate the usefulness of continuously introducing or even pulsing gas into the entrance lens region.

Apart from the sapphire spacers, obtained from SITUS Technicals GmbH, the complete trap was built by the workshop of the Physics Department at the Freie Universität Berlin.

3.7 Light Sources and Optical Detection

A diode pumped solid state (DPSS) laser (CivilLaser) with a power of 500 mW and a central wavelength of 532 nm is used for particle detection by light scattering and fluorescence. The laser beam has a diameter of 2 mm and a waist in the trap center that can be continuously reduced down to 500 μm using a biconvex lens mounted on a rail. The nominal power stability is $\leq \pm 5\%$ over two hours.

The optical setup is shown in Fig. 3.19. Up to three beam paths can be aligned through the trap center at the same time. The first passes through on the cylindrical trap axis and two more are focused into and out of the trap using off-axis parabolic mirrors. Typically, one laser is used for mass determination and a second for spectroscopy. A third laser is useful for alignment, diagnostic purpose or heating, but also allows for more advanced two-color experiments.

Light from a particle in the trap center is monitored by a CCD camera and APD. Rough alignment is achieved using an adjustable point source, *e.g.* a small lamp or a thin pin in the laser beam, on a XYZ-stage. For fine alignment, initially trapping of bright particles is confirmed using the CCD camera followed by fine tuning the APD position. As described in Sec. 4.1, the particle is moved in and out of the laser beam to verify that the signal seen at the APD is from the particle and not background.

Custom off-axis parabolic aluminum mirrors (Thorlabs GmbH), which are achromatic by nature, were used to create access for two additional laser beams. The mirrors were built according to the dimensions given in Fig. 3.20 with a focal length of $62\text{ mm} \pm 1\%$ and were mounted on a holder shown in the same figure. The dimensions were chosen such that the four mirror surfaces are part of a single paraboloid formed by rotating a parabola around the cylindrical ion-trap axis. A first mirror is used to focus a collimated laser beam into the ion-trap center while the opposing mirror will collimate the beam again and direct it out of the chamber to reduce stray light. The focal point can be moved around the trap center in all three dimensions by aligning and slightly prefocusing the incident laser beam. Similar mirrors have been used with SRETs in the past, typically to focus CO_2 laser beams for particle heating into the trap center.[67, 68] Conveniently, at around 10 μm , those beams were invisible to the sensitive APD detector, described below, and did not interfere with secular frequency measurements. Though the mirrors could potentially be used for the 532 nm scattering laser this would lead to an increase in background signal at the APD, due to small imperfections of the optical surface, making it suitable only for very bright particles. A planar mirror at the exit port could potentially be used to send the beam back through the ion trap in counter propagating direction to reduce the effect of accumulated photon impulse.[67]

The CCD camera (DMK 41AU02 - The Imaging Source Europe GmbH) images an area of approximately $8 \times 6\text{ mm}$ including the split ring electrodes, which helps with orientation.

A 35 mm, 1:1.9 objective in front of the camera is used to adjust the imaged area and allows to image a smaller section around the trap center if needed. The camera has 1280×960 pixel with an area of $4.65\ \mu\text{m}^2$ per pixel and a light sensitivity of 0.5 lx. It

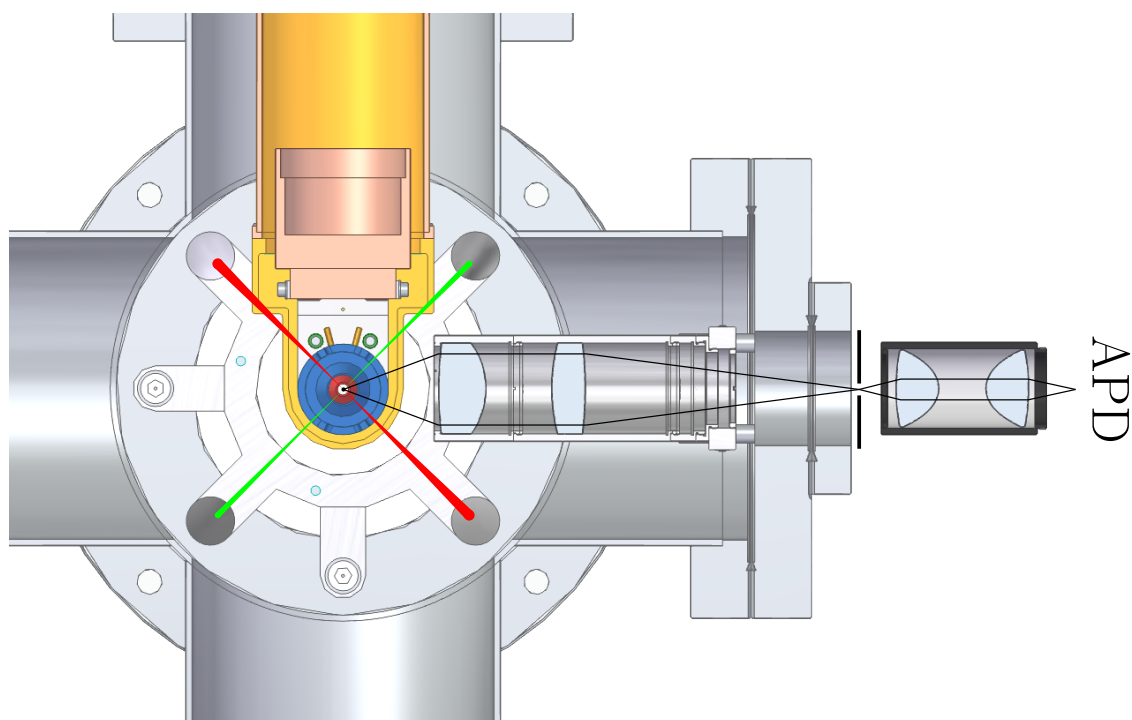


Fig. 3.19: Cross section of the ion-trap chamber, showing the ion trap and two paths for laser irradiation and one for light detection. A third laser path is available along the trap axis, orthogonal to the section plane. An iris at the focal point of the second lens is indicated by solid black lines. Ions from the pressure sensor (not shown) are used to induce charge steps (see Sec. 2.3.4)

is used mainly for diagnostic purposes and for imaging of bright particles and Coulomb crystals. In addition, it enables determination of particle amplitudes, relevant for resonant excitation measurements. The light that is scattered off the imaged ring electrodes provides valuable feedback on the laser alignment.

The APD (Count-50C - Laser Components GmbH) on the other hand has a single 100 μm diameter detection area and is capable of detecting single photons with a dark count rate of 50 Hz. Photons in the 400 to 1000 nm range can be detected with a maximum detection efficiency of 70 % at 670 nm. The 45 ns dead time allows to detect up to $20 \cdot 10^6$ photons per second, though a correction factor has to be used at the upper end to correct for saturation. For high counting rates the measurement software can turn the APD off to prevent damage.

A lens system of two achromatic lenses (#33-923, #49-374 - Edmund Optics) with diameters of 30 mm and back focal lengths of 38.1 mm and 76.2 mm, respectively, is used to collect light from the trap center. The lens next to the trap is mounted such that the trap center is close to its focal point to collimate the light emitted by a particle. The detection room angle for this system is 2.3 %, limited by the distance

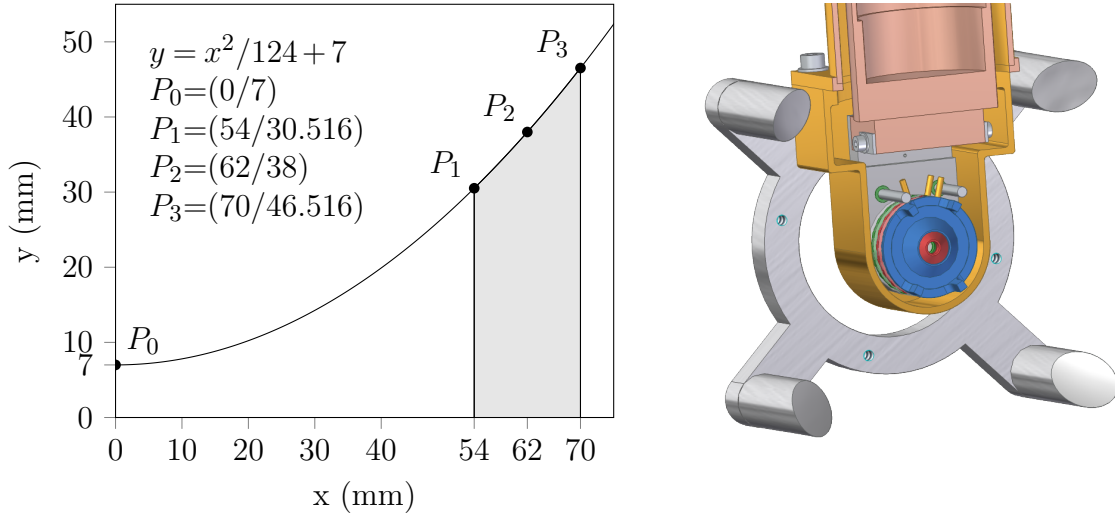


Fig. 3.20: Left: Dimensions of the four off-axis parabolic aluminum mirrors, which create two additional laser paths through the ion-trap center. Right: Cross section of the ion trap giving a 3D impression of the relative alignment of the parabolic mirrors to the trap center.

of the first lens to the trap center, which is necessary because of the radiation shield. Though a lens can be mounted directly into the radiation shield, tension induced by thermal expansion has to be considered, and materials with low thermal expansion such as sapphire or fused quartz limit transmission in the IR range. In addition, a lens in the radiation shield would block the diagonal laser paths and can accumulate charges at its surface that would affect the trapping potential.

The same system is used for both detectors and a mirror (not shown in Fig. 3.19) can be flipped in and out to switch between them. An iris was placed close to the focus point of the second lens, directly after the vacuum window, to get rid of background light that does not originate from the trap center. By blocking the reflexes from the trap electrodes it greatly simplifies alignment of the APD. Two molded aspheric condenser lenses with a focal length of 16 mm (ACL25416U - Thorlabs) are used to guide the light towards the APD. Initially a similar setup was used where light was collected from both sides of the ion trap, such that both detectors could be used simultaneously. It was changed to the current version after it was found that reflexes of the lenses on the opposite side of the ion trap increased the background signal on both detectors.

532 nm notch filters (#67-119 - Edmund Optics) can be placed in front of the CCD or APD detectors to reduce the intensity scattered laser light and thus facilitate detection of fluorescence. Lens tubes are typically blackened by anodization, in order to reduce stray light. Lenses inside the vacuum chamber, however, were mounted in unanodized lens tubes to decrease outgassing from porous anodized surfaces. An alternative design idea included pot like vacuum flanges, which would allow to move the windows in the vacuum chamber closer to the trap allowing all lenses to stay outside and easily accessible. This idea was abandoned, since it would have reduced light

collection efficiency and was not compatible with the diagonal laser paths created by the parabolic mirrors. Aspheric condenser lenses, as used for the APD optical setup, suffer from chromatic aberration. This has to be considered when switching to other scattering lasers or looking at fluorescence. For analysis of broad thermal emission another optical setup is needed,[179] however, there are currently no plans for this application with the instrument described here.

3.8 Ion Detection

While ultimately nanoparticles are detected optically in the trap center, other detectors are available for diagnostic purposes. An EM (R6985-80 - Hamamatsu) is mounted behind the trap to detect the total ion signal. Transmission of the laser beam through the EM is possible, due to an off-axis design and a custom exit hole. It features a conversion dynode, which is used with a potential of up to 8 kV. The current pulses at the EM output are amplified by a current amplifier (DLPCA-200 - FEMTO Messtechnik GmbH) and converted to transistor transistor logic (TTL) pulses using a discriminator (436 - Ortec). The TTL pulses can then be counted using data acquisition cards. A pressure-dependent background signal is generated by pressure sensors close to the EM, but they can be turned off during operation. Also, the EM should not be operated above $1 \cdot 10^{-4}$ mbar to avoid discharges.

The detection efficiency depends on the velocity of the ions impinging on the conversion dynode. No quantitative result for nanoparticle detection efficiency for this type of detector was found in literature, but detection is typically limited to particles with masses below 1 MDa (also compare Sec. 2.1).[180]

A picoammeter (9103 - RBD Instruments) was used to detect the ion signal at several positions throughout the setup. Total ion currents were measured at the skimmers, gate valve, deflector, quadrupole ion-guide entrance and exit lenses, trap entrance and at a dedicated target after the trap. A bias voltage of ± 18 V is applied to the collector lens to attract charged particles and reduce loss of signal due to electron emission on particle impact. In contrast to the EM, the detection does not depend on the velocity, but only on the charge. With a resolution of 0.01 pA at least 6000 charges per second are needed to obtain a signal.

Both detectors were mainly used in the initial stages of experimentation to check all ion optics while guiding ion beams. When using a typical 10 mmol L^{-1} test solution of sulfuric acid the concentration of molecular ions is $6 \cdot 10^{18} \text{ mL}^{-1}$. Solutions of PMMA nanoparticle on the other hand were typically prepared with a concentration of 200 nmol L^{-1} or $1.2 \cdot 10^{14}$ particles per mL, which is similar to the concentrations of impurities in typical solutions. Due to the excess of molecular ions, lack of sufficient mass selection, and the sensitivity of both detectors to molecular ions an optimization of the nanoparticle ion beam was not possible.

For $F = 90 \text{ kHz}$ and $V_0 = 720 \text{ V}$ the quadrupole ion-guide should not transmit light solvent clusters (e.g. $\eta = 30$ for $M/Q = 1000$, $Q = 1$). This is confirmed in simulations

where no transmission was possible under those conditions. However, an ion signal was detected after the quadrupole ion-guide even when using pure solvents, possibly due to the presence of larger solvent droplets in the ion beam (compare Sec. 4.3).

3.9 Cryogenic Cooling

Cryogenic cooling of the ion trap is one of the main features that distinguishes the present experimental setup from previous ones. Reducing the temperature of the ion trap, while not essential for mass spectrometry, increases the precision of an NPMS measurement by reducing the thermal motion and bringing the particle closer to the more harmonic trap center. The main advantage, however, is that the ambient temperature, and thus the temperature of the nanoparticle, can be changed over a wide range in a controllable manner. In order to compensate for heating by black body radiation and probe lasers, the ion trap temperature has to be well below the desired particle temperature. For fundamental research on those and on other types of nanoparticles even lower temperatures are desired in order to facilitate comparison of experimental and theoretical results.

The cold trap also works as a cryogenic pump, which reduces the partial pressure of residual gases. For constant pressure, the amount of collisions with buffer gas molecules or atoms increases with decreasing temperature making energy loss inside the trap more efficient and thus improves trapping performance.

The motion of the particles in the trap should be confined to a few tens of μm , limiting the acceptable vibration due to the applied cooling technique. Even for small amplitude perturbations resonances can affect the particle motion as purposely done for the resonant excitation technique (see Sec. 2.3). Thus, a low vibration cooling technique is needed. While cooling with liquid N_2 is inexpensive and easy to implement, the lower temperature limit of commercial systems is 65 K. Closed-cycle liquid helium cryostats on the other hand can achieve temperatures in the mK range, without the need to refill the cryogen.

A vibrationally isolated Gifford-McMahon type closed-cycle helium cryostat (CCS-XG-UHV/204N - Cryophysics GmbH) was used in the present setup. While these systems typically exhibit vibrational amplitudes of $10\ \mu\text{m}$ [181] they are reduced to less than 50 nm in this version. The cold head is mounted on a frame surrounding the apparatus such that there is no mechanical contact between cold head and sample mount. The space between cold head and sample mount is filled with helium heat exchange gas and sealed by a rubber bellow. The first cooling stage is connected to the radiation shield and reaches 50 K while the second cooling stage cools the ion trap down to 8 K. A $50\ \Omega$ heating cartridge and silicon diode temperature sensor, controlled by a partial integral differential (PID) controller (Model 335 - Lake Shore), are used for temperature regulation over a range of 8 to 350 K.

Compared to previous NPMS setups an additional flange is needed to mount the cryostat, making access to the trap center more difficult. This is solved in the new

setup by integration of the 90° deflector. When cooling from room temperature to 8 K the sample mount will contract by almost 1 mm. Thus, the trap has to be aligned either for high or low temperature experiments. This can be done by a port aligner (PA100-H - UHV Design / (5b) in Fig. 3.2), which is mounted between the ion-trap chamber and the sample mount. Alternatively, height changes can be compensated by alignment of the light scattering laser and the APD detector, which is especially useful for smaller temperature changes. A linear translation stage is used to adjust the vertical distance between both parts. For mounting the ion trap, a mechanical connection can be added between the cold head and sample mount such that the trap can be lifted out of the chamber in a controlled way.

3.10 Electronics, Measurement Control and Data Acquisition

Most experimental parameters are controlled using two multifunction modules (National Instruments). The module PXI 6723 provides 32 analog outputs while the module PXI 6224 provides 32 analog inputs, both between ± 10 V. Both provide two counter/timers and digital input/output lines in addition. They are mounted in a five-slot chassis (NI PXI-1033) for simple integration of further modules in the future. An interface between the acquisition cards and the further devices was built, based on commercial connector blocks (CB-68LPR - National Instruments).

An analog output board (FHI ELAB #5824) amplifies the analog outputs by a factor of 20 (maximum output is between ± 172 V) and provides outputs for connection to the corresponding ion optics. The amplified voltages are internally divided by 20 and send back to the analog inputs in order to quickly detect short-circuits or amplification faults. The counter/timers are used, depending on the measurement mode, to detect signal rates or frequencies.

Most parameters on the new NPMS setup are controlled or read out via a custom LabVIEW measurement software, which is presented in more detail in Appendix C. This provides great flexibility for continuous improvement of measurement modes and allows to save and restore the instrument configuration. Parameters are constantly written to a log file, which allows to reconstruct most experimental results, even if no files were saved by the operator. Experiments can be automated and conducted over night (e.g. monitoring a particle for several days). Using the feedback from the individual detectors a GA can optimize the ion optic potentials. The LabVIEW implementation of the GA is similar to the Lua version described in Sec. 3.6.1. The pressures in the individual vacuum chambers are constantly monitored. A home-built interlock device was designed to turn off all voltages in case of a vacuum fault or individual devices that are controlled via the digital outputs, such as the RF generator for the ion guides (Sec. 3.5) and a high-voltage supply (FHI ELAB #5725) used for the EM and ESI emitter.

The ion trap is driven by a home-built RF amplifier (Sec. 3.6.3) and another home-built device allows to apply a weak alternating potential for resonant excitation experiments. Both are controlled by the measurement software via a two channel function generator (33510B - Keysight).

3.11 Simulation of Guiding and Trapping

A virtual version of the complete instrument was created using SIMION in order to test the function of all ion optics before they were built. This allowed to estimate the potentials needed for guiding and trapping of nanoparticles and aperture sizes between differential pumping stages.

The effect of collisions with the background gas was included in the simulation by adapting the *hs1* hard sphere collision model implemented in the *collision_hs1* example provided with SIMION. The model assumes a Maxwell-Boltzmann distribution for the gas velocity and calculates the MFP according to

$$\lambda = \frac{c_{\text{ion}}}{c} \frac{1}{\sigma n}, \quad (3.19)$$

where c_{ion} is the ion speed, $\sigma = \pi(r_{\text{ion}} + r_{\text{gas}})^2$ is the collision cross section, n is the density of gas particles and c is the mean relative speed between the ion and gas particle, calculated according to

$$c = \bar{c}_{\text{gas}} \left(\left(s + (2s)^{-1} \right) \frac{\sqrt{\pi}}{2} \text{erf}(s) + \frac{1}{2} \exp(-s^2) \right), \quad (3.20)$$

with

$$\text{the mean gas speed} \quad \bar{c}_{\text{gas}} = \sqrt{\frac{8kT}{\pi m_{\text{gas}}}}, \quad (3.21)$$

$$\text{the median gas speed} \quad c_{\text{gas}}^* = \sqrt{\frac{2kT}{m_{\text{gas}}}}, \quad (3.22)$$

$$\text{and the ratio} \quad s = \frac{c_{\text{ion}}}{c_{\text{gas}}^*}. \quad (3.23)$$

Based on the ion speed and MFP the collision probability is calculated after each time step in the simulation. The simulation time step was chosen such that there are at least 20 steps per MFP in order to avoid skipping collisions. Collisions are treated as elastic scattering events in the reference frame of the colliding gas particle. Kinetic cooling and heating is simulated for ions, but neglected for the gas particles. Due to the increase of collision events with ion size and pressure, simulating charged nanoparticle guiding through the complete setup is significantly slower than for molecular ions and

takes up to one minute per particle. The simulation speed can be greatly increased in the future by calculating the effects of several collisions in one step or using a viscous drag approach.[165, 167] The random collisions, simulated in the used model, led to a distribution of velocities and trajectories of particles entering the trap, similar to the experiment, while an analytical friction will be more reproducible and thus better suited for optimizations.

The initial conditions of the particles in the ion source are currently not accessible experimentally. Assuming an ion velocity close to the speed of sound after transmission through the steel capillary, where the ions are dragged along with the background gas flow, is reasonable.[147] In addition, the gas flow and potentials in the source region will effect the particle energies. The pressure in the first vacuum chamber can be up to 50 mbar and cannot be treated with the collision model described above. Proper treatment would involve additional computational fluid dynamics (CFD) simulations, which are beyond the scope of this thesis. Charged particles produced by an ESI ion source exhibit a broad mass, charge, thermal and translational energy and angular distribution, due to formation of agglomerates, fragments, solvent clusters and molecular ions. Thus, nanoparticle trajectories were simulated for a broad range of initial conditions and for a given set of initial conditions it was always possible to find appropriate pressures and potentials for guiding and trapping, within the parameter range defined by the experimental setup. In the following an exemplary simulation will be used to discuss the most important aspects.

A ten times positively charged 25 nm particle with a mass of 5 MDa, corresponding to a single PMMA particle, was used for an exemplary simulation. It starts of in the second skimmer region at roughly the speed of sound (350 ms^{-1}). The trajectory within the experimental setup can be seen in Fig. 3.21. The particle loses two thirds of its axial kinetic energy while passing through the octopole guide at a pressure of $1 \cdot 10^{-2}$ mbar. Further collisions at a pressure of $8 \cdot 10^{-3}$ mbar between the gate valve and SRET continue to decrease the transversal kinetic energy. Upon reaching the deflector, the charge and kinetic energy are essential for successful transmission. The kinetic energy inside the deflector can be adjusted using the pressure in the front of the setup and a DC offset on all deflector lenses. When approaching the SRET, where the pressure is again $1 \cdot 10^{-2}$ mbar, the particle has lost most of its transversal kinetic energy. An Einzel lens and the ion-trap entrance-lens can be used to optimize the entrance angle and velocity for efficient trapping.

Trapping in the SRET. The SRET needs to be operated within the boundaries of the stability diagram and preferably within the region of validity of the adiabatic approximation, as introduced in Sec. 2.2, to achieve stable trapping and enable mass determination. As discussed in Sec. 3.5, trapping in multipoles can be controlled by independent DC potentials on entrance and exit lenses and poles. The same scheme is applicable to the SRET, if the two end caps have independent DC offsets. Typically, in QITs used solely for trapping and extraction of ion packets, the RF is applied to

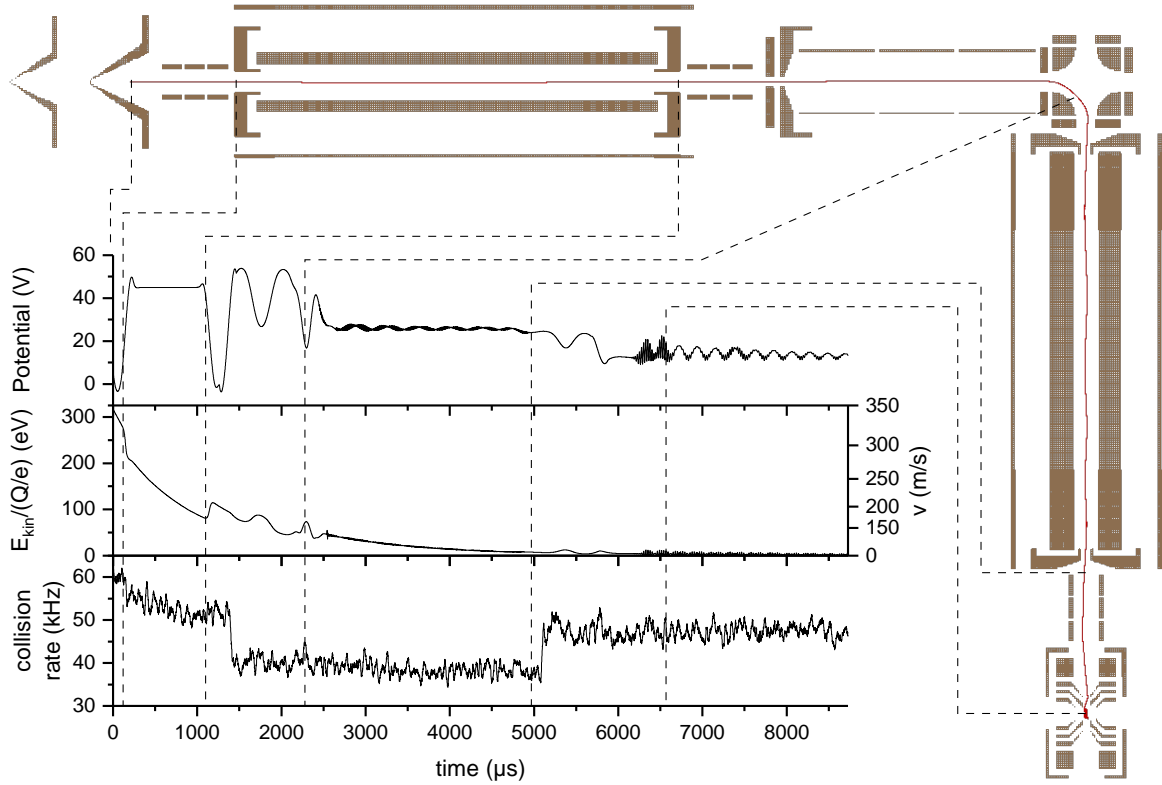


Fig. 3.21: Simulation of nanoparticle trapping. An exemplary trajectory of a PMMA nanoparticle through the NPMS setup is shown. The inset provides information about the potential at the particle position, kinetic energy, velocity and amount of collisions during the simulation. Dashed lines indicate the parameters for selected position of the particle in the setup.

the ring electrode only, making it easy to connect independent DC supplies to the end caps. Due to the offset of the effective potential created by this configuration (see Sec. 2.2), the symmetric configuration was chosen instead and thus the potential barriers at the trap entrance and exit, are symmetric. Fast particles that can overcome the effective potential barrier on the trap exit can be reflected by sufficiently large DC potentials on the excitation electrode at the trap exit. This gives an additional chance for trapping while they pass through the trap center a second time. More important, however, is an initial kinetic energy, which is just enough to pass the barrier when entering the trap and sufficient loss of energy by collisions with the buffer gas before reaching the barrier at the trap exit. Since the length of the trap is only a few mm, high pressures and preferably low temperatures are needed for efficient trapping. To optimize trapping, the kinetic energy of the particles is controlled by changing the amount of collisions during guiding towards the trap and by a DC potential offset on all trap electrodes. Alternatively, the height of the effective potential barrier can be adjusted to the incident particle energy using the RF potential amplitude and

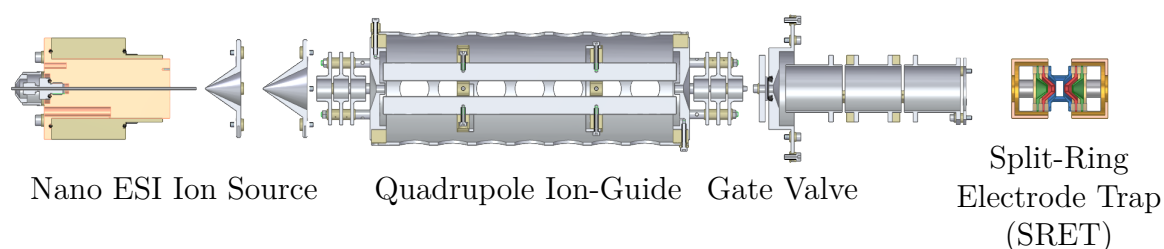


Fig. 3.22: Schematic top view of the linear version of the NPMS setup. In this version the electrostatic quadrupole deflector has been removed to reduce complexity. Ions travel on a linear trajectory from the source to the SRET.

frequency.

A different route to trapping can be implemented. It involves decreasing the RF amplitude for a few ms such that particles with low kinetic energy are guided by the SRET and are trapped, once the amplitude is restored. A DIT type generator, described in Sec. 2.2.2, is suitable for this approach. Note that there is also an imperfect trapping potential between the end caps and excitation electrodes and particles are sometimes trapped there in the simulation.

Some ion-trap experiments use a pulsed valve to achieve a high buffer gas density inside the ion trap to achieve faster thermalization and effective attachment of weakly bound atoms or molecules, often referred to as messengers when used for action spectroscopy, by three-body collisions.[182–184] In those experiments it is desirable to accumulate and cool a large number of molecular ions as fast as possible. Also, heating by collisions with the buffer gas on extraction from the ion trap can be reduced by waiting for the low pressure periods between gas pulses. Due to the open design of the SRET a large pressure gradient between the trap center and chamber is harder to achieve. After trapping, there is much more time for thermalization compared to the action spectroscopy experiments mentioned above and extraction is not needed since all information is obtained by optical detection inside the SRET. Trapping of single nanoparticles is readily possible with a continuous buffer gas supply. The gas pulse might even knock trapped nanoparticles out of the trap if not adjusted very carefully. Thus, while interesting for future experiments including additional neutral or charged molecular beams, for investigation of single nanoparticles this technique would only add a significant amount of complexity.

3.12 The Linear Setup

Due to the lack of useful feedback, described in Sec. 3.8, trapping was not possible in the initial phase of experimentation. It was unclear, if this problem was due to the ion source, the deflector, the laser, the detectors or even a combination of those. Since the ion detectors could not tell nanoparticles apart from molecular ions optimization of the source parameters was hindered. The charge and energy selective deflector could not

be optimized in a rational way, since both parameters are not accessible other than by trapping. Thus, the whole parameter space provided by the deflector and other ion optics had to be explored in a time demanding systematic fashion. Nanoparticles could simply be too fast for deflection due to insufficient amount of collisions in the ion guide. Though the laser and detectors can be roughly adjusted to a target placed in the trap center, deviations on the order of $100\ \mu\text{m}$ will significantly reduce the amount of detected light. Initial experiments were done with large particles, which scatter light efficiently, on the other hand they would sit at different heights in the trap due to their high mass. Initially, a cheap 50 mW laser was used, which had to be focused to make initial detection feasible. Later a 500 mW laser was used, which illuminated a larger area with comparable intensity, while producing less stray light. It is important to note that with a well aligned setup, particles can be detected with weak ion beams and low laser intensities. However, for the initial alignment, each of these factors adds to the complexity of the experiment.

In order to reduce complexity, the deflector was removed and the setup was modified such that the ion beam passes from the source, through the linear quadrupol ion guide, to the ion trap on a straight line. It was with this linear version, shown in Fig. 3.22, that the first trapped particle was detected. This proved that the ion source is able to bring charged nanoparticles into the gas phase. The sensitive laser and detector alignment and light collection efficiency was then improved using the feedback from trapped particles.

In the linear version, the light scattering laser is directed at the source instead of an exit window, possibly causing stray light that adds to the background signal. Since the pressure sensor in the SRET chamber is used for charge stepping and can't monitor the pressure during the experiment, a second pressure sensor was mounted at an 90° angle behind the chamber using a CF 40 T-piece. Eventually, the setup should be changed back to the original configuration to benefit from the advantages discussed in Sec. 3.4.2. It is well possible that nanoparticles have already been trapped before removing the deflector and were not detected due to insufficient alignment. However, an analysis of the nanoparticle beam charge and energy distribution for different particles, pressures and potentials should be conducted before reintroducing the deflector, in order to make informed choices of deflection potentials. Given the time frame of this thesis, it was decided to defer this project in favor of the characterization of the ion trap.

4 Characterization and Initial Observations

In the following, the procedure for preparing nanoparticle mass spectrometry (NPMS) experiments and typical operating conditions are summarized, mainly focusing on the aspects relevant to the linear NPMS setup and especially to those related to the cryogenic SRET. Nanoparticle Coulomb crystals were observed even at room temperature and are useful in the preparation of single trapped particles. Water-ice particles were trapped, indicating an additional field of application of the NPMS technique. Finally, effects observed when recording FT and resonant excitation spectra are discussed to aid interpretation of the results of long-term experiments.

4.1 Trapping a Single Particle

The first step in any NPMS experiment is the preparation of a single trapped nanoparticle. Here, the influence of relevant experimental parameters and different methods for selection of a single nanoparticle are evaluated. The particles investigated in this thesis were typically produced from 1:1 water/methanol solutions with particle concentrations ranging from $1 \cdot 10^{10}$ to $1 \cdot 10^{14}$ particles per milliliter. Initially, small amounts of H_2SO_4 , on the order of 10 mmolL^{-1} , were added to the solutions to add a source of charges. Since no effect of the added H_2SO_4 on the particle charge states and trapping efficiency was observed, it was eventually omitted. An emitter voltage of 2.1 kV and flow rates from 500 to 1000 nl/min were used. A complete set of operating parameters for a representative experiment is given in Sec. C.2. Tab. 4.1 gives an overview of trapped particles and corresponding trapping settings.

The most sensitive parameters for trapping are the pressures in the source, guide and trap regions. Collisions with the buffer gas particles between source and trap reduce the kinetic energy of the particles close to the barrier created by the effective trapping potential. Subsequently, collisions in the trap have to be sufficiently effective to prevent transmission, and thus allow for trapping (see also simulations in Sec. 3.11). A higher pressure in the source leads to an increased gas flow to the guide, which needs to be compensated by reducing the guide buffer gas flow. Trapping is possible without additional buffer gas flow to the guide. In this case, particles were transmitted to the trap, even when applying the maximum voltage of 170 V, limited by the analog output board, to the guide exit lens. When the pressure in the guide was increased to the typical value of $1 \cdot 10^{-3}$ mbar by adding argon buffer gas, the transmission was

Table 4.1: Overview of experimental parameters for different trapped particles: ρ is the bulk density, F and V_0 are the trapping frequency and amplitude, T is the trap temperature, p is the trap pressure, P is the power of the detection laser. The particle diameter d , mass M and charge state Q are given when determined. All other settings used for trapping are given for particle j in Sec. C.2 and are comparable for the other experiments.

index	Material		SRET				Laser	Particle			Trapping Time
	Type	ρ (Da nm ⁻³)	F (kHz)	V_0 (V)	T (K)	p (mbar)	P (mW)	d (nm)	M (MDa)	Q/e	(h)
a	PMMA	621	30	200	293	7 E-6	100	/	/	/	/
b	NaCl	1301	30	200	293	2 E-6	100	/	/	/	/
c	NaCl	1301	30	175	293	2 E-6	100	/	/	/	/
d	NaCl	1301	30	150	293	5 E-4	100	/	/	/	/
e	NaCl	1301	30	200	293	0.02 - 3 E-4	100	/	/	/	/
f	SiO ₂	1205	30	200	293	4 E-4	100	/	/	/	/
g	SiO ₂	1205	30	180	60 - 120	5 E-4	7	aggl. ¹	2 E3	~ 770	20
h	SiO ₂	1205	25	186	60 - 120	5 E-4	7	105	7.2 E2	~ 300	10
i	SiO ₂	1205	26	180	60 - 120	5 E-4	7	aggl. ¹	1.4 E3	~ 560	5
j	SiO ₂	1205	30	180	60 - 293	5 E-4	0.5 - 7	53.8	96	~ 270 - 305	384

¹: agglomerate of particles

noticeably reduced at 170 V but still not completely blocked. This suggests a very broad energy distribution of particles coming from the source, as expected due to the combination of acceleration in the source gas flow, different particle sizes and charge states. In the present, linear configuration of the NPMS setup the potentials of the ion optics preceding the SRET do not react very sensitively, and trapping in the SRET is always possible as long as the trap pressure is large enough. Typically, $1 \cdot 10^{-2}$ to $5 \cdot 10^{-2}$ mbar were used, and higher pressure tends to result in more efficient trapping and trapping of larger particles. The DC potential on the trap electrodes was initially used to control the energy of ions reaching the trap, but since using the pressure was much more effective and the energy distribution was broad, they were eventually all held at ground.

In NPMS, typically a single particle is investigated in order to avoid more complex coupled particle motions. However, once suitable conditions for trapping are found, more than one particle is often trapped within seconds. To obtain a single trapped particle, the trap can be dumped and refilled repeatedly until by chance only a single particle is trapped. Initially, it was planned to use the gate valve to rapidly unblock and block the particle beam to reduce the probability of multiple particle trapping. In the current setup, however, the gate valve cannot be closed, as it would also block the laser beam and cause a large background signal on the optical detectors. Alternatively, the emitter of the nano ESI ion source was moved towards and away from its operating position in front of the stainless-steel capillary with partial success. Unfortunately, this led to emission of large solvent droplets, since there was not enough time for the emission conditions to stabilize. Solvent droplets can also be trapped, depending on their size and charge (see Sec. 4.3). Trapping at room temperature is recommended to achieve fast evaporation of the solvent, since it is not directly obvious if a trapped particle is the nanoparticle of interest or a solvent droplet. The trap can be heated up to room temperature and cooled back to 60 K within less than one hour, since the trap and the cold finger of the cryostat have no mechanical connection. This is short compared to the usual time frame of an NPMS experiment. A third method to reduce the frequency of trapping events, is to operate the scattering laser close to the maximum power of 500 mW. This leads to ejection of particles due to total photon pressure, or recoil of evaporating particles leaving only particles with a strong effective potential inside the trap. The resulting high particle temperatures can be beneficial in removing ligands and adsorbates but the possibility of temperature induced changes in particle properties must be considered. Finally, solutions with lower particle concentration can be used to facilitate trapping of a single particle.

Even if a single particle is trapped directly, it might be close to the edge of stable trapping conditions. Often, particles were lost after small changes in mass, charge or pressure. The RF amplitude and frequency of the trapping potential were not always optimized after trapping, as the function generator output is interrupted when changing between certain ranges.[138] Thus, the currently most practical strategy is to start with trapping of multiple particles and gradually destabilize them until only a single particle remains. This can be achieved by decreasing the trap pressure or effective potential,

increasing the laser power or resonant ejection. Resonant ejection in combination with lower pressures can be used to selectively eject particles. A single particle was obtained faster, however, by changing the effective potential. The above-mentioned interruptions of the function generator are actually helpful, as often a single and stable particle remained in the trap.

Trapping Procedure. The current procedure for trapping a single nanoparticle on the linear setup is summarized in the following. The EM and picoammeter are only used for diagnostic purposes as described in Sec. 3.8 and are not part of the usual trapping routine. It is assumed that the APD, CCD and laser beam are already well aligned from previous experiments. After setting up the instrument parameters as described above, the trap quickly fills with multiple particles which can be observed with the CCD. Estimating the number of trapped particles is easier if they form a Coulomb crystal (see Sec. 4.2), as otherwise only a diffuse cloud is seen. Initially, a higher laser power can help with detection and fine tuning of the alignment. The source is turned off by moving the emitter away from the stainless-steel capillary and the latter is blocked by a PEEK cap, to reduce the partial pressure of residual gasses from the atmosphere. Particles are then gradually destabilized as described above until only a single particle is visible. At this point, the laser beam can be defocused and moved through the trap to detect other possibly remaining particles. It is also possible to move the particle using the potentials on the two rods and excitation electrodes. If no other particles are found, the iris in front of the window (see Fig. 3.19) can be centered to the single particle and closed enough to block the reflexes from the trap electrodes. Then, the mirror can be flipped out and the APD is aligned by iteratively optimizing the photon count rate and reducing the iris aperture. The optimal APD position depends on the temperature-dependent trap and M/Q -dependent particle position. When starting with similar conditions, trapping and single particle selection can also be monitored at the APD without the need to change between detectors.

The FT spectrum reveals, if a single or multiple particles are trapped, as the coupled motion of multiple particles will induce characteristic peaks at sum and difference frequencies, while the spectrum of a single particle will only show a radial and a two times larger axial secular frequency as well as their combinations. The coupling between particles with low charge states will be weaker and the perturbation of the secular frequency peaks correspondingly smaller. The spectrum of two weakly coupled particles can still be easily distinguished from that of a single trapped particle, due to the additional peaks. If, however, one of the particles does not emit enough light, it may only be detected indirectly by its effect on the motion of the brighter particle during resonant excitation. Once a single particle is trapped and its secular frequency determined automated NPMS experiments can be started. Depending on the type of experiment the laser power can be reduced to minimize laser heating.

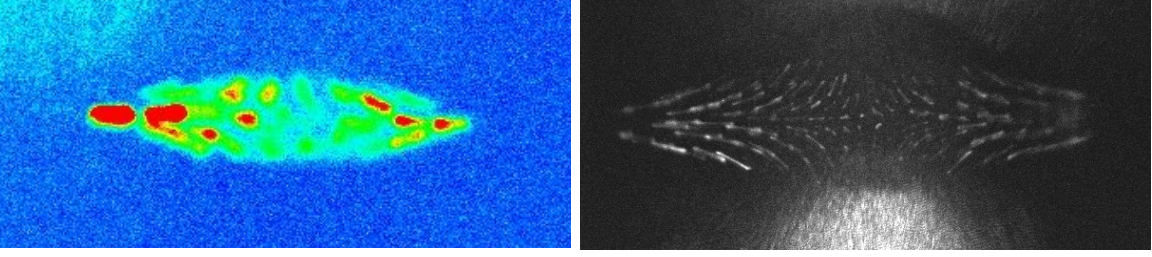


Fig. 4.1: Images of Coulomb crystals recorded with the CCD camera. Left: Coulomb crystal of PMMA particles. Right: Coulomb crystal of NaCl particles. The cylindrical trap axis is the vertical axis in the images. Both were recorded while moving the laser beam along the horizontal axis to consecutively illuminate different parts of the crystal.

4.2 Room-Temperature Coulomb Crystals

When multiple particles were trapped, the formation of Coulomb crystals was observed at sufficiently low trap temperatures and high trap pressures. A Coulomb crystal forms when a cloud of ions, *e.g.* confined by an ion trap, is dense enough that the coulomb repulsion dominates over thermal motion. This requirement is fulfilled, if

$$\Gamma = \frac{Q^2}{4\pi\epsilon_0 a k_B T} \geq 175, \quad (4.1)$$

with the plasma coupling parameter Γ and the Wigner–Seitz radius a . [185] Under such conditions the ions form a stable regular pattern. Two examples are shown in Fig. 4.1, where each point corresponds to the time-averaged trajectory of a single particle. For perfectly symmetric conditions, the crystal would be able to rotate around the cylindrical trap axis, but symmetry is broken by gravity. In addition, the crystal extends over almost the entire trap and might be affected by unsymmetrical fields from the surrounding elements.

Coulomb crystals of atomic ions are formed by laser cooling a trapped ion cloud to temperatures on the order of a few mK. [186] They have applications in solid state physics, plasma physics, astrophysics, quantum simulations and precision spectroscopy of atoms and molecular ions. For nano- or microparticles with hundreds of charges, the requirement for crystallization is already fulfilled at room temperature, as first observed by Wuerker, Shelton and Langmuir [103] and later discussed by Ikezi. [187] Coulomb crystals of such particles form in dusty plasmas, which are found in space and industrial applications. [188, 189] Melting and recrystallization is observed when changing the trap pressure and temperature, as the particle temperature depends on a competition between RF heating and collisional cooling. Coulomb crystals can be stabilized via compression by increasing the effective potential. Here, they were used as a convenient starting point to select single trapped nanoparticles as described above.

4.3 Water-Ice Particles

Water-ice particles are abundant in the atmosphere and their optical properties are of great interest due to their radiative effect.[190] Ice is also common on the surface of particles in astrophysical environments.[45] When spraying pure water, trapped ice particles were observed with the CCD detector, when using a trap pressure of about $5 \cdot 10^{-2}$ mbar. At this pressure, water droplets are expected to freeze within seconds, due to cooling by evaporation, followed by slower sublimation.[191] The trapping rate was increased by choosing source conditions where larger solvent droplets are produced by the nano ESI emitter. The particles started off large, and thus bright, and were initially located below the ion-trap center. They then quickly moved towards the center while decreasing in size, and thus losing intensity. The amplitude of motion decreased after reaching the center, indicating that the decrease in mass led to a steeper effective potential. They then continued to lose intensity, and the amplitude of motion started to increase again, as the M/Q continued to change. All particles were finally lost after only a few seconds when the trap was at room temperature. When repeating this experiment at an ion-trap temperature of 60 K, the same behavior was observed, but evaporation was dramatically slowed down and particles stayed within the trap for minutes. Even longer trapping times are expected if the trap is cooled to 8 K, which requires the use of helium buffer gas. Fundamental understanding of ice particle formation and lifetime can benefit from NPMS measurements in the future, but the acquisition of spectroscopic data will be challenging due to the comparatively short trapping times and constantly changing size.

4.4 Peak Shapes and Shifts in FT Spectra

The effects of pressure, laser alignment and intensity, particle position within the trap and gravity on peak shapes and positions in FT spectra were investigated in order to allow for identification of experimental artifacts in long-term experiments. Details can be found in the master thesis of B. Hoffmann.[138] Especially for larger particles, the radial secular frequency f_r is split into a vertical and a horizontal component f_x and f_y , respectively, due to gravity.[104] Fig. 4.2 shows an exemplary FT spectrum with labeled frequency components. As previously demonstrated using a DC potential applied to a wire below the trap, the effect of gravity can be partially compensated.[136, p. 34] Here, the potential V_{rod} on two stainless-steel rods above the trap electrodes, shown in Fig. 4.3, is used for the same purpose. This figure shows FT spectra of a single, positively charged NaCl particle (see Tab. 4.1 e) for different values of V_{rod} . The particle moves up by about 1 mm when changing V_{rod} from 20 to -30 V. When the particle is pulled up using -10 V, higher harmonics in the FT spectrum disappear, but the degeneracy of the two radial secular frequencies is lifted. At 20 V, the particle is pushed down leading to higher harmonics, but no splitting is seen. Further tests, including different particles and larger displacements, are needed to interpret those

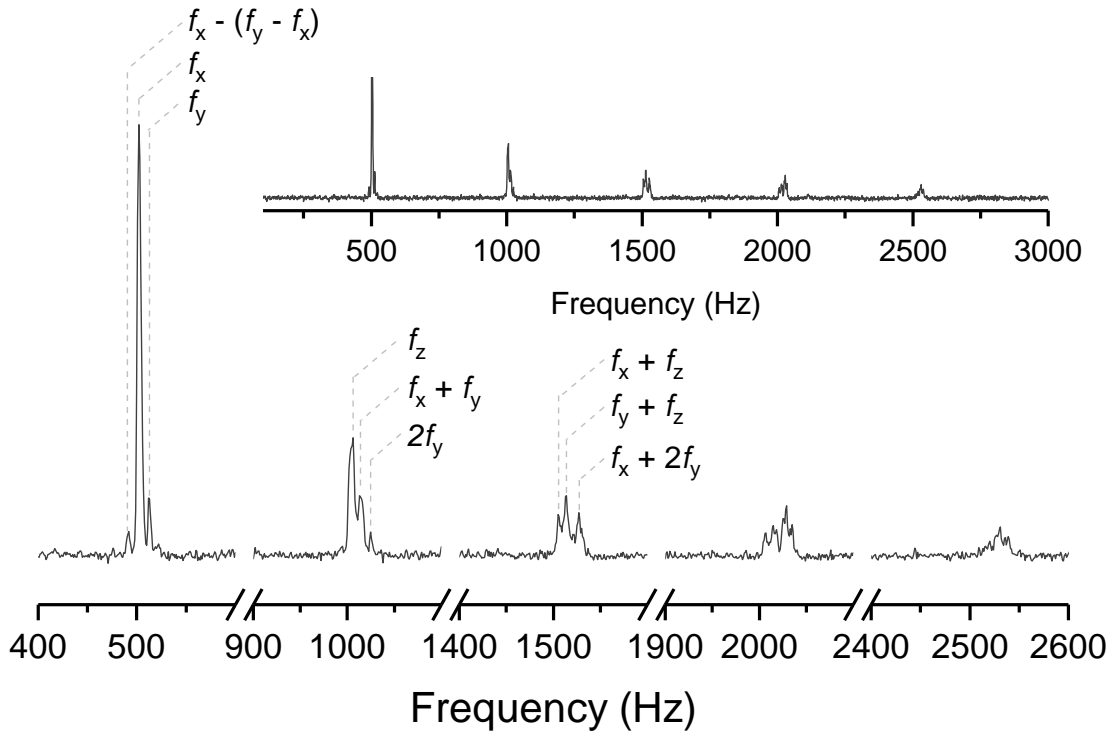


Fig. 4.2: FT spectra of a single NaCl particle (see Tab. 4.1 e) averaged over one hour. The fundamental secular frequencies f_x , f_y and f_z as well as their sum and difference frequencies are labeled. The vertical and horizontal components of the radial secular frequency, f_x and f_y , are split by gravity. Adapted from Hoffmann.[138]

results.

The peak width in FT spectra decreases with lower buffer gas pressure as shown in Fig. 4.4. This is expected, as the collisional damping becomes weaker. In Fig. 4.5 and Fig. 4.6, FT spectra with different laser power and relative position of the laser focus to the particle are shown. No measurable effect on the peak shapes and positions were found, which means that those parameters can safely be neglected in the frequency analysis. In the context of this thesis, FT spectra were mainly used to determine if a single or more particles are trapped, before resonant excitation spectra were recorded.

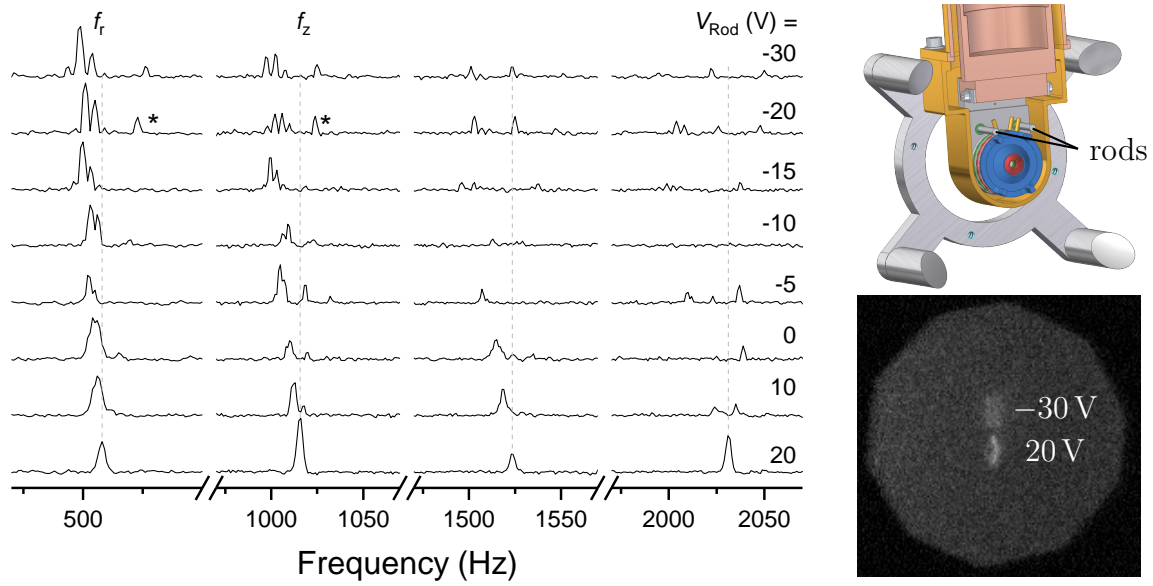


Fig. 4.3: FT spectra recorded for different particle positions. A single, positively charged NaCl particle (see Tab. 4.1 e) was moved through the trap center by applying a potential V_{Rod} to the two rods above the electrode stack (top right). The potentials, ranging from -20 to 30 V, are labeled next to the corresponding spectra. The particle position at these limits is indicated in the bottom right panel. All peaks, apart from those marked with an asterisk, can be attributed to the horizontal, vertical and axial secular frequencies and their combinations, analog to Fig. 4.2. Adapted from Hoffmann.[138]

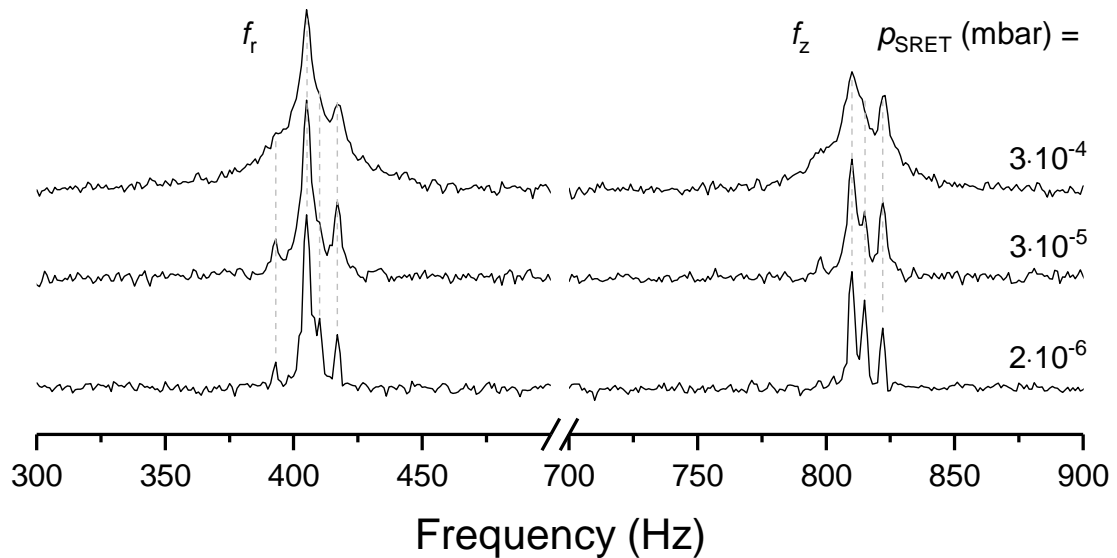


Fig. 4.4: FT spectra of a single NaCl particle (see Tab. 4.1 e), recorded at different trap pressure. Damping of the particle motion decreases with pressure and splitting due to gravity is resolved (compare Fig. 4.2). Adapted from Hoffmann.[138]

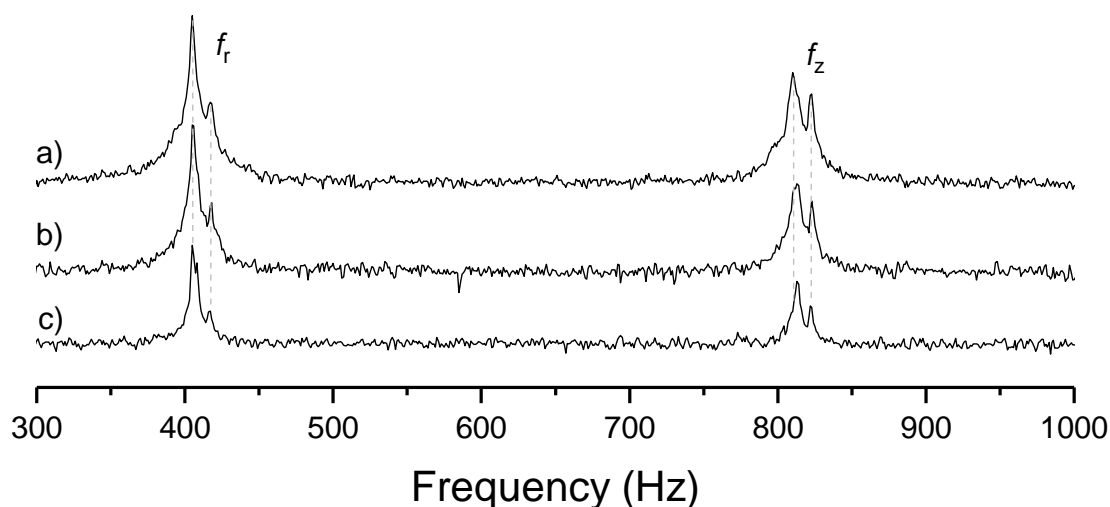


Fig. 4.5: FT spectra of a single NaCl particle (see Tab. 4.1 d), recorded at different laser positions. In trace a), the laser was aligned to maximize the intensity of scattered light. In trace c), the laser was moved away from the particle, significantly reducing the amount of scattered light. Trace b) was recorded at an intermediate position. The peak shapes, positions and relative peak intensities remain unchanged. Adapted from Hoffmann.[138]

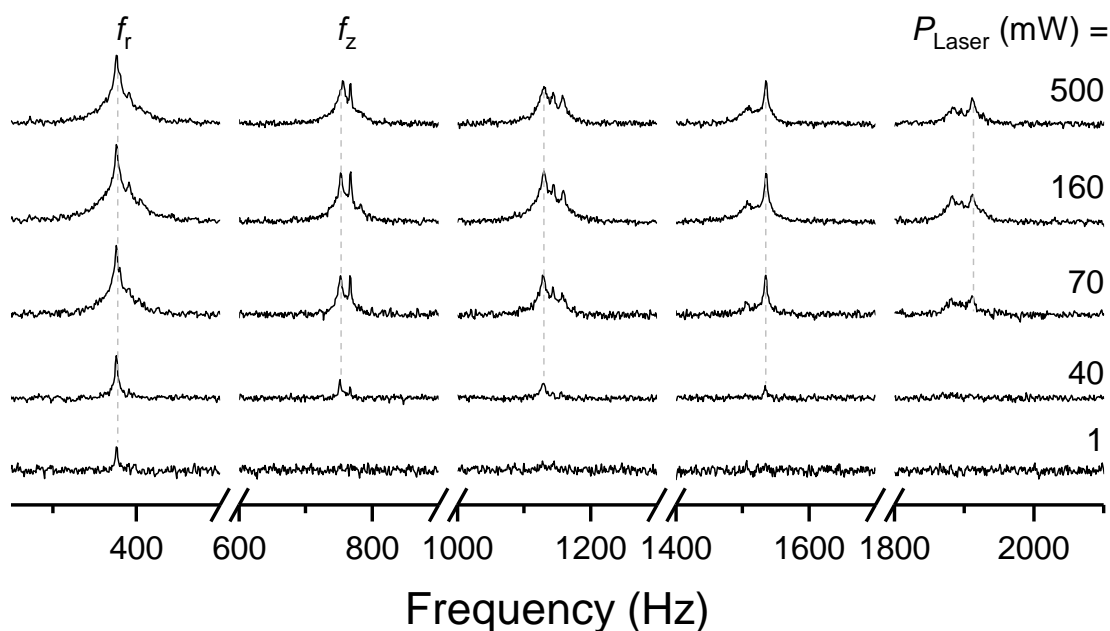


Fig. 4.6: FT spectra of a single NaCl particle (see Tab. 4.1 e), recorded at different laser power. The peak intensities decrease with laser power while peak shapes and positions remain unchanged. Adapted from Hoffmann.[138]

4.5 Peak Shapes in Resonant Excitation Spectra

Resonant excitation spectra, were obtained by applying excitation potentials with an amplitude $V_{0,\text{ex}}$ of up to 5 V, to the excitation lenses (green lenses in Fig. 3.13). The potentials were applied asymmetrically to allow excitation of the axial secular motion without adding a potential offset in the trap center. Only a single dip is seen for the axial secular frequency in resonant excitation, while multiple peaks can appear when using the FT approach as discussed previously. Thus, resonant excitation was used for the automated frequency measurements presented in Chapter 5, and this allowed to determine the axial frequency unambiguously. Fig. 4.7 shows the simulated potential in the trap center for excitation electrodes at 1 V and with all other electrodes grounded. The potential in the trap center is only 0.1 % of the applied potential, due to shielding by the end cap electrodes. This may be significantly different for other trap designs such that excitation amplitudes cannot be compared directly.

The shape of the resonant excitation curves depends on the trap temperature, RF frequency and amplitude, buffer gas type and pressure, particle mass, charge and collision cross section as well as excitation amplitude sweep rate and direction. The most interesting effect, however, is the dependence on the amplitude of motion during excitation, as it provides a way to characterize the effects of higher multipole components of the electric potential. Resonant excitation spectra were recorded in dependence of the excitation amplitude and sweep direction for two fixed sets of parameters. Spectra obtained for a single SiO₂ particle agglomerate, g in Tab. 4.1, are shown in Fig. 4.8. For the tested excitation amplitudes, the peak form remains Gaussian for both scan directions. Tab. 4.2 gives peak parameters obtained by Gaussian fits. The peak width and depth increase with increasing excitation amplitude. The center frequency shifts by less than 0.1 % in all scans, but more averaging would be needed to differentiate between noise and the effect of the sweep amplitude. The ringing in the recorded data is due to a combination of the low frequency beating of the particle motion close to resonance and the data acquisition rate of 10 Hz. Larger excitation amplitudes were not used for this agglomerate in favor of subsequent argon attachment experiments (see Chapter 5). Higher precision can be obtained using lower pressures, lower excitation amplitudes and more averaging and the limits of precision have to be assessed in further experiments. High-precision experiments are much slower and thus less practical for rapid tracking of mass changes, which was the main application of resonant excitation within the context of this thesis.

Resonant excitation curves of a single 54 nm SiO₂ particle, j in Tab. 4.1, were recorded in a subsequent experiment shown in Fig. 4.9. The settings are very similar compared to the previous example, but the secular frequency is almost one order of magnitude higher due to the lower particle mass. Since the power absorption for a driven damped harmonic oscillator is proportional to the square of the driving frequency, higher amplitudes of motion are thus reached with the same excitation amplitude.[192] In Fig. 4.9 the frequency was scanned up in the upper panel and down in the lower panel. When sweeping up, no dip is seen at excitation amplitudes

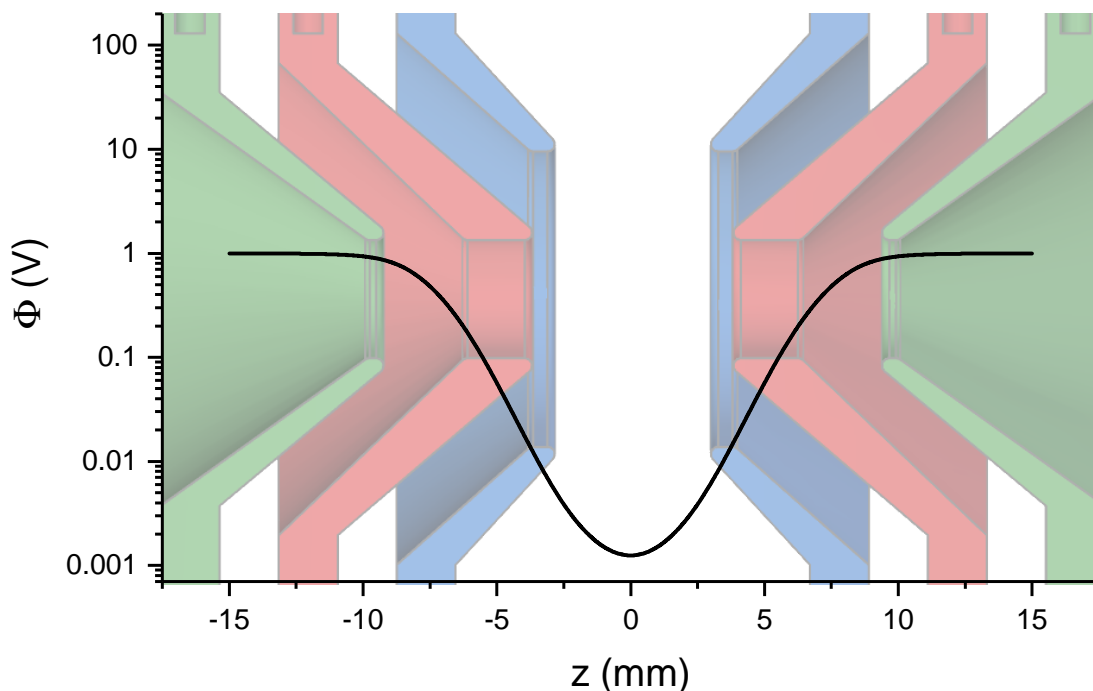


Fig. 4.7: Potential along the cylindrical ion-trap axis for excitation electrodes at 1 V and other electrodes grounded. The potential of the excitation electrodes (green) is shielded by the end cap electrodes (red). The potential curve was obtained using the SIMION model of the SRET. Note that a logarithmic scale is used for the potential axis. A section of the trap electrodes is shown in the background for orientation (see Fig. 3.13 for an overview).

below 1 V while saturation was already reached at 1.5 V. Note that the curves remain symmetric around the center frequency of the 1 V measurement. This behavior is consistent with the broadening of the peaks seen in Fig. 4.8, though the peak shape is clearly affected by the larger amplitudes of motion. When sweeping down, a larger drop in photon signal is seen at 1 V compared to sweeping up. At 1.5 V, the signal did not recover, even after reaching the lower sweep boundary at 4770 Hz. Excitation at 4770 Hz was continued for about 30 seconds, and the signal instantly recovered after it was turned off. Since the secular frequency in a non-ideal QIT depends on the amplitude of the particle motion, it will shift during the excitation. The stronger and continued excitation for decreasing excitation frequency can be explained by a decrease of the resonance frequency for higher amplitudes, which is consistent with the negative multipole coefficients c_4 and c_6 given in Tab. 3.3. Thus, when scanning up, both secular and excitation frequencies shift in opposite direction, allowing for excitation only close to the secular frequency at low amplitudes. When scanning down, on the other hand, both frequencies shift in the same direction, allowing for longer excitation. It would be interesting to see how this behavior is affected by choosing larger sweep speeds. Note, that the amplitude of a driven damped harmonic oscillator in equilibrium is non-zero below the resonance frequency but decays towards zero above it.[192] This is, however,

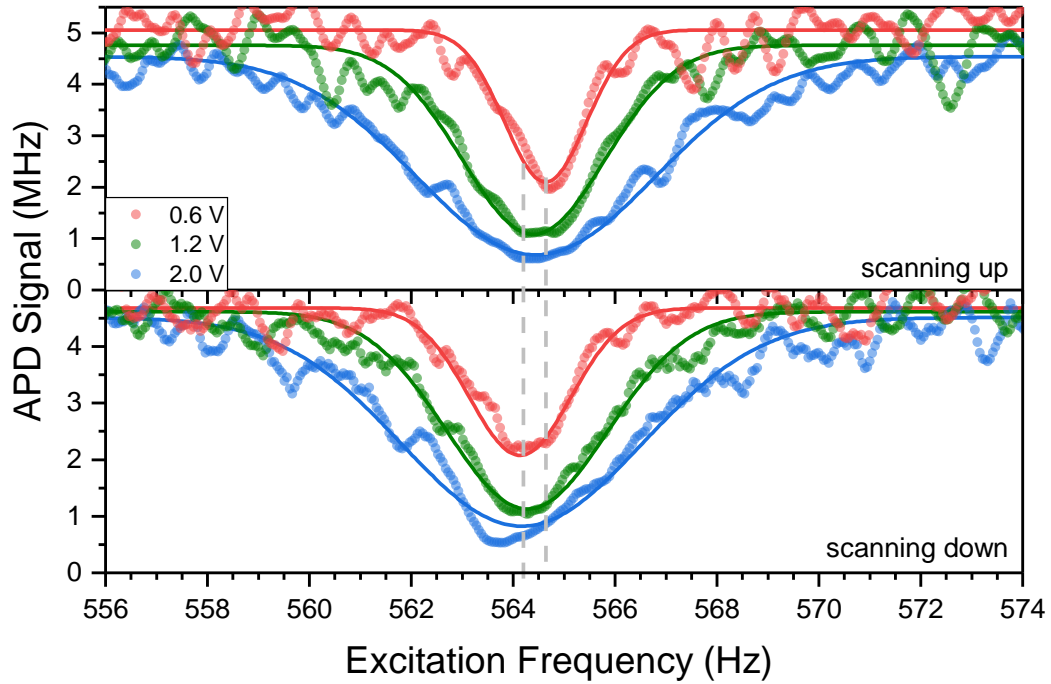


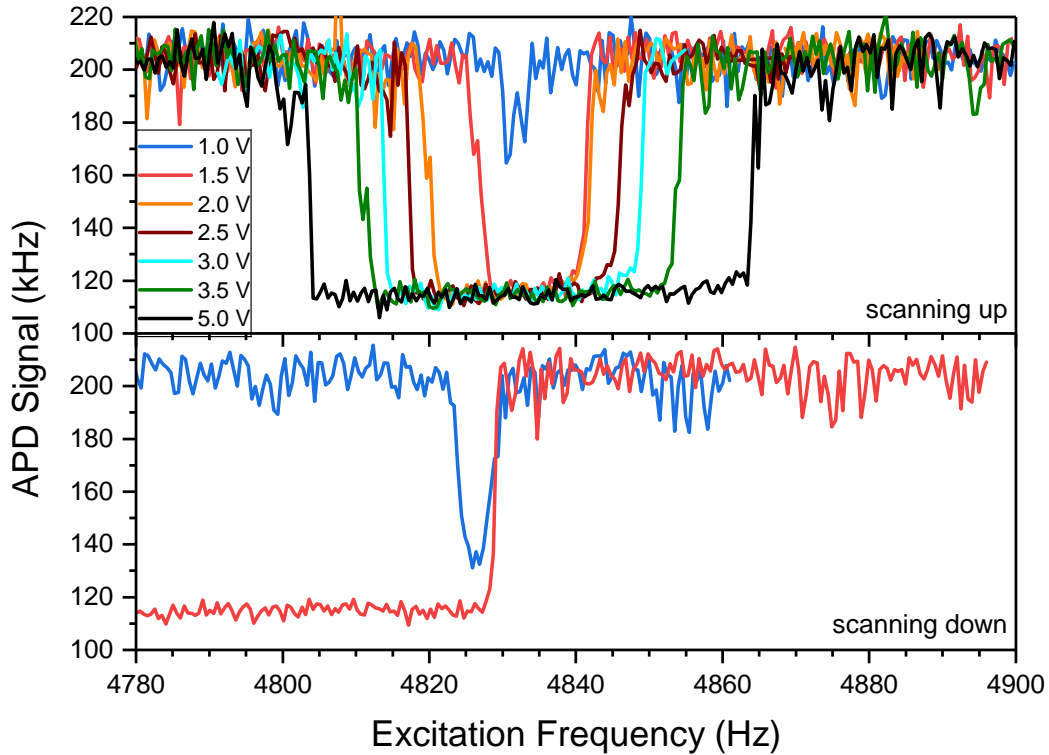
Fig. 4.8: Resonant excitation spectra at different excitation amplitudes (given in the legend) and sweep directions for a single SiO_2 particle agglomerate (see Tab. 4.1 g). The spectra were recorded with a sweep speed of 0.5 Hz s^{-1} and at a trap temperature of 120 K. A ten-point adjacent average of the original data is shown as scatter plots. Peak parameters were determined by Gaussian fits (solid lines) and are given in Tab. 4.2.

not the effect observed here, otherwise the spectra would be similar for both scanning directions.

A dependence of the peak shape on the sweep direction and excitation amplitude was also observed for spectra taken with the non-optimized SRET in the Anderson group in Utah. Different acquisition settings make a direct comparison difficult, but future experiments with a consistent set of parameters will enable an experiment-based evaluation of the geometry optimization. Due to the different trap geometries the excitation potential in the trap center will not be the same, and the relative dip in photon intensity or the maximum amplitude of motion should be used instead to obtain comparable spectra.

Table 4.2: Peak center, depth, and FWHM of the resonant excitation spectra shown in Fig. 4.8 as determined by Gaussian fits. Adapted from Hoffmann.[138]

$V_{0,\text{ex}}$ (V)	Sweeping Up			Sweeping Down		
	f_z (Hz)	Depth (MHz)	FWHM (mHz)	f_z (Hz)	Depth (MHz)	FWHM (mHz)
0.6	564.64	2.84	1.95	564.14	2.49	2.31
1.2	564.40	3.57	3.46	564.28	3.28	3.82
2.0	564.45	3.68	5.71	564.17	3.54	5.36

**Fig. 4.9:** Resonant excitation spectra at different excitation amplitudes (given in the legend) and sweep direction for a single 54 nm SiO₂ particle agglomerate (see Tab. 4.1 j). The spectra were recorded with a sweep speed of 5 Hzs⁻¹. The amplitude was not dampened back to the original state within the scanned range, when scanning from high to low frequencies. This can be explained by a decrease of the excitation frequency with increasing particle amplitudes, due to higher multiple components of the electric potential.

5 Single Nanoparticle Messenger-Tagging

It was the central goal of this thesis to lay the foundations for action spectroscopy experiments with single nanoparticles. A fundamental step towards this goal was achieved by implementing messenger tagging of single nanoparticles at low temperatures for the first time. In Sec. 5.1, first experimental results of argon tagging on SiO₂ nanoparticles at 60 K are shown to demonstrate the feasibility of the method. Temperature-dependent ad- and desorption experiments are presented in Sec. 5.2, providing insights valuable for the implementation of spectroscopy. The data shown in this chapter was recorded within two months and has to be interpreted with caution. Not all observations described in the following could be reproduced due to the limited time. Nevertheless, effects that will become relevant for the performance of action spectroscopy experiments are discussed qualitatively. Finally, experimental and theoretical requirements for a quantitative interpretation of particle temperatures and adsorbate binding energies are given in Sec. 5.3.

5.1 Argon Adsorption on Single SiO₂ Particles

The first observation of single nanoparticle messenger-tagging was made using SiO₂ particles, with a nominal diameter of 100 nm, argon gas at $5 \cdot 10^{-4}$ mbar, a laser power of 4 mW and an ion-trap temperature of 60 K, just above the freezing point of argon at this pressure. Growth due to argon adsorption on a single particle and an agglomerate is shown in Fig. 5.1 and Fig. 5.2, respectively. The axial secular frequency was obtained every minute from resonant excitation spectra using a sweep rate of 0.5 Hz s^{-1} . The absolute mass and charge state were determined by prior charge stepping.

For the single particle, h in Tab. 4.1, a linear increase in mass was observed. A linear fit was used to determine the rate of mass change as 80 kDa/min or 33 argon atoms per second. There is no indication of convergence of the mass even after seven hours of particle growth. Considering the Van-der-Waals radius of argon, $r_{\text{Ar}} = 188 \text{ pm}$, the particle radius $r_{\text{SiO}_2} = 52.5 \text{ nm}$ and assuming two-dimensional densest packing at the surface of the SiO₂ particle,[193] the mass of the first argon monolayer (ML) can be calculated as

$$M_{\text{ML}} = 0.9069 \cdot \frac{4r_{\text{SiO}_2}^2}{r_{\text{Ar}}^2} \cdot M_{\text{Ar}} = 11.3 \text{ MDa}. \quad (5.1)$$

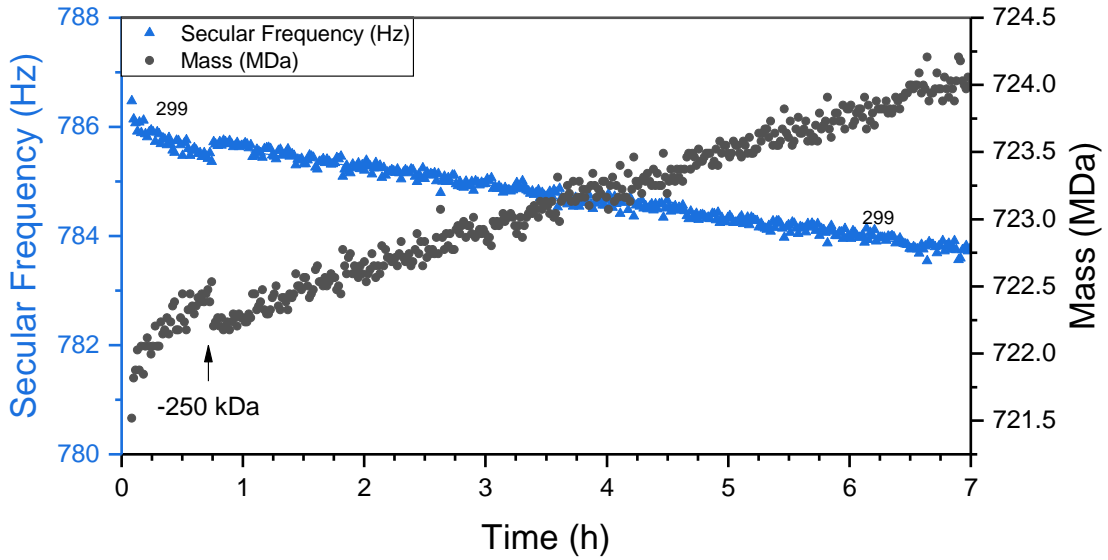


Fig. 5.1: The secular frequency (blue triangles) of a single 105 nm SiO_2 particle (see Tab. 4.1 h) was recorded every minute over seven hours and is plotted against the storage time. Previous charge stepping allowed conversion to absolute mass (gray dots). The observed increase corresponds to adsorption of argon at a trap temperature of 60 K and an argon pressure of $5 \cdot 10^{-4}$ mbar. In the first hour, the axial secular frequency changed rapidly by 0.36 Hz due to loss of mass. The charge state ($Q = 299$) does not change in the seven hour time interval. Adapted from Hoffmann.[138]

The total increase in mass during the time period shown in Fig. 5.1 is 2.25 MDa or 0.2 ML, corresponding to the formation of the first ML.

A discrete frequency step of 0.36 Hz corresponding to a mass loss of 250 kDa or 6250 argon atoms occurred in the beginning of the experiment. This is not a charge step, as the frequency change for a single charge step was previously determined to be 2.65 Hz under the given conditions. It is conceivable that this mass change is due to flaking of a lump of argon, however, a similar effect was not observed again in the subsequent experiments.

While the charge remained constant during the seven-hour measurement of the single particle, four charge steps at a distance of 2 to 3 hours were observed for the agglomerate, g in Tab. 4.1. The pressure sensor in the trap chamber, which is typically used to induce charge steps, was off and charge steps were likely induced by a second pressure sensor behind the trap chamber. Each step corresponds to loss of a single positive charge, either by emission of Ar^+ or capture of e^- . They are more frequent compared to single particles, possibly due to the larger absolute charge state of 770 or the larger collision cross section of the agglomerate.

While the amplitude used for resonant excitation was 1 V for the single particle, for the agglomerate it was increased from 0.5 to 1 V after two hours. The increase coincides with a noticeable drop in adsorption rate from 560 to 71 kDa/min, which

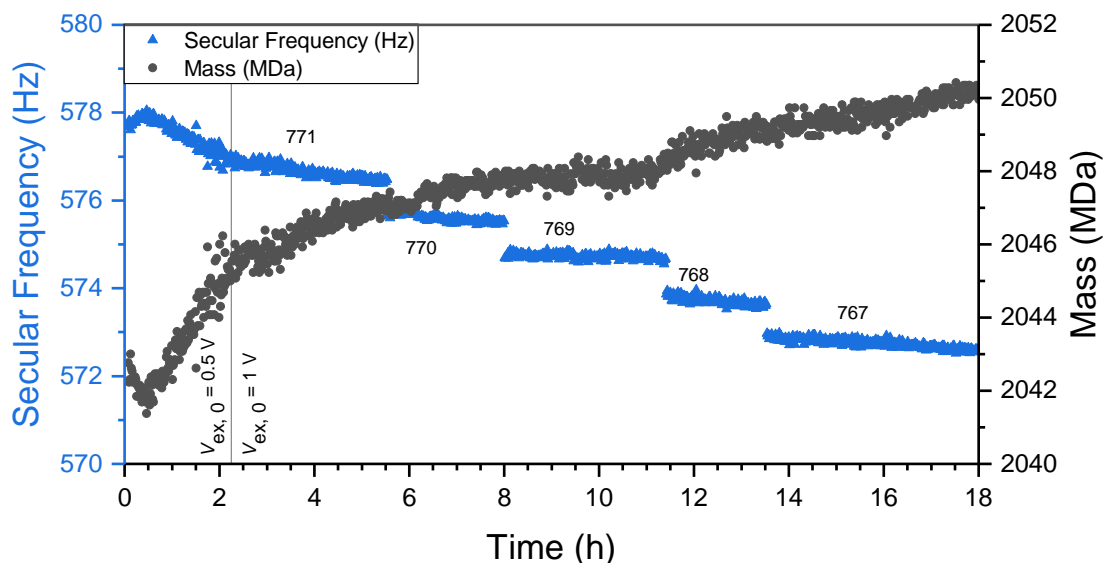


Fig. 5.2: Adsorption of argon analog to Fig. 5.1 but recorded with a SiO₂ particle agglomerate (see Tab. 4.1 g) over 18 hours with an ion-trap temperature of 60 K and an argon pressure of $5 \cdot 10^{-4}$ mbar. The charge state is indicated, next to the secular frequency. After two hours, the excitation amplitude was increased from 0.5 to 1 V to improve the signal-to-noise ratio, indicated by a vertical, solid black line. This led to a decrease in adsorption rate due to increased heating by collisions. Adapted from Hoffmann.[138]

can be explained by a higher average particle temperature due to increased collisional heating. Another indirect heating mechanism is the RF heating, which is stronger for larger particle amplitudes.[74, p. 121] The total mass increase during the 18 hour experiment is 8.5 MDa. Due to the polydispersity index of 0.2 of the used sample, the exact number of particles in the agglomerate cannot be determined from the mass. Thus, the surface area of the agglomerate and the weight of an argon monolayer cannot be estimated. However, it will certainly be larger compared to the 11.3 MDa of the single particle, and thus Fig. 5.2 most likely shows the formation of the first monolayer as well.

The PTFE tube used to introduce argon to the trap chamber, was initially attached to the radiation shield and later moved to the chamber wall, since it started to get blocked after a few days at a trap temperature of 60 K. Even for higher trap temperatures, the radiation shield can still be cold enough to freeze argon. When heating the ion trap to evaporate argon from particles and prepare a new adsorption experiment, the pressure increased because of argon desorption from the trap and radiation shield. When heating the trap up to 80 K within a few minutes, the pressure increased by an order of magnitude. In some instances, new particles were appearing in the trap during this process, even though the nano ESI ion source was not running. Typically, they evaporated within a few seconds, and sometimes they pushed the particle under investigation out of the SRET. The new particles might be argon or water-ice particles,

flaking off of the trap and radiation shield, though further experiments are needed for clarification. To avoid particle loss, it was possible to heat up the trap in several steps over approx. two hours, while monitoring the pressure in the trap chamber. At 80 K most of the argon had desorbed and the trap temperature could be safely raised to 120 K to remove the remaining argon from the particle.

5.2 Argon Ad- and Desorption Experiments on a Single SiO₂ Particle

A new experiment was started using a single SiO₂ particle (see Tab. 4.1 j), to characterize the influence of the individual experimental parameters on ad- and desorption rates as well as the long-term stability of the mass measurement in order to find suitable conditions for spectroscopy. The particle was trapped for more than two weeks, during which several tests were made. An overview of the nanoparticle mass and charge as well as trap temperature and pressure during the whole experiment is given in Fig. 5.3. The most relevant sections, labeled a) to d), are assigned in the overview figure. They are described and analyzed in the following. Sections a), b) and d) are shown in more detail in additional figures.

The stock solution of particles (43-01-102 - micromod Partikeltechnologie GmbH) with a nominal particle diameter of 100 nm was diluted 1:20 in a 1:1 water and methanol solution resulting in a concentration of 125 mg L⁻¹ or $\sim 1.25 \cdot 10^{11}$ particles per milliliter. The absolute mass was determined by charge stepping as 96 MDa, which corresponds to a diameter of $r_{\text{SiO}_2} = 53.8$ nm. Though this is significantly below the nominal diameter, the polydispersity index of 0.2, given by the manufacturer, suggests that this is not unlikely as 6 % of all particles will be in the size range of 50 to 60 nm for a Gaussian size distribution. The smaller diameter also agrees with a significantly lower intensity observed at both photodetectors, compared to previously trapped 100 nm particles.

The axial secular frequency was measured once every minute, using resonant excitation with a sweep rate of 5 Hz s⁻¹ and an excitation amplitude of 1.2 V. All settings used in this measurement are given in Sec. C.2 as a general overview of typical operation conditions. The argon pressure was held at $1 \cdot 10^{-4}$ to $7 \cdot 10^{-7}$ mbar, apart from short-term fluctuation due to heating of the ion trap. The absolute charge state was determined multiple times between ad- and desorption periods where the mass was stable. During the entire experiment the charge state increased from 276 to 307, suggesting that adsorption of Ar⁺ was the dominant process for charge changes.

Section a) Temperature Cycles. Three ion-trap temperature cycles were conducted during the first 60 hours to investigate temperature-dependent ad- and desorption (see Fig. 5.4). Adsorption periods were recorded at 60 K and the ion trap was heated up to 120 K to desorb argon. Ad- and desorption rates for linear fits are given in Tab. 5.1. Heating the trap caused an increase of pressure from $7 \cdot 10^{-4}$ mbar to up to

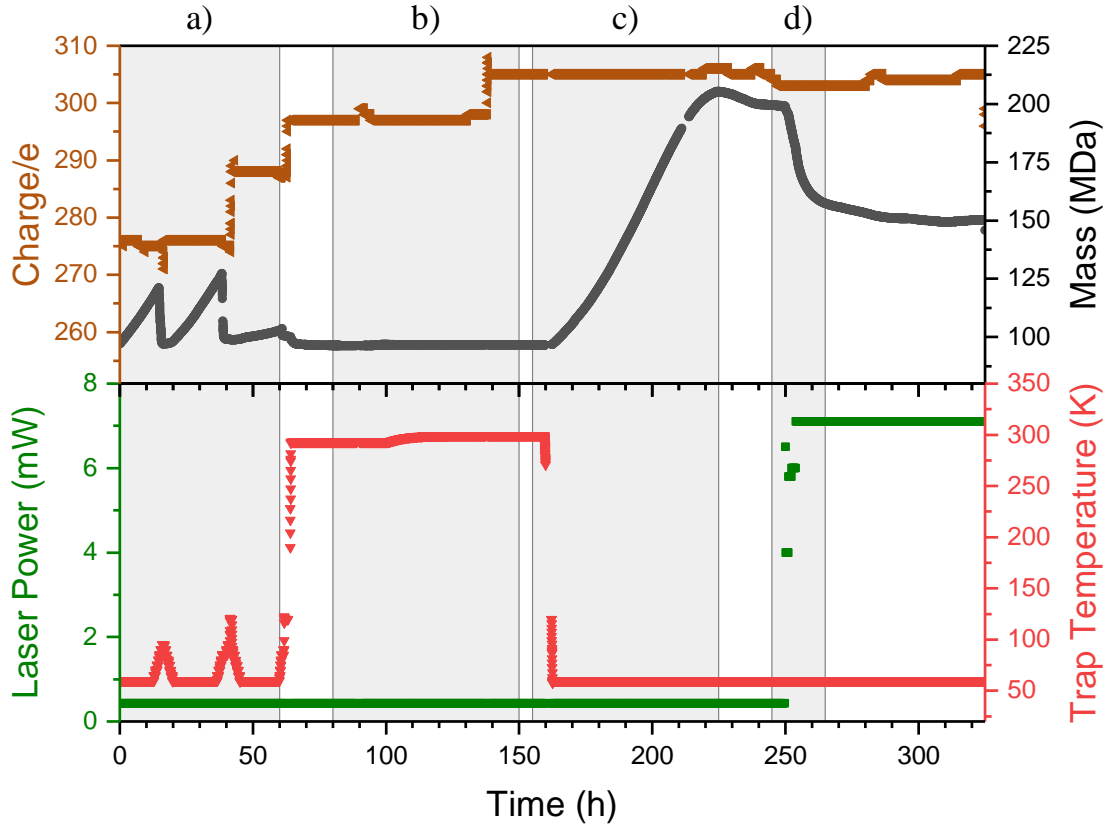


Fig. 5.3: Mass changes due to ad- and desorption of argon on a single 54 nm SiO₂ particle (see Tab. 4.1 j) over more than two weeks. The absolute mass (gray dots) and charge (brown left-facing triangles) are shown in the top panel and laser power (green squares) and ion-trap temperature (red downwards-facing triangles) in the bottom one. a) The ion-trap temperature was changed between 60 K and 120 K in three temperature cycles, inducing argon ad- and desorption. More details are shown in Fig. 5.4. b) The trap was heated to room temperature and the mass stability was monitored for over 75 hours at room temperature. More details are shown in Fig. 5.5. c) The trap was cooled back down to 60 K to start another adsorption period and the particle mass had more than doubled when reaching an equilibrium after 60 hours. d) The dependence of the argon desorption rate on particle temperature was investigated using variable laser heating at constant ion-trap temperature. More details are shown in Fig. 5.6.

$1.6 \cdot 10^{-3}$ mbar due to desorption of argon from the trap itself and from the radiation shield. This led to a slight increase of the growth rates in the beginning of the heating phases, which were hence excluded from the linear fits. Once all argon had desorbed from the trap and shield, the pressure dropped quickly and desorption of argon from the particle became dominant.

Due to the thermal expansion of the cold finger the whole trap was moving by a few 100 μm between 60 K and 120 K, significantly reducing the overlap between the particle, scattering laser and APD. Thus, both laser and APD had to be realigned

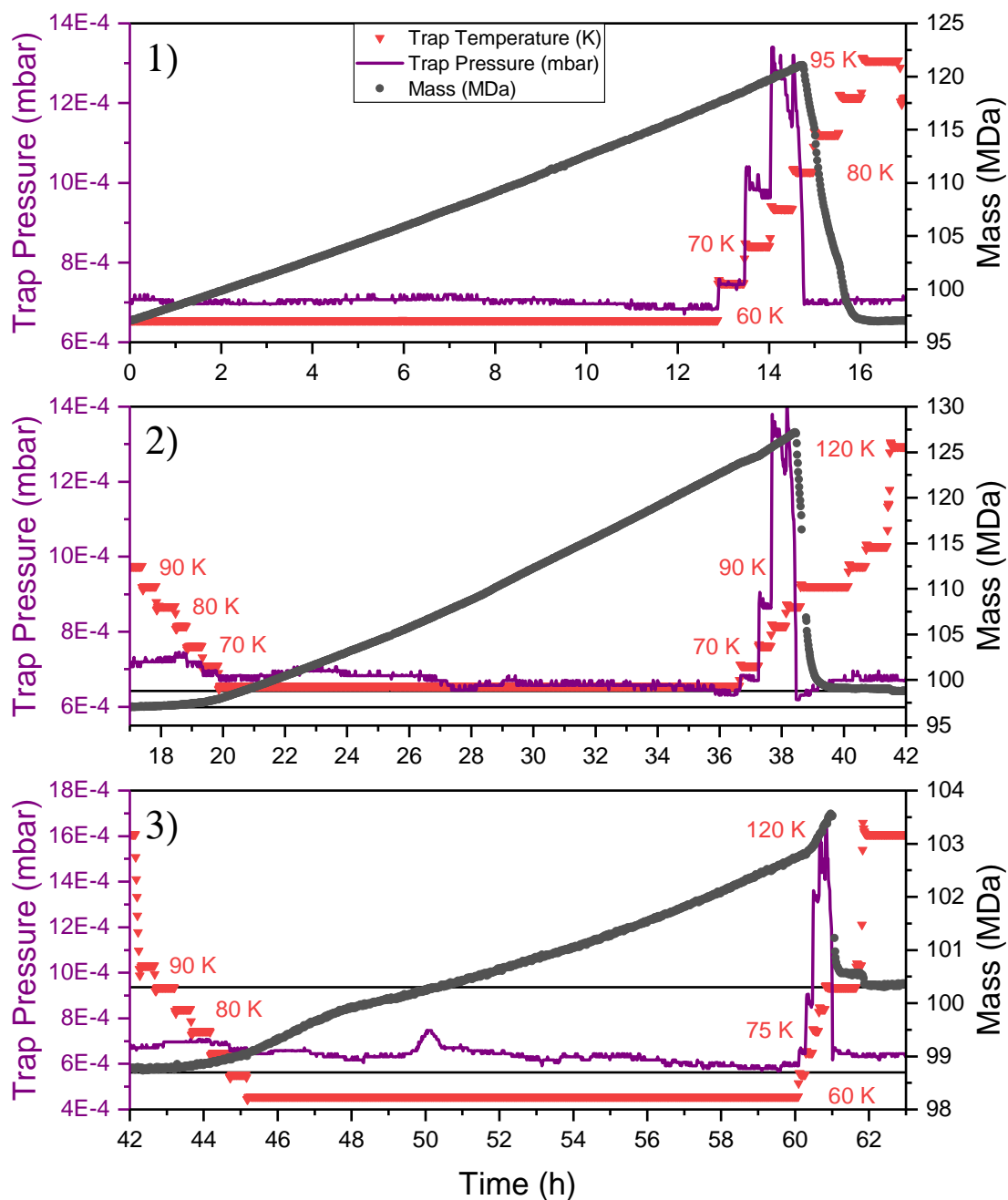


Fig. 5.4: Detailed plots of the three temperature cycles of argon ad- and desorption shown in Fig. 5.3 a). The trap temperature is indicated within the plots. Adsorption was monitored at 60 K. At the end of each temperature cycle, the trap was heated to desorb argon from the particle, which led to an increase in pressure due to desorption from the trap and radiation shield. Selected linear ad- and desorption periods and the corresponding rates are given in Tab. 5.1. Differences in mass between the temperature cycles are indicated by solid black lines.

multiple times during the heating process, to keep track of mass changes and possible charge steps. Noticeable steps are visible in the desorption periods due to change in laser overlap and thus particle temperature. While the particle position can be fixed by compensation with a DC offset on the two rods, this would induce frequency shifts as discussed in Sec. 4.4.

The adsorption rates in the temperature cycles 1) and 2) are close to 30 kDa/min corresponding to 12.5 argon atoms per second. The desorption rates are roughly ten to twenty times larger. A significantly lower growth rate of 4 kDa/min, or 1.7 argon atoms per second, is observed for temperature cycle 3). In cycles 2) and 3), the mass of the particle at 120 K converged at 1.8 MDa and 1.6 MDa, respectively, above the corresponding initial value. This difference is indicated by horizontal, solid black lines in the figure.

Both effects can be explained by the presence of a second adsorbate with lower partial pressure and higher binding energy, such that it does not desorb at 120 K. Contaminations by hydrocarbons from the vacuum system are unlikely, as oil free pumps were used exclusively. Of the residual gases present in the vacuum chamber, the most likely candidate is water vapor from the atmospheric pressure interface of the ion source though this cannot be determined with absolute certainty from the single experiment. Even though water does freeze out at the cold ion trap and radiation shield, it can still reach the particle in small amounts, due to the open trap design. Another indication for this hypothesis is, that the additional mass could be removed by heating the trap above the freezing point of water after the third temperature cycle. The next adsorption period (see section c) in Fig. 5.3) shows an adsorption rate close to that of temperature cycles 1) and 2), suggesting that argon adsorption in cycle 3) is hindered by the second adsorbate. The effect cannot be observed for cycle 1), since the frequency interval chosen for the resonant excitation was initially not large enough to keep track of the fast mass changes and the trap was not heated all the way to 120 K at the end.

Using Eq. 5.1, the mass of the first argon ML is calculated as 3 MDa. The gain of mass during the three adsorption periods was approximately 24 MDa (8 ML), 30 MDa (10 ML) and 5 MDa (1.6 ML), respectively. A difference between the adsorption rates of the first and subsequent MLs was not observed.

Section b) Long-Term Stability. After the third temperature cycle, the trap was heated up to 293 K, leading to an additional mass loss of 2 MDa compared to the equilibrium mass at 120 K. Since the trap was heated up quickly and the particle signal was temporarily lost, due to thermal expansion of the cold finger, it is not possible to tell at which temperature most of this mass loss happened. An additional mass loss of 2.5 MDa was observed over the next 24 hours at 293 K. Fig. 5.5 shows the period between 80 and 155 hours, in which mass changes were monitored. The cryostat was turned off at 90 hours, where the signal was temporary lost due to rapid thermal expansion of the cold finger, which was still much colder than the heated

trap. The trap stayed at 293 K for ten more hours while the cold finger slowly warmed up. The mass increase at 95 hours coincides with a slight increase of pressure. Since parts of the cold finger were colder than the trap this can be explained by delayed desorption of water. The relative increase of partial pressure of water might be much larger than the measured change in absolute pressure and should be monitored by a residual gas analyzer in the future. The laser alignment was re-optimized several times during this period to compensate for expansion of the cold finger which might also explain some of the mass changes that are visible before 110 hours. Once most of the water was desorbed, the mass started to decrease, as in the three ion-trap temperature cycles. Finally, the trap temperature slowly approached room temperature, which was around 299 K or 26 °C. At 110 hours the mass converged and fluctuations on the order of <math><1000\text{ ppm}</math> or 89 kDa over tens of hours can be observed, which are attributed to amplitude instabilities of the RF amplifier amplitude, trap pressure and laser power. The inset in Fig. 5.5 shows the mass distribution between 133 and 137 hours where a standard deviation of 166 ppm was obtained. The precision in this time period was limited by the individual resonant excitation measurements, which were not optimized for high precision, rather than by any long-term fluctuations.

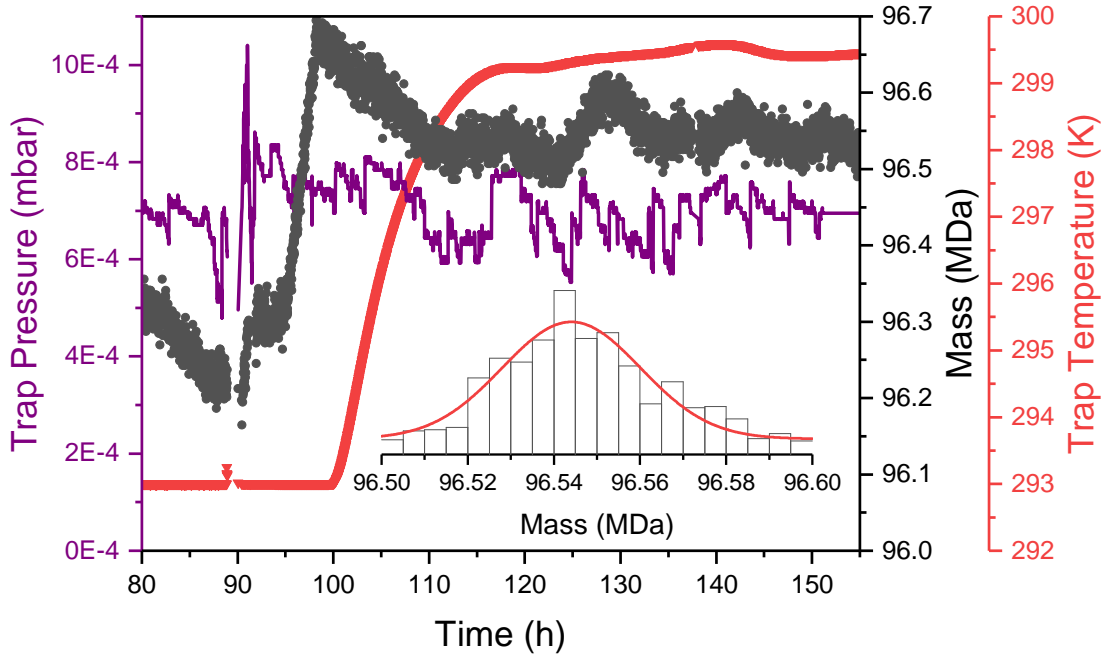


Fig. 5.5: Mass changes and long-term mass stability after heating the ion trap to room temperature. Mass changes were monitored over 75 hours (section b) in Fig. 5.3). The inset shows a histogram of the measured frequencies between 133 and 137 hours. The Gaussian fit gives a standard deviation of 16 kDa around the mean value of 96.554 MDa, which corresponds to a stability of 166 ppm over four hours.

Section c) Equilibrium Coverage at 60 K. Next, the ion trap was cooled back down to 60 K for another adsorption period (see c) in Fig. 5.3). The adsorption rate increased from 24 to 38 kDa/min in the time period between 165 and 210 hours, as the particle diameter and thus collision cross section increased. The rates are close to that of cycle 1) in Fig. 5.4, suggesting that the second adsorbate was removed during the room-temperature period. Ad- and desorption rates reached an equilibrium after 60 hours. The mass of the particle had more than doubled, starting at 96.5 MDa and stabilizing at 204.5 MDa. This mass change corresponds to 25 MLs of argon, considering the mass changes between layers. This large change in mass will cause a significant shift in the particle position within the SRET, and thus laser overlap, due to gravity. When changing the mass of a single particle over a wide range, the measured frequency can shift not only due to the direct change of M/Q but also due to anharmonic effects (see Sec. 2.2.1). Though this can be compensated using the DC offset on the two rods, much smaller growth rates and mass changes are recommended for spectroscopy, to reduce this problem. The drop in mass between regions c) and d) coincides with readjustment of the laser alignment and a temporary increase of the excitation amplitude $V_{0,\text{ex}}$ from 1.2 to 1.3 V to increase the signal-to-noise ratio.

Section d) Laser Induced Desorption. In section d) of the experiment, shown in detail in Fig. 5.6, the influence of changing the laser power instead of the ion-trap temperature was tested. The laser power was increased in steps, labeled 1) to 4), and is given together with corresponding desorption rates in Tab. 5.1. The argon desorption rates, and thus the particle temperature, immediately increased with the laser power. Unfortunately, a photodiode was not available during the measurement and the laser power was calibrated later. This might explain the inconsistent decrease in desorption rate with increasing laser power between steps 2) and 3). In the one-hour time periods after change of the laser power, the rates were constant, indicating that under the present conditions, the rates showed no strong dependence on the coverage. After the last step, the power remained constant at 7 mW for twelve hours and the mass seems to exponentially approach a new equilibrium. The pressure stayed constant, since no evaporation from the radiation shield was induced by the laser. Since the SRET temperature stays constant the trap does not move and no realignment is needed. In addition, the temperature of the particle can be controlled within seconds by laser heating compared to minutes when changing the SRET temperature.

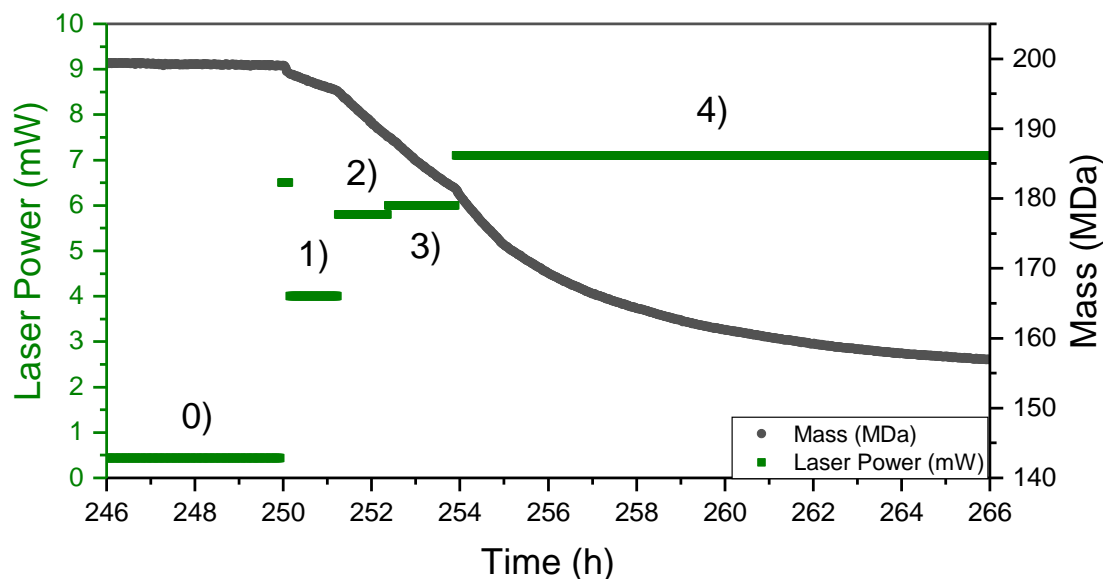


Fig. 5.6: Mass changes due to modulation of the laser power (section d) in Fig. 5.3). After reaching an equilibrium at 0.5 mW, the laser power and thus particle temperature was increased in steps. The desorption rate changed instantly and was determined by a linear fit. The rates and corresponding powers are given in Tab. 5.1. Adapted from Hoffmann.[138]

Table 5.1: Ad- and desorption rates for argon on a single 54 nm SiO₂ particle obtained from linear least square fits. The laser power for each experimental section is given. The time periods, in hours, used for fitting in Fig. 5.4 are indicated in parenthesis next to the rates. Note that the rates given here are labeled according to the dominant process, but are the result of simulations ad- and desorption.

Ad- / Desorption Period	Laser Power (mW)	mR_{ad} (kDa/min)	mR_{des} (kDa/min)
Fig. 5.4 1)	0.5	27 (1.0-12.5)	495 (14.9-15.5)
Fig. 5.4 2)	0.5	28 (25.1-36.1)	1024 (38.5-38.8)
Fig. 5.4 3)	0.5	4 (50.8-59.8)	451 (61.0-61.1)
Fig. 5.3 c)	0.5	24-38	
Fig. 5.6 0)	0.5		<1
Fig. 5.6 1)	3.7		38
Fig. 5.6 2)	5.8		96
Fig. 5.6 3)	6.0		80
Fig. 5.6 4)	7.0		120

5.3 Ad- and Desorption Kinetics of Single Nanoparticles

To avoid changes in trap pressure and laser overlap, experiments should be conducted in a limited mass range and using laser heating at constant ion-trap temperature. Further characterization of collisional heating and amplitude-dependent frequency shifts in resonant excitation are needed, to assure they do not interfere with spectroscopic applications. If the photon count rate is large enough, the FT method should be used to eliminate the effect of collisional heating induced by resonant excitation. Further a residual gas analyzer can be attached to the trap chamber, to quantify the composition of the background gas, which is vital for the interpretation of the observed ad- and desorption rates.

Though relative changes in desorption rates are sufficient as an indicator for changes in the absorption cross section, and thus enable acquisition of action spectra, more information such as particle temperature and adsorbate binding energies can be obtained by a more detailed analysis. This will be helpful to calibrate the relative intensities in single nanoparticle action spectra. The experiments described above represent a special case of temperature programmed desorption (TPD). In TPD experiments, gases or gas mixtures are adsorbed on a sufficiently cold surface.[194] While sample temperatures are gradually increased with a heating rate of a few Ks^{-1} in TPD, much faster heating can be achieved by (pulsed) lasers in laser induced thermal desorption (LiTD) enabling investigation of energy redistribution processes.[195] Typically, desorbed gases are detected by means of mass spectrometry. Due to its sensitivity to changes in the particle mass, NPMS enables TPD-like experiments with single nanoparticles, which do not emit enough adsorbate particles for conventional detection.

For single 500 nm SiO_2 particles, such experiments have already been reported by Schlemmer *et al.*[105] The equilibrium particle temperature was estimated considering absorption of laser and thermal background radiation as well as radiation emission. The desorption process is described by the following relation, based on the Redhead model for first order desorption:[196, 197]

$$\frac{\Delta M}{mR_{\text{des}}} = \frac{N_{\text{ad}}}{R_{\text{des}}} = \tau = \nu^{-1} e^{E_{\text{des}}/k_B T} \quad (5.2)$$

with the mass of one ML ΔM , the mass of the adsorbate m , the number of total surface adsorption sites N_{ad} , the desorption rate R_{des} , the mean residency time of adsorbates at the surface τ , the vibrational frequency of the adsorbate at the surface ν , the desorption energy E_{des} , equivalent to the adsorbate binding energy for non-dissociative desorption, the Boltzmann constant k_B and the particle temperature T . Using this relation and a simple kinetic model, it was possible to determine the binding energies of hydrocarbon-containing molecules and C_{60} in the first ML and in multilayers. In addition, surface sensitivity has been shown by comparing electron sticking and secondary electron emission on electron bombardment for a bare and C_{60} covered SiO_2

particle. A more detailed discussion of those experiments and the kinetic model used for their interpretation is given by Wellert.[197]

There are three main differences to the experiments reported in Chapter 5 and the above-mentioned study. First, a 532 nm laser was used here instead of a 10.6 μm CO_2 laser. While the latter can heat the particle by interaction with optical phonons, the former is not absorbed in the bulk, due to the band gap of 9 eV.[198] This is reflected by an extinction coefficient of zero for amorphous SiO_2 at this wavelength.[199] Since laser power dependent desorption rates have been observed, alternative absorption mechanisms including defect sites and surface states need to be considered.

Second, the binding energy of argon to the SiO_2 surface is about ten times smaller than the binding energies reported for C_{60} . It is expected to lie in the range from 600 to 1000 cm^{-1} , based on values determined for a variety of substrates.[200] Due to different binding sites at the surface, a range of binding energies may exist. The rates given in Tab. 5.1 are mainly related to desorption of argon from layers beyond the first ML. Thus, the enthalpy of vaporization of argon, 546 cm^{-1} , [201] should be used instead for further analysis.

Finally, the particle temperature is much smaller due to cryogenic cooling. Even when heating with a laser power of 7 mW, an equilibrium with multiple argon MLs is approached as seen in Fig. 5.6. Changing the SRET temperature from 60 to 80 K, however, removes most of the attached argon quickly. This suggest that laser heating here, changed the particle temperature only by a few K as opposed to up to 200 K. As a consequence, the mass changes upon laser heating are slow, suggesting that the desorption rate is only slightly larger than the adsorption rate. Thus, the adsorption rate cannot be neglected, as is the case for the fast desorption periods in the study mentioned above. To quantify the particle temperature and argon binding energies from the present experimental data, more advanced models for the ad- and desorption kinetics and laser absorption must be developed. Alternatively the experiment can be repeated with a flexible gas manifold, which allows to quickly change between argon and helium gas, while keeping the total pressure constant. When using helium, argon adsorption is still possible by desorption of remaining argon from the radiation shield of the trap, but adsorption rates should be significantly reduced.

6 Outlook

In this doctoral thesis, a novel nanoparticle mass spectrometry (NPMS) setup for action spectroscopy of single nanoparticles was designed, built and characterized. Single nanoparticles are transferred from solutions into the instrument using a nano ESI ion source. They are trapped in a cryogenic split-ring electrode trap (SRET), with optimized electric potential, which forms the central part of the setup. Optical detection of the particle motion inside the trap allows to determine the mass-to-charge ratio (M/Q) ratio, and charge stepping is used to determine the absolute mass and charge. Messenger tagging of single nanoparticles was demonstrated for the first time and forms the first step towards action spectroscopy. The applicability of different techniques for mass determination and for calibration of ad- and desorption rates were evaluated. Mass determination using FT spectra avoids artifacts due to large amplitude motion and collisional heating and is preferred for particles with sufficiently light scattering or fluorescence intensities. Resonant excitation on the other hand, is much more sensitive for mass determination of dim particles. To quantify the relative intensities in single nanoparticle action spectra, TPD-like analysis of laser induced desorption rates is suggested. The remaining challenges, open questions and suggestions for future work are addressed in Sec. 6.1. Further improvements and general perspectives for experiments on the new NPMS setup are discussed in Sec. 6.2 and Sec. 6.3, respectively.

6.1 Towards Action Spectroscopy of Single Nanoparticles

The new NPMS setup is almost ready for single nanoparticle action spectroscopy. The essential steps are summarized in the following and a feasible detection scheme is presented. A single trapped particle is prepared, starting with a Coulomb crystal and destabilizing all but one particle (see Sec. 4.1). The absolute mass is detected either by FT or resonant excitation combined with charge stepping (see Sec. 4.4 and Sec. 4.5). It can be continuously tracked to monitor laser induced mass changes. (see Chapter 5)

The final step is the selection of a tunable laser system and its integration into the experimental workflow. Suitable spectral ranges, required power and advantages and disadvantages of pulsed and continuous wave (CW) laser have to be determined in proof of concept experiments and may vary for different particles. Model systems for initial experiments are presented in Sec. 6.1.1 below. Electronic and vibrational degrees of freedom are probed with UV-VIS and IR lasers, respectively. Both absorption

mechanisms are expected to be more efficient than the absorption of the 532 nm laser by defect sites and surface states, see Sec. 5.3, and hence a laser power of a few mW should be sufficient. CW lasers are preferred as they reduce the risk of radiation damage and particle loss due to total photon pressure or one-sided evaporation. Currently there are two laser systems on the shortlist. First, quasi-CW supercontinuum white light lasers can be used for spectroscopy in the visible and near-IR spectral range. This type of laser produces a broad spectrum, but a filter system can be used to select and scan a transmission window. The usable power depends on the laser model and transmission window width. For example, an output power of 10 to 40 mW in the spectral range of 400 to 2400 nm is provided when using a combination of the SuperK FIANIUM FIU-15 laser with the SuperK VARIA filter from NKT Photonics Technology GmbH and a transmission window of 10 nm. A calibration for constant intensity, strongly desired for this new type of action spectroscopy, is possible with this system. Second, quantum cascade lasers can be used in the mid- and far-IR range. For example, the MIRcat-QT from Daylight Solutions provides up to 500 mW in the spectral range from 5.4 to 11.2 μm . In either case, the optical setup must be modified to allow coupling to the tunable laser. The laser-instrument alignment can be stabilized using an optical fiber. The laser beam can be introduced to the trap center directly via the parabolic mirrors, or by superposition with the detection laser in a beam splitter. When using the parabolic mirrors, a large background signal is expected at the APD (see Sec. 3.7). In addition, the signal due to scattering of the tunable laser at the trapped particle can also interfere with the measurement. A band pass filter for 532 nm in front of the APD can be used to block the light of the tunable laser, to avoid interference with the mass measurement.

The laser power induced changes of desorption rate shown in Fig. 5.6 represent a significant step towards action spectroscopy. An action spectrum of a single nanoparticle will be obtained by recording the desorption rate while changing the laser wavelength instead of the power. Since, for the data presented here, the desorption rates appear to be constant over hours, it may be sufficient to record mass changes over a few minutes or even less for each wavelength step. This will allow to cover the spectral range of interest in a reasonable amount of time and reduce the risk of unintended charge steps and the effect of long-term instabilities of the RF amplifier during acquisition of the spectrum. The initial number of adsorbed messenger atoms or molecules has to be chosen large enough to prevent saturation effects due to complete depletion. Since desorption rates will also depend on the number of adsorbates, it might be necessary to restore a fixed surface coverage before each wavelength step. This may be avoided if two spectra are recorded with identical initial coverage but reverse scan directions and the agreement between the two is reasonable. Other messenger gases with lower binding energies, like helium or neon, can be used to increase the sensitivity for surface vibrations probed by IR spectroscopy.[65] For certain particles and temperatures, mixtures of messenger and helium gas may be useful to adjust the adsorption rate while keeping the total pressure constant. Proof of concept experiments are planned within the next few months, to evaluate the applicability of the above-mentioned tunable laser sources.

Insights, obtained in those experiments, will reveal the current limits of acquisition speed, resolution and sensitivity, and indicate ways for their improvement.

6.1.1 Future Research and Applications

March and Todd [74, p. 74] state that "*in most applications a single ion is rarely of great value*". While this is certainly true, the experiments that are planned based on the results presented in this thesis, are part of a whole branch of science where "great value" can only be achieved by single particle techniques.

The type of experiments conducted in the near future will depend on the decision on the accessible spectral range. Though proof of concept experiments in the visible and near-IR range are easier and cheaper to implement, access to the mid- and far-IR spectral range is needed to obtain detailed information on the particle surface structure.

Useful systems for experiments in the visible range are dye labeled particles such as the rhodamine B labeled PMMA particles used in the characterization of the current NPMS setup. Energy uptake by fluorescence is more efficient compared to absorption by defect sites and surface states, and correspondingly lower laser power requirements are expected compared to the experiments presented in Chapter 5.

Quantum dots have applications in light-emitting diodes, solar cells, optoelectronics and bioimaging.[22] CdSe/ZnS core shell quantum dots with a nominal diameter of 4 nm were used in the early stages of characterization. They were not detected in the SRET, as they only weakly fluoresce unless they are thermally brightened with a suitable laser.[143] Intermittent fluorescence, *i.e.* blinking, has been observed in NPMS experiments with such particles and was tentatively attributed to changes in the band gap due to background gas adsorption.[135] The blinking rates are thus expected to depend on adsorption rates and thus on the particle temperature. This effect can be studied for CdSe/ZnS, and other quantum dots, in more detail using spectroscopy in the visible spectral range at different SRET temperatures.

In interstellar dust, nanoparticles with water and other ice layers are formed in cold, dense regions like pre-stellar cores.[38, 45, 47, 202] When the particles are heated, *e.g.* during star formation, they affect the gas-phase chemistry by ice evaporation.[39] To improve current models of those processes, ad- and desorption rates, surface mobility and reactivity, binding energies and residency times can be investigated for corresponding model systems.[203]

Vanadium oxides are used in lithium batteries, bolometric detectors, ferromagnetic nanotubes and in catalysis.[57] They represent an unique model system for proof of concept experiments in the far-IR range, as not only IR spectra for molecular clusters[57] but also for macroscopic surfaces[64, 65] are already available for direct comparison. The latter are among the first of their kind, as surface action spectroscopy has been developed only very recently.

As mentioned in Sec. 2.4.1, particles with diameters below 50 nm are particularly interesting and challenging. While detection of dye labeled particles is straight forward, it might not always be possible to add dye labels without changing particle properties.

A reproducible standard method needs to be found for detection of non-fluorescing particles. While detection by co-trapping of a fluorescent probe particle has been shown in a proof of concept experiment,[143] further work is needed to routinely use this technique. Ultimately, this might even allow for investigation of infrared quantum dots, which are used for a broad range of optoelectronic applications.[204]

6.2 Suggested Instrumental Upgrades

Future applications may require optimization of the source conditions to control charge states and level of agglomeration. Other diagnostic tools can help to characterize and optimize the particle beam composition much faster compared to successive single particle analysis. Especially for particles with M/Q below $1 \text{ MDa} e^{-1}$ installation of a TOFMS can prove useful (see Sec. 2.1). Another option is to install a removable graphite target or grid for IBD and subsequent analysis via AFM or TEM. Both detection systems can be installed straight after the deflector, in the non-linear version of the NPMS setup. Information on the particle mass and charge distribution will also be useful to select suitable deflection and trapping parameters.

The installation of a conventional QIT with subsequent ion detection at this position would be a relatively cheap alternative, as it does not need to be optimized for high precision and low temperatures and can share the existing RF amplifier with the SRET.

When the gate valve closes in case of vacuum problems the two parts of the instrument are still connected via the backing pump. To increase safety another automated valve can be introduced to the fore lines.

For certain dimensions of stainless-steel capillaries in nano ESI ion sources, the gas flow inside the capillary starts off laminar but turns into a turbulent flow as the gas reaches the speed of sound and can't accelerate further. Ion signal is lost where the gas flow becomes turbulent, which can be avoided by using shorter capillaries and heating.[147] It is possible to use shorter capillaries, but the source block needs to be adapted as well. This effect can be investigated by simulations that consider the present capillary diameter and length.

Several options are available for improvement of the optical setup. The light of the scattering laser can be introduced into the trap with optical fibers. A lens at the fiber output, inside the trap, can achieve a tighter beam waist compared to the present setup.[129, p. 57] In addition, the fiber would move with the trap, making the alignment independent on the trap temperature. An optical fiber can also be used for light collection, though it should remain outside the vacuum chamber to allow for fast alignment.[179] The currently used planar windows should be replaced by windows at the Brewster angle to maximize transmission.

Conventional CCD cameras are well suited for detection of scattered and fluorescent light. For dim particles, where the number of photons reaching the detector is well below 100 per pixel, it can help to use an intensified charge coupled device (ICCD) or electron-multiplying charge coupled device (EMCCD) instead. Apart of an increased

sensitivity those detectors also provide faster readout rates which is useful for imaging of the particle trajectory.

6.3 Other Directions for NPMS Experiments

NPMS experiments can provide valuable information on optical properties of nanoparticles.[130] It would be intriguing to see how optical properties of a single nanoparticle change with size or surface composition. One candidate for such an experiment are Si nanoparticles. It is assumed that blue light emission from Si nanoparticles is enabled by recombination of excitons in a SiO_x surface layer.[205] This effect can be studied in more detail by NPMS experiments on Si nanoparticles that are gradually oxidized by controlling the partial pressure of oxygen in the ion-trap chamber. Emitted blue light can be detected selectively using an appropriate optical filter.

Another possibility for future applications is the investigation of nanoparticle properties using soft X-rays. The size and surface structure of SiO_2 particles with diameters in the range from 150 to 250 nm were investigated by scattering of soft X-rays by a free nanoparticle beam.[206] In another study, NPMS was applied to investigate charging mechanisms of single 500 nm SiO_2 particles.[207] For high charge states, collisions with residual gases or ion desorption led to charge loss. Additional decrease of charge by reintroduction of electrons can be used to restore well-defined initial conditions between individual measurements. Since changes in charge state by emission of electrons can be detected with 100 % efficiency for particles with less than a few hundred charges, X-ray absorption spectroscopy (XAS) of single nanoparticles is possible. Both of the above-mentioned studies were using synchrotron radiation produced at BESSY-II in Berlin. As the current NPMS was designed to be mobile, experiments using this and other external light sources are possible in the future.

A long-term goal for NPMS is to synthesize new particles by adding or removing atoms or molecules in a controlled way.[76] The ion source can be set up to produce an atomic or molecular ion beam for deposition on a trapped nanoparticle. To this end, an appropriate RF supply must be installed, to operate the linear quadrupole ion-guide in the mass-selective mode. The deposition efficiency can be increased by preparing the nanoparticle in a highly charged state and choosing a beam of opposite polarity. Thermal cycles induced by laser heating may be useful to trigger desorption, chemical reactions or decomposition processes on the particle surface. If the NPMS setup is rebuilt to the non-linear version, it is even possible to attach a neutral molecular beam source. While production of a significant number of particles, useful for industrial applications, cannot be the goal in single particle experiments, investigation of individual tailored particles can provide useful insights for large scale production.

Appendix A

Deconstructing Prominent Bands in the Terahertz Spectra of H_7O_3^+ and H_9O_4^+ : Intermolecular Modes in Eigen Clusters *

Recent ultrafast, IR spectroscopic studies of excess protons in water have provided new insights into the nature of aqueous proton transfer, in general, and the role of Zundel- vs Eigen-like motifs, in particular.[1, 2] The spectral diffusion associated with the characteristic IR absorptions of these local hydration motifs has been disentangled by gas-phase vibrational action spectroscopy on cold protonated water clusters $\text{H}^+(\text{H}_2\text{O})_n$, which directly correlates local distortions of the hydrogen-bonded network with vibrational frequencies in the mid- and near-IR spectral regions as a function of the displacement of the transferring proton.[3] However, the characteristic spectral signatures of $\text{H}^+(\text{H}_2\text{O})_n$ clusters in the far-IR or terahertz region ($<600\text{ cm}^{-1}$), namely, intermolecular hydrogen-bond stretching and deformation modes[4–7] remain largely ill-characterized. Infrared photodissociation (IRPD) spectra in this spectral region, which require the intense and widely tunable radiation from an IR free electron laser, have only been reported for some of the larger ($n \geq 5$) clusters,[8–10] but not for the prototypical Eigen ion, $\text{H}_3\text{O}^+(\text{H}_2\text{O})_3$, itself. Such spectra are reported here for the first time. The IRPD spectra of small protonated water clusters,[3, 8, 10–20] especially the one for H_9O_4^+ , have been the subject of numerous theoretical analyses,[3, 10, 14, 21–24] using VPT2 theory and also “on-the-fly” ab initio molecular dynamics simulations of the IR spectra (both using DFT or MP2 electronic energies) and with conflicting conclusions about whether the experimental spectra are for the Eigen[19, 21] or Zundel[22] isomers. Recently, Qi Yu and Joel M. Bowman reported many-body representations of the potential and dipole moment surfaces that are suitable for a variety of postharmonic analyses.[20, 23, 24] The representation for the potential is

*Chapter Based on: Tim K. Esser, Harald Knorke, Knut R. Asmis, Wieland Schöllkopf, Qi Yu, Chen Qu, Joel M. Bowman, and Martina Kaledin. “Deconstructing Prominent Bands in the Terahertz Spectra of H_7O_3^+ and H_9O_4^+ : Intermolecular Modes in Eigen Clusters”. In: “The Journal of Physical Chemistry Letters” (2018), pp. 798–803

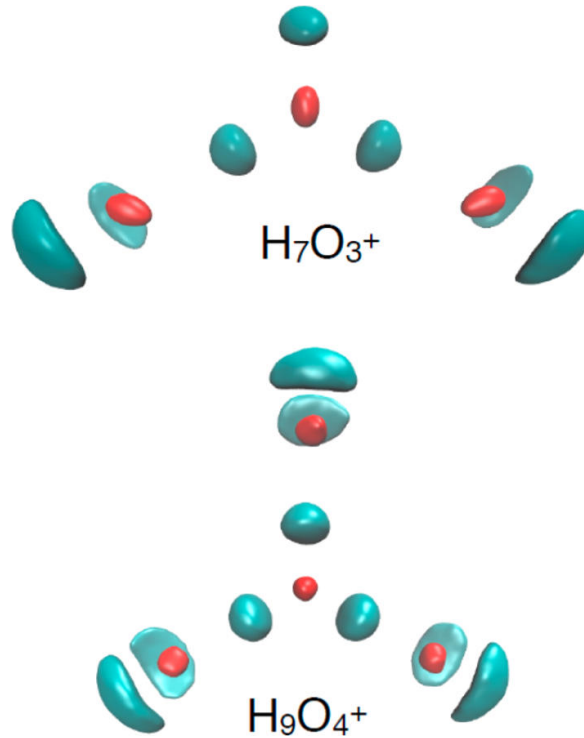


Fig. A.1: Isosurface plots of the ground vibrational wave functions of $H^+(H_2O)_3$ (3E) and $H^+(H_2O)_4$ (4E) obtained from diffusion Monte Carlo calculations. Red represents the O nuclei and turquoise the H nuclei.

based on the CCSD(T)-level of theory, currently the “gold standard” method. Details of the many-body representations of the potential energy and dipole moment surfaces and validation are given elsewhere.[20, 24] They were recently used in coupled-mode vibrational self-consistent field/virtual state configuration interaction (VSCF/VCI) quantum calculations, employing the exact Watson Hamiltonian, of the IR spectra of $H_7O_3^+$ and $H_9O_4^+$ to unambiguously confirm the original assignment[11] that these ions exhibit Eigen-type (hydronium ion) cores (see Fig. A.1), i.e., they correspond to $H_3O^+(H_2O)_2$ (3E) and $H_3O^+(H_2O)_3$ (4E), respectively.[20, 23, 24]

Here, the IRPD spectra of the cryogenically cooled, D_2 -tagged protonated water trimer, $H^+(H_2O)_3-D_2$, denoted as 3H- D_2 , and tetramer, $H^+(H_2O)_4-D_2$ (4H- D_2), in the spectral region $210-2200\text{ cm}^{-1}$, are presented. Tagging is required to probe the linear absorption regime and D_2 was chosen to mitigate well-documented tagging issues. The spectral features to hydrogen-bond stretching as well as water wagging modes are conclusively assigned, based on anharmonic calculations using the high-level potential and dipole moment surfaces mentioned above. These calculations include the previous VSCF/VCI ones in the spectral range above 1000 cm^{-1} and quasiclassical molecular dynamics (QCMD) calculations, described below for the spectral range below 1000 cm^{-1} . Unfortunately, in this range the quantum approach becomes prohibitively difficult, as the large-amplitude, torsional motion of the flanking waters is poorly

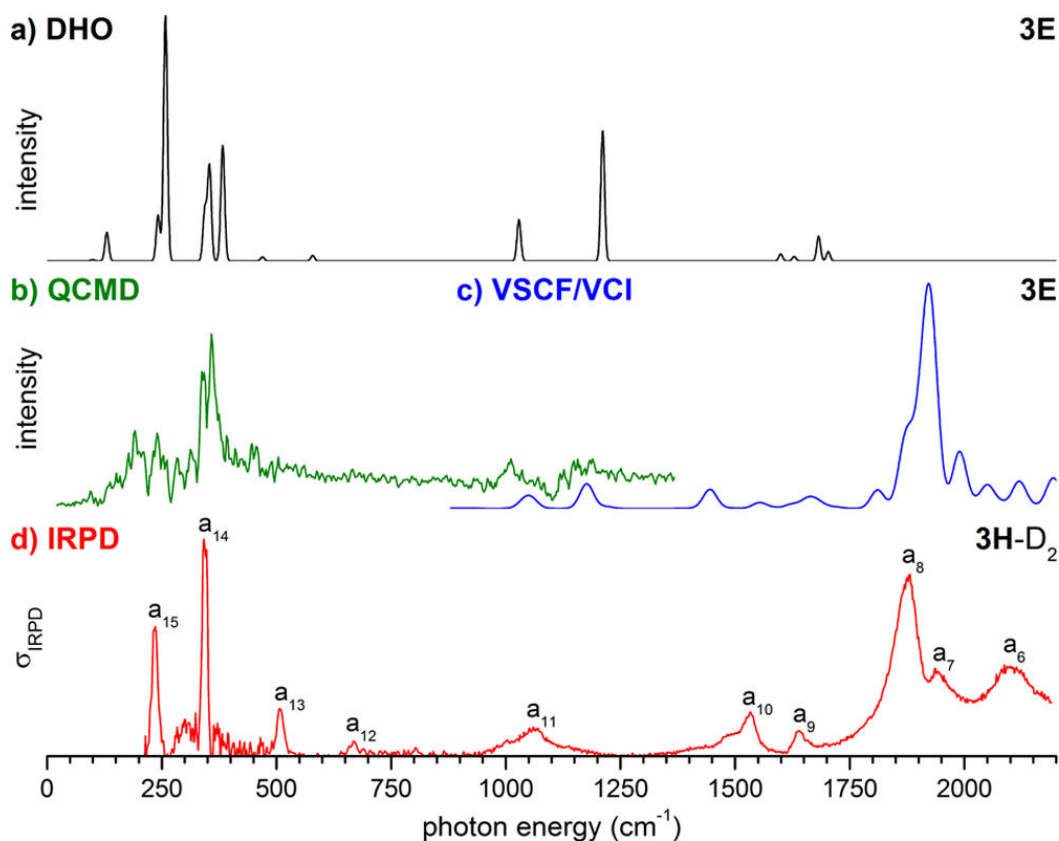


Fig. A.2: Comparison of the calculated (a) double-harmonic (DHO), (b) QCMD and (c) VSCF/VCI vibrational spectra of 3E to the (d) experimental IRPD spectrum of 3H-D₂ in the spectral region from 0 to 2200 cm⁻¹. See Tab. A.1 for band positions and assignments. The calculated DHO and VSCF/VCI spectra were convoluted with Gaussian line shape functions with a fwhm width of 10 and 30 cm⁻¹, respectively.

described by the Watson Hamiltonian. Classical MD simulations of IR spectra for low frequency modes are expected to be a substantial improvement over double harmonic oscillator (DHO) ones, as has been amply demonstrated in the literature, and also here. Addition of zero-point energy may also improve MD spectra[24, 25] and so that is done here, but only for the intermolecular modes. This approach is essentially the well-known quasiclassical one, used in reaction dynamics calculations and so the term “quasiclassical” molecular dynamics is used above. Some analysis of the QCMD spectra is done using driven molecular dynamics (DMD), which is the mechanical analogue of the classical interaction of an external oscillating electric field with the molecular dipole. The details are given elsewhere.[26–28] Finally, rigorous diffusion Monte Carlo calculations are done for the zero-point wave functions of 3E and 4E. These are shown, without comment, in Fig. A.1. The experimental IRPD spectrum of 3H-D₂ in the spectral range 210 to 2200 cm⁻¹ is compared to the DHO, QCMD spectra and previous VSCF/VCI calculations (above 900 cm⁻¹) of (bare) 3E in Fig. A.2. Experimental band

Table A.1: Experimental IRPD Band Positions (in cm^{-1}) of 3H-D₂, Computed Harmonic (HO), VSCF/VCI, and QCMD Vibrational Wavenumbers (in cm^{-1}) of 3E and Assignments

label	IRPD	IRPD ^a	HO	VSCF/VCI ^a	QCMD	assignment ^b
a6	2100	2109		2098–2246		low freq modes + H ₃ O ⁺ bend + IHB antisym. stretch, H ₃ O ⁺ frust. rotation + H ₂ O bend + IHB sym. stretch
a7	1942	1943	2692	2034		2ν H ₃ O ⁺ wag + IHB sym. stretch
a8	1875	1878	2518	1910–1976		IHB antisym stretch, H ₃ O ⁺ frust. rotation + H ₃ O ⁺ umbrella + IHB antisym. stretch
a9	1640	1639	1721,1743	1688,1701		H ₃ O ⁺ bend
a10	1533	1534	1636,1666	1477		H ₂ O bend + IHB antisym. stretch
a11	1060	1059	1240 1051	1202 1081	1176 1015	H ₃ O ⁺ umbrella H ₃ O ⁺ wag
a12	668		593			H ₃ O ⁺ frust. rotation
a13	508		479		456	comb of low freq modes
	344		390			antisym. HB-stretch (H ₃ O ⁺ rattle)
a14			362 351		355	sym. HB-stretch H ₂ O rock
a15	234		264 247		241	H ₂ O wag

^a From ref [20]. ^bBand assignments for a_6 to a_{11} from ref [20].

positions and assignments, based on calculations, are listed in Tab. A.1. The IRPD spectrum reveals (at least) 10 features, labeled with a_6 to a_{15} (see ref [20] for bands a_1 to a_5). Bands a_6 - a_{11} agree satisfactorily with the previously published data for 3H-D₂ by Duong et al.[20] Minor discrepancies with respect to relative intensities are observed for a_6 and the low-energy shoulder of a_{10} , which may be attributed to the slightly different conditions in the two experiments. Features a_{12} to a_{15} have not been previously reported and, in particular, the three prominent bands at 508 cm^{-1} (a_{13}), 344 cm^{-1} (a_{14}), and 234 cm^{-1} (a_{15}) correspond to the first experimental observation of transitions involving the intermolecular water modes in the protonated water trimer.

As usual, theory is used to assign/interpret the experimental spectra, with a specific focus on the new experimental bands. First, consider the DHO spectrum, which does have a single intense band and a higher-energy doublet in the range of experimental bands a_{15} and a_{14} . However, there are other strong bands in the DHO spectrum that are not present in experiment and vice versa. Clearly then, DHO is not reliable, or at least not globally reliable. By contrast, the QCMD spectra are in good agreement with experiment over the expected range of applicability of these spectra, and beyond that range the VSCF/VCI spectrum continues the good agreement with experiment. The QCMD spectrum was analyzed using DMD, and the results are that for the bands around 241 and 355 cm^{-1} the energy absorption continues monotonically. This is an indication from DMD that these are intense bands, in agreement with the QCMD results (and also the DHO ones) and experiment. By contrast, the energy absorbed stops for the two intense DHO bands at 1051 and 1240 cm^{-1} (see Tab. A.1), indicating that these are in fact weak absorbers. This agrees with the QCMD spectrum and also experiment; however, not with the DHO results. Note that there are no DHO peaks

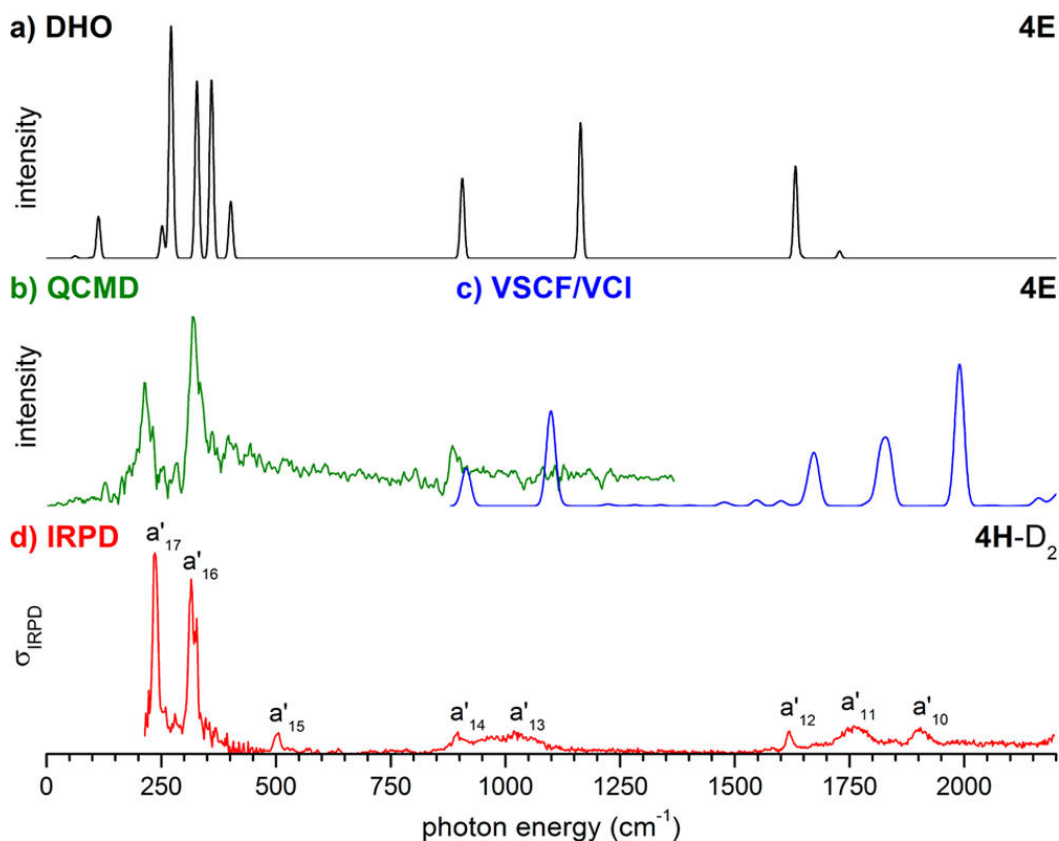


Fig. A.3: Comparison of the calculated (a) double-harmonic (DHO), (b) QCMD and (c) VSCF/VCI vibrational spectra of 4E to the (d) experimental IRPD spectrum of 4H-D₂ in the spectral region from 0 to 2200 cm⁻¹. See Tab. A.2 for band positions and assignments. The calculated DHO and VSCF/VCI spectra were convoluted with Gaussian line shape functions with a fwhm width of 10 and 30 cm⁻¹, respectively.

in the spectral range 1750-2200 cm⁻¹, in contrast to experimental and VSCF/VCI spectra. The experimental IRPD spectrum of 4H-D₂ in the spectral range from 210 to 2200 cm⁻¹ is compared to the DHO and QCMD spectra of bare 4E in Fig. A.3. Band positions and assignments are listed in Tab. A.2. The IRPD spectrum shows eight bands (a'₁₀-a'₁₇) in total, with two characteristic and intense IR bands and a weaker feature in the far IR region at 316 cm⁻¹ (a'₁₆), 236 cm⁻¹ (a'₁₇), and 503 cm⁻¹ (a'₁₅). Bands a'₁₀-a'₁₄ agree satisfactorily with the previously reported spectrum of 4H-D₂ by Wolke et al.[3] Minor discrepancies (-10 cm⁻¹) with respect to the position of the band maximum of a'₁₀ and of a'₁₁ are observed and due to slightly different band profiles.

The assignments of the prominent experimental bands labeled a'₁₇/a'₁₅ and a'₁₆/a'₁₄ is discussed first. By examining trajectories that correspond to these, the intensity of bands a'₁₇/a'₁₅ is due to mainly “wagging” motion of the flanking H₂O molecules and for bands a'₁₆/a'₁₄ it is the embedded H₃O⁺ hydrogen bond stretching (or “H₃O⁺ rattle”) mode that is the dominant motion. In both cases, there is evidently a large

Table A.2: Experimental IRPD Band Positions (in cm^{-1}) of 4H-D₂, Computed Harmonic (HO), VSCF/VCI, and QCMD Vibrational Wavenumbers (in cm^{-1}) of 4E and Assignments

label	IRPD	IRPD ^a	HO	VSCF/VCI ^b	QCMD	assignment ^c
a10'	1898	1909		2033		H ₃ O ⁺ umbrella + H ₃ O ⁺ wag
a11'	1760	1770		1859,1877		overtone H ₃ O ⁺ wag, comb 2 H ₃ O ⁺ wag
a12'	1615	1615	1669–1768	1712		H ₃ O ⁺ and H ₂ O bends
a13'	1014		1190	1124	1154	H ₃ O ⁺ umbrella
a14'	894		928	937	910	H ₃ O ⁺ wag
a15'	503					comb of low freq modes
a16'	316		335–411		331	antisym. HB - stretch (H ₃ O ⁺ rattle)
						sym. HB - stretch
a17'	236		258–284		216	H ₂ O wag

^a From ref [3]. ^b From refs [23] and [24]. ^c Band assignments for a'_{10} to a'_{14} from refs [3], [23], and [24].

change in the dipole moment. This is worth investigating in detail, and this is done in Fig. A.4, where the components of the full dipole moment are plotted along with the component from the above many-body representation of the dipole moment, as a function of the corresponding intermolecular normal mode corresponding closest to the quasiclassical motion. Even though this normal mode may not be as accurate a description of the QC motion, it suffices for this qualitative explanation of the intensity. In the upper panel, for the wagging motion, it is seen that the sum of the 1-body water and 2-body water dipole tracks the full dipole nearly exactly as a function of Q. The magnitude is less but the derivative is nearly identical and so it is safe to assign the intensity to the change in the sum of the water monomer dipole moments. The lower panel shows a more complex picture for the dipole moment of the H₃O⁺ hydrogen bond stretching mode; however, it is clear that change in the 1-body hydronium dipole plus the 2-body hydronium water dipole moment are the main contributors to the intensity. This picture is not as obvious as the one for the wagging of the flanking water; however, it results from coupling of the hydronium and the water intermolecular modes, in this case the H₃O⁺ hydrogen bond stretch mode.

Comparison of the intense bands below 800 cm^{-1} with those observed between 800 and 2100 cm^{-1} in the IRPD spectra of 3H-D₂ and 4H-D₂ reveals that the lower frequency bands are considerably narrower, exhibiting fwhm widths of less than $\sim 15 \text{ cm}^{-1}$, similar (a) to the bands found in the free O-H stretching region[3, 20] as well as (b) to the corresponding bands in the spectra of 5H-D₂ and 6H-H₂. [8, 10] The QCMD results predict broader band profiles for a_{13}/a_{14} (3E) and a'_{16}/a'_{17} (4E), but these bands from theory do show some sensitivity to the energy of the trajectories; this is typical of MD approaches. No evidence was found that this narrowness originates from multiphoton absorption effects. Modest laser pulse energies were applied ($< 1 \text{ mJ}$ below 500 cm^{-1}) and estimates of the dissociation limit, when zero-point and internal energies are considered, support that single photon photodissociation is feasible. Tagging effects should also not alter the band widths dramatically, but probably do contribute to

the deviations regarding the band positions and relative intensities. Tab. A.3 and Tab. A.4, which contain the harmonic MP2 frequencies with and without the D₂ tag, can be consulted for guidance on the effect of tagging. However, because the spectra in the THz region are highly anharmonic and coupled, the numerical values of the shifts should not be taken as accurate. Summarizing, the intermolecular stretching and wagging frequencies appear surprisingly insensitive to the inherent floppiness of these hydrogen-bonded ions.

Finally, it is of interest to discuss how the present values for the IR-active low-frequency modes compare to those in larger protonated water clusters and in solution (see Tab. A.5). The Eigen ion 4E exhibits 12 vibrational normal modes in the terahertz spectral region ($<600\text{ cm}^{-1}$), which correspond to frustrated translations and rotations of the flanking water molecules. These are, in order of decreasing frequency, the three hydrogen bond stretching, three water wagging, three water rocking, and three hydrogen bond deformation (bending) modes. Each set consists of a symmetric and a doubly degenerate antisymmetric combination, of which only the antisymmetric hydrogen bond stretching and water wagging modes carry significant IR intensity. These are observed at 316 and 236 cm^{-1} , respectively, in the spectrum of 4H-D₂. Removal of one of the flanking waters leads to 3E with only single antisymmetric stretching and wagging modes (3H-D₂: 344 cm^{-1} and 234 cm^{-1} , respectively).

While it proves difficult to unambiguously identify the wagging modes of the flanking water molecules in larger water clusters, due to their delocalized nature over an increased number of water molecules, the respective hydrogen-bond stretching modes involving the embedded H₃O⁺ can be traced all the way to the solution phase data (see Tab. A.5). The asymmetrically solvated H₃O⁺ in 5E and 6E results in a splitting of the IR-active (antisymmetric) hydrogen bond stretches, one that is blue-shifted in the spectra of 5H-D₂ (405 cm^{-1})[10] and 6H-D₂ (373 cm^{-1})[8] and another that is red-shifted (5H-D₂: 298 cm^{-1} , 6H-D₂: 279 cm^{-1}), with respect to their position in the 4H-D₂ spectrum. This yields mean frequencies for these modes of 351 cm^{-1} ($n = 5$) and 326 cm^{-1} ($n = 6$). At $n = 21$, H₃O⁺ is more symmetrically solvated again, and the 21H-D₂ spectrum[9] features a single, prominent broad IR-active band at 341 cm^{-1} , very close to the solution value of 340 cm^{-1} . [7] Summarizing, the mean frequencies of the IR-active hydrogen-bond stretching modes involving the hydronium core in protonated water clusters lie in a narrow spectral window ($\sim 310\text{-}360\text{ cm}^{-1}$) and seem to have converged close to the bulk value of 340 cm^{-1} ($n = \infty$) already for $n = 21$, suggesting a rather localized nature of these modes.

A.1 Experimental Details

IRPD experiments are performed using a 6 K ion-trap triple mass spectrometer described previously.[29] In brief, protonated water clusters are generated in a nanoelectrospray source from a 10 M solution of sulfuric acid in a 1:1 water/methanol mixture, thermalized at room temperature in a gas-filled radio frequency (RF) ion-guide, mass-

selected using a quadrupole mass filter, and focused in a RF ring-electrode ion-trap. The trap is continuously filled with D_2 buffer gas, cooled with a closed-cycle He cryostat, and held at temperatures between 13 to 15 K. Many collisions of the trapped ions with the buffer gas provide gentle cooling of the internal degrees of freedom close to the ambient temperature. At sufficiently low ion-trap temperatures, ion-messenger complexes are formed via three body collisions.[30, 31] All ions are extracted either every 100 or 200 ms, depending on the lasers used, and focused both temporally and spatially into the center of the extraction region of an orthogonally mounted reflectron time-of-flight (TOF) tandem photofragmentation mass spectrometer. Here, the ions are irradiated with a counter-propagating IR laser pulse produced either by the free electron laser FHI FEL[32] ($210\text{-}1200\text{ cm}^{-1}$) at the Fritz Haber Institute in Berlin or an OPO/OPA/AgGaSe₂ IR laser system[33] ($700\text{-}2000\text{ cm}^{-1}$). All parent and photofragment ions are then accelerated toward an MCP detector and monitored simultaneously as the laser wavelength is scanned. The photodissociation cross section σ_{IRPD} is determined as described previously.[29, 34] The individual IRPD spectra using the two laser systems are then scaled in intensity such that the intensity of common peaks in the overlapping region ($700\text{-}1200\text{ cm}^{-1}$) match, in order to correct for changes in laser beam/ion cloud overlap. The FHI FEL is operated at 5 Hz with a bandwidth of approximately 3 cm^{-1} and an average power of 50 mJ per macropulse (laser pulse). IR pulse energies are reduced by attenuators to less than 6 mJ ($<1\text{ mJ}$ below 500 cm^{-1}) to avoid saturation. IRPD spectra are recorded by averaging over 50-75 TOF mass spectra per wavelength step and scanning the wavelength of the laser pulse. The OPO/OPA laser system is operated at 10 Hz with a bandwidth of approximately 3 cm^{-1} and an average power of 1-1.5 mJ per laser pulse. IRPD spectra are measured by continuously scanning the laser wavelength, which is monitored online using a HighFinesse WS6-600 wavelength meter, with a scan speed such that an averaged TOF mass spectrum (over 100 laser shots) is obtained every 2 cm^{-1} . Typically, at least three scans are measured.

A.2 Computational Details *

The IR spectra of $H_7O_3^+$ and $H_9O_4^+$ in the region 0 to 1200 cm^{-1} were calculated using a quasiclassical molecular dynamics (QCMD) approach to obtain the dipole-dipole correlation function, the Fourier transform of which provides the IR spectrum. The used QCMD approach is a minor modification of the procedure described by Van-Oanh et al.,[25] where zero-point energy is given initially to each normal mode of a molecule. This approach is widely used in reaction dynamics, where it is referred to as the quasiclassical approach, and so that terminology is used here. It is well-known that this approach suffers from “zero-point leak”, because it is actually an approximate semiclassical quantization procedure and thus mode-mode energy transfer can occur. (This “leak” would in principle be eliminated if exact semiclassical quantization of the

*Calculations have been performed by Qi Yu and Chen Qu in the group headed by Joel M. Bowman at the Emory University, Atlanta, Georgia.

zero-point state was done.) The energy transfer from high-frequency intramolecular modes to low-frequency intermolecular ones can result in rapid dissociation of the molecule/complex. To mitigate this rapid dissociation, approximate quasiclassical quantization was applied to intermolecular modes only and zero energy was given initially to the intramolecular modes. One hundred trajectories were performed for each complex. The initial conditions were obtained by random sampling of the harmonic normal-mode phase space, with harmonic zero-point energy given to the intermolecular modes. Each trajectory was propagated for 12 ps and the standard dipole-dipole correlation function was obtained for each, then averaged over the set of trajectories, and finally Fourier transformed to obtain the spectra. No smoothing of the spectra was done.

A.3 References

- [1] M. Thämer, L. D. Marco, K. Ramasesha, A. Mandal and A. Tokmakoff. “Ultrafast 2D IR Spectroscopy of the Excess Proton in Liquid Water”. In: “Science” 350.6256 (2015), pp. 78–82.
- [2] F. Dahms, B. P. Fingerhut, E. T. J. Nibbering, E. Pines and T. Elsaesser. “Large-Amplitude Transfer Motion of Hydrated Excess Protons Mapped by Ultrafast 2D IR Spectroscopy”. In: “Science” 357.6350 (2017), pp. 491–495.
- [3] C. T. Wolke, J. A. Fournier, L. C. Dzugan, M. R. Fagiani, T. T. Odbadrakh, H. Knorke, K. D. Jordan, A. B. McCoy, K. R. Asmis and M. A. Johnson. “Spectroscopic Snapshots of the Proton-Transfer Mechanism in Water”. In: “Science” 354.6316 (2016), pp. 1131–1135.
- [4] L. B. Braly, K. Liu, M. G. Brown, F. N. Keutsch, R. S. Fellers and R. J. Saykally. “Terahertz Laser Spectroscopy of the Water Dimer Intermolecular Vibrations. II. $(\text{H}_2\text{O})_2$ ”. In: “J. Chem. Phys.” 112.23 (2000), pp. 10314–10326.
- [5] F. N. Keutsch and R. J. Saykally. “Water Clusters: Untangling the Mysteries of the Liquid, One Molecule at a Time”. In: “PNAS” 98.19 (2001), pp. 10533–10540.
- [6] R. J. Saykally and D. J. Wales. “Pinning Down the Water Hexamer”. In: “Science” 336.6083 (2012), pp. 814–815.
- [7] D. Decka, G. Schwaab and M. Havenith. “A THz/FTIR Fingerprint of the Solvated Proton: Evidence for Eigen Structure and Zundel Dynamics”. In: “Phys. Chem. Chem. Phys.” 17.17 (2015), pp. 11898–11907.
- [8] N. Heine, M. R. Fagiani, M. Rossi, T. Wende, G. Berden, V. Blum and K. R. Asmis. “Isomer-Selective Detection of Hydrogen-Bond Vibrations in the Protonated Water Hexamer”. In: “J. Am. Chem. Soc.” 135.22 (2013), pp. 8266–8273.

- [9] J. A. Fournier, C. T. Wolke, C. J. Johnson, M. A. Johnson, N. Heine, S. Gewinner, W. Schöllkopf, T. K. Esser, M. R. Fagiani, H. Knorke and K. R. Asmis. “Site-Specific Vibrational Spectral Signatures of Water Molecules in the Magic $H_3O^+(H_2O)_{20}$ and $Cs^+(H_2O)_{20}$ Clusters”. In: “PNAS” 111.51 (2014), pp. 18132–18137.
- [10] M. R. Fagiani, H. Knorke, T. K. Esser, N. Heine, C. T. Wolke, S. Gewinner, W. Schöllkopf, M.-P. Gaigeot, R. Spezia, M. A. Johnson and K. R. Asmis. “Gas Phase Vibrational Spectroscopy of the Protonated Water Pentamer: The Role of Isomers and Nuclear Quantum Effects”. In: “Phys. Chem. Chem. Phys.” 18.38 (2016), pp. 26743–26754.
- [11] M. Okumura, L. I. Yeh, J. D. Myers and Y. T. Lee. “Infrared Spectra of the Cluster Ions $H_7O_3^+ \cdot H_2$ and $H_9O_4^+ \cdot H_2$ ”. In: “J. Chem. Phys.” 85.4 (1986), pp. 2328–2329.
- [12] J.-C. Jiang, Y.-S. Wang, H.-C. Chang, S. H. Lin, Y. T. Lee, G. Niedner-Schatteburg and H.-C. Chang. “Infrared Spectra of $H^+(H_2O)_{5-8}$ Clusters: Evidence for Symmetric Proton Hydration”. In: “J. Am. Chem. Soc.” 122.7 (2000), pp. 1398–1410.
- [13] K. R. Asmis, N. L. Pivonka, G. Santambrogio, M. Brümmer, C. Kaposta, D. M. Neumark and L. Wöste. “Gas-Phase Infrared Spectrum of the Protonated Water Dimer”. In: “Science” 299.5611 (2003), pp. 1375–1377.
- [14] J. M. Headrick, E. G. Diken, R. S. Walters, N. I. Hammer, R. A. Christie, J. Cui, E. M. Myshakin, M. A. Duncan, M. A. Johnson and K. D. Jordan. “Spectral Signatures of Hydrated Proton Vibrations in Water Clusters”. In: “Science” 308.5729 (2005), pp. 1765–1769.
- [15] G. E. Douberly, R. S. Walters, J. Cui, K. D. Jordan and M. A. Duncan. “Infrared Spectroscopy of Small Protonated Water Clusters, $H^+(H_2O)_n$ ($N=2-5$): Isomers, Argon Tagging, and Deuteration”. In: “J. Phys. Chem. A” 114.13 (2010), pp. 4570–4579.
- [16] K. Mizuse and A. Fujii. “Infrared Photodissociation Spectroscopy of $H^+(H_2O)_6 \cdot M_m$ ($M = Ne, Ar, Kr, Xe, H_2, N_2,$ and CH_4): Messenger-Dependent Balance between H_3O^+ and $H_5O_2^+$ Core Isomers”. In: “Phys. Chem. Chem. Phys.” 13.15 (2011), pp. 7129–7135.
- [17] K. Mizuse and A. Fujii. “Tuning of the Internal Energy and Isomer Distribution in Small Protonated Water Clusters $H^+(H_2O)_{4-8}$: An Application of the Inert Gas Messenger Technique”. In: “J. Phys. Chem. A” 116.20 (2012), pp. 4868–4877.
- [18] N. Heine, M. R. Fagiani and K. R. Asmis. “Disentangling the Contribution of Multiple Isomers to the Infrared Spectrum of the Protonated Water Heptamer”. In: “J. Phys. Chem. Lett.” 6.12 (2015), pp. 2298–2304.

-
- [19] J. A. Fournier, C. T. Wolke, M. A. Johnson, T. T. Odbadrakh, K. D. Jordan, S. M. Kathmann and S. S. Xantheas. “Snapshots of Proton Accommodation at a Microscopic Water Surface: Understanding the Vibrational Spectral Signatures of the Charge Defect in Cryogenically Cooled $\text{H}^+(\text{H}_2\text{O})_{n=2-28}$ Clusters”. In: “*J. Phys. Chem. A*” 119.36 (2015), pp. 9425–9440.
- [20] C. H. Duong, O. Gorlova, N. Yang, P. J. Kelleher, M. A. Johnson, A. B. McCoy, Q. Yu and J. M. Bowman. “Disentangling the Complex Vibrational Spectrum of the Protonated Water Trimer, $\text{H}^+(\text{H}_2\text{O})_3$, with Two-Color IR-IR Photodissociation of the Bare Ion and Anharmonic VSCF/VCI Theory”. In: “*J. Phys. Chem. Lett.*” (2017), pp. 3782–3789.
- [21] K. Yagi and B. Thomsen. “Infrared Spectra of Protonated Water Clusters, $\text{H}^+(\text{H}_2\text{O})_4$, in Eigen and Zundel Forms Studied by Vibrational Quasi-Degenerate Perturbation Theory”. In: “*J. Phys. Chem. A*” (2017).
- [22] H. Wang and N. Agmon. “Reinvestigation of the Infrared Spectrum of the Gas-Phase Protonated Water Tetramer”. In: “*J. Phys. Chem. A*” (2017).
- [23] Q. Yu and J. M. Bowman. “Communication: VSCF/VCI Vibrational Spectroscopy of H_7O_3^+ and H_9O_4^+ Using High-Level, Many-Body Potential Energy Surface and Dipole Moment Surfaces”. In: “*The Journal of Chemical Physics*” 146.12 (2017), p. 121102.
- [24] Q. Yu and J. M. Bowman. “High-Level Quantum Calculations of the IR Spectra of the Eigen, Zundel, and Ring Isomers of $\text{H}^+(\text{H}_2\text{O})_4$ Find a Single Match to Experiment”. In: “*J. Am. Chem. Soc.*” (2017).
- [25] N.-T. Van-Oanh, C. Falvo, F. Calvo, D. Lauvergnat, M. Basire, M.-P. Gaigeot and P. Parneix. “Improving Anharmonic Infrared Spectra Using Semiclassically Prepared Molecular Dynamics Simulations”. In: “*Phys. Chem. Chem. Phys.*” 14.7 (2012), pp. 2381–2390.
- [26] J. M. Bowman, X. Zhang and A. Brown. “Normal-Mode Analysis without the Hessian: A Driven Molecular-Dynamics Approach”. In: “*J. Chem. Phys.*” 119.2 (2003), pp. 646–650.
- [27] M. Kaledin, A. Brown, A. L. Kaledin and J. M. Bowman. “Normal Mode Analysis Using the Driven Molecular Dynamics Method. II. An Application to Biological Macromolecules”. In: “*J. Chem. Phys.*” 121.12 (2004), pp. 5646–5653.
- [28] M. Kaledin, A. L. Kaledin and J. M. Bowman. “Vibrational Analysis of the H_5O_2^+ Infrared Spectrum Using Molecular and Driven Molecular Dynamics”. In: “*J. Phys. Chem. A*” 110.9 (2006), pp. 2933–2939.
- [29] N. Heine and K. R. Asmis. “Cryogenic Ion Trap Vibrational Spectroscopy of Hydrogen-Bonded Clusters Relevant to Atmospheric Chemistry”. In: “*International Reviews in Physical Chemistry*” 34.1 (2015), pp. 1–34.

- [30] M. Brümmer, C. Kaposta, G. Santambrogio and K. R. Asmis. “Formation and Photodepletion of Cluster Ion-Messenger Atom Complexes in a Cold Ion Trap: Infrared Spectroscopy of VO^+ , VO_2^+ , and VO_3^+ ”. In: “The Journal of Chemical Physics” 119.24 (2003), pp. 12700–12703.
- [31] D. J. Goebbert, G. Meijer and K. R. Asmis. “10 K Ring Electrode Trap Tandem Mass Spectrometer for Infrared Spectroscopy of Mass Selected Ions”. In: “AIP Conf. Proc.” 1104.1 (2009), pp. 22–29.
- [32] W. Schöllkopf, S. Gewinner, H. Junkes, A. Paarmann, G. von Helden, H. Bluem and A. M. M. Todd. “The New IR and THz FEL Facility at the Fritz Haber Institute in Berlin”. In: “Proc. SPIE” 9512 (2015), p. 95121L.
- [33] W. R. Bosenberg and D. R. Guyer. “Broadly Tunable, Single-Frequency Optical Parametric Frequency-Conversion System”. In: “J. Opt. Soc. Am. B” 10.9 (1993), pp. 1716–1722.
- [34] N. Heine and K. R. Asmis. “Cryogenic Ion Trap Vibrational Spectroscopy of Hydrogen-Bonded Clusters Relevant to Atmospheric Chemistry (International Reviews in Physical Chemistry, 2015, Vol. 34, No. 1, 1–34)”. In: “International Reviews in Physical Chemistry” 35.3 (2016), pp. 507–507.

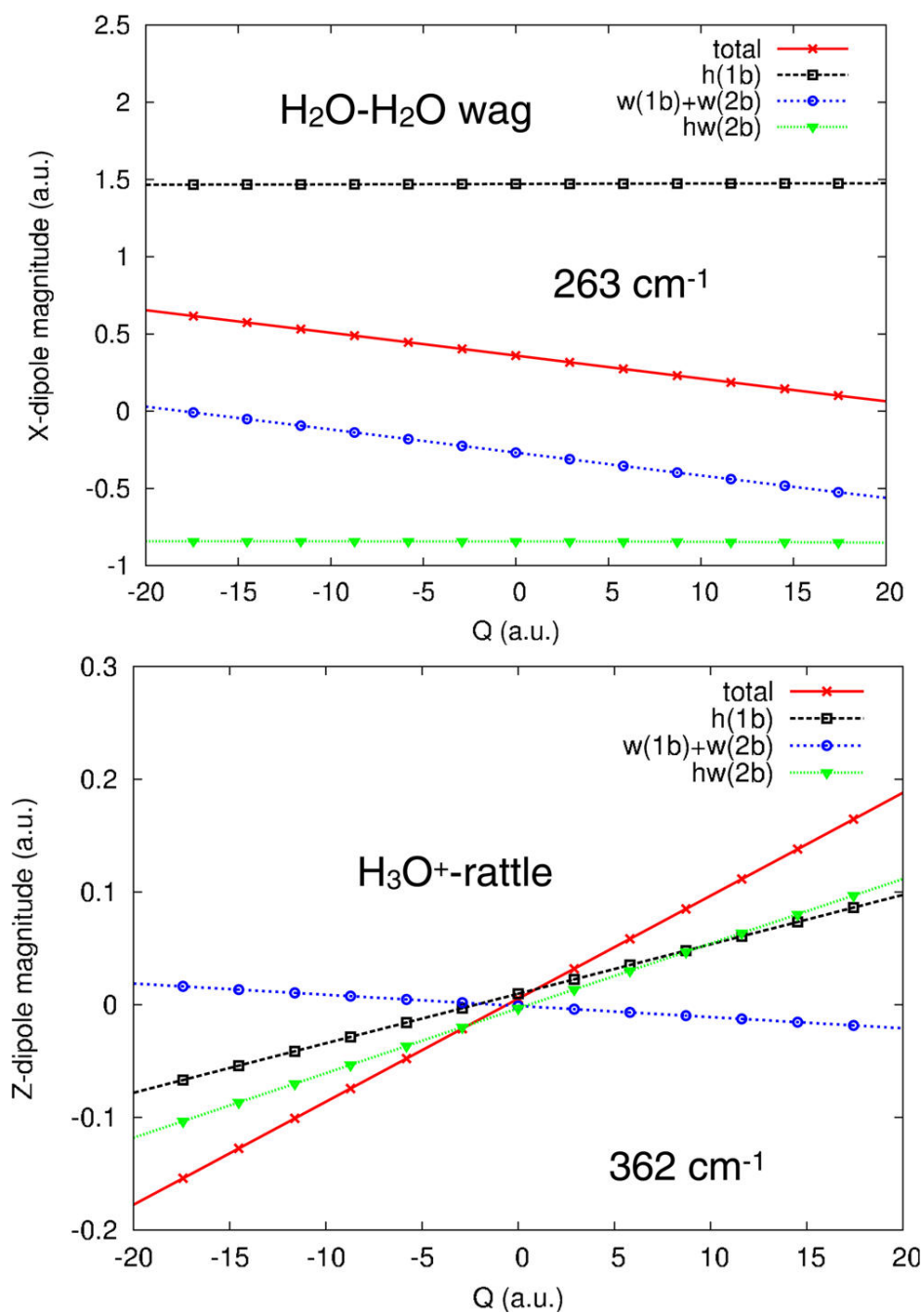


Fig. A.4: Normal mode dependence of the major component of the dipole moment for bands a_{15} and a_{14} of 3E. See text for details.

Table A.3: MP2/aVDZ Harmonic Frequencies (cm^{-1}) for $H_7O_3^+$ and $H_7O_3^+ \cdot D_2$.

$H_7O_3^+$	$H_7O_3^+ \cdot D_2$
	54
76	64
83	74
	78
128	103
	122
240	213
254	248
	278
352	347
369	360
403	378
404	402
485	435
615	583
	646
1077	1067
1265	1240
1605	1622
1633	1634
1699	1697
1702	1719
2464	2557
2620	2696
	3143
3789	3700
3790	3789
3812	3791
3897	3896
3897	3899

Table A.4: MP2/aVDZ Harmonic Frequencies (cm^{-1}) for $H_9O_4^+$ and $H_9O_4^+ \cdot D_2$.

$H_9O_4^+$	$H_9O_4^+ \cdot D_2$
	24
	37
63	61
63	63
70	70
114	76
114	114
125	121
	165
259	197
281	262
	280
281	281
285	288
344	341
344	349
378	376
378	389
419	413
	464
725	729
972	965
972	982
1202	1208
1623	1623
1623	1624
1638	1639
1709	1709
1709	1711
2938	2883
2938	2960
3010	3016
	3130
3782	3756
3782	3783
3783	3783
3901	3884
3901	3901

Table A.5: Evolution of the Band Positions (in cm^{-1}) of the IR-Active Hydrogen-Bond Stretching Vibrations Associated with the H_3O^+ Core in the Experimental IR Spectra of Protonated Water Clusters $\text{H}^+(\text{H}_2\text{O})_n$ with Cluster Size n up to the Condensed Phase Limit

n	experiment
3	344
4	316
5 ^a	405/298
6 ^b	373/279
21 ^c	341
∞ ^d	340

^a Ref [10]. ^b Ref [8]. ^c Ref [9]. ^d Ref [7].

Appendix B

Influence of Argon and D₂ Tagging on the Hydrogen Bond Network in Cs⁺(H₂O)₃; Kinetic Trapping Below 40 K *

B.1 Introduction

Strong intermolecular (ion-neutral) interactions play key roles in impacting solution,[1, 2] atmospheric,[3, 4] and biological chemistry,[5–8] by adjusting the orientation of precursors, the acceleration of reaction rates, and the configuration of macromolecules, respectively. These chemical processes occur at or near room temperature (\sim 250–310 K), where slight changes can alter the balance between competing forces such as ion-molecule and hydrogen bond interactions. At lower temperatures, two additional factors can play a role. The first is the competition between enthalpic and entropic effects,[9–14] with the former more dominant as temperatures reach cryogenic regimes (10–80 K). The second is kinetic trapping,[15–19] when the energy barriers are large compared to thermal energies, preventing the system of interest from reaching its ground (lowest energy) state.[20] Such effects have even been observed for weakly bound neutral species.[21, 22] Understanding these effects involves a combination of experimental and theoretical approaches. From an experimental perspective, the vibrational spectroscopy of cluster ions has been particularly useful, as molecular vibrations, both intramolecular and intermolecular, are particularly sensitive to intermolecular interactions and conformer structure.[23–25] By utilizing the charged nature of the clusters, mass-spectrometric methods enable these systems to be studied as a function of ion-type, neutral binding partner(s), and cluster size/composition.[26, 27] The addition of weakly-bound neutral “messenger” species, such as He, Ne, Ar, H₂

*Chapter based on: Tim K. Esser, Harald Knorke, Daria Ruth Galimberti, Flavio Siro-Brigiano, Knut R. Asmis, Marie-Pierre Gaigeot, and James M. Lisy. “Influence of argon and D₂ tagging on the hydrogen bond network in Cs⁺(H₂O)₃; Kinetic trapping below 40 K”. In: “Phys. Chem. Chem. Phys.” (2018), pp. 28476–28486.

and D₂, facilitates single photon IRPD in the linear spectroscopy regime, typically with minor perturbation to the cluster ion of interest.[27–33] Computation studies, using traditional electronic structure calculations (ab initio and density functional) providing structures and scaled infrared frequencies,[34–36] or Born-Oppenheimer Molecular Dynamics (BOMD) that directly give anharmonic vibrational frequencies and intensities,[37] are often used to compare with the experimental observations. The experimental and theoretical data are essentially independent of one another and have been combined synergistically in collaborative studies by a large number of research groups.[4, 11, 38–47]

The competition between enthalpic- and entropic-favored structures of cluster ions has been carefully examined by recent IRPD studies using temperature-controlled ion traps. Two examples involve the partial breaking of hydrogen bonds, NO₃[−](H₂O) and I[−](H₂O)₂. [11, 39] As NO₃[−](H₂O) was heated from 50 to 350 K, the entropically-favored structure with a single hydrogen bond could be observed at temperatures above 200 K. Only the enthalpically-favored structure with bidentate hydrogen bonding was seen spectroscopically below this temperature. With I[−](H₂O)₂, the water-water hydrogen bond began to break at temperatures above 70 K, and the dissociation energy was determined to be (4.6 ± 0.4) kJ mol^{−1}, approximately 1/3 of the gas-phase dissociation energy of the water dimer.[11]

Mapping out the potential energy landscape for hydrogen-bonded clusters is particularly challenging as the relative differences in conformer energies, and barrier heights can be small, on the order of a few kJ mol^{−1}. These energies are close to the limit of predictive reliability of computational methods. In a previous study of Li⁺(H₂O)[4, 16] it was observed that the presence of one argon atom messenger led to two distinct conformers with different hydrogen-bonded configurations. Neither of these represented the lowest energy configuration, where the four waters are configured in a tetrahedral arrangement about the lithium ion with no water-water hydrogen bonds. Subsequent BOMD simulations of the cluster ion formation at ~75 K revealed the barrier to breaking pre-existing hydrogen bonds was greater than the thermal energy.[48] This resulted in kinetic trapping of the higher energy conformers, a process that did not occur at higher temperatures ~300-400 K. The height of the barriers to rearrangement was due to the strong electrostatic influence of the lithium ion. Its significant ability to polarize the water molecule and strengthen the hydrogen bonds between water molecules in the first and second hydration layers was the determining factor at these temperatures.

There has been a long-standing concern over the role that messengers can play in influencing the structure of hydrated cations. This has been a major issue in protonated water[27] and methanol[49] cluster ions. From the earliest use of messengers in H₇O₃⁺ and H₉O₄⁺,[28] there was the potential that even the attachment of H₂ was sufficient to perturb the system. This has been verified by studies from the Johnson group.[11, 29] For protonated methanol, the binding energy of various messengers has been exploited to influence the effective temperature of the cluster ions.[49] This has been used to influence the balance between enthalpically- and entropically-favored structures. In both of these protonated systems, the mobility of the excess proton and the variety of

chain and ring structures are particularly susceptible to the presence of a messenger, with differences even noted between Ar, Ne, H₂ and He.[49–51] Differences between argon-tagged protonated and deuterated systems have been observed as well, with the argon preferentially binding to the OD group in Ar–H₄DO₂⁺.^[4]

While it has generally been assumed that H₂ or D₂ tagging has a minimal effect on the structure of cluster ions, there have been some subtle effects noted in earlier studies. In protonated glycine, both He and H₂ tags bind at the protonation site, but there is evidence that with three H₂ molecules, at least one H₂ molecule binds to the uncharged carboxylic acid.[52] In this study, argon and D₂ tagging to Cs⁺(H₂O)₃ is reported, where two structures with different hydrogen-bond networks are present for both tagging species. Amazingly, each tag has its own preferred hydrogen-bond network; argon-tagging is associated with the most stable conformer with two hydrogen bonds, while D₂-tagging favors a higher-energy conformer with a single, weaker hydrogen bond. The relative population of these two conformers can be changed over a temperature range of 12 to 21 K. In the case of argon, the higher energy conformer is only observable at temperatures less than 40 K. The role that D₂ plays as both buffer gas and tag is largely responsible for the formation of this higher energy conformer. Metadynamics analysis provides a solid interpretation for this effect, consistent with the experimental observations.

B.2 Experimental Details

Infrared photodissociation (IRPD) experiments were carried out using the Leipzig 6 K ring-electrode ion trap triple mass spectrometer.[53] Neutral (H₂O)_nAr_m clusters were produced using a pulsed Amsterdam piezo valve (MassSpecpecD BV)[54] by expanding a water vapor/argon mixture at 3 bar through a 200 μm nozzle at 700 Hz. Cs⁺(H₂O)_nAr_m ions were formed by evaporative cooling after collisions with cesium cations, produced ~3 cm downstream from the nozzle by an axial molecular beam ionizer (Extrel CMS), which is schematically shown in Fig. B.1. The two main components are the filament and cylindrical grid, indicated by spirals and dashed lines in the figure. The filament was coated with a CsCl-containing molecular sieve paste and thermionically emitted cesium cations when heated. The latter were directed towards the neutral beam by a potential difference between the filament and grid, held at +18.7 V and +14.4 V respectively. When a similar ion source was used at Illinois,[55] Cs⁺(H₂O)_nAr_m ions were extracted from the ionization region perpendicular to the neutral cluster beam, while they were extracted along the axis of the molecular beam in Leipzig, as shown in Fig. B.1. The ion cluster beam was collimated in two He-filled RF octupole ion guides where collisions with the buffer gas reduced the ion beam kinetic energy. The cluster ions were not thermalized to room temperature by these collisions as Cs⁺(H₂O)_n cluster ions with multiple argon atoms were detected upon exiting the ion guides. Ions of interest were mass-selected in a quadrupole mass-filter, deflected by 90°, and focused into an RF ring-electrode ion-trap. To allow for continuous ion

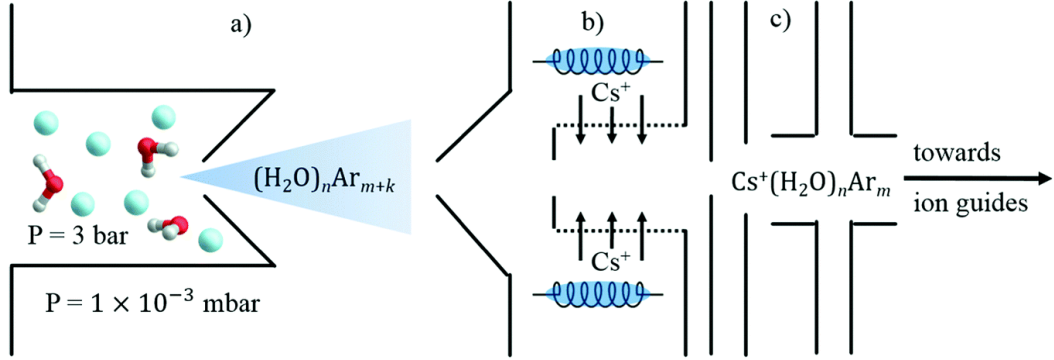


Fig. B.1: (a) Neutral $(\text{H}_2\text{O})_n\text{Ar}_m$ clusters were produced using a pulsed piezo valve by expanding a water vapor/argon mixture at 3 bar through a 200 μm nozzle at 700 Hz. (b) Thermionically-emitted cesium ions, provided by an axial molecular beam ionizer (Extrel CMS) with a CsCl containing molecular sieve paste coated filament held at +18.7 V, collided with the neutral species ~ 3 cm downstream from the nozzle, forming (evaporatively cooled) $\text{Cs}^+(\text{H}_2\text{O})_n\text{Ar}_m$ ions. (c) The ions are then extracted from the formation region using a stack of DC lenses.

loading and thermalization close to the ion trap temperature, the trap was continuously filled with He or D₂ gas. The latter was used to form $\text{Cs}^+(\text{H}_2\text{O})_n(\text{D}_2)_z$ complexes by three-body collisions in the ion trap.[30] Note, under such experimental conditions some ions will not be fully thermalized. However, these “hot” ions will also not tag efficiently and hence their effect on the IRPD measurements is small and negligible, for the present purpose.

Every 100 ms, all ions are extracted and focused both temporally and spatially into the center of the extraction region of an orthogonally mounted reflectron TOF tandem photofragmentation mass spectrometer. The reflectron was used to select complexes with single D₂ molecules. Thereafter, the ion packet is irradiated with the tunable infrared radiation in the spectral range from 1500 to 3900 cm^{-1} supplied by an optical parametric oscillator/amplifier (LaserVision) laser system[56] operated at 10 Hz with a bandwidth of $\sim 3 \text{ cm}^{-1}$ and a pulse energy of 1-10 mJ, adequately attenuated to avoid saturation.

All parent and photofragment ions are then accelerated toward an MCP detector. An IRPD spectrum is measured by continuously scanning the laser wavelength, which is monitored online using a HighFinesse WS6-600 wavelength meter, with a scan speed such that an averaged TOF mass spectrum (over 100 laser shots) is obtained every 2 cm^{-1} . Typically, at least two scans are measured and averaged and the photodissociation cross section, σ_{IRPD} , was determined as described previously.[53, 57]

Table B.1: Ranking of electronic and zero-point energy (ZPE) corrected energies for $\text{Cs}^+(\text{H}_2\text{O})_3$ I-IV clusters. Energies are in kJ mol^{-1} . Structures are presented in Fig. B.2. Conformer I is the lowest in energy and its energy is set to zero; conformer II-IV energies are given with respect to this reference (ΔE , ΔE^{ZPE}). MP2 versus B3LYP-D3 electronic representations, geometry optimizations using the aug-cc-pVDZ Gaussian basis set. CCSD(T) calculations (basis set aug-cc-pVDZ for O, H, D and Ar atoms, Los Alamos double zeta for the Cs) are single points on the MP2 optimized structures, the ZPE is the one obtained at the MP2 level of representation.

	MP2	B3LYP-D3	CCSD(T)//MP2	MP2 ZPE corrected	B3LYP-D3 ZPE corrected	CCSD(T)//MP2 ZPE corrected
I	0.00	0.00	0.00	0.00	0.00	0.00
II	-3.77	-0.75	-4.2	5.52	2.13	4.7
III	26.02	17.53	25.3	13.10	7.15	12.5
IV	13.89	13.26	13.1	9.25	7.87	8.5

B.3 Computational details *

Untagged and Ar-/D₂-tagged structures of $\text{Cs}^+(\text{H}_2\text{O})_3$ clusters have been optimized at the MP2 and DFT-B3LYP-D3BJ levels of electronic representation, with the Gaussian09 package.[58] In the following, only the DFT calculations will be used. Tab. B.1 is reporting rankings in energies. Optimized geometries are reported in Fig. B.2, for untagged and Ar/D₂-tagged $\text{Cs}^+(\text{H}_2\text{O})_3$ clusters.

The labeling is with a Roman numeral-number coding I to IV for untagged (by increasing order of energy), the additional number is for tagged clusters, e.g. I-2, III-1, etc. The reference of energy is the I-conformer for untagged clusters, and it is the I-1 conformer for tagged clusters. For the four untagged clusters, rankings in electronic energies, in the vibrational zero-point energy (ZPE), and in free energies calculated at 20 K, i.e. E , E^{ZPE} , and $\Delta G_{20\text{K}}$, respectively are reported in Fig. B.1. Tab. B.1 also reports these values for the untagged clusters, with a comparison and validation to MP2 and CCSD(T) calculations.

The ‘OP’ sign in Fig. B.2 refers to the position of the Ar/D₂ tag being located out-of-the plane formed by the oxygen atoms of the water molecules. The reliability of the B3LYP-D3 electronic representation has been tested on MP2 and CCSD(T) calculations, with a good agreement in terms of geometries, energy ranking and binding energies. All calculations are performed with the Los Alamos double-zeta basis set[59] with an effective core potential for Cs, and the correlated all-electron basis set aug-cc-PVDZ[60] for all other atoms. Harmonic frequencies have been systematically calculated in order to check for minima on the potential energy surface, and are further

*Calculations have been performed by Daria Ruth Galimberti and Flavio Siro-Brigiano in the group headed by Marie-Pierre Gageot at the University of Evry, France.

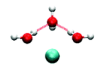
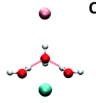
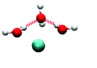
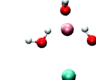
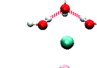
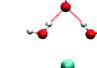
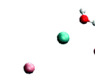

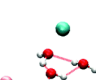
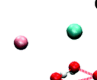
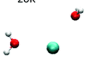
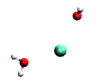
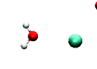
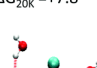
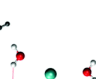
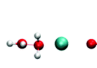
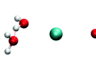
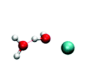
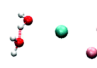
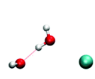
	Untagged	Tagged					
		1	2	3	4	5	6
I	$\Delta G_{20K}=0.0$  $\Delta E^{ZPE}=0.0$ $\Delta E=0.0$	 OP Ar: 0.0 D ₂ : 0.0	 Ar: +0.7 D ₂ : +1.3	 OP Ar: -1.3 D ₂ : +0.4	 Ar: +0.8 D ₂ : +0.6	 Ar: 0.0 D ₂ : -	 OP Ar: +0.8 D ₂ : +0.8
II	$\Delta G_{20K}=+2.2$  $\Delta E^{ZPE}=+2.1$ $\Delta E=-0.8$	 OP Ar: +2.5 D ₂ : +2.8			 OP Ar: +1.3 D ₂ : +3.2		
III	$\Delta G_{20K}=+6.8$  $\Delta E^{ZPE}=+7.2$ $\Delta E=+17.5$	 OP Ar: +5.8 D ₂ : +9.2	 OP Ar: +5.8 D ₂ : +8.4				
IV	$\Delta G_{20K}=+7.8$  $\Delta E^{ZPE}=+7.9$ $\Delta E=+13.2$	 OP Ar: +8.9 D ₂ : +9.1	 OP Ar: +8.7 D ₂ : +8.3	 OP Ar: +8.74 D ₂ : +9.2	 OP Ar: +6.2 D ₂ : +8.4	 Ar: +7.2 D ₂ : -	 Ar: - D ₂ : +9.0

Fig. B.2: Optimized structures of untagged Cs⁺(H₂O)₃ and Ar/D₂ tagged Cs⁺(H₂O)₃ clusters from B3LYP-D3/aug-cc-pVDZ electronic representation. Energies are given in units of kJmol⁻¹. Untagged structures: the zero of energy is taken for the I conformer. Tagged clusters: the zero of energy is taken for the I-1 conformer. ‘OP’ refers to the tag atom/molecule located out-of-the plane formed by the oxygen atoms of the water molecules. Cs⁺ is represented in blue, Ar is in pink, D₂ is in light grey. H-bonds are represented by red dashed lines. Relative energy rankings: E stands for electronic energy, E^{ZPE} accounts for ZPE corrections, ΔG_{20K} free energy calculated at 20 K. Tagged structures are presented with the Ar-tag for I-III conformers, and presented with the D₂-tag for the IV-conformer (at the exception of structure IV-5 that can be optimized only with Ar). Whenever ‘-’ is written, the associated conformer does not exist (i.e. IV-5 exists only for Ar-tagged, IV-6 exists only for D₂-tagged).

used for harmonic vibrational spectra in order to interpret and assign the experimental IRPD spectra. To that end, harmonic frequencies are scaled by a 0.9686 factor,[61] very close to the 0.97 scaling factor used in previous work by the Lisy group[9] and found by the systematic alignment of the O–H stretching band position between calculation and experiment for the Cs⁺(H₂O)₂ cluster.[62]

To estimate the role of entropy on the relative stability of the conformers at finite temperatures, free energy profiles have been calculated for the untagged I-IV inter-conversion and for the III cluster stability at three temperatures (10 K, 20 K, 50 K).

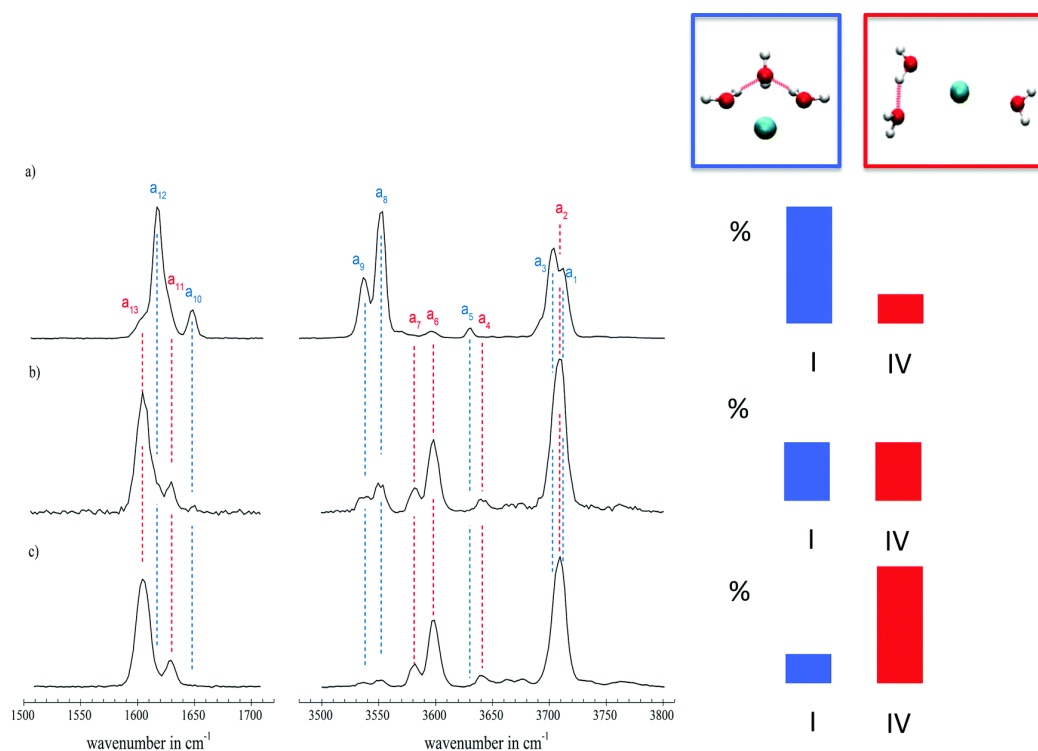


Fig. B.3: IRPD spectra of (a) $\text{Cs}^+(\text{H}_2\text{O})_3\text{Ar}$ at nominal ion trap temperature of 7 K, (b) $\text{Cs}^+(\text{H}_2\text{O})_3\text{D}_2$ where $\text{Cs}^+(\text{H}_2\text{O})_3\text{Ar}$ was mass selected in the quadrupole mass filter and Ar was replaced by D_2 in the ion trap at 12 K and (c) $\text{Cs}^+(\text{H}_2\text{O})_3\text{D}_2$ where $\text{Cs}^+(\text{H}_2\text{O})_3$ was mass selected and the complex was formed at 12 K. Assignment of the conformers (I & IV) responsible for the IRPD features on the left side: the red and blue bars illustrate an estimate of the relative contribution of the two isomers to the spectra. See main text for all details.

This is done through biased metadynamics DFT-BLYP-D3 based molecular dynamics simulations using the CP2K code.[37, 63] Metadynamics are performed with a time step of 0.4 fs, the bias has been chosen along the O–O distance between the oxygens of the two H-bonded water molecules.

B.4 Results

The IRPD spectra were recorded in both the OH stretching region, from 3500 to 3800 cm^{-1} , and the H_2O bending region, from 1500 to 1700 cm^{-1} . These are presented in Fig. B.3, with trap temperatures of 7 K for $\text{Cs}^+(\text{H}_2\text{O})_3\text{Ar}$, and 12 K for $\text{Cs}^+(\text{H}_2\text{O})_3\text{D}_2$, the latter spectra were obtained under two different cluster ion preparation methods.

The individual spectral features are labeled a_1 to a_{13} . Assignments of these features (as discussed below) are given in Tab. B.2. The temperature dependence for both tagged species were also obtained over a range of 7 to 40 K for $\text{Cs}^+(\text{H}_2\text{O})_3\text{Ar}$, and 12 to 21 K for $\text{Cs}^+(\text{H}_2\text{O})_3\text{D}_2$, as shown in Fig. B.4. The temperature range for D_2 is

Table B.2: Experimental IRPD band positions (in cm⁻¹), computed vibrational frequencies (in cm⁻¹) and assignments for bands of Cs⁺(H₂O)₃Ar and Cs⁺(H₂O)₃D₂. The calculated frequencies are scaled by the factor 0.9686.

Label	IRPD ^a	Theory	Assignment
a1	3712	3748	Free OH stretch I-conformer
a2	3709	3753	Free OH stretch IV-conformer
a3	3703	3740	Free OH stretch I-conformer
a4	3641	3668	Symmetric H ₂ O OH stretch IV-conformer
a5	3630	3653	Symmetric H ₂ O OH stretch I-conformer
a6	3598	3572	H-bonded OH stretch IV-conformer
a7	3581	-	H-bonded OH stretch IV-conformer
a8	3552	3550	H-bonded OH stretch I-conformer
a9	3538	3525	H-bonded OH stretch I-conformer
a10	1648	1616	H ₂ O bend I-conformer
a11	1630	1592	H ₂ O bend IV-conformer
a12	1617	1575	H ₂ O bend I-conformer
a13	1604	1561	H ₂ O bend IV-conformer

^a Band position are given with an error of 5 cm⁻¹.

reduced, as at temperatures below 12 K D₂ condenses on the ion trap, and the weak binding of D₂ to Cs⁺(H₂O)₃ leads to loss of the D₂ tag at temperatures above 25 K.

H₂O bending region. Calculations revealed that the addition of either argon or D₂ to the Cs⁺(H₂O)₃ conformers I-IV has a negligible impact on the water bending vibrational frequency. As a result the bending frequencies of the untagged conformers were used for comparison with the experimental data and to make structural assignments for Cs⁺(H₂O)₃Ar, and Cs⁺(H₂O)₃D₂, verified further in the O–H stretching region.

When formed with argon as Cs⁺(H₂O)₃Ar₁, there is a dyad with peaks at 1617 and 1648 cm⁻¹ (*a*₁₂ and *a*₁₀, in Fig. B.3a) with apparent shoulders on either side of the 1617 cm⁻¹ peak that fade with increasing trap temperature (from 7 to 40 K). This dyad is consistent with the computed spectrum of the lower energy conformer I, with a calculated splitting of 32 cm⁻¹, nearly identical to the observed splitting of 31 cm⁻¹, as shown in Fig. B.5. The computed harmonic frequencies are however lower than the experimental values by ~35 cm⁻¹.

When formed as Cs⁺(H₂O)₃ and trapped at 12 K with D₂ as Cs⁺(H₂O)₃D₂, there is a dyad with peaks at 1604 and 1630 cm⁻¹ (*a*₁₃ and *a*₁₁ in Fig. B.3c). These bands match closely to the shoulders observed on either side of the 1617 cm⁻¹ band of Cs⁺(H₂O)₃Ar₁. This new dyad, with an observed splitting of 24 cm⁻¹, is shifted to lower frequency (~13 cm⁻¹ for the low frequency component of each dyad) relative to that observed for Cs⁺(H₂O)₃Ar₁. Of the three other conformers, only conformer IV has a dyad with a shift to lower frequency (14 cm⁻¹), and a splitting (29 cm⁻¹) that is consistent with experiment (Fig. B.5).

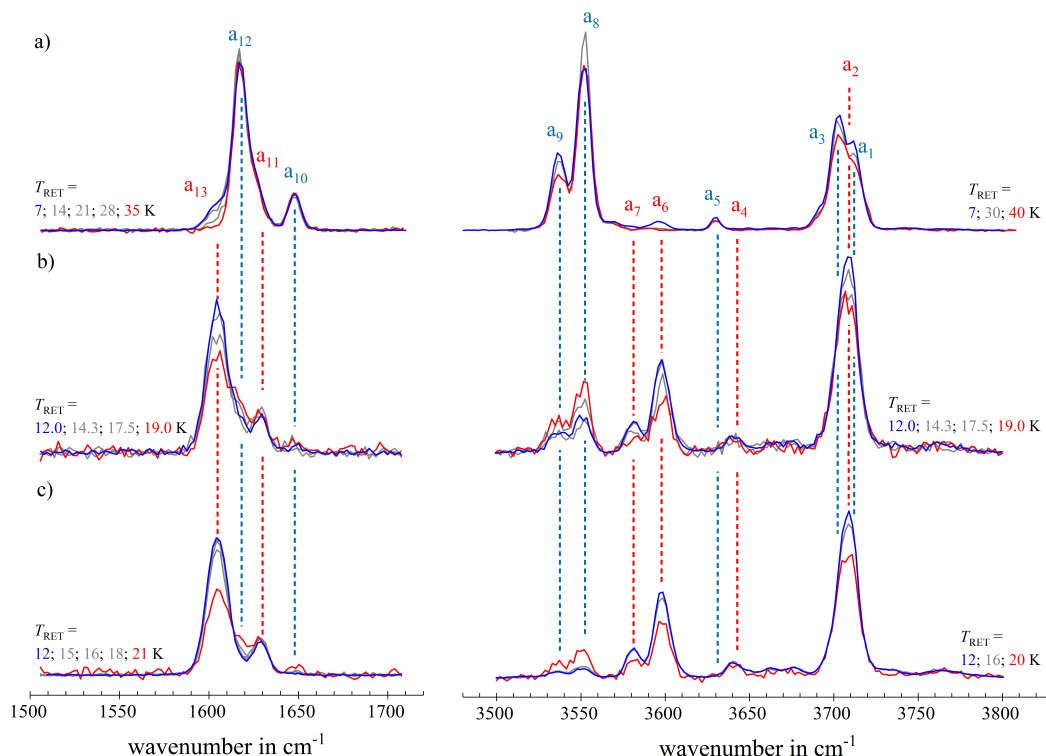


Fig. B.4: Temperature dependence of the IRPD spectra of a) $\text{Cs}^+(\text{H}_2\text{O})_3\text{Ar}$, b) $\text{Cs}^+(\text{H}_2\text{O})_3\text{D}_2$ where $\text{Cs}^+(\text{H}_2\text{O})_3\text{Ar}$ was mass selected in the quadrupole mass filter and Ar was replaced by D_2 in the ion trap, and c) $\text{Cs}^+(\text{H}_2\text{O})_3\text{D}_2$ where $\text{Cs}^+(\text{H}_2\text{O})_3$ was mass selected and the complex was formed in the ion trap. Nominal ion trap temperatures are indicated in the figure.

A second method of forming $\text{Cs}^+(\text{H}_2\text{O})_3\text{D}_2$ was also examined (Fig. B.3b). Here $\text{Cs}^+(\text{H}_2\text{O})_3\text{Ar}$ is selected from the source and trapped at 12 K with D_2 . Following collisional loss of Ar in the trap, $\text{Cs}^+(\text{H}_2\text{O})_3$ is tagged with D_2 , and spectroscopy is performed on $\text{Cs}^+(\text{H}_2\text{O})_3\text{D}_2$. Under these conditions, the 1604 and 1630 cm^{-1} bands are dominant, but some signal is also observed at 1648 cm^{-1} (a_{10}). This suggests that both I and IV conformers may be present under these conditions. Although the presence of conformers II and III cannot be entirely ruled out (Fig. B.5a), as the single OH bending IR band calculated for these conformers systematically overlaps with one of the dyads of conformers I or IV, the more direct assignment of the two experimental dyads is through conformers I and IV.

OH stretching region. When formed with argon as $\text{Cs}^+(\text{H}_2\text{O})_3\text{Ar}$, the spectrum recorded in Leipzig is similar to that reported in previous work from Illinois[9, 64] as shown in Fig. B.6. The assignment of the dominant bands follows from the previous work. The 3538 (a_9) and 3552 (a_8) cm^{-1} bands correspond to hydrogen-bonded OH stretches, from the symmetric and antisymmetric combinations respectively, of the two

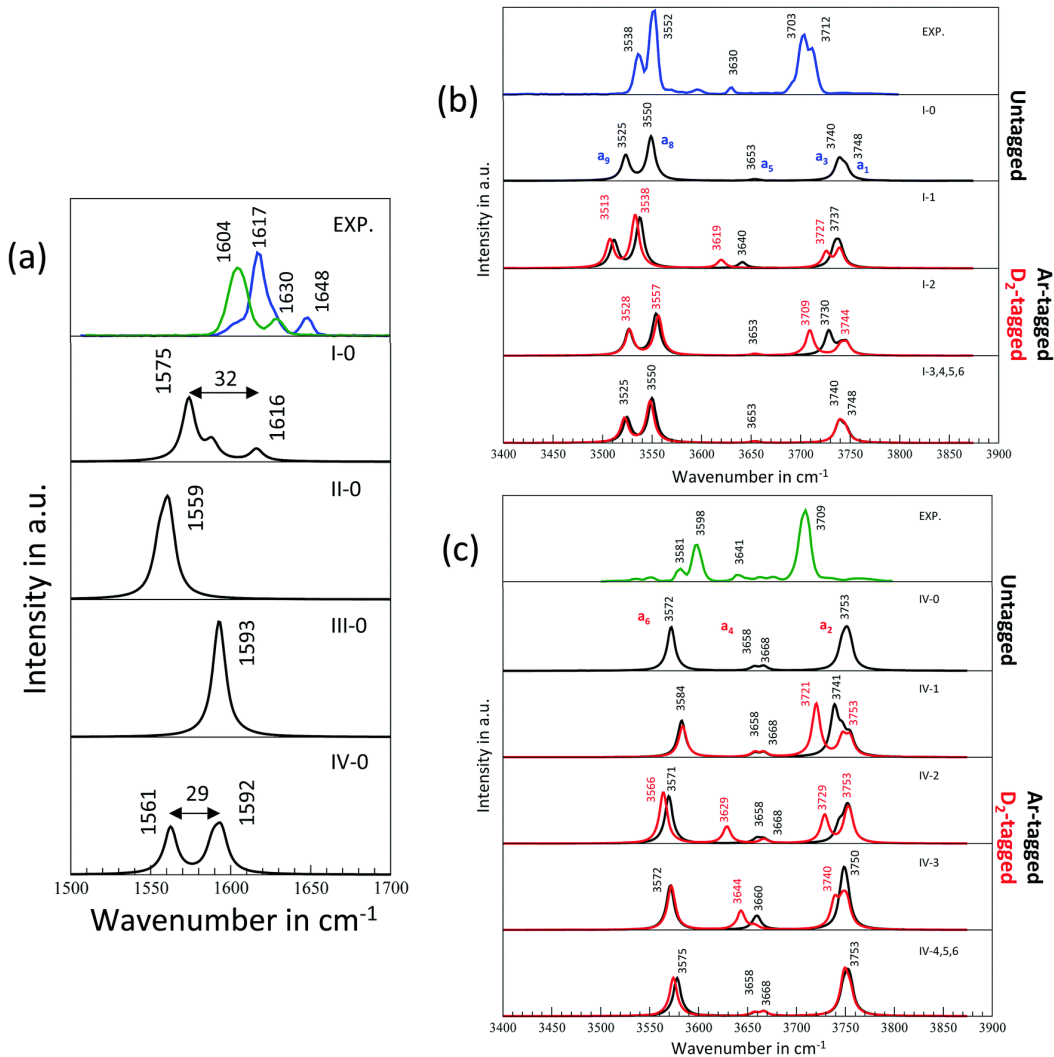


Fig. B.5: (a) Calculated harmonic vibrational spectra for untagged conformers I-IV in the H₂O bending region. Note that only conformers I and IV have a doublet structure, with the IV-conformer shifted 14 cm⁻¹ to lower frequency. (b) Calculated harmonic spectra in the O-H stretching region of the I-conformer, both untagged and tagged, and (c) of the IV-conformer, both untagged and tagged. Scaled frequencies (0.9686). The labels ‘a_n’ refer to the same band labeling as in the IRPD experiments; see Fig. B.3.

equivalent hydrogen-bonded OH groups in conformer I. A small peak at 3630 cm⁻¹ (a₅) has been assigned to the symmetric stretch of the second shell water of the I-conformer and the doublet at 3703 and 3712 cm⁻¹ (a₃, a₁) to the remaining free OH stretching modes. These five features are consistent with the calculated spectral features for the I-conformer, as seen in Fig. B.5b, and assigned as such in Tab. B.2 in accord with previous investigations.[9, 65] A weaker band at 3598 cm⁻¹ (a₆) is also present and will be discussed later.

Attempts to more precisely specify the position of the argon atom should be viewed

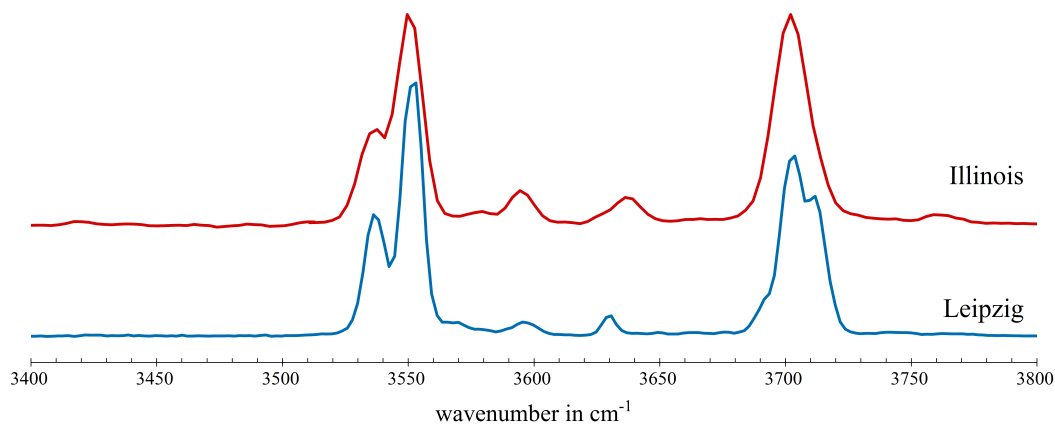


Fig. B.6: Spectra of $\text{Cs}^+(\text{H}_2\text{O})_3\text{Ar}$ recorded at Illinois[12] and at Leipzig both formed by evaporative loss of argon, with the latter additionally cooled to 7 K by collisions with He in a ring electrode trap.

with caution. It is clear that there are only small energy differences between the six conformers, I-1 to I-6, as given in Fig. B.2, and minor variations of the OH stretching frequencies in the computed spectra as shown in Fig. B.5b. However, the lack of a large splitting in the free OH stretching region suggests that conformer I-2 is not present. Of the other five conformers, I-1 is the only one that shows a small, but noticeable shift for the symmetric OH stretch (a_5) of about 10 cm^{-1} to lower frequency. This conformer is the only one where the argon interacts directly with the second shell water molecule. Conformers I-4 to I-6, where the Ar interacts with the cation, and conformer I-3 where the out-of-plane Ar interacts with the three water molecules also have the free O–H and H-bonded stretches that match the a_3 - a_1 and a_9 - a_8 experimental bands and could be present as well.

When formed as $\text{Cs}^+(\text{H}_2\text{O})_3$ and trapped at 12 K with D_2 as $\text{Cs}^+(\text{H}_2\text{O})_3\text{D}_2$, the 3538 and 3552 cm^{-1} a_9 - a_8 bands, associated with the I-conformer are barely observed, while the a_7 - a_6 bands at 3581 and 3598 cm^{-1} are dominant (Fig. B.3c). A small peak at 3641 cm^{-1} (a_4) and single free O–H peak at 3709 cm^{-1} (a_2) are present. The free OH stretch is narrower than in the argon case.

It is clear that the dominant structure for the D_2 -tagged species has a weaker hydrogen-bond network than the Ar-tagged species. Among the four conformers identified in the computational study, I, II, and IV possess hydrogen bonds (Fig. B.2), however, only conformer IV has a substantially weaker hydrogen bond, based on the present calculations. The computed spectra associated with the untagged and tagged IV-conformers are shown in Fig. B.5c. Previous computational work on $\text{Cs}^+(\text{H}_2\text{O})_3$ did not suggest that the IV conformer (a single water and a water dimer subunit structure) had all three water molecules interacting with the cesium ion, which would weaken further the water-water hydrogen bond in the dimer subunit.[10, 62, 65] However, the

current computational analysis with a larger basis set indicates that this structure is indeed stable and relatively low-lying in energy with respect to the most stable I conformer ($\sim 8 \text{ kJ mol}^{-1}$, Fig. B.2). A recent study by Paesani and co-workers has not only identified this IV conformer, but has also confirmed the other three structures, I, II and III within $\sim 5 \text{ kJ mol}^{-1}$ of each other (ZPE-corrected).[66]

There is less than 1 kJ mol^{-1} difference in energy between the five D₂-tagged IV-conformers. In addition, it should be noted that the D₂ binding energy is substantially less than that for argon; the D₂-tagged clusters are not observed for trap temperatures above 25 K. It is possible that D₂ may freely “roam” about Cs⁺(H₂O)₃, and with the vibrational spectrum of Cs⁺(H₂O)₃D₂ represented by a combination of conformers.

None of the D₂-tagged IV-conformers have an IR-active doublet similar to the experimental 17 cm^{-1} split a_7 - a_6 dyad, but instead display one single H-bonded stretching band. The calculated frequency for this band is located at 3572 cm^{-1} for the untagged IV-conformer. It shifts to higher or lower frequency depending on the location of the D₂ tag. Once all five conformers are taken into account, a dyad would be expected in this region, with a splitting of 10 to 20 cm^{-1} , as in the a_6 - a_7 dyad. Moving up in frequency, the experimental a_4 band, at 3641 cm^{-1} , assigned to the symmetric O–H stretching of the water, is 11 cm^{-1} higher in frequency than that observed (a_5) for Cs⁺(H₂O)₃Ar. This shift is consistent with the calculated results, with the symmetric stretch for the IV-conformer, 13 cm^{-1} higher in frequency. Of the D₂-tagged IV-conformers, IV-1, IV-4, and IV-6, have symmetric stretches at the same frequency as the untagged IV-conformer. While not ruling out the presence of conformers IV-2 and IV-3, the other binding locations for D₂ may be preferentially populated. Turning to the free OH stretching region, the experimental spectrum has a single feature at 3709 cm^{-1} (a_2), which is narrower than the doublet observed for Cs⁺(H₂O)₃Ar. This suggests that D₂ does not bind directly to an OH group as depicted by conformer IV-1, with a calculated splitting of 22 cm^{-1} . Of the three conformers that are consistent with the experimental a_4 band, conformers IV-4 and IV-6 have single free OH stretches. It is worth noting that both of these conformers have the D₂ binding to Cs⁺, either in the plane of the heavy (oxygen and cesium) atoms or out-of-plane. Only these two D₂-tagged IV conformers have calculated spectra that are consistent with all of the experimental OH stretching bands.

As mentioned earlier, Cs⁺(H₂O)₃Ar has a small band (a_6) at 3598 cm^{-1} . This can now be assigned to the presence of a minor population of the IV-conformer.

Using the second method of forming Cs⁺(H₂O)₃D₂ by selecting Cs⁺(H₂O)₃Ar from the source and trapping at 12 K with D₂, the collisional/exchange process, as can be seen in Fig. B.3, substantially reduces the population of the I-conformer in favor of the IV-conformer. Thus it seems that with the loss of argon, sufficient energy is imparted to nascent Cs⁺(H₂O)₃ to rupture (partially or completely) the hydrogen bond network of the I-conformer. This in turn leads to the formation of the IV-conformer as the nascent Cs⁺(H₂O)₃ is converted to Cs⁺(H₂O)₃D₂, through 3-body collisions with cold D₂. The 3538 and 3552 cm^{-1} a_9 - a_8 bands associated with the I-conformer have $\sim 1/3$ the intensity of the a_7 - a_6 bands at 3581 and 3598 cm^{-1} . The remaining features at

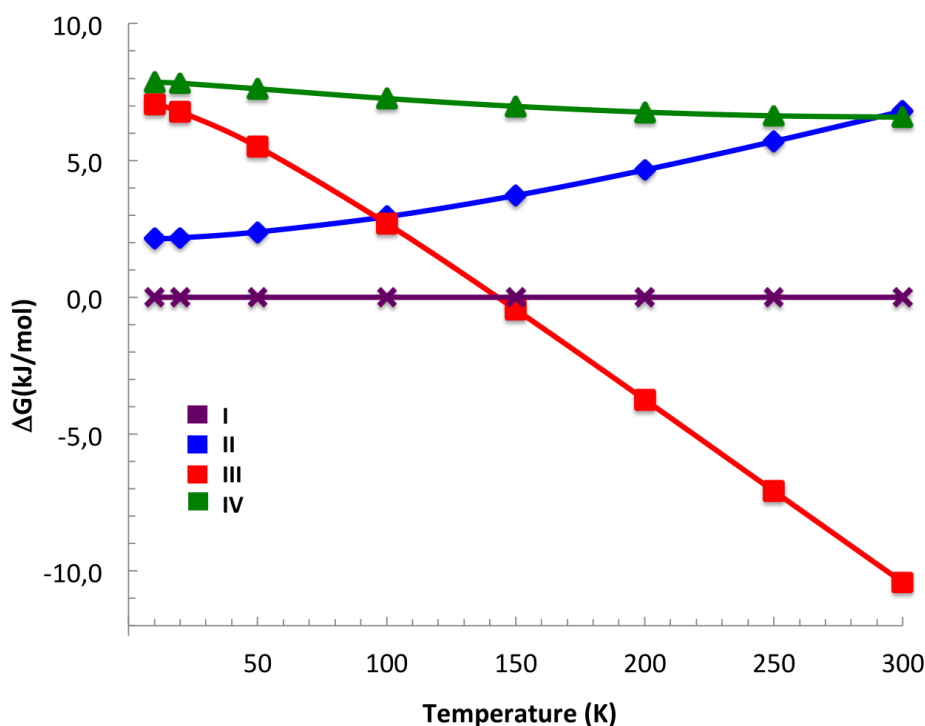


Fig. B.7: Free energy profiles as a function of increasing temperature calculated with the harmonic approximation. The relative free energy stability of the four untagged $\text{Cs}^+(\text{H}_2\text{O})_3$ clusters (labeled I-IV) is hence shown. Comparison of this figure with Fig. B.9, where free energy profiles have been calculated with DFT-MD biased metadynamics provides hints on anharmonic entropic effects.

3641 cm^{-1} and 3709 cm^{-1} reflect the dominance of the IV-conformer. At this point, it is unclear whether the presence of the I-conformer is due to (1) retention of a fraction of the I-conformer population following the loss of argon, (2) reformation of I-conformer from the IV-conformer, or (3) the formation of both conformers from the III-conformer that has no hydrogen bonds. The collisional exchange process of D_2 for argon will be addressed in the discussion below.

Temperature dependence. The 3-body collisional generation of the I- and IV-conformers indicated that a low barrier may exist between the two conformers that enables kinetic trapping of the IV-conformer. As a result, the temperature dependence of the IR spectra of these species were examined over a trap temperature range of 12 to 21 K, for $\text{Cs}^+(\text{H}_2\text{O})_3\text{D}_2$, and 7-40 K, for $\text{Cs}^+(\text{H}_2\text{O})_3\text{Ar}$, with the results shown in Fig. B.7. The dependence on temperature is clearly seen for $\text{Cs}^+(\text{H}_2\text{O})_3\text{D}_2$, but somewhat less apparent for $\text{Cs}^+(\text{H}_2\text{O})_3\text{Ar}$. Difference spectra, generated by subtracting the lowest temperature spectra (7 K for argon, 12 K for D_2) from those taken at higher temperatures, indicate the growth or reduction of individual spectral features. These are presented in Fig. B.8.

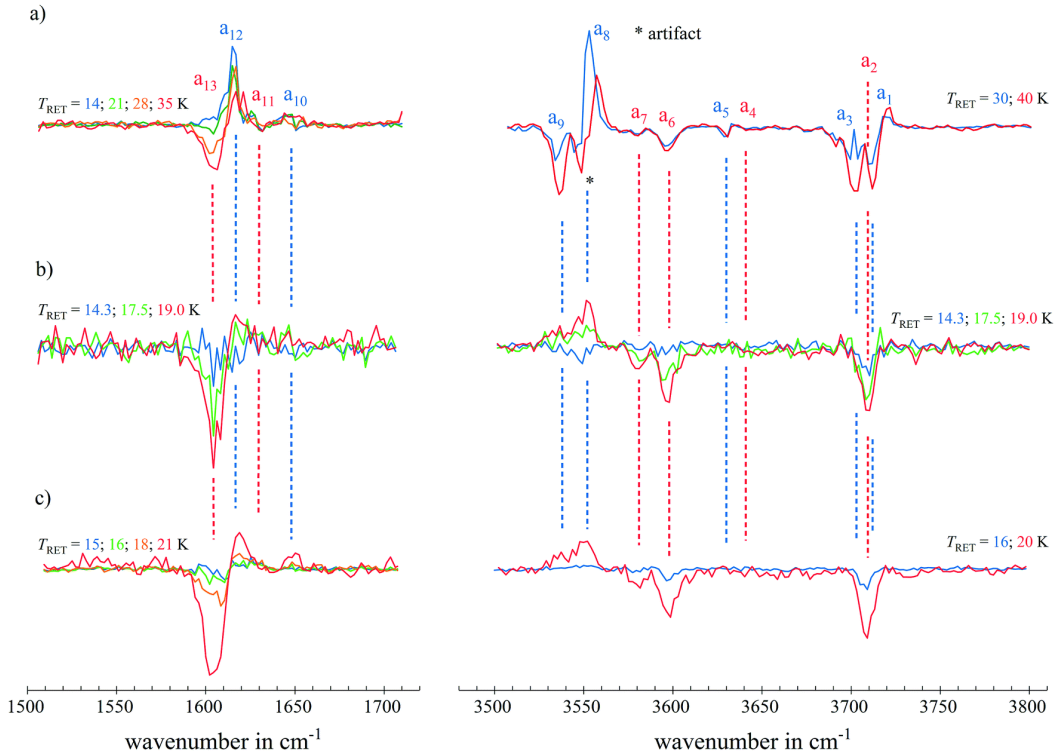


Fig. B.8: Difference IRPD spectra of: (a) Cs⁺(H₂O)₃Ar between 7 K and given temperature; (b) Cs⁺(H₂O)₃D₂ (formed by collisional loss of argon in the trap) between 12 K and given temperature; (c) Cs⁺(H₂O)₃D₂ (formed from Cs⁺(H₂O)₃ and tagged with D₂) between 12 K and given temperature. Negative deviations indicate loss of intensity. Positive deviations indicate gain of intensity. * This feature is due to slightly different peak shapes in the original 7 and 40 K spectra (see Fig. B.4) and does not represent an IR absorption.

As seen in Fig. B.8 and Fig. B.7 for Cs⁺(H₂O)₃D₂, an increase in temperature enables the bands associated with the I-conformer in the H₂O bending region (*a*₁₀ and *a*₁₂) and the OH stretching region (*a*₈ and *a*₉) to gain intensity. Conversely, bands associated with the IV-conformer, *a*₁₃ in the bend, and in the stretch, *a*₆, *a*₇, and *a*₂, lose intensity. Thus, there is strong evidence that increasing the ion-trap temperature by 8 K is sufficient to alter the relative contributions of conformers I and IV to the ensemble of Cs⁺(H₂O)₃D₂ cluster ions. The temperature dependence of the Cs⁺(H₂O)₃Ar spectrum depicts slight changes in the relative intensity of the I-conformer bands. For spectral regions associated with the IV-conformer (~1603 cm⁻¹ for *a*₁₃, and 3598 cm⁻¹ for *a*₆), there is a clear loss of intensity with increasing temperature. So for both Cs⁺(H₂O)₃D₂ and Cs⁺(H₂O)₃Ar, an increase in temperature leads to a reduction in the population of the higher energy IV-conformer.

To consider the relative stability of these two conformers as a function of temperature, metadynamics calculations were performed at three temperatures: 10, 20 and 50 K. Three free energy profiles are presented in Fig. B.9a, depicting the interconversions

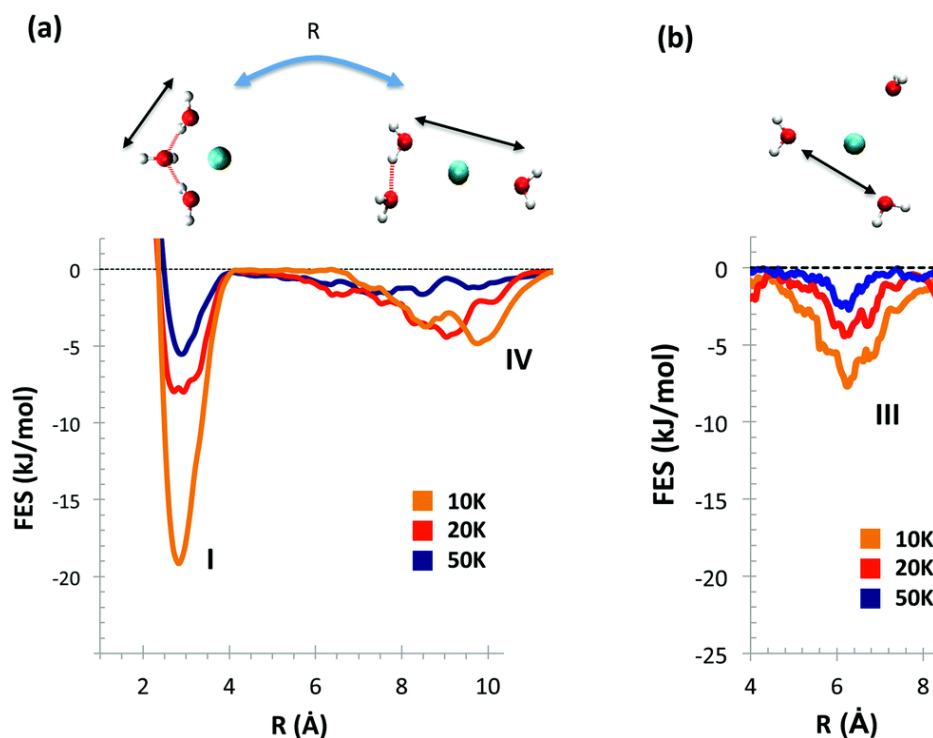


Fig. B.9: Free energy profiles from the finite temperatures metadynamics MD simulations (including anharmonicities and entropic effects): (a) the interconversion between the I and IV conformers. R measures the distance between the oxygens of the middle and top water molecules in the I-conformer, (b) the stability of the conformer III. R measures the distance between the oxygens of two water molecules in this conformer.

between the $\text{Cs}^+(\text{H}_2\text{O})_3$ I and IV conformers. Entropic effects are clearly seen in these two profiles. While conformer I is favored by free energy at all three temperatures, the barrier to reach the IV-conformer is substantially reduced at 50 K (20 kJ mol^{-1} at 10 K vs. 5 kJ mol^{-1} at 50 K). Conversely, the barrier to reach the I-conformer from the IV-conformer is reduced from 5 kJ mol^{-1} at 10 K to less than 2 kJ mol^{-1} at 50 K. Furthermore, the free energy well of the IV-conformer is rather flat at 50 K, so the effective population of this conformer will be small to non-existent. Thus, the metadynamics calculations are consistent with the experimental temperature dependence of the $\text{Cs}^+(\text{H}_2\text{O})_3\text{D}_2$ and $\text{Cs}^+(\text{H}_2\text{O})_3\text{Ar}$ spectra recorded under all three experimental conditions (a through c in Fig. B.3). An increase in temperature for either tagged species will tend to favor the I-conformer over the IV-conformer, as the IV-conformer becomes unstable.

Mechanisms of formation of the tagged clusters and final conclusions. In these experiments, either $\text{Cs}^+(\text{H}_2\text{O})_3\text{Ar}$ or $\text{Cs}^+(\text{H}_2\text{O})_3$ are generated by evaporative cooling of nascent cluster ions formed when cesium ions collide with neutral clusters of $(\text{H}_2\text{O})_m\text{Ar}_n$ in the source region. From previous studies by the Illinois group, estimates for the

effective temperature for these clusters depend on the binding of the most labile constituent of the cluster ion. Cs⁺(H₂O)₃Ar is formed by evaporative cooling of argon, and has an effective temperature of 80 to 100 K. Cs⁺(H₂O)₃ is formed by evaporative cooling of water, which binds more strongly to the ion, and results in a higher effective temperature of approximately 300 K.[10] After a small number of collisions with He in the RF octopole ion-guides, mass selection and focusing into an RF ring-electrode ion-trap, the cluster ions undergo a significant number of collisions with either He or D₂ at trap temperatures ranging from 7 to 40 K, and 12 to 21 K, respectively.

The spectrum for Cs⁺(H₂O)₃Ar in the OH stretching region at 7 K in this study, and the previously published spectrum of Cs⁺(H₂O)₃Ar by Ke and co-workers[65] formed by evaporative cooling of argon are similar as mentioned earlier (Fig. B.6). The 7 K spectrum resulting from collisions with cold helium gas in this report has sharper, narrower features that would be expected in comparison to the warmer spectrum with a temperature established by evaporative cooling of argon. As noted above, the dominant conformer is structure I, which is also the minimum energy structure, with a small contribution from conformer IV. Analysis of the computed spectra suggests that the argon is likely located near the second shell water molecule, conformer I-1. These spectra demonstrate that a few collisions with He, which do not dislodge the argon atom from Cs⁺(H₂O)₃Ar, do not impart sufficient energy to affect the ensemble generated by evaporative cooling of argon.

The Cs⁺(H₂O)₃D₂ spectra, formed from either Cs⁺(H₂O)₃Ar or Cs⁺(H₂O)₃ via the 3-body collisions with cryogenic D₂, are very different from the Cs⁺(H₂O)₃Ar spectrum. The dominant conformer in both cases is structure IV, with a single hydrogen bond. The location of the D₂ is unclear. While conformers IV-4 and IV-6 have computed bands consistent with all of the experimental features, the small differences in binding energy would allow contributions from other conformers as well. As Cs⁺(H₂O)₃D₂ was generated in two ways, first consider the formation from the Cs⁺(H₂O)₃ precursor. The nascent cluster ion, as it enters the RF ring-electrode ion-trap, has an effective temperature of 300 K based on earlier work.[10] Under these conditions, the dominant conformer with the lowest free energy is structure III (no hydrogen bonds, see Fig. B.7 for temperature-dependent free energies), with small contributions from conformers I and IV.[9] However based on the free energy analysis, the most stable conformer at or below 80 K is the I-conformer with two hydrogen bonds. Collisions with cryogenic D₂ at temperatures of 12-20 K, rapidly quenching a warm cluster ensemble of Cs⁺(H₂O)₃ and rapid cooling of conformer III would follow a pathway leading to the IV-conformer with a single hydrogen bond, and then to the more stable I-conformer with two hydrogen bonds. From the metadynamics analysis, kinetic trapping of the IV-conformer is possible as the temperature drops below 50 K, as seen in Fig. B.9a, with a substantial barrier to a path leading to the I-conformer. The barrier decreases with increasing temperature, enabling a portion of the IV-conformer to convert to the I-conformer. Fig. B.9b reveals a decrease in stability for the III-conformer from 10 K to 50 K, with a barrier of ~ 2 kJ mol⁻¹ from another free energy well at 50 K. The free energy minimum of III-conformer is also shrinking in width, showing large entropic effects. If there were

vibrational signatures for the III-conformer, they would only appear for temperatures below 50 K.

The other production route involves collisional loss of Ar from $\text{Cs}^+(\text{H}_2\text{O})_3\text{Ar}$ in the ion trap, followed by collisional cooling with D_2 , and its subsequent attachment via three-body collisions. The collisional loss of Ar clearly increases the internal energy of the $\text{Cs}^+(\text{H}_2\text{O})_3$ product by an amount sufficient to induce a change in the distribution of conformers from the initial $\text{Cs}^+(\text{H}_2\text{O})_3\text{Ar}$ cluster ion distribution. Since conformer IV is dominant when $\text{Cs}^+(\text{H}_2\text{O})_3\text{D}_2$ is formed directly from $\text{Cs}^+(\text{H}_2\text{O})_3$, it appears that the collisional process involving $\text{Cs}^+(\text{H}_2\text{O})_3\text{Ar}$ generates an ensemble with an effective temperature range, based on the argon binding energy of 80 to 120 K,[9] where both conformers I and III have comparable free energies (Fig. B.7). Additional collisions with cryogenic D_2 to temperatures of 12-20 K preserved both IV and I conformers with the same temperature dependence as observed when $\text{Cs}^+(\text{H}_2\text{O})_3$ was the precursor. Thus the same arguments provided for the direct cryogenic cooling of $\text{Cs}^+(\text{H}_2\text{O})_3$ leading to a temperature dependence of the relative contributions of the IV- and I-conformers, as described in the preceding paragraph, apply here as well. The only difference is due to the initial distribution of III and I conformers between nascent $\text{Cs}^+(\text{H}_2\text{O})_3$ as opposed to $\text{Cs}^+(\text{H}_2\text{O})_3$ formed by collisional loss of argon in the trap.

The combined experimental (Ar/ D_2 tagging IRPD spectroscopy and temperature dependence) and theoretical (harmonic vibrational spectra and free energy profiles from finite temperature metadynamics MD simulations) strategies can be generalized to any cluster. Even at cryogenic temperatures, conformers can display a preference depending on the tagging species, and a measurable temperature dependence over a range of ~ 30 K. The experimental methods of cluster ion formation and cooling, and the topology of the potential energy surface, suggest that kinetic trapping can have a considerable effect on the conformer distribution.

B.5 References

- [1] R. Cabot and C. A. Hunter. “Molecular Probes of Solvation Phenomena”. In: “Chem. Soc. Rev.” 41.9 (2012), pp. 3485–3492.
- [2] C. A. Hunter. “Quantifying Intermolecular Interactions: Guidelines for the Molecular Recognition Toolbox”. In: “Angewandte Chemie International Edition” 43.40 (2004), pp. 5310–5324.
- [3] V. Vaida, H. G. Kjaergaard and K. J. Feierabend. “Hydrated Complexes: Relevance to Atmospheric Chemistry and Climate”. In: “International Reviews in Physical Chemistry” 22.1 (2003), pp. 203–219.
- [4] L. R. McCunn, J. R. Roscioli, B. M. Elliott, M. A. Johnson and A. B. McCoy. “Why Does Argon Bind to Deuterium? Isotope Effects and Structures of $\text{Ar} \cdot \text{H}_5\text{O}_2^+$ Complexes”. In: “J. Phys. Chem. A” 112.27 (2008), pp. 6074–6078.

- [5] S. I. Stupp and L. C. Palmer. “Supramolecular Chemistry and Self-Assembly in Organic Materials Design”. In: “Chem. Mater.” 26.1 (2014), pp. 507–518.
- [6] N. Veljkovic, S. Glisic, V. Perovic and V. Veljkovic. “The Role of Long-Range Intermolecular Interactions in Discovery of New Drugs”. In: “Expert Opinion on Drug Discovery” 6.12 (2011), pp. 1263–1270.
- [7] A. M. van Oijen. “Single-Molecule Approaches to Characterizing Kinetics of Biomolecular Interactions”. In: “Current Opinion in Biotechnology” 22.1 (2011), pp. 75–80.
- [8] A. B. Wolk, C. M. Leavitt, E. Garand and M. A. Johnson. “Cryogenic Ion Chemistry and Spectroscopy”. In: “Acc. Chem. Res.” 47.1 (2014), pp. 202–210.
- [9] D. J. Miller and J. M. Lisy. “Hydrated Alkali-Metal Cations: Infrared Spectroscopy and Ab Initio Calculations of M⁺(H₂O)_{x=2-5}Ar Cluster Ions for M = Li, Na, K, and Cs”. In: “J. Am. Chem. Soc.” 130.46 (2008), pp. 15381–15392.
- [10] D. J. Miller and J. M. Lisy. “Entropic Effects on Hydrated Alkali-Metal Cations: Infrared Spectroscopy and Ab Initio Calculations of M⁺(H₂O)_{x=2-5} Cluster Ions for M = Li, Na, K, and Cs”. In: “J. Am. Chem. Soc.” 130.46 (2008), pp. 15393–15404.
- [11] C. T. Wolke, F. S. Menges, N. Tötsch, O. Gorlova, J. A. Fournier, G. H. Weddle, M. A. Johnson, N. Heine, T. K. Esser, H. Knorke, K. R. Asmis, A. B. McCoy, D. J. Arismendi-Arrieta, R. Prosimiti and F. Paesani. “Thermodynamics of Water Dimer Dissociation in the Primary Hydration Shell of the Iodide Ion with Temperature-Dependent Vibrational Predissociation Spectroscopy”. In: “J. Phys. Chem. A” 119.10 (2015), pp. 1859–1866.
- [12] B. Bandyopadhyay, K. N. Reishus and M. A. Duncan. “Infrared Spectroscopy of Solvation in Small Zn⁺(H₂O)_n Complexes”. In: “J. Phys. Chem. A” 117.33 (2013), pp. 7794–7803.
- [13] L. Voronina and T. R. Rizzo. “Spectroscopic Studies of Kinetically Trapped Conformations in the Gas Phase: The Case of Triply Protonated Bradykinin”. In: “Phys. Chem. Chem. Phys.” 17.39 (2015), pp. 25828–25836.
- [14] J. S. Prell, T. C. Correra, T. M. Chang, J. A. Biles and E. R. Williams. “Entropy Drives an Attached Water Molecule from the C- to N-Terminus on Protonated Proline”. In: “J. Am. Chem. Soc.” 132.42 (2010), pp. 14733–14735.
- [15] V. Brites, A. Cimas, R. Spezia, N. Sieffert, J. M. Lisy and M.-P. Gaigeot. “Stalking Higher Energy Conformers on the Potential Energy Surface of Charged Species”. In: “J. Chem. Theory Comput.” 11.3 (2015), pp. 871–883.
- [16] O. Rodriguez and J. M. Lisy. “Revisiting Li⁺(H₂O)₃₋₄Ar₁ Clusters: Evidence of High-Energy Conformers from Infrared Spectra”. In: “J. Phys. Chem. Lett.” 2.12 (2011), pp. 1444–1448.

-
- [17] J. D. Rodriguez and J. M. Lisy. “Infrared Spectroscopy of Gas-Phase Hydrated $K^+ : 18\text{-Crown-6}$ Complexes: Evidence for High Energy Conformer Trapping Using the Argon Tagging Method”. In: “International Journal of Mass Spectrometry” 283.1 (2009), pp. 135–139.
- [18] N. Khanal, C. Masellis, M. Z. Kamrath, D. E. Clemmer and T. R. Rizzo. “Glycosaminoglycan Analysis by Cryogenic Messenger-Tagging IR Spectroscopy Combined with IMS-MS”. In: “Anal. Chem.” 89.14 (2017), pp. 7601–7606.
- [19] J. S. Prell, T. M. Chang, J. A. Biles, G. Berden, J. Oomens and E. R. Williams. “Isomer Population Analysis of Gaseous Ions From Infrared Multiple Photon Dissociation Kinetics”. In: “J. Phys. Chem. A” 115.13 (2011), pp. 2745–2751.
- [20] J. A. Silveira, K. L. Fort, D. Kim, K. A. Servage, N. A. Pierson, D. E. Clemmer and D. H. Russell. “From Solution to the Gas Phase: Stepwise Dehydration and Kinetic Trapping of Substance P Reveals the Origin of Peptide Conformations”. In: “J. Am. Chem. Soc.” 135.51 (2013), pp. 19147–19153.
- [21] R. M. Forck, J. M. Dieterich, C. C. Pradzynski, A. L. Huchting, R. A. Mata and T. Zeuch. “Structural Diversity in Sodium Doped Water Trimers”. In: “Phys. Chem. Chem. Phys.” 14.25 (2012), pp. 9054–9057.
- [22] C. W. Dierking, F. Zurheide, T. Zeuch, J. Med, S. Perez and P. Slavíček. “Revealing Isomerism in Sodium-Water Clusters: Photoionization Spectra of $\text{Na}(\text{H}_2\text{O})_n$ ($n = 2\text{--}90$)”. In: “J. Chem. Phys.” 146.24 (2017), p. 244303.
- [23] J. M. Lisy. “Spectroscopy and Structure of Solvated Alkali-Metal Ions”. In: “International Reviews in Physical Chemistry” 16.3 (1997), pp. 267–289.
- [24] T. Ebata, A. Fujii and N. Mikami. “Vibrational Spectroscopy of Small-Sized Hydrogen-Bonded Clusters and Their Ions”. In: “International Reviews in Physical Chemistry” 17.3 (1998), pp. 331–361.
- [25] E. J. Bieske and O. Dopfer. “High-Resolution Spectroscopy of Cluster Ions”. In: “Chem. Rev.” 100.11 (2000), pp. 3963–3998.
- [26] O. Dopfer. “IR Spectroscopy of Microsolvated Aromatic Cluster Ions: Ionization-Induced Switch in Aromatic Molecule–Solvent Recognition”. In: “Zeitschrift für Physikalische Chemie” 219.2 (2005), pp. 125–168.
- [27] K. Mizuse and A. Fujii. “Infrared Photodissociation Spectroscopy of $\text{H}^+(\text{H}_2\text{O})_6 \cdot \text{M}_m$ ($M = \text{Ne}, \text{Ar}, \text{Kr}, \text{Xe}, \text{H}_2, \text{N}_2, \text{and CH}_4$): Messenger-Dependent Balance between H_3O^+ and H_5O_2^+ Core Isomers”. In: “Phys. Chem. Chem. Phys.” 13.15 (2011), pp. 7129–7135.
- [28] M. Okumura, L. I. Yeh, J. D. Myers and Y. T. Lee. “Infrared Spectra of the Cluster Ions $\text{H}_7\text{O}_3^+ \cdot \text{H}_2$ and $\text{H}_9\text{O}_4^+ \cdot \text{H}_2$ ”. In: “J. Chem. Phys.” 85.4 (1986), pp. 2328–2329.

- [29] C. J. Johnson, A. B. Wolk, J. A. Fournier, E. N. Sullivan, G. H. Weddle and M. A. Johnson. “Communication: He-Tagged Vibrational Spectra of the SarGlyH⁺ and H⁺(H₂O)_{2,3} Ions: Quantifying Tag Effects in Cryogenic Ion Vibrational Predissociation (CIVP) Spectroscopy”. In: “The Journal of Chemical Physics” 140.22 (2014), p. 221101.
- [30] M. Brümmer, C. Kaposta, G. Santambrogio and K. R. Asmis. “Formation and Photodepletion of Cluster Ion-Messenger Atom Complexes in a Cold Ion Trap: Infrared Spectroscopy of VO⁺, VO₂⁺, and VO₃⁺”. In: “The Journal of Chemical Physics” 119.24 (2003), pp. 12700–12703.
- [31] E. Garand. “Spectroscopy of Reactive Complexes and Solvated Clusters: A Bottom-Up Approach Using Cryogenic Ion Traps”. In: “J. Phys. Chem. A” 122.32 (2018), pp. 6479–6490.
- [32] J. M. Voss, K. C. Fischer and E. Garand. “Accessing the Vibrational Signatures of Amino Acid Ions Embedded in Water Clusters”. In: “J. Phys. Chem. Lett.” 9.9 (2018), pp. 2246–2250.
- [33] J. M. Voss, S. J. Kregel, K. C. Fischer and E. Garand. “IR-IR Conformation Specific Spectroscopy of Na⁺(Glucose) Adducts”. In: “J. Am. Soc. Mass Spectrom.” 29.1 (2018), pp. 42–50.
- [34] C.-W. Liu and Y. Q. Gao. “Understanding the Microsolvation of Salts in Molecular Clusters”. In: “International Journal of Quantum Chemistry” 115.9 (2015), pp. 541–544.
- [35] Y. Wang and J. M. Bowman. “Coupled-Monomers in Molecular Assemblies: Theory and Application to the Water Tetramer, Pentamer, and Ring Hexamer”. In: “J. Chem. Phys.” 136.14 (2012), p. 144113.
- [36] K. Szalewicz. “Interplay between Theory and Experiment in Investigations of Molecules Embedded in Superfluid Helium Nanodroplets”. In: “International Reviews in Physical Chemistry” 27.2 (2008), pp. 273–316.
- [37] J. Hutter, M. Iannuzzi, F. Schiffmann and J. VandeVondele. “Cp2k: Atomistic Simulations of Condensed Matter Systems”. In: “Wiley Interdisciplinary Reviews: Computational Molecular Science” 4.1 (2014), pp. 15–25.
- [38] C. T. Wolke, J. A. Fournier, L. C. Dzugan, M. R. Fagiani, T. T. Odbadrakh, H. Knorke, K. D. Jordan, A. B. McCoy, K. R. Asmis and M. A. Johnson. “Spectroscopic Snapshots of the Proton-Transfer Mechanism in Water”. In: “Science” 354.6316 (2016), pp. 1131–1135.
- [39] N. Heine, E. G. Kratz, R. Bergmann, D. P. Schofield, K. R. Asmis, K. D. Jordan and A. B. McCoy. “Vibrational Spectroscopy of the Water–Nitrate Complex in the O–H Stretching Region”. In: “J. Phys. Chem. A” 118.37 (2014), pp. 8188–8197.

- [40] V. Brites, A. L. Nicely, N. Sieffert, M.-P. Gaigeot and J. M. Lisy. “High Energy Conformers of $M^+(APE)(H_2O)_{0-1}Ar_{0-1}$ Clusters Revealed by Combined IR-PD and DFT-MD Anharmonic Vibrational Spectroscopy”. In: “Phys. Chem. Chem. Phys.” 16.26 (2014), pp. 13086–13095.
- [41] J. P. Beck, A. Cimas, J. M. Lisy and M.-P. Gaigeot. “O–H Anharmonic Vibrational Motions in $Cl^...(CH_3OH)_{1-2}$ Ionic Clusters. Combined IRPD Experiments and AIMD Simulations”. In: “Spectrochimica Acta Part A: Molecular and Biomolecular Spectroscopy” 119 (2014), pp. 12–17.
- [42] J. P. Beck, M.-P. Gaigeot and J. M. Lisy. “Anharmonic Vibrations of N-H in $Cl(N\text{-Methylacetamide})_1(H_2O)_{0-2}Ar_2$ Cluster Ions. Combined IRPD Experiments and BOMD Simulations”. In: “Phys. Chem. Chem. Phys.” 15.39 (2013), pp. 16736–16745.
- [43] N. Yang, C. H. Duong, P. J. Kelleher, M. A. Johnson and A. B. McCoy. “Isolation of Site-Specific Anharmonicities of Individual Water Molecules in the $F\cdot(H_2O)_2$ Complex Using Tag-Free, Isotopomer Selective IR-IR Double Resonance”. In: “Chemical Physics Letters” 690 (2017), pp. 159–171.
- [44] G. E. Doublerly, R. S. Walters, J. Cui, K. D. Jordan and M. A. Duncan. “Infrared Spectroscopy of Small Protonated Water Clusters, $H^+(H_2O)_n$ ($N=2-5$): Isomers, Argon Tagging, and Deuteration”. In: “J. Phys. Chem. A” 114.13 (2010), pp. 4570–4579.
- [45] B. M. Elliott, R. A. Relph, J. R. Roscioli, J. C. Bopp, G. H. Gardenier, T. L. Guasco and M. A. Johnson. “Isolating the Spectra of Cluster Ion Isomers Using Ar-“tag” -Mediated IR-IR Double Resonance within the Vibrational Manifolds: Application to $NO_2\text{-}H_2O$ ”. In: “The Journal of Chemical Physics” 129.9 (2008), p. 094303.
- [46] B. M. Marsh, J. M. Voss, J. Zhou and E. Garand. “Coordination Structure and Charge Transfer in Microsolvated Transition Metal Hydroxide Clusters $[MOH]^+(H_2O)_{1-4}$ ”. In: “Phys. Chem. Chem. Phys.” 17.35 (2015), pp. 23195–23206.
- [47] X. Lei, X. Kong, B. Zhang, Z. Zhao, D. Dai, X. Yang and L. Jiang. “Temperature-Dependent Infrared Photodissociation Spectroscopy of $(CO_2)_3^+$ Cation”. In: “J. Phys. Chem. A” 122.40 (2018), pp. 8054–8057.
- [48] V. Brites, J. M. Lisy and M.-P. Gaigeot. “Infrared Predissociation Vibrational Spectroscopy of $Li^+(H_2O)_{3-4} Ar_{0,1}$ Reanalyzed Using Density Functional Theory Molecular Dynamics”. In: “J. Phys. Chem. A” 119.11 (2015), pp. 2468–2474.
- [49] T. Shimamori, J.-L. Kuo and A. Fujii. “Stepwise Internal Energy Change of Protonated Methanol Clusters By Using the Inert Gas Tagging”. In: “J. Phys. Chem. A” 120.46 (2016), pp. 9203–9208.

- [50] Y.-C. Li, T. Hamashima, R. Yamazaki, T. Kobayashi, Y. Suzuki, K. Mizuse, A. Fujii and J.-L. Kuo. “Hydrogen-Bonded Ring Closing and Opening of Protonated Methanol Clusters H⁺(CH₃OH)_n (n = 4–8) with the Inert Gas Tagging”. In: “Phys. Chem. Chem. Phys.” 17.34 (2015), pp. 22042–22053.
- [51] T. Hamashima, Y.-C. Li, M. C. H. Wu, K. Mizuse, T. Kobayashi, A. Fujii and J.-L. Kuo. “Folding of the Hydrogen Bond Network of H⁺(CH₃OH)₇ with Rare Gas Tagging”. In: “J. Phys. Chem. A” 117.1 (2013), pp. 101–107.
- [52] A. Masson, E. R. Williams and T. R. Rizzo. “Molecular Hydrogen Messengers Can Lead to Structural Infidelity: A Cautionary Tale of Protonated Glycine”. In: “The Journal of Chemical Physics” 143.10 (2015), p. 104313.
- [53] N. Heine and K. R. Asmis. “Cryogenic Ion Trap Vibrational Spectroscopy of Hydrogen-Bonded Clusters Relevant to Atmospheric Chemistry”. In: “International Reviews in Physical Chemistry” 34.1 (2015), pp. 1–34.
- [54] D. Irimia, D. Dobrikov, R. Kortekaas, H. Voet, D. A. van den Ende, W. A. Groen and M. H. M. Janssen. “A Short Pulse (7 Us FWHM) and High Repetition Rate (Dc-5kHz) Cantilever Piezovalve for Pulsed Atomic and Molecular Beams”. In: “Review of Scientific Instruments” 80.11 (2009), p. 113303.
- [55] O. M. Cabarcos, C. J. Weinheimer, T. J. Martinez and J. M. Lisy. “The Solvation of Chloride by Methanol—Surface versus Interior Cluster Ion States”. In: “The Journal of Chemical Physics” 110.19 (1999), pp. 9516–9526.
- [56] W. R. Bosenberg and D. R. Guyer. “Broadly Tunable, Single-Frequency Optical Parametric Frequency-Conversion System”. In: “J. Opt. Soc. Am. B” 10.9 (1993), pp. 1716–1722.
- [57] N. Heine and K. R. Asmis. “Cryogenic Ion Trap Vibrational Spectroscopy of Hydrogen-Bonded Clusters Relevant to Atmospheric Chemistry (International Reviews in Physical Chemistry, 2015, Vol. 34, No. 1, 1–34)”. In: “International Reviews in Physical Chemistry” 35.3 (2016), pp. 507–507.
- [58] M. J. Frisch, G. W. Trucks, H. B. Schlegel, G. E. Scuseria, M. A. Robb, J. R. Cheeseman, G. Scalmani, V. Barone, B. Mennucci, G. A. Petersson, H. Nakatsuji, M. Caricato, X. Li, H. P. Hratchian, A. F. Izmaylov, J. Bloino, G. Zheng, J. L. Sonnenberg, M. Hada, M. Ehara, K. Toyota, R. Fukuda, J. Hasegawa, M. Ishida, T. Nakajima, Y. Honda, O. Kitao, H. Nakai, T. Vreven, J. A. Montgomery, J. E. Peralta, F. Ogliaro, M. Bearpark, J. J. Heyd, E. Brothers, K. N. Kudin, V. N. Staroverov, R. Kobayashi, J. Normand, K. Raghavachari, A. Rendell, J. C. Burant, S. S. Iyengar, J. Tomasi, M. Cossi, N. Rega, J. M. Millam, M. Klene, J. E. Knox, J. B. Cross, V. Bakken, C. Adamo, J. Jaramillo, R. Gomperts, R. E. Stratmann, O. Yazyev, A. J. Austin, R. Cammi, C. Pomelli, J. W. Ochterski, R. L. Martin, K. Morokuma, V. G. Zakrzewski, G. A. Voth, P. Salvador, J. J. Dannenberg, S. Dapprich, A. D. Daniels, Farkas, J. B. Foresman,

-
- J. V. Ortiz, J. Cioslowski and D. J. Fox. *Gaussian 09, Revision C.01*, Gaussian, Inc. Wallingford CT: Gaussian, Inc., 2009.
- [59] T. H. Dunning Jr. and P. J. Hay. “Gaussian Basis Sets for Molecular Calculations”. In: H. F. Schaefer. *Methods of Electronic Structure Theory*. Springer US, 1977.
- [60] R. A. Kendall, T. H. Dunning and R. J. Harrison. “Electron Affinities of the First-row Atoms Revisited. Systematic Basis Sets and Wave Functions”. In: “J. Chem. Phys.” 96.9 (1992), pp. 6796–6806.
- [61] J. P. Merrick, D. Moran and L. Radom. “An Evaluation of Harmonic Vibrational Frequency Scale Factors”. In: “J. Phys. Chem. A” 111.45 (2007), pp. 11683–11700.
- [62] M. Kołaski, H. M. Lee, Y. C. Choi, K. S. Kim, P. Tarakeshwar, D. J. Miller and J. M. Lisy. “Structures, Energetics, and Spectra of Aqua-Cesium (I) Complexes: An Ab Initio and Experimental Study”. In: “J. Chem. Phys.” 126.7 (2007), p. 074302.
- [63] J. VandeVondele, M. Krack, F. Mohamed, M. Parrinello, T. Chassaing and J. Hutter. “Quickstep: Fast and Accurate Density Functional Calculations Using a Mixed Gaussian and Plane Waves Approach”. In: “Computer Physics Communications” 167.2 (2005), pp. 103–128.
- [64] H. Ke, C. van der Linde and J. M. Lisy. “Insights into Gas-Phase Structural Conformers of Hydrated Rubidium and Cesium Cations, $M^+(H_2O)_n$ Ar ($M = Rb, Cs$; $n = 3-5$), Using Infrared Photodissociation Spectroscopy”. In: “J. Phys. Chem. A” 118.8 (2014), pp. 1363–1373.
- [65] H. Ke, C. van der Linde and J. M. Lisy. “Insights into the Structures of the Gas-Phase Hydrated Cations $M^+(H_2O)_n$ Ar ($M = Li, Na, K, Rb, \text{ and } Cs$; $n = 3-5$) Using Infrared Photodissociation Spectroscopy and Thermodynamic Analysis”. In: “J. Phys. Chem. A” 119.10 (2015), pp. 2037–2051.
- [66] M. Riera, S. E. Brown and F. Paesani. “Isomeric Equilibria, Nuclear Quantum Effects, and Vibrational Spectra of $M^+(H_2O)_{n=1-3}$ Clusters, with $M = Li, Na, K, Rb, \text{ and } Cs$, through Many-Body Representations”. In: “J. Phys. Chem. A” (2018).

Appendix C

LabVIEW Measurement Software

The main purpose and features of the LabVIEW measurement software have been discussed in Sec. 3.10. Here, the implementation will be discussed in more detail, but without claim for completeness. This chapter should help to understand the general structure of the software and enable future operators, with basic LabVIEW knowledge, to add new features and implement communication for new devices. This is no manual as operation of the software is best learned by new users along with the general training on the instrument.

The user interface consists of a single window, the front panel of the virtual instrument (VI) NPMS_Main_UI.vi, shown in Fig. C.1. Three tab controls allow to display a combination of instrument parameters, acquisition settings and measured values, suitable for a given task. Measurement modes are provided for acquisition of FT and resonant excitation spectra as well as monitoring several detectors over time for signal optimization. A custom mode is available, which allows the user to record any set of parameters in dependence of any other parameter.

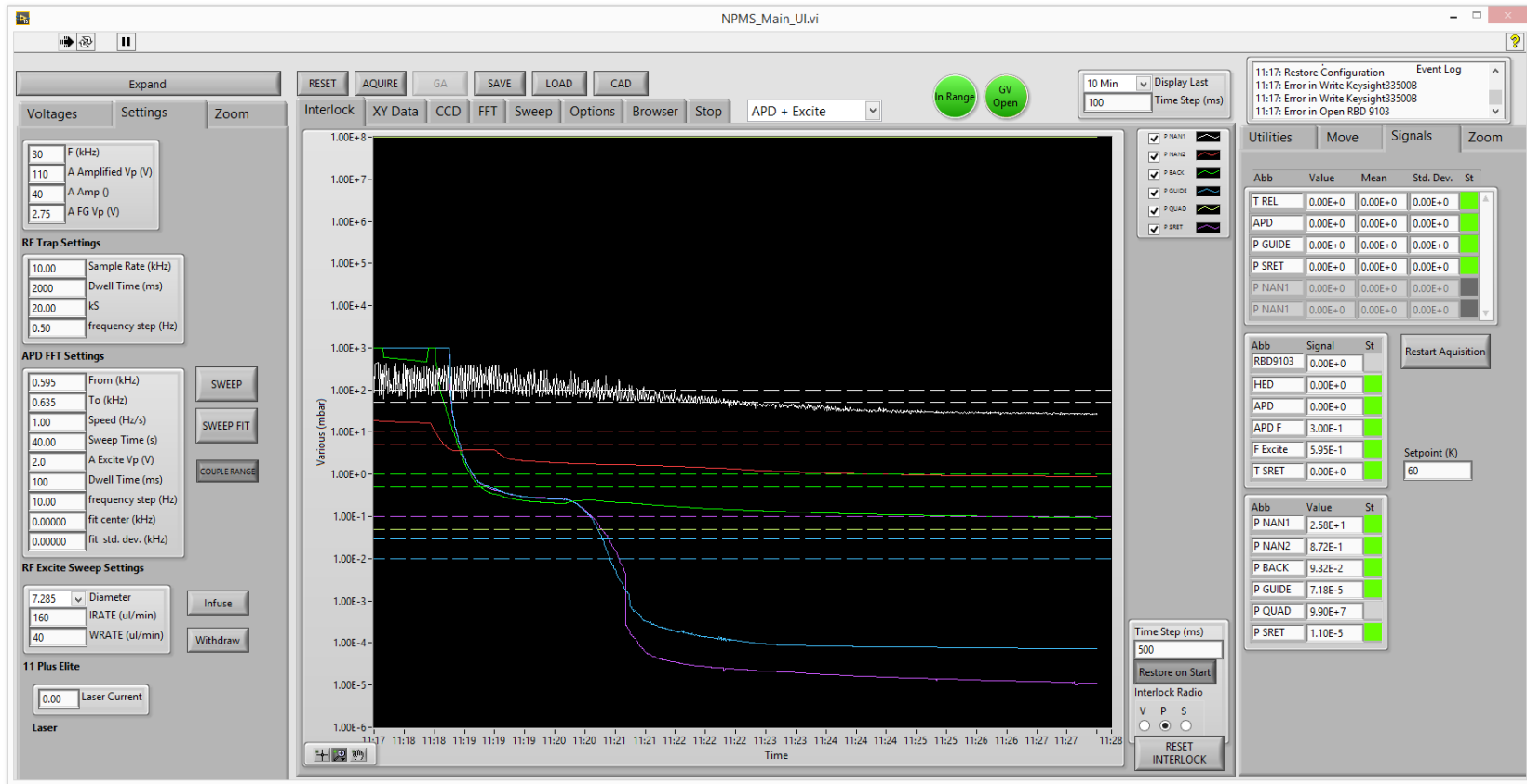


Fig. C.1: NPMS Software User Interface. The tab controls on the sides provide access to most experimental parameters and settings. The tab control in the middle allows to switch between program options, graphs for the specific measurement modes and the interlock, where the change of all parameters during the last day can be seen.

C.1 Implementation and Device Communication

The measurement software is implemented following the queued state machine (QSM) design pattern, where both the software itself and the user can insert states, represented by variables of the data type enum, into a queue. A single while loop handles the states and redirects more time consuming tasks to parallel running VIs. Multiple VIs were created to handle specific tasks, which will be discussed in the following. In order to avoid redundancy and incompatible data types, when data is shared between VIs and with the controls and indicators in the user interface, global variables and references are provided by NPMS_Globals.vi. Global references and corresponding controls and indicators are linked to type definitions such that they always remain consistent. In addition, enum variables that are used across multiple VIs are also linked to type definitions.

For each external device a dedicated VI was created, which implements cases to open and close communication and to read and write data and settings. The implementation of these cases is based on examples provided by the manufacturers. While it is specific for each device, the basic functionality is often identical, allowing to generalize the communication concept. To that end, NPMS_Background_Worker.vi iterates over all devices, initializes communication and creates parallel running instances of NPMS_READ_DEV_LOOP.vi, which triggers data acquisition for each device in appropriate intervals. The global variables and references are used to store the data for further processing or to display it directly to the user. When the main program is stopped, a global variable is set to stop all parallel VIs, and device communication is closed for each device by NPMS_Background_Worker.vi. When device settings or the measurement mode need to be changed, the devices are accessed directly from the QSM and NPMS_Background_Worker.vi is restarted to reinitialize devices if applicable.

C.2 Recording and Saving of Data

As the data is constantly updated in the background, data analysis, display and saving to files is independent of possible communication delays. All parameters are constantly recorded and saved to a text file by NPMS_Interlock.vi. The data from the last 24 hours is displayed in the measurement software. This allows the operator to monitor long-term stability of all parameters and to quickly correlate changes in the detected signal to changes in experimental parameters. Most experimental results can later be restored from the automatically saved data, even if no files were saved by the operator. Similarly Get_XY_Data_Indirect.vi records and displays data for a subset of parameters and at a time interval specified by the operator.

When the operator wants to save data, NPMS_Load_Save.vi suggests a filename based on the date, project and file counter. All available instrument parameters are then formatted by NPMS_Format_Parse.vi into human and machine readable text blocks and saved to a .txt configuration file. If applicable, data for user specified

parameters, FT and resonant excitation spectra are saved to text files with .dat, .fft and .swe extensions, respectively. The same two VIs are also responsible to load settings from a configuration file.

In File C.1, the complete set of settings used for the experiments described in Sec. 5.2 is provided to demonstrate the structure of the configuration file and to give an idea of typical operation conditions. The potential of the nano ESI ion source emitter (~ 2.1 kV), the amplitude and frequency of the ion guides (≤ 700 V, ~ 100 kHz), the position of the detectors and the laser power are not yet acquired by the measurement software. The amplitude and frequency of the trapping potential is controlled by the measurement software, but should also be monitored at all times, using an additional data acquisition card, to identify long-term fluctuations and possible malfunction. Saving of the source flow rate, typically 500 to 1000 nl/min, has been implemented after the example file below had been saved. The pressure on the SRET chamber is typically $1 \cdot 10^{-3}$ to $5 \cdot 10^{-2}$ mbar for trapping and $< 5 \cdot 10^{-4}$ mbar for frequency analysis. The pressure in the multipole guide behind the ion source is regulated up to $2 \cdot 10^{-3}$ mbar during trapping. Note that the amplification factors, voltage monitors and upper and lower limits of the analog voltages were removed from the CONTROLS block below for better display. The abbreviations used in the CONTROLS block are defined in Fig. C.2.

File C.1: Exemplary configuration file of the NPMS measurement software.

```
NPMS Aquisition Software Version 1.0 Tim Esser 2017 - 2018
Saved on 2018-10-20 (14:17:07)
Aquisition Mode: APD + Excite
```

```
BEGIN NOTES
Particle: SiO2
d Nominal: 100
Last Updated: 2018-01-24 (14:54:24)
Save Counter: 407
END NOTES
```

```
BEGIN PRESSURES
Abb      Pressure
-----
P NAN1   5.48E+0
P NAN2   2.59E-1
P BACK   6.40E-2
P GUIDE  2.08E-5
P QUAD   9.90E+7
P SRET   3.18E-4
END PRESSURES
```

```
BEGIN SIGNALS
Abb      Value      Unit
-----
RBD9103  0.0000E+0    pA
HED      0.0000E+0    Hz
APD      1.8815E+5    Hz
APD F    5.7759E-1    kHz
F Excite 2.8557E+0    kHz
T SRET   6.0001E+1    K
END SIGNALS
```


C.2 Recording and Saving of Data

```

BEGIN CONTROLS
Abb      Label                AOB Pin   AO Channel   AI Channel   Voltage
-----
SC       S Capillary              A         PXI1Slot2/ao20  PXI1Slot6/ai20  -80.0000
SK1     S Skimmer 1             B         PXI1Slot2/ao21  PXI1Slot6/ai21  140.9500
SK2     S Skimmer 2             C         PXI1Slot2/ao22  PXI1Slot6/ai22  20.7500
GE1A    G Einzel 1A             Guide 1    PXI1Slot2/ao0   PXI1Slot6/ai0   17.0000
GE1B    G Einzel 1B             Guide 2    PXI1Slot2/ao1   PXI1Slot6/ai1   -16.5675
GIN     G Entrance                Guide 3    PXI1Slot2/ao2   PXI1Slot6/ai2   21.5000
GDC     G Polebias              D         PXI1Slot2/ao23  PXI1Slot6/ai23  14.4000
GOUT    G Exit                   Guide 4    PXI1Slot2/ao3   PXI1Slot6/ai3   11.0000
G2EA    G Einzel 2A             Guide 5    PXI1Slot2/ao4   PXI1Slot6/ai4   9.0174
G2EB    G Einzel 2B             Guide 6    PXI1Slot2/ao5   PXI1Slot6/ai5   -6.3428
GVIN    Gatevalve IN            E         PXI1Slot2/ao24  PXI1Slot6/ai24  14.0000
GVOUT   Gatevalve OUT           F         PXI1Slot2/ao25  PXI1Slot6/ai25  -22.0000
BEA     B Einzel A              Bender 5    PXI1Slot2/ao10  PXI1Slot6/ai10  0.0000
BEB     B Einzel B              Bender 4    PXI1Slot2/ao9   PXI1Slot6/ai9   0.0000
BA      B Deflector A           Bender 3    PXI1Slot2/ao8   PXI1Slot6/ai8   0.0000
BB      B Deflector B           Bender 2    PXI1Slot2/ao7   PXI1Slot6/ai7   0.0000
BC      B Lenses                 Bender 1    PXI1Slot2/ao6   PXI1Slot6/ai6   0.0000
QIN     Q Entrance               Quad 1     PXI1Slot2/ao11  PXI1Slot6/ai11  0.0000
QDC     Q Polebias              G         PXI1Slot2/ao26  PXI1Slot6/ai26  0.0000
QOUT    Q Exit                   Quad 2     PXI1Slot2/ao12  PXI1Slot6/ai12  0.0000
QEA     Q Einzel A              Quad 3     PXI1Slot2/ao13  PXI1Slot6/ai13  0.0000
QEB     Q Einzel B              Quad 4     PXI1Slot2/ao14  PXI1Slot6/ai14  0.0000
TIN     T Entrance               SRET 1     PXI1Slot2/ao15  PXI1Slot6/ai15  0.0000
TEDC+   T Exite DC +            SRET 2     PXI1Slot2/ao16  PXI1Slot6/ai16  0.0000
TDC     T Polebias              H         PXI1Slot2/ao27  PXI1Slot6/ai27  0.0000
TEDC-   T Exite DC -            SRET 3     PXI1Slot2/ao17  PXI1Slot6/ai17  0.0000
TOUT    T Exit                   SRET 4     PXI1Slot2/ao18  PXI1Slot6/ai18  0.0000
RodA    T Rod A                  SRET 5     PXI1Slot2/ao19  PXI1Slot6/ai19  0.0000
RodB    T Rod B                  I         PXI1Slot2/ao28  PXI1Slot6/ai28  0.0000
free0   free0                    J         PXI1Slot2/ao29  PXI1Slot6/ai29  0.0000
free1   free1                    K         PXI1Slot2/ao30  PXI1Slot6/ai30  0.0000
free2   free2                    L         PXI1Slot2/ao31  PXI1Slot6/ai31  0.0000
END CONTROLS

BEGIN XY CHANNELS
Abb
-----
T REL
APD
P GUIDE
P SRET
END XY CHANNELS

BEGIN RF SRET
Abb      Value
-----
F Trap   3.0000E+1
A Trap   1.8000E+2
END RF SRET

BEGIN APD FFT
Abb      Value
-----
Rate     2.0000E+1
Time     2.0000E+3
END APD FFT

BEGIN RF Excite
Abb      Value
-----
From     2.5671E+0
To       2.8671E+0

```

Appendix C LabVIEW Measurement Software

```
Speed      5.0000E+0  
Amp        1.2000E+0  
Center     2.7171E+0  
StdDev     5.9631E-3  
END RF Excite
```

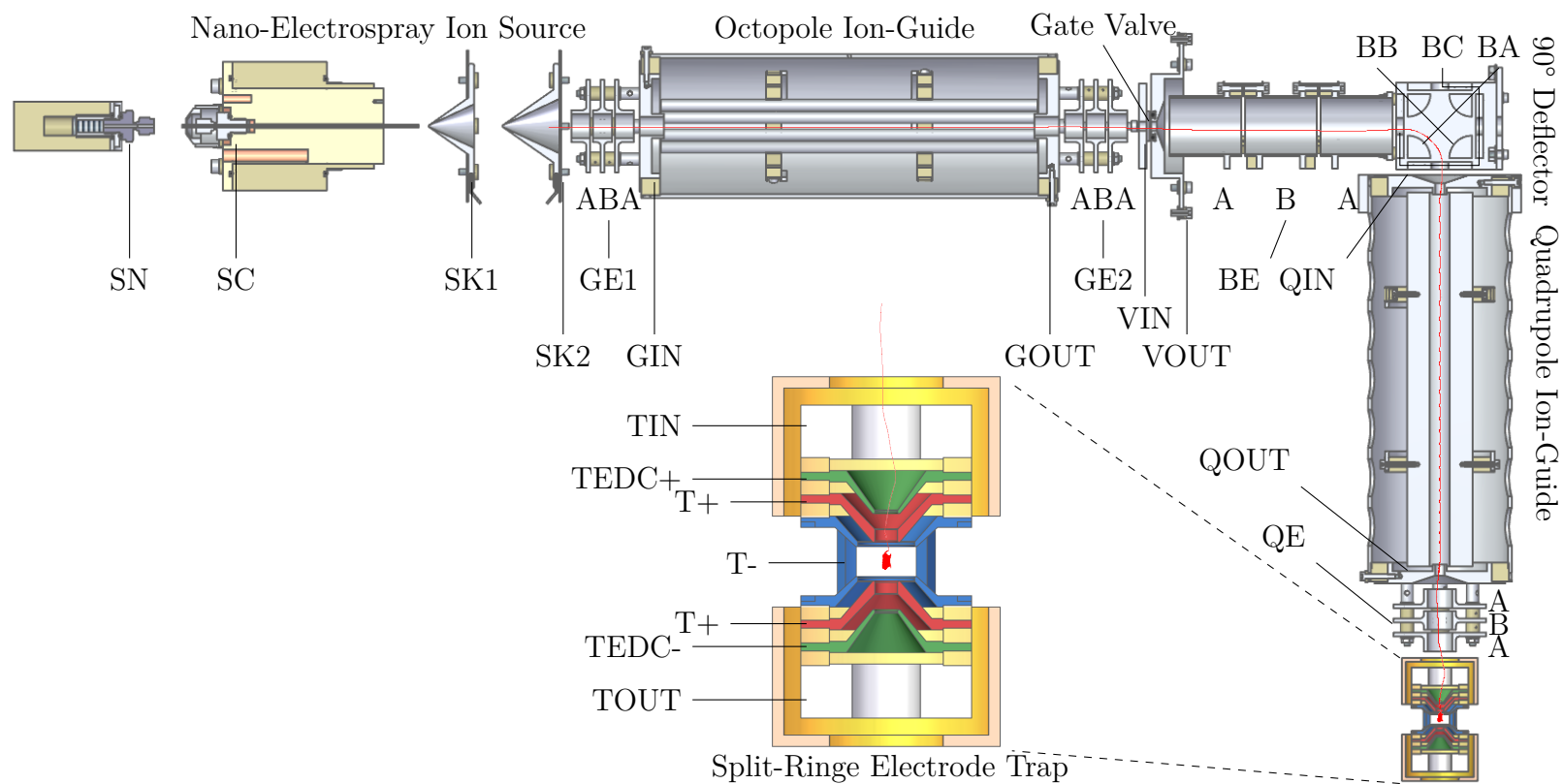


Fig. C.2: Schematic cross section of the nanoparticle mass spectrometry (NPMS) setup. The electrodes are labeled according to the abbreviations used in the measurement software and configuration files. A simulated ion trajectory is indicated in red. See Sec. 3.1 for a general overview of the displayed components.

C.3 Devices and Corresponding VIs

In the following the purpose of each VI related to communication with external devices is briefly described.

NPMS_11_Plus_Elite.vi Handles communication with the syringe pump (11 Plus Elite - Harvard Instruments) via USB. It allows to configure syringe diameter and flow rate and to start and stop the pump.

NPMS_AI_Count.vi Handles communication with the module PXI-6224 from National Instruments and cannot be used simultaneously with NPMS_APD_Count.vi and NPMS_EXCITE.vi as the sample clock settings are not compatible. Reads the monitor voltages at the analog inputs and the count rates for the APD (Count-50C - Laser Components GmbH) and EM (R6985-80 - Hamamatsu) using the same sample clock.

NPMS_AO.vi Handles communication with the module PXI-6723 from National Instruments. Writes the voltages for the analog outputs, which are amplified and redirected to the ion optics by the analog output board (FHI ELAB #5824).

NPMS_AO_Laser.vi Handles communication with the module PXI-6723 from National Instruments. Sets the voltage on an analog output channel, which is used to control the laser power of the DPSS laser from CivilLaser.

NPMS_APD_Count.vi Handles communication with the module PXI-6224 from National Instruments and cannot be used simultaneously with NPMS_AI_Count.vi and NPMS_EXCITE.vi as the sample clock settings are not compatible. Reads the signal from the APD with larger sample rates to enable calculation of FT spectra. Since the amount of data is too large if the monitor voltages are acquired at the same sample rate, they are not available when using this VI.

NPMS_DMK_41AU02.vi Handles communication with the CCD (DMK 41AU02 - The Imaging Source Europe GmbH) via USB. Acquires images to display to the user or save to file. Also allows to define the region of interest and sample rate.

NPMS_EXCITE.vi Handles communication with the module PXI-6224 from National Instruments and cannot be used simultaneously with NPMS_AI_Count.vi and NPMS_APD_Count.vi as the sample clock settings are not compatible. Reads the signal from the APD and the channel of the function generator (33510B - Keysight) used for resonant excitation.

NPMS_KeySight_33500B.vi Handles communication with the function generator (33510B - Keysight) via USB. Allows to control the amplitude and frequency of the trapping voltage. Also allows to control the amplitude, frequency range and sweep speed for resonant excitation.

NPMS_LakeShore_335.vi Handles communication with the temperature controller (Model 335 - Lake Shore) via USB. Allows to read and set the ion trap temperature.

NPMS_RBD_9103.vi Handles communication with the picoammeter (9103 - RBD Instruments) via USB. Allows to set sample range and rate, activate the bias voltage on the collection electrode and to read the current.

NPMS_TIC.vi Handles communication with the pressure sensor controller (TIC instrument controller - Edwards) via RS232. Allows to read the pressure of all active sensors. Also implements a setpoint logic, which enables or disables high voltages based on the pressures.

C.4 Anticipated Upgrades

The core features needed for trapping and acquisition of FT and resonant excitation spectra as well as automation of spectra acquisition over extended time periods are complete. The integration of a file browser with integrated graphs to display data and relevant information is planned to help with data analysis. In addition, analysis of data, which is currently done with separate LabVIEW programs, should be integrated into the measurement software to use the same VIs and allow for automated analysis during acquisition. Further devices, especially the laser used for spectroscopy, will be added to the experimental setup in the future and should also be controlled by the measurement software.

Appendix D

Lua Programs for the Virtual Setup and Trap Geometry Optimization

D.1 SIMION User Programs

The Lua programs, which were used to create and run the virtual setup as well as for analysis and optimization of the trap geometry, are distributed over multiple files. Due to the amount of required pages the code is not reproduced here. A copy of all related files remains accessible on the group server for further applications. The main features will be briefly summarized in the following. More details are provided by the comments within the files.

NPMS_Setup.lua This is the main SIMION workbench program for control of the simulation of ion guiding and trapping in the complete, non-linear, virtual NPMS setup. Ion parameters, the type, pressure and temperature of the background gas in different regions of the setup and ion optics potentials and frequencies are read from a configuration file. Automatic optimization of parameters for specific conditions is possible using the GA, however, in most cases manual optimization is sufficient to quickly find usable parameters for any given initial conditions. The workbench consists of ten overlapping potential arrays, which make use of symmetry to reduce memory consumption when possible. The most important parameters along the ion trajectory can be exported to a file for further analysis. Collisions are implemented using the collision model *hs1* (see Sec. 3.11).

NPMS_Setup_linear.lua This is essentially the same as NPMS_Setup.lua but for the linear version of the NPMS setup. Only five potential arrays are used.

NPMS_Setup_Parameters.lua This code defines the dimensions and relative positions for all simulated ion optics and creates a unique index for each electrode. All potential arrays are based on geometry files, which reference those parameters to assure that electrodes that appear in multiple potential arrays will always have consistent dimensions and indices.

NPMS_Functions.lua Functions that are used across several workbench programs are collected in NPMS_Functions.lua. This includes the collision model *hs1* and several smaller functions.

SRET_analyze_potential.lua This workbench program applies a DC potential to the ring and end cap electrodes and lets two neutrals fly along the symmetry axis. The electric potential and field are determined along the particle trajectories and used to calculate the characteristic parameters z_0 and r_0 , their mean values and standard deviations for a defined region around the trap center. The results are saved into a file for further analysis. They are also written to a global variable, which represents the interface to the GA.

SRET_trap_and_excite.lua This workbench program is used for simulation of ion trapping and resonant excitation. An asymmetric potential array should be used for resonant excitation since the potentials on the excitation electrodes have a phase shift of 180° . All parameters can also be controlled by the user during the simulation using SIMION adjustable variables.

SRET_GA_RUN.lua This Lua program controls the optimization of the SRET geometry. First, it loads initial geometry parameters from a configuration file and creates a corresponding directory for all output files. For each new set of parameters determined by the GA it creates a geometry file and generates and refines a potential array based on this. It also generates a workbench program that uses SRET_analyze_potential.lua to analyze the potential of the current trap geometry, evaluates the fitness function and returns the result to the GA. During optimization the geometry file and the output of SRET_analyze_potential.lua are saved for the best set of parameters in each generation. In addition, the geometry and most important parameters are summarized in a PDF file (see Fig. 3.14) generated using L^AT_EX. The PDF files of all generations can be combined in an animation to give a convenient overview of the optimization process. The program also creates a simple graph where the increase of the fitness function is plotted against the number of generations.

D.2 Concept and Implementation of the Genetic Algorithm

The genetic algorithm used for the SRET geometry optimization was implemented in the file GA.lua. The basic concept and general implementation of the GA are discussed here, based on Esser.[162] A manual and usage examples of the Lua and LabVIEW implementations will remain accessible on the group server for further applications.

Concept. GAs represent one way to find maxima and minima in large and complex search spaces. They belong to the group of evolutionary algorithms, which, like swarm algorithms, exploit randomness for an efficient search. GAs are used in situations where the complexity of the problem, or a lack of information, prevents an analytical solution being reached in reasonable time. Any problem that can be formulated as a fitness function, a way to express the quality of the solution as a number called *fitness*, can be treated by a GA. No information about the problem is needed, except, the set of parameters to optimize, called “DNA” (referring to deoxyribonucleic acid in biology), and the corresponding results of the fitness function. Depending on the problem, there is no guarantee to find the global optimum, nor information on how far apart the obtained results are. In these situations, the only goal can be to find an adequate solution to the problem. It is often hard to deduce, why the result obtained by a GA is correlated to a better fitness and which parameters have more influence than others. In biological terms, this is called the distinction of genotype (information contained in the DNA) and phenotype (part of the information that is most relevant to the problem). Once implemented, a GA can be used for many different problems by adapting the fitness function and input parameters.

Implementational Details. A continuous GA was implemented in Lua and LabVIEW. Both implementations are equivalent regarding the GA, but differ in the interfaces. This section serves to explain the basic concept of the GA, which is schematically shown in Fig. D.1. It was developed with ideas from the book "Practical GAs"[208] and the MIT OpenCourseWare Lecture "Multidisciplinary System Design Optimization".[209]

The key element of the GA is the *population*, which contains all information about the current generation. It is represented by a matrix (see Fig. D.1), where the first column contains the fitness and each of the subsequent columns represents a parameter, that can be optimized. Each parameter corresponds to a *gene* and its actual value to an *allele*. Each row in the matrix forms a set of alleles corresponding to the DNA of an individual. Subsets of the DNA are called *chromosomes*. The total number of rows represent the population size. The population is further divided into *parents* and *children*.

For the initialization, empirically found start values as well as mutation parameters for each *gene* are needed. The empirical start values correspond to the first individual and are stored in the first row of the population matrix. A new individual can be created by mutation of the first individual, which is done separately for each *gene* using the mutation parameters: RATE, MINIMUM value, MAXIMUM value and RANGE. The RATE is an integer between 0 and 100 and specifies the probability that the parameter changes on mutation. In that case a random number, picked with equal probability from the interval $[-\text{RANGE}, +\text{RANGE}]$, is added to the previous value. The search space is confined to physically reasonable values, using the MINIMUM and MAXIMUM values. The mutated value is coerced to the limits if it exceeds them. The initialization is completed when the population matrix is filled.

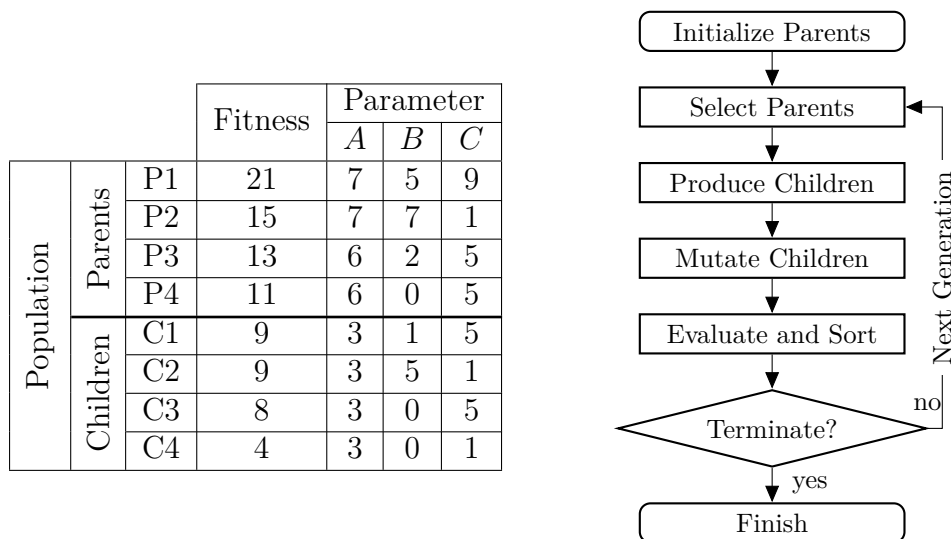


Fig. D.1: Exemplary population matrix and scheme of the continuous GA: All information is stored in a population matrix, which is divided into parents and children. In each generation, new children are created by mixing and mutating parents. They become parents in the next generation, if their fitness is higher than the fitness of the worst parent of the current generation. In that case, the quality of the solutions represented by the parents increases.

The GA then continues and evaluates the population, *i.e.*, all sets of parameters are applied consecutively and the corresponding (averaged) fitness values are assigned. The population is then sorted according to the fitness values so that the parents represent the best solutions and the children the poorest.

In the next step, children of the last generation are replaced by new ones, created by two parents, picked by rank or tournament selection. Rank selection ensures that parents corresponding to a higher fitness have higher probability to contribute to new children. The implementation uses Eq. D.1 to assign an accumulated selection probability P_n^a to the n^{th} parent in the population, where N is the number of parents, P_n is the selection probability for the n^{th} rank and n starts at 1.

$$P_n = \frac{N - n + 1}{\sum_{i=1}^N i}$$

$$P_n^a = \sum_{i=1}^n P_i \tag{D.1}$$

An example is given in Tab. D.1. The first parent, starting from the top, with an accumulated probability P_n^a that exceeds a random number between zero and one, is selected. Tournament selection, on the other hand, increases the contribution of poor parents, which are needed to keep genetic diversity. In the present implementation three parents are picked with equal probability and the best one of them is selected. Both selection schemes have a probability of 50% to be used if a parent is required.

Table D.1: Example of rank selection for a population with four parents.[208]

n	P_n	P_n^a
1	0.4	0.4
2	0.3	0.7
3	0.2	0.9
4	0.1	1

Once two parents are selected, they are used to create two children in a process called crossover, which is described in Eq. D.2 for a single parameter.

$$\begin{aligned}
 c_1 &= p_1 \cdot \alpha + p_2 \cdot (1 - \alpha) \\
 c_2 &= p_1 \cdot (1 - \alpha) + p_2 \cdot \alpha
 \end{aligned}
 \tag{D.2}$$

Here c_1 , c_2 and p_1 , p_2 are parameters of the children and parents, respectively, and α is a random number between zero and one, which is generated separately for each parameter. The new children are mutated, as described above, and then evaluated. After this, the population is sorted again.

If the optimization is stopped by the operator or converges, the best settings of the current generation are returned. Convergence is detected when there were no improvements in a specified number of previous generations. Though the best fitness can jump a lot from one generation to the next when using a GA, this behavior is barely observed in practice after the above convergence criterion is fulfilled. If non of the above criteria is met, a new generation is started.

Bibliography

- [1] R. P. Feynman. “There’s Plenty of Room at the Bottom”. In: “Engineering and Science” 23 (1960), pp. 22–36.
- [2] A. de Bettencourt-Dias and J.-I. Hahm. “Women in Nanotechnology: Toward Better Materials through a Better Understanding of Low-Dimensional Systems”. In: “ACS Nano” 12.8 (2018), pp. 7417–7420.
- [3] W. W. C. Chan, M. Chhowalla, S. Glotzer, Y. Gogotsi, J. H. Hafner, P. T. Hammond, M. C. Hersam, A. Javey, C. R. Kagan, A. Khademhosseini, N. A. Kotov, S.-T. Lee, Y. Li, H. Möhwald, P. A. Mulvaney, A. E. Nel, P. J. Nordlander, W. J. Parak, R. M. Penner, A. L. Rogach, R. E. Schaak, M. M. Stevens, A. T. S. Wee, C. G. Willson, L. E. Fernandez and P. S. Weiss. “Nanoscience and Nanotechnology Impacting Diverse Fields of Science, Engineering, and Medicine”. In: “ACS Nano” 10.12 (2016), pp. 10615–10617.
- [4] M.-C. Daniel and D. Astruc. “Gold Nanoparticles: Assembly, Supramolecular Chemistry, Quantum-Size-Related Properties, and Applications toward Biology, Catalysis, and Nanotechnology”. In: “Chem. Rev.” 104.1 (2004), pp. 293–346.
- [5] J. Jeevanandam, A. Barhoum, Y. S. Chan, A. Dufresne and M. K. Danquah. “Review on Nanoparticles and Nanostructured Materials: History, Sources, Toxicity and Regulations”. In: “Beilstein Journal of Nanotechnology” 9.1 (2018), pp. 1050–1074.
- [6] N. Ichinose, Y. Ozaki and S. Kashu. *Superfine Particle Technology*. Springer Science & Business Media, 2012. 230 pp.
- [7] G. Ganteför. *Alles NANO oder was?: Nanotechnologie für Neugierige*. 1. Weinheim: Wiley-VCH, 2013. 280 pp.
- [8] D. Schaming and H. Remita. “Nanotechnology: From the Ancient Time to Nowadays”. In: “Found Chem” 17.3 (2015), pp. 187–205.
- [9] Y. Li, J. He, Z. Xie, D. Jiang and Y. Li. “Frontier Development of Chips Design and Production”. In: “Procedia Computer Science” 139 (2018), pp. 554–560.
- [10] P. Kulkarni, P. A. Baron and K. Willeke. *Aerosol Measurement: Principles, Techniques, and Applications*. John Wiley & Sons, 2011. 904 pp.
- [11] J. Laskin, A. Laskin and S. A. Nizkorodov. “Mass Spectrometry Analysis in Atmospheric Chemistry”. In: “Anal. Chem.” 90.1 (2018), pp. 166–189.

- [12] F. Gottschalk, T. Sun and B. Nowack. “Environmental Concentrations of Engineered Nanomaterials: Review of Modeling and Analytical Studies”. In: “Environmental Pollution” 181 (2013), pp. 287–300.
- [13] D. Thompson. “Michael Faraday’s Recognition of Ruby Gold: The Birth of Modern Nanotechnology”. In: “Gold Bull” 40.4 (2007), pp. 267–269.
- [14] I. Khan, K. Saeed and I. Khan. “Nanoparticles: Properties, Applications and Toxicities”. In: “Arabian Journal of Chemistry” (2017).
- [15] T. Kondow and F. Mafun. *Progress in Experimental and Theoretical Studies of Clusters*. World Scientific, 2003. 293 pp.
- [16] A. P. Alivisatos. “Semiconductor Clusters, Nanocrystals, and Quantum Dots”. In: “Science” 271.5251 (1996), pp. 933–937.
- [17] M. Brust and C. J. Kiely. “Some Recent Advances in Nanostructure Preparation from Gold and Silver Particles: A Short Topical Review”. In: “Colloids and Surfaces A: Physicochemical and Engineering Aspects” 202.2 (2002), pp. 175–186.
- [18] W. A. de Heer. “The Physics of Simple Metal Clusters: Experimental Aspects and Simple Models”. In: “Rev. Mod. Phys.” 65.3 (1993), pp. 611–676.
- [19] H. Haberland. *Clusters of Atoms and Molecules: Theory, Experiment, and Clusters of Atoms*. Springer Science & Business Media, 1994. 435 pp.
- [20] A. Kongkanand, K. Tvrđy, K. Takechi, M. Kuno and P. V. Kamat. “Quantum Dot Solar Cells. Tuning Photoresponse through Size and Shape Control of CdSe-TiO₂ Architecture”. In: “J. Am. Chem. Soc.” 130.12 (2008), pp. 4007–4015.
- [21] M. Law, L. E. Greene, J. C. Johnson, R. Saykally and P. Yang. “Nanowire Dye-Sensitized Solar Cells”. In: “Nature Materials” 4.6 (2005), pp. 455–459.
- [22] D. Bera, L. Qian, T.-K. Tseng and P. H. Holloway. “Quantum Dots and Their Multimodal Applications: A Review”. In: “Materials” 3.4 (2010), pp. 2260–2345.
- [23] G. A. Somorjai, R. L. York, D. Butcher and J. Y. Park. “The Evolution of Model Catalytic Systems; Studies of Structure, Bonding and Dynamics from Single Crystal Metal Surfaces to Nanoparticles , and from Low Pressure (10^{-3} Torr) to High Pressure (>math>10^{-3}</math> Torr) to Liquid Interfaces”. In: “Physical Chemistry Chemical Physics” 9.27 (2007), pp. 3500–3513.
- [24] V. Mazumder, Y. Lee and S. Sun. “Recent Development of Active Nanoparticle Catalysts for Fuel Cell Reactions”. In: “Advanced Functional Materials” 20.8 (2010), pp. 1224–1231.
- [25] D. Gust, T. A. Moore and A. L. Moore. “Solar Fuels via Artificial Photosynthesis”. In: “Acc. Chem. Res.” 42.12 (2009), pp. 1890–1898.

- [26] F. Sanchez and K. Sobolev. “Nanotechnology in Concrete – A Review”. In: “Construction and Building Materials” 24.11 (2010), pp. 2060–2071.
- [27] A. Jordan, R. Scholz, P. Wust, H. Föhling and Roland Felix. “Magnetic Fluid Hyperthermia (MFH): Cancer Treatment with AC Magnetic Field Induced Excitation of Biocompatible Superparamagnetic Nanoparticles”. In: “Journal of Magnetism and Magnetic Materials” 201.1 (1999), pp. 413–419.
- [28] W. C. W. Chan, A. Khademhosseini, W. Parak and P. S. Weiss. “Cancer: Nanoscience and Nanotechnology Approaches”. In: “ACS Nano” 11.5 (2017), pp. 4375–4376.
- [29] C. Corot, P. Robert, J.-M. Idée and M. Port. “Recent Advances in Iron Oxide Nanocrystal Technology for Medical Imaging”. In: “Advanced Drug Delivery Reviews” 58.14 (2006), pp. 1471–1504.
- [30] A. G. Skirtach, A. M. Javier, O. Kreft, K. Köhler, A. P. Alberola, H. Möhwald, W. J. Parak and G. B. Sukhorukov. “Laser-Induced Release of Encapsulated Materials inside Living Cells”. In: “Angewandte Chemie” 118.28 (2006), pp. 4728–4733.
- [31] T. M. Allen and P. R. Cullis. “Liposomal Drug Delivery Systems: From Concept to Clinical Applications”. In: “Advanced Drug Delivery Reviews” 65.1 (2013), pp. 36–48.
- [32] A. Nel, T. Xia, L. Mädler and N. Li. “Toxic Potential of Materials at the Nanolevel”. In: “Science” 311.5761 (2006), pp. 622–627.
- [33] S. J. Ghan and S. E. Schwartz. “Aerosol Properties and Processes: A Path from Field and Laboratory Measurements to Global Climate Models”. In: “Bull. Amer. Meteor. Soc.” 88.7 (2007), pp. 1059–1084.
- [34] C. E. Parker, T. W. Pearson, N. Leigh Anderson and C. H. Borchers. “Mass-Spectrometry -Based Clinical Proteomics – a Review and Prospective”. In: “Analyst” 135.8 (2010), pp. 1830–1838.
- [35] A. Lesur and B. Domon. “Advances in High-Resolution Accurate Mass Spectrometry Application to Targeted Proteomics”. In: “PROTEOMICS” 15.5-6 (2015), pp. 880–890.
- [36] M. Bantscheff, S. Lemeer, M. M. Savitski and B. Kuster. “Quantitative Mass Spectrometry in Proteomics: Critical Review Update from 2007 to the Present”. In: “Anal Bioanal Chem” 404.4 (2012), pp. 939–965.
- [37] P. R. Buseck and K. Adachi. “Nanoparticles in the atmosphere”. In: “ELEMENTS” 4.6 (2008), pp. 389–394.
- [38] E. Herbst, Q. Chang and H. M. Cuppen. “Chemistry on Interstellar Grains”. In: “J. Phys.: Conf. Ser.” 6.1 (2005), p. 18.

- [39] A. Potapov, C. Jäger and T. Henning. “Temperature Programmed Desorption of Water Ice from the Surface of Amorphous Carbon and Silicate Grains as Related to Planet-Forming Disks”. In: “ApJ” 865.1 (2018), p. 58.
- [40] C. E. Kolb and D. R. Worsnop. “Chemistry and Composition of Atmospheric Aerosol Particles”. In: “Annual Review of Physical Chemistry” 63.1 (2012), pp. 471–491.
- [41] U. Lohmann and J. Feichter. “Global Indirect Aerosol Effects: A Review”. In: “Atmospheric Chemistry and Physics” 5.3 (2005), pp. 715–737.
- [42] D. V. Spracklen, K. S. Carslaw, M. Kulmala, V.-M. Kerminen, S.-L. Sihto, I. Riipinen, J. Merikanto, G. W. Mann, M. P. Chipperfield, A. Wiedensohler, W. Birmili and H. Lihavainen. “Contribution of Particle Formation to Global Cloud Condensation Nuclei Concentrations”. In: “Geophysical Research Letters” 35.6 (2008).
- [43] S. Fuzzi, U. Baltensperger, K. Carslaw, S. Decesari, H. Denier van der Gon, M. C. Facchini, D. Fowler, I. Koren, B. Langford, U. Lohmann, E. Nemitz, S. Pandis, I. Riipinen, Y. Rudich, M. Schaap, J. G. Slowik, D. V. Spracklen, E. Vignati, M. Wild, M. Williams and S. Gilardoni. “Particulate Matter, Air Quality and Climate: Lessons Learned and Future Needs”. In: “Atmospheric Chemistry and Physics” 15.14 (2015), pp. 8217–8299.
- [44] J. Steinacker, M. Andersen, W.-F. Thi, R. Paladini, M. Juvela, A. Bacmann, V.-M. Pelkonen, L. Pagani, C. Lefèvre, T. Henning and A. Noriega-Crespo. “Grain Size Limits Derived From 3.6 μm and 4.5 μm Coreshine”. In: “A&A” 582 (2015), A70.
- [45] S. Cazaux, M. Minissale, F. Dulieu and S. Hocuk. “Dust as Interstellar Catalyst - II. How Chemical Desorption Impacts the Gas”. In: “A&A” 585 (2016), A55.
- [46] V. Pirronello, C. Liu, L. Shen and G. Vidali. “Laboratory Synthesis of Molecular Hydrogen on Surfaces of Astrophysical Interest”. In: “ApJ” 475.1 (1997), p. L69.
- [47] H. J. Fraser, M. P. Collings, M. R. S. McCoustra and D. A. Williams. “Thermal Desorption of Water Ice in the Interstellar Medium”. In: “Mon Not R Astron Soc” 327.4 (2001), pp. 1165–1172.
- [48] J. Lang and A. Meyer-Plath. *Characterisation of Substances at Nanoscale as Background for the Regulation in the Framework of the Regulation (EC). 1907/2006 (REACH)*. Dortmund: Bundesanstalt für Arbeitsschutz und Arbeitsmedizin, 2013.
- [49] E. Antonsson, H. Bresch, R. Lewinski, B. Wassermann, T. Leisner, C. Graf, B. Langer and E. Rühl. “Free Nanoparticles Studied by Soft X-Rays”. In: “Chemical Physics Letters” 559 (2013), pp. 1–11.

-
- [50] U. K. Krieger, C. Marcolli and J. P. Reid. “Exploring the Complexity of Aerosol Particle Properties and Processes Using Single Particle Techniques”. In: “Chem. Soc. Rev.” 41.19 (2012), pp. 6631–6662.
- [51] K. C. Neuman and S. M. Block. “Optical Trapping”. In: “Rev Sci Instrum” 75.9 (2004), pp. 2787–2809.
- [52] J. Lee, S.-Y. Teh, A. Lee, H. H. Kim, C. Lee and K. K. Shung. “Transverse Acoustic Trapping Using a Gaussian Focused Ultrasound”. In: “Ultrasound in Medicine & Biology” 36.2 (2010), pp. 350–355.
- [53] C. A. Noble and K. A. Prather. “Real-Time Single Particle Mass Spectrometry: A Historical Review of a Quarter Century of the Chemical Analysis of Aerosols”. In: “Mass Spectrometry Reviews” 19.4 (2000), pp. 248–274.
- [54] D. Z. Keifer and M. F. Jarrold. “Single-Molecule Mass Spectrometry”. In: “Mass Spec Rev” 36.6 (2016), pp. 715–733.
- [55] N. Heine. “Vibrational Spectroscopy of Gaseous Hydrogen-Bonded Clusters: On the Role of Isomer-Specificity and Anharmonicity”. Berlin: Freie Universität Berlin, 2014.
- [56] N. Heine and K. R. Asmis. “Cryogenic Ion Trap Vibrational Spectroscopy of Hydrogen-Bonded Clusters Relevant to Atmospheric Chemistry”. In: “International Reviews in Physical Chemistry” 34.1 (2015), pp. 1–34.
- [57] K. R. Asmis and J. Sauer. “Mass-Selective Vibrational Spectroscopy of Vanadium Oxide Cluster Ions”. In: “Mass Spectrometry Reviews” 26.4 (2007), pp. 542–562.
- [58] A. Fujii and K. Mizuse. “Infrared Spectroscopic Studies on Hydrogen-Bonded Water Networks in Gas Phase Clusters”. In: “Int. Rev. Phys. Chem.” 32.2 (2013), pp. 266–307.
- [59] M. A. Duncan. “Frontiers in the Spectroscopy of Mass-Selected Molecular Ions”. In: “International Journal of Mass Spectrometry” 200.1–3 (2000), pp. 545–569.
- [60] E. J. Bieske and O. Dopfer. “High-Resolution Spectroscopy of Cluster Ions”. In: “Chem. Rev.” 100.11 (2000), pp. 3963–3998.
- [61] J. Roithová, A. Gray, E. Andris, J. Jasík and D. Gerlich. “Helium Tagging Infrared Photodissociation Spectroscopy of Reactive Ions”. In: “Acc. Chem. Res.” 49.2 (2016), pp. 223–230.
- [62] N. C. Polfer and J. Oomens. “Vibrational spectroscopy of bare and solvated ionic complexes of biological relevance”. In: “Mass Spectrometry Reviews” 28.3 (2009), pp. 468–494.
- [63] H. Schwarz and K. R. Asmis. “Identification of Active Sites and Structural Characterization of Reactive Ionic Intermediates by Cryogenic Ion Trap Vibrational Spectroscopy”. In: “Chemistry – A European Journal” (2019).

- [64] Z. Wu, A. Płucienik, F. E. Feiten, M. Naschitzki, W. Wachsmann, S. Gewinner, W. Schöllkopf, V. Staemmler, H. Kuhlenbeck and H.-J. Freund. “Vibrational Action Spectroscopy of Solids: New Surface-Sensitive Technique”. In: “Phys. Rev. Lett.” 119.13 (2017), p. 136101.
- [65] Z. Wu, A. Płucienik, Y. Liu, M. Naschitzki, W. Wachsmann, S. Gewinner, W. Schöllkopf, H. Kuhlenbeck and H.-J. Freund. “Surface Action Spectroscopy with Rare Gas Messenger Atoms”. In: “Review of Scientific Instruments” 89.8 (2018), p. 083107.
- [66] A. J. Trevitt, P. J. Wearne and E. J. Bieske. “Coalescence of Levitated Polystyrene Microspheres”. In: “Journal of Aerosol Science” 40.5 (2009), pp. 431–438.
- [67] D. Gerlich and S. Decker. “Trapping Ions at High Temperatures: Thermal Decay of C60 +”. In: “Appl. Phys. B” (2013), pp. 1–10.
- [68] C. R. Howder, D. M. Bell and S. L. Anderson. “Optically Detected, Single Nanoparticle Mass Spectrometer with Pre-Filtered Electrospray Nanoparticle Source”. In: “Review of Scientific Instruments” 85.1 (2014), p. 014104.
- [69] W. Wien. *Ueber die Fragen, welche die translatorische Bewegung des Lichtäthers betreffen: (Referat für die 70. Versammlung deutscher Naturforscher und Aerzte in Düsseldorf, 1898, Section Physik)*. Barth, 1898. 18 pp.
- [70] P. R. A. Millikan. “XXII. A New Modification of the Cloud Method of Determining the Elementary Electrical Charge and the Most Probable Value of That Charge”. In: “The London, Edinburgh, and Dublin Philosophical Magazine and Journal of Science” 19.110 (1910), pp. 209–228.
- [71] K. A. Nier, A. L. Yergey and P. Jane Gale. “A General Chronicle of Mass Spectrometry and Guide to the Scope of the Volume”. In: *The Encyclopedia of Mass Spectrometry*. Boston: Elsevier, 2016, pp. 7–12.
- [72] H.-C. Lin, J.-L. Lin and C.-H. Chen. “Novel Mass Spectrometry Technology Development for Large Organic Particle Analysis”. In: “RSC Adv.” 4.9 (2013), pp. 4523–4534.
- [73] P. H. Dawson, ed. *Quadrupole Mass Spectrometry and Its Applications*. Elsevier, 2013. 372 pp.
- [74] R. E. March and J. F. Todd. *Quadrupole Ion Trap Mass Spectrometry*. Auflage: 2. Auflage. Hoboken, N.J: John Wiley & Sons, 2005. 392 pp.
- [75] W.-P. Peng, Y. Cai and H.-C. Chang. “Optical Detection Methods for Mass Spectrometry of Macroions”. In: “Mass Spectrom. Rev.” 23.6 (2004), pp. 443–465.
- [76] D. Gerlich. “Molecular Ions and Nanoparticles in RF and AC Traps”. In: *Atomic Physics at Accelerators: Stored Particles and Fundamental Physics*. Ed. by H. Knudsen, J. U. Andersen and H.-J. Kluge. Springer Netherlands, 2003, pp. 293–306.

- [77] D. Nolting, R. Malek and A. Makarov. “Ion Traps in Modern Mass Spectrometry”. In: “Mass Spectrometry Reviews” 0.0 (2017), pp. 1–19.
- [78] K. G. Standing and M. L. Vestal. “Time-of-Flight Mass Spectrometry (TOFMS): From Niche to Mainstream”. In: “International Journal of Mass Spectrometry” 377 (2015), pp. 295–308.
- [79] R. A. Zubarev and A. Makarov. “Orbitrap Mass Spectrometry”. In: “Anal. Chem.” 85.11 (2013), pp. 5288–5296.
- [80] A. G. Marshall, C. L. Hendrickson and G. S. Jackson. “Fourier Transform Ion Cyclotron Resonance Mass Spectrometry”. In: *Encyclopedia of Analytical Chemistry*. American Cancer Society, 2006.
- [81] I. S. Gilmore and M. P. Seah. “Ion Detection Efficiency in SIMS:: Dependencies on Energy, Mass and Composition for Microchannel Plates Used in Mass Spectrometry”. In: “International Journal of Mass Spectrometry” 202.1 (2000), pp. 217–229.
- [82] J. Park, Z. Aksamija, H.-C. Shin, H. Kim and R. H. Blick. “Phonon-Assisted Field Emission in Silicon Nanomembranes for Time-of-Flight Mass Spectrometry of Proteins”. In: “Nano Lett.” 13.6 (2013), pp. 2698–2703.
- [83] F. Dubois, R. Knochenmuss and R. Zenobi. “Optimization of an Ion-to-Photon Detector for Large Molecules in Mass Spectrometry”. In: “Rapid Communications in Mass Spectrometry” 13.19 (1999), pp. 1958–1967.
- [84] A. Casaburi, E. Esposito, M. Ejrnaes, K. Suzuki, M. Ohkubo, S. Pagano and R. Cristiano. “A 2×2 mm² Superconducting Strip-Line Detector for High-Performance Time-of-Flight Mass Spectrometry”. In: “Supercond. Sci. Technol.” 25.11 (2012), p. 115004.
- [85] W. H. Benner, D. M. Horn, J. M. Jaklevic, M. Frank, C. Mears, S. Labov and A. T. Barfknecht. “Simultaneous Measurement of Flight Time and Energy of Large Matrix-Assisted Laser Desorption Ionization Ions with a Superconducting Tunnel Junction Detector”. In: “J Am Soc Mass Spectrom” 8.10 (1997), pp. 1094–1102.
- [86] M. Frank, S. E. Labov, G. Westmacott and W. H. Benner. “Energy-Sensitive Cryogenic Detectors for High-Mass Biomolecule Mass Spectrometry”. In: “Mass Spectrom. Rev.” 18.3-4 (1999), pp. 155–186.
- [87] M. Frank. “Mass Spectrometry with Cryogenic Detectors”. In: “Nuclear Instruments and Methods in Physics Research Section A: Accelerators, Spectrometers, Detectors and Associated Equipment” 444.1 (2000), pp. 375–384.
- [88] J. Snijder, R. J. Rose, D. Veessler, J. E. Johnson and A. J. R. Heck. “Studying 18 MDa Virus Assemblies with Native Mass Spectrometry”. In: “Angew. Chem. Int. Ed.” 52.14 (2013), pp. 4020–4023.

- [89] A. Makarov and E. Denisov. “Dynamics of Ions of Intact Proteins in the Orbitrap Mass Analyzer”. In: “J Am Soc Mass Spectrom” 20.8 (2009), pp. 1486–1495.
- [90] A. Dyachenko, G. Wang, M. Belov, A. Makarov, R. N. de Jong, E. T. J. van den Bremer, P. W. H. I. Parren and A. J. R. Heck. “Tandem Native Mass-Spectrometry on Antibody–Drug Conjugates and Submillion Da Antibody–Antigen Protein Assemblies on an Orbitrap EMR Equipped with a High-Mass Quadrupole Mass Selector”. In: “Anal. Chem.” 87.12 (2015), pp. 6095–6102.
- [91] R. Chen, X. Cheng, D. W. Mitchell, S. A. Hofstadler, Q. Wu, A. L. Rockwood, M. G. Sherman and R. D. Smith. “Trapping, Detection, and Mass Determination of Coliphage T4 DNA Ions of 10^8 Da by Electrospray Ionization Fourier Transform Ion Cyclotron Resonance Mass Spectrometry”. In: “Anal. Chem.” 67.7 (1995), pp. 1159–1163.
- [92] D. Z. Keifer, D. L. Shinholt and M. F. Jarrold. “Charge Detection Mass Spectrometry with Almost Perfect Charge Accuracy”. In: “Anal. Chem.” 87.20 (2015), pp. 10330–10337.
- [93] J. Chaste, A. Eichler, J. Moser, G. Ceballos, R. Rurali and A. Bachtold. “A Nanomechanical Mass Sensor with Yoctogram Resolution”. In: “Nature Nanotechnology” 7.5 (2012), pp. 301–304.
- [94] B. Ilic, Y. Yang and H. G. Craighead. “Virus Detection Using Nanoelectromechanical Devices”. In: “Appl. Phys. Lett.” 85.13 (2004), pp. 2604–2606.
- [95] E. Sage, A. Brenac, T. Alava, R. Morel, C. Dupré, M. S. Hanay, M. L. Roukes, L. Duraffourg, C. Masselon and S. Hentz. “Neutral Particle Mass Spectrometry with Nanomechanical Systems”. In: “Nature Communications” 6 (2015), p. 6482.
- [96] M. A. Philip, F. Gelbard and S. Arnold. “An Absolute Method for Aerosol Particle Mass and Charge Measurement”. In: “Journal of Colloid and Interface Science” 91.2 (1983), pp. 507–515.
- [97] E. J. Davis and A. K. Ray. “Single Aerosol Particle Size and Mass Measurements Using an Electrodynamic Balance”. In: “Journal of Colloid and Interface Science” 75.2 (1980), pp. 566–576.
- [98] W.-P. Peng, Y. Cai, Y. T. Lee and H.-C. Chang. “Laser-Induced Fluorescence/Ion Trap as a Detector for Mass Spectrometric Analysis of Nanoparticles”. In: “International Journal of Mass Spectrometry” 229.1–2 (2003), pp. 67–76.
- [99] L. D. Plath, A. Ozdemir, A. A. Aksenov and M. E. Bier. “Determination of Iron Content and Dispersity of Intact Ferritin by Superconducting Tunnel Junction Cryodetection Mass Spectrometry”. In: “Anal. Chem.” 87.17 (2015), pp. 8985–8993.

-
- [100] Y. Ge, I. N. Rybakova, Q. Xu and R. L. Moss. “Top-down High-Resolution Mass Spectrometry of Cardiac Myosin Binding Protein C Revealed That Truncation Alters Protein Phosphorylation State”. In: “PNAS” 106.31 (2009), pp. 12658–12663.
- [101] J. W. Smith, E. E. Siegel, J. T. Maze and M. F. Jarrold. “Image Charge Detection Mass Spectrometry: Pushing the Envelope with Sensitivity and Accuracy”. In: “Anal. Chem.” 83.3 (2011), pp. 950–956.
- [102] M. S. Hanay, S. Kelber, A. K. Naik, D. Chi, S. Hentz, E. C. Bullard, E. Colinet, L. Duraffourg and M. L. Roukes. “Single-Protein Nanomechanical Mass Spectrometry in Real Time”. In: “Nature Nanotechnology” 7.9 (2012), pp. 602–608.
- [103] R. F. Wuerker, H. Shelton and R. V. Langmuir. “Electrodynamic Containment of Charged Particles”. In: “Journal of Applied Physics” 30.3 (1959), pp. 342–349.
- [104] S. Schlemmer, J. Illema, S. Wellert and D. Gerlich. “Nondestructive High-Resolution and Absolute Mass Determination of Single Charged Particles in a Three-Dimensional Quadrupole Trap”. In: “J. Appl. Phys.” 90.10 (2001), pp. 5410–5418.
- [105] S. Schlemmer, S. Wellert, F. Windisch, M. Grimm, S. Barth and D. Gerlich. “Interaction of Electrons and Molecules with a Single Trapped Nanoparticle”. In: “Appl. Phys. A” 78.5 (2004), pp. 629–636.
- [106] A. J. Trevitt, P. J. Wearne and E. J. Bieske. “Calibration of a Quadrupole Ion Trap for Particle Mass Spectrometry”. In: “International Journal of Mass Spectrometry” 262.3 (2007), pp. 241–246.
- [107] W.-P. Peng, Y.-C. Yang, M.-W. Kang, Y.-K. Tzeng, Z. Nie, H.-C. Chang, W. Chang and C.-H. Chen. “Laser-Induced Acoustic Desorption Mass Spectrometry of Single Bioparticles”. In: “Angewandte Chemie International Edition” 45.9 (2006), pp. 1423–1426.
- [108] Y. Cai, W.-P. Peng, S.-J. Kuo, Y. T. Lee and H.-C. Chang. “Single-Particle Mass Spectrometry of Polystyrene Microspheres and Diamond Nanocrystals”. In: “Anal. Chem.” 74.1 (2002), pp. 232–238.
- [109] R. Ramisetty, A. Abdelmonem, X. Shen, H. Saathoff, T. Leisner and C. Mohr. “Exploring Femtosecond Laser Ablation in Single-Particle Aerosol Mass Spectrometry”. In: “Atmospheric Measurement Techniques” 11.7 (2018), pp. 4345–4360.
- [110] W. Paul. “Electromagnetic Traps for Charged and Neutral Particles”. Nobel Lecture. 1989.
- [111] W. Paul and M. Raether. “Das elektrische Massenfilter”. In: “Z. Physik” 140.3 (1955), pp. 262–273.

- [112] W. Paul. “Ein Ionenkäfig”. In: “Forschungsberichte des Wirtschafts- und Verkehrsministeriums Nordrhein-Westfalen” 415 (1958).
- [113] E. Fischer. “Die dreidimensionale Stabilisierung von Ladungsträgern in einem Vierpolfeld”. In: “Z. Physik” 156.1 (1959), pp. 1–26.
- [114] M. Soni, V. Frankevich, M. Nappi, R. E. Santini, J. W. Amy and R. G. Cooks. “Broad-Band Fourier Transform Quadrupole Ion Trap Mass Spectrometry”. In: “Anal. Chem.” 68.19 (1996), pp. 3314–3320.
- [115] D. J. Wineland, W. M. Itano and R. S. Van Dyck. “High-Resolution Spectroscopy of Stored Ions”. In: *Advances in Atomic and Molecular Physics*. Ed. by D. Bates and B. Bederson. Vol. 19. Academic Press, 1983, pp. 135–186.
- [116] P. H. Dawson, J. W. Hedman and N. R. Whetten. “A Simple Mass Spectrometer”. In: “Review of Scientific Instruments” 40.11 (1969), pp. 1444–1450.
- [117] G. C. Stafford Jr., P. E. Kelley, J. E. P. Syka, W. E. Reynolds and J. F. J. Todd. “Recent Improvements in and Analytical Applications of Advanced Ion Trap Technology”. In: “International Journal of Mass Spectrometry and Ion Processes” 60.1 (1984), pp. 85–98.
- [118] R. E. March and J. F. J. Todd. *Practical Aspects of Ion Trap Mass Spectrometry*. CRC Press, 1995. 452 pp.
- [119] R. D. Knight. “The General Form of the Quadrupole Ion Trap Potential”. In: “International Journal of Mass Spectrometry and Ion Physics” 51.1 (1983), pp. 127–131.
- [120] W. R. Plass, H. Li and R. G. Cooks. “Theory, Simulation and Measurement of Chemical Mass Shifts in RF Quadrupole Ion Traps”. In: “International Journal of Mass Spectrometry” 228.2–3 (2003), pp. 237–267.
- [121] D. Gerlich. “Inhomogeneous RF Fields: A Versatile Tool for the Study of Processes with Slow Ions”. In: *Adv. Chem. Phys.* Ed. by C.-Y. Ng, M. Baer, I. Prigogine and S. A. Rice. John Wiley & Sons, Inc., 1992, pp. 1–176.
- [122] É. Mathieu. “Mémoire sur le mouvement vibratoire d’une membrane de forme elliptique.” In: “Journal de Mathématiques Pures et Appliquées” 13 (1868), pp. 137–203.
- [123] D. Leibfried, R. Blatt, C. Monroe and D. Wineland. “Quantum Dynamics of Single Trapped Ions”. In: “Rev. Mod. Phys.” 75.1 (2003), pp. 281–324.
- [124] H. G. Dehmelt. “Radiofrequency Spectroscopy of Stored Ions I: Storage”. In: *Advances in Atomic and Molecular Physics*. Ed. by D. R. Bates and I. Estermann. Vol. 3. Academic Press, 1968, pp. 53–72.
- [125] E. C. Beaty. “Simple Electrodes for Quadrupole Ion Traps”. In: “Journal of Applied Physics” 61.6 (1987), pp. 2118–2122.
- [126] S. Fanghänel. *Private Communication*. 2016.

- [127] Y. Wang, J. Franzen and K. P. Wanczek. “The Non-Linear Resonance Ion Trap. Part 2. A General Theoretical Analysis”. In: “International Journal of Mass Spectrometry and Ion Processes” 124.2 (1993), pp. 125–144.
- [128] S. Bandelow, G. Marx and L. Schweikhard. “The Stability Diagram of the Digital Ion Trap”. In: “International Journal of Mass Spectrometry” 336 (2013), pp. 47–52.
- [129] J. Illemann. “Präzisionsmassebestimmung Einzelner Partikel Im Femtogramm-bereich Und Anwendungen in Der Oberflächenphysik”. Technische Universität Chemnitz, 2000.
- [130] C. R. Howder, B. A. Long, D. M. Bell, K. H. Furakawa, R. C. Johnson, Z. Fang and S. L. Anderson. “Photoluminescence of Charged CdSe/ZnS Quantum Dots in the Gas Phase: Effects of Charge and Heating on Absorption and Emission Probabilities”. In: “ACS Nano” 8.12 (2014), pp. 12534–12548.
- [131] C. R. Howder, B. A. Long, D. Gerlich, R. N. Alley and S. L. Anderson. “Single Nanoparticle Mass Spectrometry as a High Temperature Kinetics Tool: Sublimation, Oxidation, and Emission Spectra of Hot Carbon Nanoparticles”. In: “J. Phys. Chem. A” 119.50 (2015), pp. 12538–12550.
- [132] S. Bandelow, G. Marx and L. Schweikhard. “The 3-State Digital Ion Trap”. In: “International Journal of Mass Spectrometry” 353 (2013), pp. 49–53.
- [133] G. Hars and Z. Tass. “Application of Quadrupole Ion Trap for the Accurate Mass Determination of Submicron Size Charged Particles”. In: “Journal of Applied Physics” 77.9 (1995), pp. 4245–4250.
- [134] Z. Nie, Y.-K. Tzeng, H.-C. Chang, C.-C. Chiu, C.-Y. Chang, C.-M. Chang and M.-H. Tao. “Microscopy-Based Mass Measurement of a Single Whole Virus in a Cylindrical Ion Trap”. In: “Angewandte Chemie” 118.48 (2006), pp. 8311–8314.
- [135] D. M. Bell, C. R. Howder, R. C. Johnson and S. L. Anderson. “Single CdSe/ZnS Nanocrystals in an Ion Trap: Charge and Mass Determination and Photophysics Evolution with Changing Mass, Charge, and Temperature”. In: “ACS Nano” 8.3 (2014), pp. 2387–2398.
- [136] C. R. Howder. “THE PHOTOPHYSICS AND SURFACE CHEMISTRY OF TRAPPED NANOPARTICLE IONS AS STUDIED BY ION TRAP NANOPARTICLE MASS SPECTROMETRY”. Salt Lake City: University of Utah, 2016.
- [137] D. M. Bell. “NEW METHODS AND DEVELOPMENTS IN NANOPARTICLE MASS SPECTROMETRY AND MODE- AND BOND- SPECIFIC REACTIONS OF HOD⁺”. Salt Lake City: University of Utah, 2014.
- [138] B. Hoffmann. “Characterisation of a Novel Nanoparticle Mass Spectrometer and Adsorption Experiments at Single Nanoparticles in the Gas Phase”. Master Thesis. Universität Leipzig, 2018.

- [139] S. Arnold. “Determination of Particle Mass and Charge by One Electron Differentials”. In: “Journal of Aerosol Science” 10.1 (1979), pp. 49–53.
- [140] W.-P. Peng, Y. T. Lee, J. W. Ting and H.-C. Chang. “Averaging Peak-to-Peak Voltage Detector for Absolute Mass Determination of Single Particles with Quadrupole Ion Traps”. In: “Review of Scientific Instruments” 76.2 (2005), p. 023108.
- [141] I. Cermak. *Private Communication*. 2016.
- [142] C. F. Bohren and D. R. Huffman. *Absorption and Scattering of Light by Small Particles*. Wiley, 1983. 548 pp.
- [143] C. R. Howder, B. A. Long, D. M. Bell and S. L. Anderson. “Thermally Brightened CdSe/ZnS Quantum Dots as Noncontact Probes for Surface Chemistry Studies of Dark Nanoparticles Trapped in the Gas Phase”. In: “J. Phys. Chem. C” 119.26 (2015), pp. 14561–14570.
- [144] G. C. Possa and L. F. Roncaratti. “Stability Diagrams for Paul Ion Traps Driven by Two-Frequencies”. In: “J. Phys. Chem. A” (2016).
- [145] J. H. Moore, C. C. Davis and M. A. Coplan. *Building Scientific Apparatus: A Practical Guide to Design and Construction*. Westview Press, 2002. 676 pp.
- [146] W. Wißdorf. “Simulation of Ion Dynamics in Atmospheric Pressure Ionization Sources”. 2014.
- [147] L. Bernier, H. Pinfeld, M. Pauly, S. Rauschenbach and J. Reiss. “Gas Flow and Ion Transfer in Heated ESI Capillary Interfaces”. In: “J. Am. Soc. Mass Spectrom.” 29.4 (2018), pp. 761–773.
- [148] M. Dole, L. L. Mack, R. L. Hines, R. C. Mobley, L. D. Ferguson and M. B. Alice. “Molecular Beams of Macroions”. In: “The Journal of Chemical Physics” 49.5 (1968), pp. 2240–2249.
- [149] J. B. Fenn, M. Mann, C. K. Meng, S. F. Wong and C. M. Whitehouse. “Electrospray Ionization for Mass Spectrometry of Large Biomolecules”. In: “Science” 246.4926 (1989), pp. 64–71.
- [150] J. B. Fenn. “Electrospray Wings for Molecular Elephants”. Nobel Lecture. 2002.
- [151] S. Warnke, G. von Helden and K. Pagel. “Protein Structure in the Gas Phase: The Influence of Side-Chain Microsolvation”. In: “J. Am. Chem. Soc.” 135.4 (2013), pp. 1177–1180.
- [152] A. Ozdemir, J.-L. Lin, M. Gulfen, S.-H. Lai, C.-J. Hsiao, N. G. Chen and C.-H. Chen. “ESI MS for Microsized Bioparticles”. In: “Anal. Chem.” 89.24 (2017), pp. 13195–13202.
- [153] T. Doussineau, M. Kerleroux, X. Dagany, C. Clavier, M. Barbaire, J. Maurelli, R. Antoine and P. Dugourd. “Charging Megadalton Poly(Ethylene Oxide)s by Electrospray Ionization. A Charge Detection Mass Spectrometry Study”. In: “Rapid Communications in Mass Spectrometry” 25.5 (2011), pp. 617–623.

-
- [154] L. Konermann, E. Ahadi, A. D. Rodriguez and S. Vahidi. “Unraveling the Mechanism of Electrospray Ionization”. In: “Anal. Chem.” 85.1 (2013), pp. 2–9.
- [155] Y. Tani, S. Kobayashi and H. Kawazoe. “Characterization of Electrospray Ion-Beam-Deposited CdSe/ZnS Quantum Dot Thin Films from a Colloidal Solution”. In: “Journal of Vacuum Science & Technology A” 26.4 (2008), pp. 1058–1061.
- [156] M. R. Fagiani. “Cryogenic Ion Vibrational Spectroscopy of Gas-Phase Clusters: Structure, Anharmonicity and Fluxionality”. Berlin: Freie Universität Berlin, 2017.
- [157] P. Kebarle and U. H. Verkerk. “Electrospray: From Ions in Solution to Ions in the Gas Phase, What We Know Now”. In: “Mass Spectrometry Reviews” 28.6 (2009), pp. 898–917.
- [158] G. I. Taylor and A. D. McEwan. “The Stability of a Horizontal Fluid Interface in a Vertical Electric Field”. In: “Journal of Fluid Mechanics” 22.1 (1965), pp. 1–15.
- [159] G. T. T. Gibson, S. M. Mugo and R. D. Oleschuk. “Nanoelectrospray Emitters: Trends and Perspective”. In: “Mass Spectrom Rev” 28.6 (2009 Nov-Dec), pp. 918–936.
- [160] G. Vazquez, E. Alvarez and J. M. Navaza. “Surface Tension of Alcohol Water + Water from 20 to 50 °C”. In: “J. Chem. Eng. Data” 40.3 (1995), pp. 611–614.
- [161] F. S. Roberts and S. L. Anderson. “Hollow Cathode Lamp with Integral, High Optical Efficiency Isolation Valve: A Modular Vacuum Ultraviolet Source”. In: “Rev. Sci. Instrum.” 84.12 (2013), p. 126101.
- [162] T. K. Esser. “The Effect of Partially Deiodination on the Structure of Periodinated Closo-Dodecaborate Probed by Infrared Photodissociation Spectroscopy - Implementation of a Genetic Algorithm for Ion Optics Optimization”. Master Thesis. Freie Universität Berlin, 2013.
- [163] D. Gerlich. “Applications of Rf Fields and Collision Dynamics in Atomic Mass Spectrometry”. In: “Journal of Analytical Atomic Spectrometry” 19.5 (2004), pp. 581–590.
- [164] K. J. Boyd, A. Łapicki, M. Aizawa and S. L. Anderson. “A Phase-Space-Compressing, Mass-Selecting Beamline for Hyperthermal, Focused Ion Beam Deposition”. In: “Review of Scientific Instruments” 69.12 (1998), pp. 4106–4115.
- [165] A. V. Tolmachev, I. V. Chernushevich, A. F. Dodonov and K. G. Standing. “A Collisional Focusing Ion Guide for Coupling an Atmospheric Pressure Ion Source to a Mass Spectrometer”. In: “Nuclear Instruments and Methods in Physics Research Section B: Beam Interactions with Materials and Atoms” 124.1 (1997), pp. 112–119.

- [166] S. Rauschenbach. “ELECTROSPRAY ION BEAM DEPOSITION AND MASS SPECTROMETRY OF NONVOLATILE MOLECULES AND NANOMATERIALS”. 2007.
- [167] C. M. Lock and E. W. Dyer. “Simulation of Ion Trajectories through a High Pressure Radio Frequency Only Quadrupole Collision Cell by SIMION 6.0”. In: “Rapid Communications in Mass Spectrometry” 13.5 (1999), pp. 422–431.
- [168] I. E. Dayton, F. C. Shoemaker and R. F. Mozley. “The Measurement of Two-Dimensional Fields. Part II: Study of a Quadrupole Magnet”. In: “Review of Scientific Instruments” 25.5 (1954), pp. 485–489.
- [169] D. A. Dahl. “SIMION for the Personal Computer in Reflection”. In: “International Journal of Mass Spectrometry” 200.1–3 (2000), pp. 3–25.
- [170] R. Ierusalimschy, L. H. de Figueiredo and W. C. Filho. “Lua—An Extensible Extension Language”. In: “Software: Practice and Experience” 26.6 (1996), pp. 635–652.
- [171] S. Decker. “Fullerene Im Strahlungsgleichgewicht- Untersuchungen in Einem Quadrupolspeicher”. Technische Universität Chemnitz, 2009.
- [172] S. Fanghänel, O. Asvany and S. Schlemmer. “Optimization of RF Multipole Ion Trap Geometries”. In: “Journal of Molecular Spectroscopy” 332 (2017), pp. 124–133.
- [173] S. Fanghänel. “Low Temperature Collisions and Reactions in a 22-Pole Ion Trap”. Dissertation. Universität zu Köln, 2017.
- [174] D. J. Goebbert, G. Meijer and K. R. Asmis. “10 K Ring Electrode Trap Tandem Mass Spectrometer for Infrared Spectroscopy of Mass Selected Ions”. In: “AIP Conf. Proc.” 1104.1 (2009), pp. 22–29.
- [175] S. D. S. Gordon and A. Osterwalder. “A 3D Printed Beam Splitter for Polar Neutral Molecules”. In: (2016).
- [176] S. Burghartz and B. Schulz. “Thermophysical Properties of Sapphire, AlN and MgAl₂O₄ down to 70 K”. In: “Journal of Nuclear Materials” 212-215 (1994), pp. 1065–1068.
- [177] E. R. Dobrovinskaya, L. A. Lytvynov and V. Pishchik. “Properties of Sapphire”. In: *Sapphire: Material, Manufacturing, Applications*. Ed. by V. Pishchik, L. A. Lytvynov and E. R. Dobrovinskaya. Boston, MA: Springer US, 2009, pp. 55–176.
- [178] S. L. Anderson and D. E. Heisler. *Private Communication*. 2016.
- [179] B. A. Long, D. J. Rodriguez, C. Y. Lau and S. L. Anderson. “Thermal Emission Spectroscopy for Single Nanoparticle Temperature Measurement: Optical System Design and Calibration”. In: “Appl. Opt., AO” 58.3 (2019), pp. 642–649.
- [180] S. Berkenkamp, F. Kirpekar and F. Hillenkamp. “Infrared MALDI Mass Spectrometry of Large Nucleic Acids”. In: “Science” 281.5374 (1998), pp. 260–262.

-
- [181] L. Mauritsen, D. Snow, A. Woitke, M. Chase and I. Henslee. *Low Vibration, Low Thermal Fluctuation System for Pulse Tube and Gifford-McMahon Cryocoolers*. Vol. 15. 2009.
- [182] P. J. Kelleher, C. J. Johnson, J. A. Fournier, M. A. Johnson and A. B. McCoy. “Persistence of Dual Free Internal Rotation in $\text{NH}_4^+(\text{H}_2\text{O})\cdot\text{He}_{n=0-3}$ Ion–Molecule Complexes: Expanding the Case for Quantum Delocalization in He Tagging”. In: “J. Phys. Chem. A” (2015).
- [183] A. Günther, P. Nieto, D. Müller, A. Sheldrick, D. Gerlich and O. Dopfer. “BerlinTrap: A New Cryogenic 22-Pole Ion Trap Spectrometer”. In: “Journal of Molecular Spectroscopy” 332 (2017), pp. 8–15.
- [184] D. Gerlich. “Infrared Spectroscopy of Cold Trapped Molecular Ions Using He-tagging”. In: “Journal of the Chinese Chemical Society” (2018).
- [185] M. Drewsen. “Ion Coulomb Crystals”. In: “Physica B: Condensed Matter” 460 (2015), pp. 105–113.
- [186] D. J. Wineland, J. C. Bergquist, W. M. Itano, J. J. Bollinger and C. H. Manney. “Atomic-Ion Coulomb Clusters in an Ion Trap”. In: “Phys. Rev. Lett.” 59.26 (1987), pp. 2935–2938.
- [187] H. Ikezi. “Coulomb Solid of Small Particles in Plasmas”. In: “The Physics of Fluids” 29.6 (1986), pp. 1764–1766.
- [188] C. K. Goertz. “Dusty Plasmas in the Solar System”. In: “Reviews of Geophysics” 27.2 (1989), pp. 271–292.
- [189] T. Trottenberg, A. Melzer and A. Piel. “Measurement of the Electric Charge on Particulates Forming Coulomb Crystals in the Sheath of a Radiofrequency Plasma”. In: “Plasma Sources Sci. Technol.” 4.3 (1995), p. 450.
- [190] E. Järvinen, O. Jourdan, D. Neubauer, B. Yao, C. Liu, M. O. Andreae, U. Lohmann, M. Wendisch, G. M. McFarquhar, T. Leisner and M. Schnaiter. “Additional Global Climate Cooling by Clouds Due to Ice Crystal Complexity”. In: “Atmospheric Chemistry and Physics” 18.21 (2018), pp. 15767–15781.
- [191] I. Satoh, K. Fushinobu and Y. Hashimoto. “Freezing of a Water Droplet Due to Evaporation—Heat Transfer Dominating the Evaporation–Freezing Phenomena and the Effect of Boiling on Freezing Characteristics”. In: “International Journal of Refrigeration” 25.2 (2002), pp. 226–234.
- [192] W. Demtröder. *Experimentalphysik 1: Mechanik Und Wärme*. 8th ed. Springer Spektrum, 2018.
- [193] J. Pach and P. K. Agarwal. *Combinatorial Geometry*. John Wiley & Sons, 2011. 374 pp.
- [194] R. I. Masel and R. I. Masel. *Principles of Adsorption and Reaction on Solid Surfaces*. John Wiley & Sons, 1996. 826 pp.

- [195] A. Vertes, R. Gijbels and R. D. Levine. “Homogeneous Bottleneck Model of Matrix-Assisted Ultraviolet Laser Desorption of Large Molecules”. In: “Rapid Communications in Mass Spectrometry” 4.6 (1990), pp. 228–233.
- [196] P. A. Redhead. “Thermal Desorption of Gases”. In: “Vacuum” 12.4 (1962), pp. 203–211.
- [197] S. Wellert. “Wechselwirkung von Elektronen und Molekülen mit einzelnen SiO₂-Nanopartikeln: Massenanalyse in einer Vierpolfalle”. Chemnitz: Technischen Universität Chemnitz, 2003.
- [198] E. Vella, F. Messina, M. Cannas and R. Boscaino. “Unraveling Exciton Dynamics in Amorphous Silicon Dioxide: Interpretation of the Optical Features from 8 to 11 eV”. In: “Phys. Rev. B” 83.17 (2011), p. 174201.
- [199] R. Kitamura, L. Pilon and M. Jonasz. “Optical Constants of Silica Glass from Extreme Ultraviolet to Far Infrared at near Room Temperature”. In: “Appl. Opt., AO” 46.33 (2007), pp. 8118–8133.
- [200] Schlichting, Hartmut. “Methoden Und Mechanismen Der Thermischen Desorption - Adsorptions-, Desorptions-Kinetik, Epitaxie Und Ordnung von Edeltgasschichten Auf Ru(001)”. München: Technische Universität München, 1990.
- [201] Y. Zhang, J. R. G. Evans and S. Yang. “Corrected Values for Boiling Points and Enthalpies of Vaporization of Elements in Handbooks”. In: “J. Chem. Eng. Data” 56.2 (2011), pp. 328–337.
- [202] D. Gerlich and M. Smith. “Laboratory Astrochemistry: Studying Molecules under Inter- and Circumstellar Conditions”. In: “Phys. Scr.” 73.1 (2006), p. C25.
- [203] V. Wakelam, J.-C. Loison, R. Mereau and M. Ruaud. “Binding Energies: New Values and Impact on the Efficiency of Chemical Desorption”. In: “Molecular Astrophysics” 6 (2017), pp. 22–35.
- [204] H. Lu, G. M. Carroll, N. R. Neale and M. C. Beard. “Infrared Quantum Dots: Progress, Challenges, and Opportunities”. In: “ACS Nano” (2019).
- [205] S. Yang, W. Li, B. Cao, H. Zeng and W. Cai. “Origin of Blue Emission from Silicon Nanoparticles: Direct Transition and Interface Recombination”. In: “J. Phys. Chem. C” 115.43 (2011), pp. 21056–21062.
- [206] H. Bresch, B. Wassermann, B. Langer, C. Graf, R. Flesch, U. Becker, B. Österreicher, T. Leisner and E. Rühl. “Elastic Light Scattering from Free Sub-Micron Particles in the Soft X-Ray Regime”. In: “Faraday Discuss.” 137.0 (2008), pp. 389–402.
- [207] M. Grimm, B. Langer, S. Schlemmer, T. Lischke, U. Becker, W. Widdra, D. Gerlich, R. Flesch and E. Rühl. “Charging Mechanisms of Trapped Element-Selectively Excited Nanoparticles Exposed to Soft X Rays”. In: “Phys. Rev. Lett.” 96.6 (2006), p. 066801.

- [208] R. L. Haupt and S. E. Haupt. *Practical Genetic Algorithms, Second Edition*. 2004.
- [209] M. OpenCourseWare. *Multidisciplinary System Design Optimization*. 2010. URL: <http://ocw.mit.edu/courses/engineering-systems-division/esd-77-multidisciplinary-system-design-optimization-spring-2010/> (visited on 04/08/2013).

List of Publications

In order of descending publication date.

7. **T. K. Esser**, H. Knorke, D. R. Galimberti, F. Siro-Brigiano, K. R. Asmis, M. - P. Gageot and J. M. Lisy. “Influence of argon and D₂ tagging on the hydrogen bond network in Cs⁺(H₂O)₃; Kinetic trapping below 40 K”. In: “Phys. Chem. Chem. Phys.” (2018), pp. 28476–28486.
6. **T. K. Esser**, H. Knorke, K. R. Asmis, W. Schöllkopf, Q. Yu, C. Qu, J. M. Bowman and M. Kaledin. “Deconstructing Prominent Bands in the Terahertz Spectra of H₇O₃⁺ and H₉O₄⁺: Intermolecular Modes in Eigen Clusters”. In: “The Journal of Physical Chemistry Letters” (2018), pp. 798–803.
5. M. R. Fagiani, H. Knorke, **T. K. Esser**, N. Heine, C. T. Wolke, S. Gewinner, W. Schöllkopf, M. - P. Gageot, R. Spezia, M. A. Johnson and K. R. Asmis. “Gas phase vibrational spectroscopy of the protonated water pentamer: the role of isomers and nuclear quantum effects”. In: “Physical Chemistry Chemical Physics” 18 (2016), pp. 26743–26754.
4. C. T. Wolke, F. S. Menges, N. Tötsch, O. Gorlova, J. A. Fournier, G. H. Weddle, M. A. Johnson, N. Heine, **T. K. Esser**, H. Knorke, K. R. Asmis, A. B. McCoy, D. J. Arismendi-Arrieta, R. Prosmiti and F. Paesani “Thermodynamics of Water Dimer Dissociation in the Primary Hydration Shell of the Iodide Ion with Temperature-Dependent Vibrational Predissociation Spectroscopy”. In: “The Journal of Physical Chemistry A” 119 (2015), pp. 1859–1866.
3. M. R. Fagiani, L. Liu Zeonjuk, **T. K. Esser**, D. Gabel, T. Heine, K. R. Asmis, and J. Warneke. “Opening of an icosahedral boron framework: A combined infrared spectroscopic and computational study”. In: “Chemical Physics Letters” 625 (2015), pp. 48–52.
2. G. B. S. Miller, **T. K. Esser**, H. Knorke, S. Gewinner, W. Schöllkopf, N. Heine, K. R. Asmis and E. Uggerud. “Spectroscopic Identification of a Bidentate Binding Motif in the Anionic Magnesium-CO₂ Complex ([ClMgCO₂]⁻)”. In: “Angewandte Chemie” 126 (2014), pp. 14635–14638.
1. J. A. Fournier, C. T. Wolke, C. J. Johnson, M. A. Johnson, N. Heine, S. Gewinner, W. Schöllkopf, **T. K. Esser**, M. R. Fagiani, H. Knorke and K. R. Asmis. “Site-specific vibrational spectral signatures of water molecules in the magic H₃O⁺(H₂O)₂₀ and

Cs⁺(H₂O)₂₀ clusters”. In: “Proceedings of the National Academy of Sciences” 111 (2014), pp. 18132–18137.

Talks and Poster Contributions

- 2018 **Towards a Molecular Understanding of Atmospheric Aerosols** "A High Resolution Cryogenic Single Nanoparticle Mass Spectrometer", talk
- 2017 **Horizons in Cold Cluster Spectroscopy** "A Cryogenic Nanoparticle Mass and IR Spectrometer ", talk
Max-Planck-Institute for Solid State Research - Nanotechnology Department Seminar "A High Resolution Cryogenic Nanoparticle Mass and IR Spectrometer - Genetic Algorithms for Ion Trap Experiments", talk
DPG Frühjahrstagung der Sektion AMOP. "A Cryogenic Single Nanoparticle Mass and IR Spectrometer", talk
- 2016 **European Conference on Trapped Ions (ECTI).** "A Cryogenic Single Nanoparticle Mass and IR Spectrometer", poster
Technische Universität Berlin - Dopfer Group Seminar "A High Resolution Cryogenic Nanoparticle Mass and IR Spectrometer - Genetic Algorithms for Ion Trap Experiments", talk
- 2015 **University of Utah - Anderson Group Seminar** "A High Resolution Cryogenic Nanoparticle Mass and IR Spectrometer", talk
Bunsentagung. "Gas Phase Vibrational Spectroscopy of small Protonated Water Clusters Measured into the Terahertz Spectral Range (200 to 1200 cm⁻¹)", talk
- 2014 **Gordon Research Seminar: Molecular & Ionic Clusters.** "Metal-Ion Selectivity of a Fluorescent Sensor Probed by Gas Phase IR Spectroscopy", talk
Gordon Research Conference: Molecular & Ionic Clusters. "Metal-Ion Selectivity of a Fluorescent Sensor Probed by Gas Phase IR Spectroscopy", poster
DPG Frühjahrstagung der Sektion AMOP. "Characterization of a 6 K Ring-Electrode Ion-Trap used for IR Photodissociation Experiments", talk and poster

Curriculum Vitae

Tim Kaspar David Esser, born June 16th, 1989 in Duisburg, Germany

- 2014 – pres **Ph.D.** student at the Wilhelm-Ostwald-Institut der Universität Leipzig, Leipzig (Prof. Dr. Knut R. Asmis)
- 2013 – 2014 **Ph.D.** student at the Fritz-Haber-Institut der Max-Planck-Gesellschaft, Berlin (Prof. Dr. Knut R. Asmis)
- 2011 – 2013 **M.Sc.** in Physics at the Freie Universität Berlin / Fritz-Haber-Institut der-Max-Planck Gesellschaft, Berlin (Prof. Dr. Knut R. Asmis)
Thesis: "The Effect of Partially Deiodination on the Structure of Peri-
odinated Closo-Dodecaborate Probed by Infrared Photodissociation
Spectroscopy"
- 2008 – 2011 **B.Sc.** in Physics at the Freie Universität Berlin, Berlin (Prof. Dr. Daniel Sebastiani)
Thesis: "Crystal Structure Review of Hydrogen Storage Material
 Li_2NH with Ab Initio Simulations"
- 2008 Abitur at the Leonardo-da-Vinci-Gymnasium, Berlin

Ort, Datum

Tim Esser

Danksagung / Acknowledgments

Die vorliegende Arbeit wurde nur durch die Unterstützung zahlreicher Menschen möglich. Zuerst möchte ich Prof. Dr. Knut Asmis danken, für die Betreuung dieser Arbeit und das große Vertrauen das er mir von Beginn an entgegengebracht hat. Mit dieser Arbeit hat er es mir ermöglicht meine wissenschaftlichen Interessen zu verfolgen und dabei wertvolle Erfahrungen in einer Vielzahl von Gebieten zu sammeln. Ich bin insbesondere dankbar für die Ermöglichung des dreiwöchigen Forschungsaufenthaltes bei Scott Anderson und der Teilnahme an zahlreichen Konferenzen. Durch den Umzug vom Fritz-Haber-Institut in Berlin an das Wilhelm-Ostwald-Institut an der Universität Leipzig ergaben sich viele weitere spannende Eindrücke. Weiterhin danke ich Prof. Dr. Stephan Schlemmer für die Übernahme des Zweitgutachtens.

Direkt am Experiment mitgearbeitet haben Johanna Rademacher und Benjamin Hoffmann. Beide hatten mich als Vertiefungsstudenten auf dem steinigen Weg der schrittweisen Inbetriebnahme der neuen Spektrometers unterstützt und motiviert. Benjamin hatte dabei so ein große Vertrauen das er für seine Masterarbeit blieb, was schon in seiner ersten Woche durch das erste gefangene Teilchen belohnt wurde. Ich danke dir für ein ironisch scherzhaftes und produktives Umfeld im Labor und die unschätzbare Unterstützung in der letzten Phase dieser Arbeit. Ich wünsche dir viel Erfolg und Freude bei deiner Doktorarbeit an der NPMS Apparatur.

Besonderer Dank gilt den weiteren aktuellen und ehemaligen Arbeitsgruppenmitgliedern die mich in den letzten fünf Jahren auf die eine oder andere Art unterstützt haben. Harald Knorke danke ich für seine beiläufig brillianten Ideen und das initiieren legendärer Teerunden, die Energie für die Spätschicht geliefert haben. Ich danke Martin Mayer für die tägliche, liebevoll und immer korrekt zubereitete Tasse Ingwertee und die Unterstützung im Praktikum während des Zusammenschreibens. Max Grellmann danke ich für seine Hilfe beim Reinigen und Zusammenbauen der Ionenoptiken. Nadja Heine danke ich für das Korrekturlesen. Des Weiteren danke ich für ihre ständige Hilfsbereitschaft: Alexandra Giermann, Manuela Reichelt, Jürgen Jäschke, Julia Farkas, John Kelly, Matias Fagiani, Xiaowei Song, Sreekanta Debnath, Marcel Jorewitz, Arghya Chakraborty und Yake Li.

Ich danke Dieter Gerlich für die hilfreichen Gespräche in der Planungsphase. Außerdem danke ich Ivo Cermak für seine ausführlichen Hinweise zu RF Generatoren und Verstärkern. I want to thank Scott Anderson and his group, especially Bryan Long, for hosting me in Utah and for sharing the plans for the RF amplifier, developed by Dale Heisler. Scott and Bryan accompanied the experiments in Leipzig with great interest and advice. I thank Edward Brewer who joined for a three-month internship, funded by the DAAD RISE program, for support with the instrument assembly.

Diese Arbeit wäre ohne die Unterstützung mehrerer Werkstätten nicht möglich gewesen. Ich danke Detlef Müller, stellvertretend für die Feinmechanik Werkstatt des Fachbereichs Physik der Freien Universität Berlin, für den Bau der Ionenfalle. Marina Zehle, Sandra Böhm, Peter Lorenz und Rainer Sommerweiß, von der Feinmechanik Werkstatt des Fachbereichs Physik der Universität Leipzig, danke ich für die konstruktiven Gespräche während der Planung und Herstellung der Ionenoptiken. Auch Wolfgang Erlebach und Hendrik Haak möchte ich für die vielen nützlichen Hinweise danken. Marko Kutschbauch war unverzichtbar bei allen Elektronikfragen in Leipzig. Vielen Dank dafür und für den RF Verstärker. Ein großer Teil der Elektronik wurde noch am Fritz-Haber-Institut gefertigt. Mein Dank dafür gilt Thomas Zehentbauer, Viktor Platschkowski und Enrico Merten. Ich danke auch Johanna Hofmann, Christian Schewe, Doo-Sik Ahn, Silvio Marx, Alex Woodham, Christian Kerpel und all den anderen Doktoranden am Fritz-Haber-Institut für die schöne Zeit.

Further, I want to thank all people who were involved in the IRPD experiments and who performed the corresponding calculations: Joel Bowman, Qi Yu, Chen Qu, Martina Kaledin, James Lisy, Daria Ruth Galimberti, Flavio Siro-Brigiano, Marie-Pierre Gageot, Einar Uggerud, Glen Miller and Ling Jiang. Ich danke Sandy Gewinner, Wieland Schöllkopf, Nadja Heine, Matias Fagiani und Harald Knorke für die legendäre dreitägige FHI-FEL Messzeit.

Schließlich danke ich Robert Schlag, für den Feinschliff der Arbeit und für das Lösen aller sonstigen Probleme, Thabata Funke, auf die ich mich immer verlassen kann, und Kerstin Seier, für die Korrekturen und für die versteckten Botschaften im Labor. Außerdem danke ich Libusche Ralenovsky für ihre Begleitung in den letzten Jahren. Ich danke meiner Familie für ihre unendliche Geduld. Ihr alle habt dafür gesorgt das ich mich während der Promotion nicht nur wissenschaftlich weiterentwickeln konnte.